Magnetic polaron in (Cd,Mn)Te quantum dot inserted in ZnTe nanowire

Alberto Artioli

Communauté
UNIVERSITÉ Grenoble Alpes

THÈSE

Pour obtenir le grade de

DOCTEUR DE la Communauté UNIVERSITÉ GRENOBLE ALPES

Spécialité : **Physique/Nanophysique**

Arrêté ministériel : 7 Août 2006

Présentée par

Alberto ARTIOLI

Thèse dirigée par **David FERRAND**

préparée au sein **Institut Néel**
et de **Université Grenoble Alpes**

Magnetic Polaron in (Cd,Mn)Te quantum dot inserted in ZnTe nanowire

Thèse soutenue publiquement le **17 Juin 2016**,
devant le jury composé de :

Etienne GHEERAERT
Université Grenoble Alpes, Professeur, Président

Denis SCALBERT
Laboratoire Charles Coulomb, Montpellier, directeur de recherche CNRS, Rapporteur

Olivier KREBS
Laboratoire de Photonique et Nanostructures, Marcoussis, directeur de recherche CNRS, Rapporteur

Jean Pierre HERMIER
Université de Versailles St Quentin en Yvelynes, Professeur, Examinateur

Nicolas CHAUVIN
Institut des Nanotechnologies de Lyon, Chargé de recherche CNRS, Examinateur

David FERRAND
Université Grenoble Alpes, Maitre de conférence, HDR, Directeur de thèse

Acknowledgements

Here I would like to thank all the people who helped and supported me during my doctoral study. First of all, I would like to thank my supervisor, David FERRAND. I really appreciate his attitude in dealing with scientific problems and his ability to understand and to explain the physics behind them. Moreover I would like to thank David for its kindness and helpfulness that helped me a lot during my arrival and my integration in France.

I thank Prof. Joël Cibert for his help in understanding all the experimental data and for very helpful discussions. I really liked the time spent with him and David to highlight the physics behind the experimental data.

I thank all my colleagues of the equipe "Nanophysique et Semiconducteurs" (NPSC) and especially all the people of the II-VI growing team. I have to say a big thank you to Pamela Rueda Carolina Fonseca for the growth of the samples that i have characterized during my PhD thesis and Marta Orrú that took the place of Pamela growing other samples for me.

I thank Petr Stepanov for all his help in the learning of the optical set-up and for the time spent to measure with me at the beginning of my PhD .

I thank Sebastian Klembt, Thibault Cremel and Mathieu Jeannin for the time that we spent together in performing some experiments: it was really a very nice and enjoyable experience.

It is my pleasure to thank all the people composing my jury, for their kindness to accept my invitation and for their help in the correction of my manuscript.

I want to say a big thank you to my parents, Gianni Artioli and Lauretta Ferrari: they have always supported me in all my life choices giving me the strength to realize my dreams.

Finally but not least, i thank my girlfriend Natascia Siviero and my little daughter Maya Artioli. Natascia is the person who helped me more during these three years, supporting and encouraging me in all the work and life problems that we had to face. Despite her young age, i want to thank also Maya for her cheerfulness that helped me to relax a bit during the preparation of my PhD defense. You are my life.

Abstract

In this PhD work we study the optical properties of anisotropic (Cd,Mn)Te magnetic quantum dots inserted in ZnTe nanowires. The quantum dots containing typically 10% of Mn spins are elongated along the nanowire axis which tend to stabilize a light hole ground state with a spin susceptibility perpendicular to the nanowire axis. The main goal was to study the formation of exciton Magnetic Polarons in such quantum dots and to determine their magnetic anisotropy. We investigate first the optical properties of ZnTe and ZnTe/(Zn,Mg)Te core shell nanowires. We model the elastic strain profile in core-shell nanowires and in elongated quantum dots. From the strain profiles, we estimate the value of the light hole heavy hole splitting expected in the dot and in the nanowire. In a second step we study single nanowires containing magnetic and non magnetic quantum dots by magneto-optical spectroscopy. The exchange interactions between confined carriers and Mn spins induce a large Zeeman shift of the exciton line (Giant Zeeman Effect). To extract quantitative parameters, we combine different experimental techniques (photo and cathodoluminescence, energy dispersive X ray spectroscopy) on the same nanowire. We use also different magnetic field orientations in order to determine the hole anisotropy in the dot. The experimental values are smaller than the theoretical ones suggesting a weak confinement of the holes in the dot due to a small (Cd,Mn)Te/ZnTe valence band offset. In a third step we study nanowires containing (Cd,Mn)Te quantum dots surrounded by a (Zn,Mg)Te alloy. Thanks to the better hole confinement induced by the (Zn,Mg)Te alloy, the formation of exciton magnetic polarons can be observed. We perform time resolved photoluminescence studies on single nanowires in order to determine the energy and the formation time of magnetic polarons from 5K to 50K. The quantum dot emission line shows an unusual Zeeman shift, characteristic of a light hole magnetic polaron. We develop a theoretical model describing the formation of exciton magnetic polaron in quantum dots. We use this model, based on the free energy and valid for any temperature and magnetic field, to fit the whole set of experimental data. It allows us to determine the characteristic parameters of the light hole magnetic polarons (energy, orientation and magnitude of the magnetic moment, exchange volume, hole anisotropy).

Contents

Introduction

The so called "**Spintronics**" research started to be strongly investigated since the discovery of spin-dependent electron transport phenomena in the 1980s. The possibility to use both the charge and the spin of electrons have attracted attention thanks to the discovery of the giant magneto-resistance effect, originated by spin-dependent scattering of electrons diffusing in thin metallic films [1]. The possibility of generating spin-polarized currents, passing through a magnetic material, leaded to the concept of spin field-transistor as proposed in [2].

Spin-polarized electron currents for data-storage or optoelectronic applications, can be obtained by using **Diluted Magnetic Semiconductor materials** (DMS): these are semiconductor alloys in which magnetic impurities, such as Fe, Co and Mn (with concentration less than 20% to keep the semiconductor properties of the alloy), are incorporated randomly in the crystal. The exchange interactions between free carriers and spins can lead to carrier-induced ferromagnetism as, for example, in Mn doped III-V [3] and II-VI [4] alloys. It has been shown in (Cd,Mn)Te quantum wells [5], that a ferromagnetic phase can be obtained and manipulated by photon illumination or bias voltages by modulating the carrier density in interaction with Mn spins. The highest critical temperature (Curie temperature T_C) obtained so far in (Ga,Mn)As alloy is T_C=200K. Despite a lower T_C, (Cd,Mn)Te compounds have attracted a large interest among the DMS family, thanks to the easier fabrication and incorporation of magnetic atoms by means of Molecular Beam Epitaxy (MBE). Mn atoms have an electronic structure ($4s^2 3d^5$). In II-VI DMS, they substitute the group II element and introduce localized spins $S = \frac{5}{2}$ randomly in the crystal. Without carriers, II-VI DMS are paramagnetic materials. Carriers have to be introduced by doping or using a photoexcitation in order to polarize Mn spins. In contrast to III-V DMS (Mn is an acceptor and introduces both a localized spin and a hole), this offers the opportunity to control independently Mn spins and the carriers in low dimensionality nanostructures.

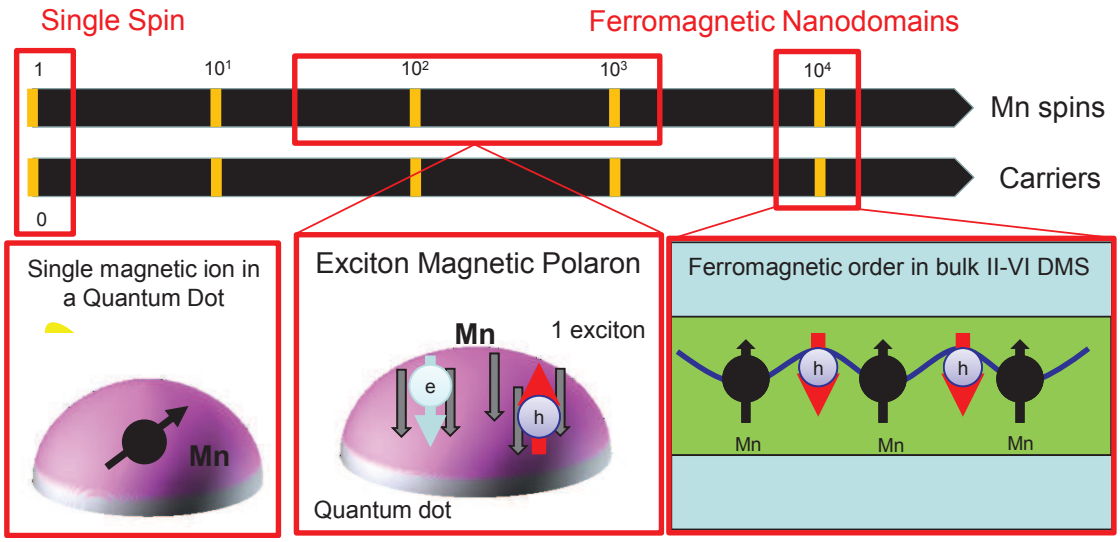

FIGURE 1: From single ion characterization to ferromagnetic order!

The discovery of Molecular Beam Epitaxy (MBE) in 1970s and the fast progresses in the micro-fabrication techniques, starting from 1980s, stimulated the development of **hetero** and **nanostructures**. The use of nanostructures allowed to spatially localized carriers, in nanometric volumes (of the order of $100nm^3$). The ultimate limit of spatially localization is the 0D confinement: such structures are called quantum dots and can be considered as "artificial atoms" thanks to the discretization of the energy levels.

II-VI DMS nanostructures are the perfect candidates to study the exchange interactions between 0D confined carriers and localized spins. Thanks to the reduced dimensionality, it is possible to localize and control carriers or electron-hole pairs (excitons) that will be coupled, by exchange interactions, with magnetic Mn atoms. This gives us, the possibility to study the coupling of a few electron-hole pairs with a large number of Mn spins [6] (typically 10^1 to 10^3 spins for an alloy with a Mn concentration of about 10%) or with a single Mn atom [7, 8]. Intensive studies have been done on 0D confined charge or excitons in concentrated II-VI DMS ((Cd,Mn)Te for example). In these systems, the exchange interactions between the localized carriers and Mn spins induce a Mn spins polarization within the charge or the exciton confinement volume: this local Mn spins polarization is called **Magnetic Polaron** (Mn spins which are not localized within the exciton or charge Böhr radius remain not polarized in zero field). The Magnetic Polaron formation has been observed first in II-VI bulk crystals, with a localized charge [9–11] (electrons on donors or holes on acceptors) polarizing the Mn spins (Bound Magnetic Polaron). Several experimental studies have been done also with magnetic self-assembled quantum dots where the

magnetic order is induced by a 0D confined exciton [12] (Exciton Magnetic Polaron). Both systems have limitations:

- In the case of bulk crystals, the position of donors and acceptors are random and the Böhr radius is fixed by the Coulomb potential. In self assembled quantum dots the polarization volume is determined by the confinement potential which may be modulated by the quantum dot shape. Due to the self-assembled quantum dots growth mechanism, it is extremely difficult to control the quantum dot shape. Self assembled quantum dots are flat, with a typical diameter (D) of 20nm and a height (L) of few nm.

- Another strong limitation of these structures is that, without being able to control the quantum dot shape, it is not possible to choose the orientation of the polaron magnetic moment via the **hole anisotropy**. In DMS alloys with a large spin orbit coupling, holes have a total kinetic momentum $J = \frac{3}{2}$. In anisotropic quantum dots, the kinetic momentum degeneracy is lifted and the hole ground state is split into a heavy hole and a light states. Flat quantum dots ($\frac{L}{D}$<1) promote heavy hole ground states with a large hole spin susceptibility along the growth axis. Elongated quantum dot ($\frac{L}{D}$>1) promote light hole ground state with a large hole spin susceptibility perpendicular to the growth axis.

The splitting (ΔE) between the heavy hole and light hole level defines the hole anisotropy and hence the exciton anisotropy (confined electrons have an isotropic s=$\frac{1}{2}$ spin). The hole anisotropy induces the magnetic one: in the case of a heavy hole Magnetic Polaron the orientation of the magnetic moment will be along the growth axis while for a light hole Magnetic Polaron the magnetic moment is oriented in the plane perpendicular to the growth axis. The control of the energy splitting ΔE is then a really important parameter of the dots for future applications like DMS based magnetic memories.

By contrast to self assembled quantum dot growth, the nanowire growth mechanism gives the possibility to control the quantum dot shape: the quantum dot diameter is controlled by the size of the gold droplet (the growth catalyzer) while the height depends on the growth time. By controlling the quantum dot shape, we can choose the aspect ratio $\frac{L}{D}$ and hence determine the preferential orientation of the magnetic moment. The hole anisotropy can be also affected by the elastic strain. In core-shell hetero-structure, as the ones studied in the present work, the differences between

the lattice parameters of the different materials induce complex elastic strain profiles which affects the anisotropy of the hole confined in the dot. Core-shell structure allows us also to passivate the surface, increasing then the emission efficiency [13], or to insert charges, in the quantum dot, by doping the shell (PhD Marta Orrú). The insertion of charges in a magnetic quantum dot offers the possibility to have a permanent Magnetic Polaron and hence a superparamagnetic order of the spins. Another interesting property of using nanowires, instead of bulk crystals or self assembled quantum dots, is that we can easily characterize and manipulate them with an electronic microscope and then perform different types of measurements on the same nanowire (for example EDX and TEM analysis, cathodoluminescence and microphotoluminescence measurements, as done during my PhD work).

The aim of my PhD work was to study the optical properties of magnetic (Cd,Mn)Te quantum dot inserted in ZnTe nanowire and to analyze the exchange coupling between exciton and Mn spins that manifests itself through the Giant Zeeman effect. The final objective was to observe Magnetic Polaron in highly concentrated (Cd,Mn)Te anisotropic quantum dots, to determine the nature of the hole ground state and the value of the hole anisotropy (ΔE).

Outline of the manuscript

In the **first Chapter** we recall the structural and electronic properties of II-VI semiconductors materials. In a first part, we give a brief review of the properties of II-VI magnetic and non magnetic nanostructures highlighting the interest on studying them by means of optics. After we will explain the MBE growth process, used to realize the samples studied during this PhD work (done by Pamela Rueda-Fonseca [14] and Marta Orrú). In a second part we recall the common model used to describe the Giant Zeeman effect, in a magnetic (Cd,Mn)Te quantum dot, using a Kondo-like exchange Hamiltonian, a Mean Field Approximation (MFA) and a Virtual Crystal Approximation (VCA). Then we recall the model (”Exchange Box Model”) commonly used to describe 0D Magnetic Polaron. This model describes the Magnetic Polaron properties as function of temperature and applied magnetic fields. In self assembled quantum dot, the model is applied to heavy hole Magnetic Polarons with magnetic field applied parallel to the growth axis. We will extend this model to the case of light hole Magnetic Polaron and to arbitrary orientations of applied magnetic field. In the

last part of the Chapter we describe the experimental set-ups and the patterned supports used to perform single nanowire studies.

We start the **second Chapter** by discussing the elastic strain that affects nanowire nanostructures (core-shell and quantum dot inserted in a nanowire). We explain how to evaluate the effect of such elastic strain by solving the Lamé-Clapeyron-Navier equation. From the calculated strain profiles, it is possible to determine the fundamental state in the quantum dot ((Cd,Mn)Te in our case) and the energy splitting between the heavy hole and light hole levels (the hole anisotropy described by the energy splitting ΔE). In a second part we present the different samples that have been characterized by optical spectroscopy in zero field using exciton spectroscopy and time resolved photoluminescence experiments. We show also the cathodoluminescence experiments done to spatially localized the quantum dot along the nanowire. In conclusion of this Chapter, we present an original experiment that uses Fourier microscopy (collaboration with Mathieu Jeannin and Gilles Nogues) to reveal, in zero field, the hole character (heavy hole or light hole) of a confined quantum dot inserted in a nanowire.

In the **third Chapter** we analyze the exchange coupling between carrier and Mn spins in different ZnTe nanowires containing a single (Cd,Mn)Te quantum dot with a Mn concentration of 10%. Under magnetic field, we observe large exciton photoluminescence red shifts. The quantitative analysis of the exciton Zeeman shift (especially the ones obtained with the nanowire characterized both in optics and in TEM-EDX) with the Giant Zeeman effect model introduced in Chapter 1 allows us to extract the Zeeman shifts at saturation for electrons and holes. By analyzing magneto-optical experiments done with different magnetic field orientations (parallel and perpendicular to the nanowire growth axis) we succeed to estimate the quantum dot hole anisotropy ΔE.

In the **fourth Chapter** we present the measurements done on nanowires containing a single (Cd,Mn)Te quantum dot surrounded by a (Zn,Mg)Te shell. For the first time, we observed the formation of a light hole Magnetic Polaron. We show how to extract all the Magnetic Polaron parameters by combining different experimental techniques such as time resolved measurements, temperature studies and magneto-optical photoluminescence. To explain the experimental results, we develop a theoretical model based on the calculation of the total free energy. We use this model to reproduce all the experimental measurements with the same set of fitting parameters. This type of model was introduced, for the first time, to calculate the Magnetic

Polaron energy associated to donors in (Cd,Mn)Se bulk crystals [9, 15]. In our case, we extend it to quantum dots. We keep the ”Exchange Box Model” approximation but we relax the MFA one. This model is applied to an exciton Magnetic Polaron and takes into account the hole anisotropy succeeding to determine the magnitude and orientation (respect to the growth axis) of the polaron magnetic moment for any value of the applied magnetic field and at any temperature.

Chapter 1

Properties of (Cd,Mn)Te magnetic quantum dot inserted in ZnTe nanowire

1.1 Introduction

In this Chapter we are going to present the system constituted by (Cd,Mn)Te quantum dot inserted in ZnTe nanowire. Figure 1.1shows a scheme of a typical nanowire studied in this thesis.

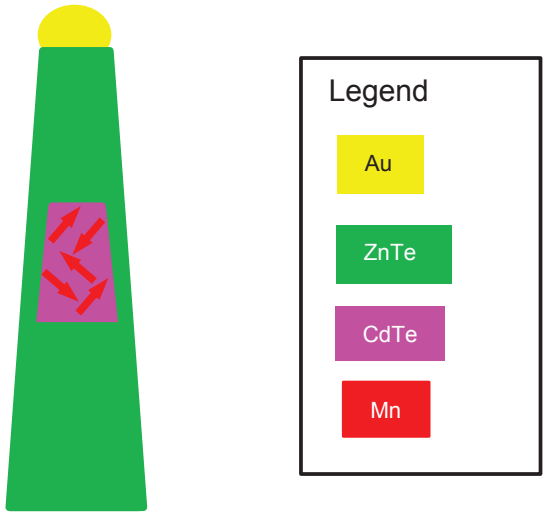

FIGURE 1.1: Scheme of the system studied in this thesis

As mentioned in the Introduction, the samples were grown by Pamela Rueda Carolina Fonseca and all the details concerning the growth of the nanowires could be found in [14]. The realization of (Cd,Mn)Te quantum dot inserted in ZnTe nanowires was a completely new task and it required difficult and different intermediate steps. First we checked the good crystal quality of the ZnTe nanowires where, for the first time, the exciton photoluminescence signal was measured[16].
As a second step, CdTe quantum dots were inserted in the ZnTe nanowire: a full optical characterization was done by Petr Stepanov [17]. Antibunching (up to 100K) has been observed, proof of a single photon emission [18], showing the good quality of the CdTe quantum dots.
Finally Mn atoms were added inside the CdTe quantum dots and the goal of this thesis was to study the optical properties of such a system.
This Chapter is organized as follows: in the first part we briefly present the crystal and electronic properties of II-VI semiconductors.
In the second part we will present a review of the main optical and magneto-optical results that have been observed with II-VI nanostructures.
In the third part we first introduce what is a Magnetic Polaron state in Diluted Magnetic Semiconductors (DMS) and we will present some experimental examples where this state has been observed. In the last part we will show how to model the different nature of Magnetic Polaron state (light hole and heavy hole one) under different configurations of applied magnetic field.

1.2 Properties of II-VI nanostructures

The system (Cd,Mn)Te/ZnTe belongs to the II-VI semiconductors family: it is in fact composed by elements from the II column of the periodic table (Cd, Zn, Mn) and one element (Te) from the VI column. Group II elements have two valence electrons on their external s-shell while the group VI elements have six valence electrons, two on a s-shell and four on a p-shell. The II-VI alloy is formed by covalent bonds.
The typical crystalline structures of a II-VI alloy is shown in Figure 1.2.

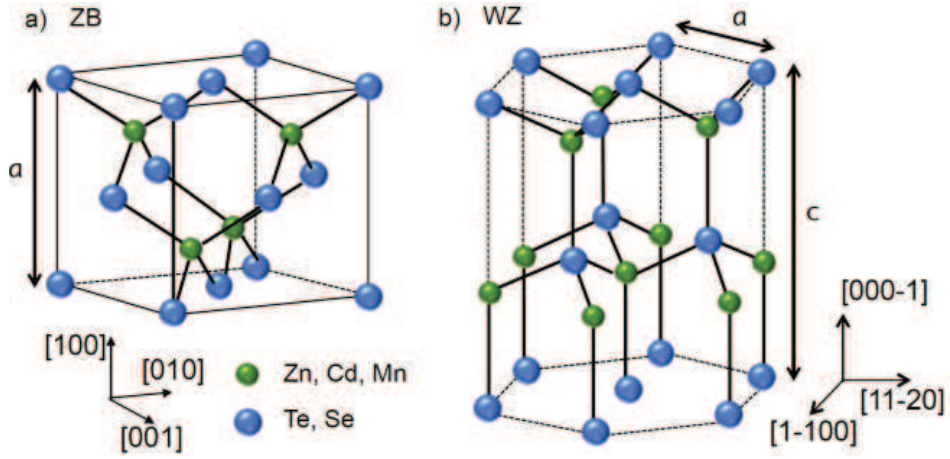

FIGURE 1.2: a) Zinc-blende (ZB) and b) Wurtzite (WZ) crystal structure of II-VI semiconductors taken from [14]

As you will see later on, our samples present two different types of nanowires: cylinder-shaped nanowires with a wurtzite crystalline structure and cone-shaped nanowires with a zinc-blende one. In this thesis, we will study nanowires with a zinc-blende (ZB) structure (see Figure 1.2a): the wurtzite type nanowires are less abundant on the as-grown sample and they remain to be fully characterized.
The zinc-blende symmetry is the typical crystalline bulk structure of ZnTe, CdTe, (Zn,Mg)Te and (Cd,Mn)Te alloys. It consists of two cubic lattices, one composed by the II elements and the other one, shifted by $\frac{1}{4}$ of the distance along the $\langle 111 \rangle$ direction, by the VI elements.
In the following table we remind the different lattice parameters of some II-VI compounds:

	ZnTe	CdTe	MgTe	MnTe
a(Å)	6.104	6.481	6.42	6.337

1.2.1 Diluted Magnetic Semiconductor (DMS) in heterostructures

Diluted Magnetic Semiconductor materials ($A_{1-x}B_xC$) are compounds where a fraction x of the cations is substituted by magnetic atoms (in this thesis Mn atoms) and hence the alloy will acquire magnetic properties. This class of new materials would lie then in between magnetic and semiconductor materials.
Another very useful properties of DMS materials is that it is possible to integrate them into heterostructures and realize different types of configurations. For example by playing with their shape factor it is possible to control the anisotropy of the system (see Chapter 2).
The final goal in the realization of DMS, is to obtain ferromagnetic order at room temperature: this property could be used to realize for example new spin valves and integrate them in semiconductor heterostructures for electronic or optoelectronic applications [19].
To achieve a ferromagnetic order inside the DMS material, it is necessary to couple the carriers with the magnetic atoms. To have a stronger ferromagnetic order it is needed to optimize the overlap between the carrier envelop function and Mn spins: it is in fact the exchange interaction between the carriers and the magnetic atoms that originates the ferromagnetic order. One solution to control the spatial localization is to use quantum confinement: this effect limits the motion of the carriers along any spatial directions and confines the carriers also in very small volumes (with the sizes of the Bohr radius).
There are different ways to obtain quantum confinement: it is possible to create small particle of DMS (colloidal quantum dots) or inserting a DMS with a small band gap inside a larger band gap semiconductor.
By playing with the different band gaps (see Figure 1.3), it is possible to confine the carriers in 2D (quantum well), 1D (quantum wire) and 0D (quantum dot) nanostructures [20].

From Figure 1.3 we see that by reducing the dimensions, one confines the carriers that have then discrete energy band dispersions.
In the case of a 0D confinement, we are in the presence of the so called "quantum dot". The first discrete energy state is called exciton and it is a state formed by an electron and a hole that are coupled by Coulomb interaction. The excited state of the quantum dot will be constituted by an higher number of electrons and holes but as these particles are fermions of total angular momentum projection $\pm\frac{1}{2}$ (electrons), $\pm\frac{3}{2}$ (heavy holes), $\pm\frac{1}{2}$ (light holes) it is possible to have at maximum two carriers on

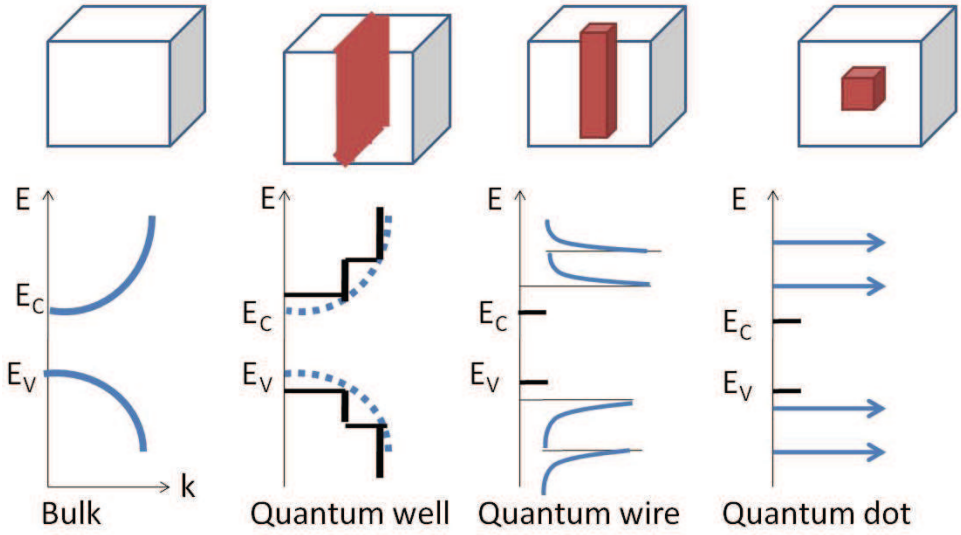

FIGURE 1.3: Different confinement properties and relative energy dispersion, taken from [21]

the same confined level due to the Pauli exclusion principle. The ground state and some excited state of a quantum dot are shown in Figure 1.4.

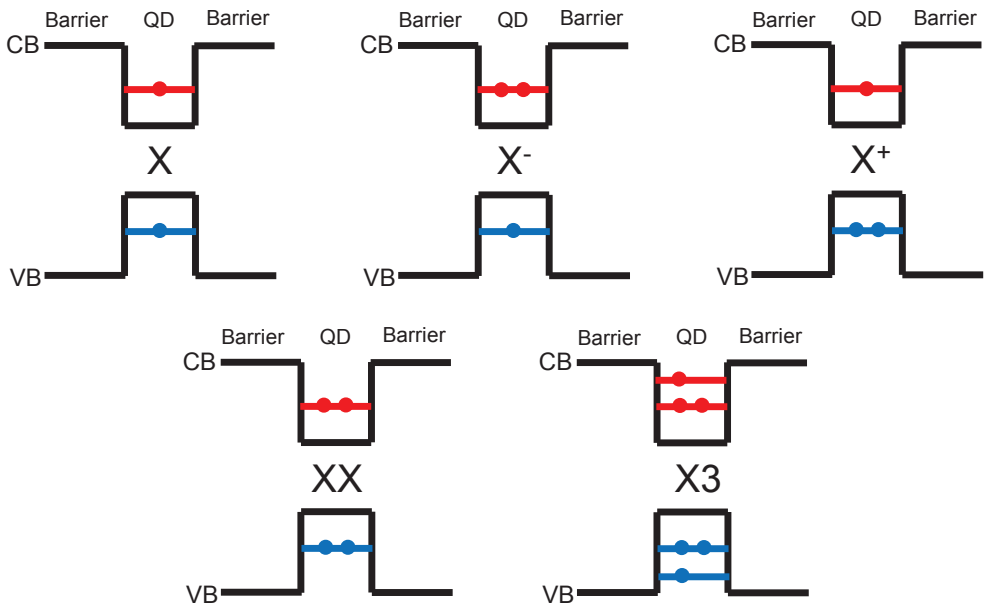

FIGURE 1.4: Different types of quantum dot states

The exciton can coexist with an extra carrier (negatively charged exciton in the case of an electron, positively charged exciton for a hole) with then a different emission energy, shifted at lower or higher energy compared to the neutral exciton state (due to the different Coulomb interaction).

The biexciton is a state where two excitons are populating the quantum dot while the triexciton is composed by three excitons.

1.2.2 Electronic Properties

In solid state physics, the band theory is used to calculate the energies of carriers: in the approximation of a perfect and infinite crystal, the energy levels of carriers are described by Bloch states grouped in bands or energy bands [20].
The two elements that compose II-VI semiconductor materials, have eight external electron levels (two type s and six type p orbitals). Hybridization of these atomic orbitals leads to four populated bounding states (one s and three p orbitals) at lower energies and four empty anti-bounding states at higher ones (one s and three p orbitals). The lowest empty state is the anti-bonding s orbital: the conduction band. The valence band is constituted by the three bonding p orbitals. The exact calculation of the band structure has been done in the $\vec{k}\cdot\vec{p}$ approximation by G. Fishman and can be found in [22]. In Figure 1.5 we show the band structure of CdTe that is a direct bandgap semiconductor: the maximum of the valence band and the minimum of the conduction one are in the center of the Brillouin zone at $\vec{k}=0$ (the Γ point).

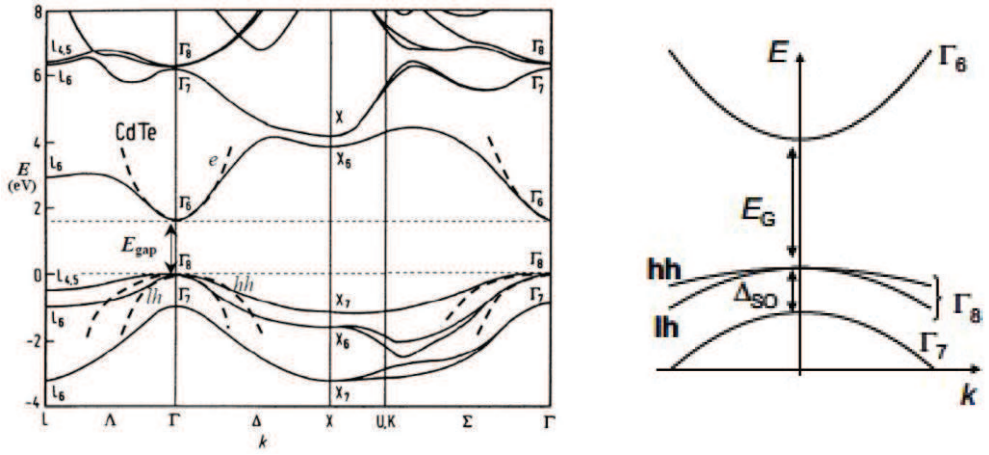

FIGURE 1.5: Electronic band of a CdTe compound where in dash is highlighted the parabolic approximation (see text)

We are interested to the ground state of the system and then to the proximity of the Γ point. The dispersions of the bands around this point can be treated with a parabolic

approximation: the conduction band has spin projection $\sigma_z = \pm\frac{1}{2}$ (with Γ_6 symmetry) and is splitted by the bandgap energy E_g from to the valence band (with Γ_8 symmetry) (see Figure 1.5). The Γ_7 subband can be not considered because the spin-orbit coupling Δ_{so} is large in CdTe . The valence band (Γ_8 symmetry) is composed by two subbands associated to a total kinetic momentum $J = \frac{3}{2}$: the heavy hole subband correspond to spin projection $J_z = \pm\frac{3}{2}$ while the light hole one correspond to spin projection $J_z = \pm\frac{1}{2}$. By symmetry considerations, it is possible to describe the valence band around the Γ point by using the Luttinger Hamiltonian [23] and calculate an expression for $E(\vec{k})$ in the second order in $\vec{k}$ (parabolic approximation). The dispersion of the bands, in the parabolic approximation is given by:

$$E(\vec{k}) = E(\vec{k} = 0) + \frac{\hbar k^2}{2m^*} \tag{1.1}$$

Where m^* is the effective mass. In CdTe, for the conduction band the effective mass of the electron is isotropic and is equal to:

$$m_e^* = 0.1 m_0 \tag{1.2}$$

Where m_0 is the free electron mass. For the heavy hole and light hole masses it depends on the direction of $\vec{k}$. In $\langle 001 \rangle$ direction the effective masses are [24]:

$$m_{hh}^* = 0.6 m_0, \quad m_{lh}^* = 0.12 m_0 \tag{1.3}$$

While in the $\langle 111 \rangle$ the effective masses are given by [24]:

$$m_{hh}^* = 0.69 m_0, \quad m_{lh}^* = 0.11 m_0 \tag{1.4}$$

When working with heterostructures of reduced dimensionality we have other effects that affect the electronic properties of the system. It is better to always have in mind the electronic properties of the different compounds (see Figure 1.6).

The composition of different alloys used in the structure (in our case (Cd,Mn)Te quantum dot in ZnTe nanowires) leads to strain effects (originated by the differences

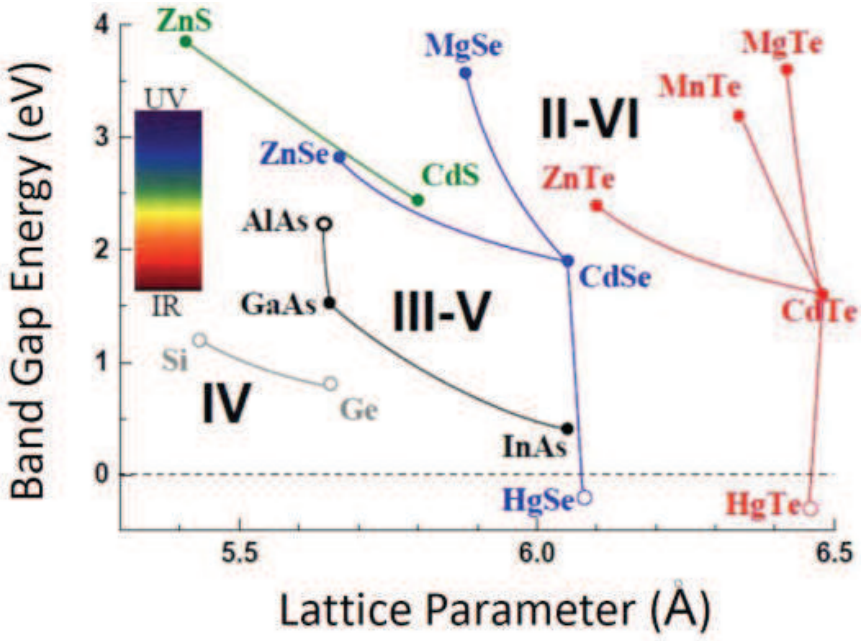

FIGURE 1.6: Band gap energy variation, at $T = 4K$, as a function of the lattice parameter for different semiconductor alloys (filled and empty symbols correspond respectively to direct and indirect band gap materials)

of the lattice parameters): these affect the bandgap and hence the emission properties of such systems [20]. When we study heterostructures by means of photoluminescence we have then to take properly into account the effect of strain (a more detailed analysis on the strain in different heterostructures geometries will be presented in Chapter 2).

In the following table we report the main informations, concerning the electronic properties, that we will use in this thesis.

	ZnTe	CdTe	MgTe	MnTe
a(Å)	6.104	6.481	6.42	6.337
E_g (meV)	2391	1606	3600	3198

For ternary alloys $(A_{1-x}B_xC)$, the lattice parameter a can be deduced by using the Vegard's law [25] leading to:

$$a(A_{1-x}B_xC) = (1-x)a(AC) + xa(BC) \tag{1.5}$$

The bandgap (E_g) of a ternary alloy $(A_{1-x}B_xC)$ presents a non linear behaviour with the composition x and can be calculated by using the following expression:

$$E_g^{ABC}(x) = (1-x)E_g^{AC} + xE_g^{BC} - b_{ABC}x(1-x) \tag{1.6}$$

where b is the bowing parameter that is determined experimentally. In the following we give the expressions for the band gap variation of the compounds used in this thesis.

$$E_g(\mathrm{Cd}_{1-x}\mathrm{Mn}_x\mathrm{Te}) = 1606 + 1592x \tag{1.7}$$

$$E_g(\mathrm{Zn}_{1-x}\mathrm{Mg}_x\mathrm{Te}) = 2391 + 959x + 250x^2 \tag{1.8}$$

By using equations 1.8 we can reconstruct the expected band profiles for an unstrained (Cd,Mn)Te quantum dot inserted in a ZnTe nanowire (see Figure 1.7).

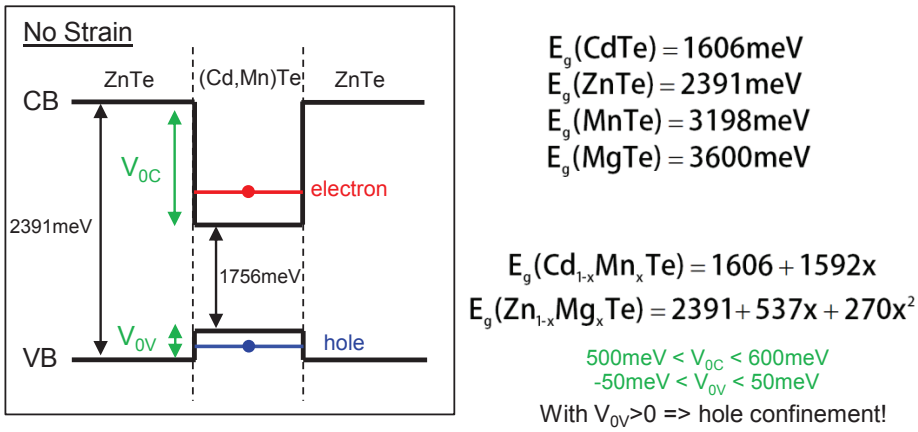

FIGURE 1.7: Band profiles for an unstrained (Cd,Mn)Te quantum dot in a ZnTe nanowire

Where the position of the valence and conduction band offsets have been estimated and taken from [17].

1.2.3 Semiconductor in a magnetic field: Zeeman effect

We saw that the ground state of a quantum dot (exciton) is a state composed by an electron hole pair: the electron has a spin projection $\pm\frac{1}{2}$ while the hole has a total kinetic momentum projection $\pm\frac{3}{2}$ (heavy hole) and $\pm\frac{1}{2}$ (light hole). The two-fold degeneracy of the spin will be lifted by the application of a magnetic field: this is the so

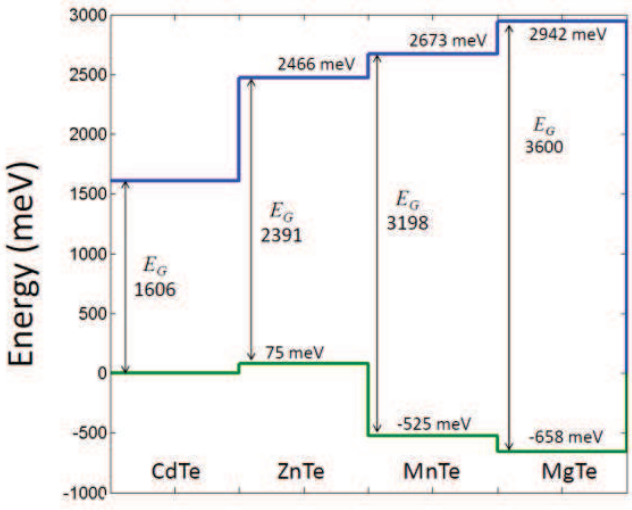

FIGURE 1.8: Band offsets for some II-VI compounds, image taken from [17]

called Zeeman effect [26].
If we consider an electron and a heavy hole, the Zeeman Hamiltonians that describe the interaction with the applied magnetic field are given by:

$$H_e = g_e \mu_B \vec{B} \cdot \vec{\sigma}_e \tag{1.9}$$

$$H_{hh} = g_{hh} \mu_B \vec{B} \cdot \vec{J}_{hh} \tag{1.10}$$

Where μ_B is the Bohr's magneton, $\vec{\sigma}_e$ and $\vec{J}_h$ are the spin operators for electron and hole and g_e,g_h are the corresponding Landé factors. If for example we consider an exciton with a heavy hole ground state ($J_{h_z} = \pm\frac{3}{2}$) we can trace the Zeeman splitting induced under magnetic field (see Figure 1.9).

The two optically allowed transitions are circularly polarized and they have different energies. The increasing of the energy separation between two degenerated states with the magnetic field is not more than $0.1\frac{\text{meV}}{T}$. This effect is very weak compared to the Giant Zeeman effect induced by the exchange coupling with Mn atoms, as you will see in the next paragraph.

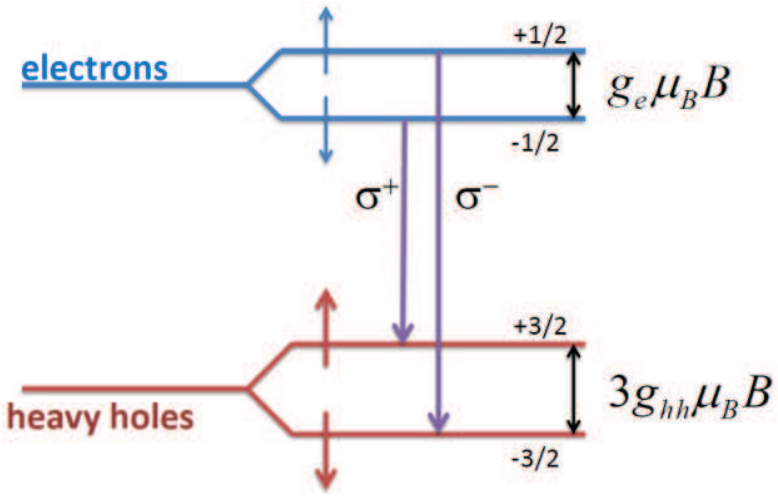

FIGURE 1.9: Zeeman effect in a quantum dot with a heavy hole ground state, image taken from [17]

1.2.4 DMS in a magnetic field: Giant Zeeman effect (GZE)

1.2.4.1 Spin polarization of the magnetic impurities

For the samples studied in this thesis, it has been chosen to incorporate Mn atoms inside the CdTe leading to a $A_{1-x}Mn_xC$ DMS alloy. Mn is an element of the II column of the periodic table: it has an electronic structure $[Ar]3d^5\ 4s^2$ that has two valence electrons and 5d electrons with a spin state $S = \frac{5}{2}$.
In this Section we will show how we can model the behaviour of the magnetic impurities under an applied magnetic field.
The Zeeman Hamiltonian describing the interaction of the Mn atoms with an applied magnetic field is given by:

$$H_{Mn} = g_{Mn}\mu_B \vec{S}\cdot\vec{B} = -\vec{M}\cdot\vec{B} \tag{1.11}$$

where $\vec{S}$ is the spin operator of the Mn atom and g_{Mn} is the Landé factor given by:

$$g = 1 + \frac{J(J+1) + S(S+1) - L(L+1)}{2J(J+1)} \tag{1.12}$$

Where, in the case of Mn atoms, $L = 0$ and $S = \frac{5}{2}$ leading to $g_{Mn} = 2$.
Assuming a paramagnetic behaviour of the Mn atoms, it is possible to calculate the average magnetization $\langle S_z \rangle$ (for an applied magnetic field along the z axis), after having defined the partition function of the system (see Appendix A).

$$\langle S_z \rangle = -S\mathrm{B}_{\frac{5}{2}}\left(\frac{g_{Mn}\mu_B BS}{k_B T}\right) \tag{1.13}$$

Where $\mathrm{B}_{\frac{5}{2}}$ is the Brillouin function for a particle with $S = \frac{5}{2}$ (see Appendix B). Assuming that each cation site of the lattice, defined by $\vec{R}_i$, is occupied whether by one Mn atom ($x_i = 1$) or by a Cd one ($x_i = 0$), the projection on the z axis of the total magnetization is given by [27]:

$$M_z(\vec{r}) = -\sum_i x_i \delta\left(\vec{r} - \vec{R}_i\right) g_{Mn}\mu_B S_{zi} \tag{1.14}$$

It is possible now to do some approximation to retrieve an easier expression of the projected total magnetization. If we use the Mean Field Approximation (MFA, S_{zi} replaced by its value at thermal equilibrium $\langle S_{zi} \rangle$) and a Virtual Crystal Approximation (VCA, x_i replaced by x where x denotes the average number of cation sites occupied by the Mn atoms and the Dirac function is replaced by the volume density of cation sites N_0) we have:

$$\langle M_z \rangle = -g_{Mn}\mu_B x N_0 S\mathrm{B}_{\frac{5}{2}}\left(\frac{g_{Mn}\mu_B BS}{k_B T}\right) \tag{1.15}$$

When the Mn concentration inside the DMS semiconductor is high, there are deviation from the Brillouin function (equation 1.15) due to the anti-ferromagnetic interactions between nearest and more distant neighbors Mn atoms. The effect of these interactions is modeled by a modified Brillouin function (valid at low temperature) introduced by J.Gaj, R. Planel and G. Fishman [28]:

$$\langle M_z \rangle = -g_{Mn}\mu_B x_{eff} N_0 S\mathrm{B}_{\frac{5}{2}}\left(\frac{g_{Mn}\mu_B BS}{k_B\left(T + T_{AF}\right)}\right) = -M_{sat}\mathrm{B}_{\frac{5}{2}}\left(\frac{g_{Mn}\mu_B BS}{k_B\left(T + T_{AF}\right)}\right) \tag{1.16}$$

Where $M_{sat} = g_{Mn}\mu_B \rho_{eff} S$ with $\rho_{eff} = N_0 x_{eff}$, x_{eff} is the volumetric Mn concentration (Mn atoms that are not coupled by anti-ferromagnetic interactions). T_{AF} is the anti-ferromagnetic temperature that takes into account the anti-ferromagnetic coupling between nearest and more distant neighbors Mn atoms. We trace x_{eff} and T_{AF} as a function of the Mn concentration in Figure 1.10.

When magnetic atoms are introduced inside a DMS compound, these atoms don't interact just with the applied magnetic field (as we have seen so far) but they interact

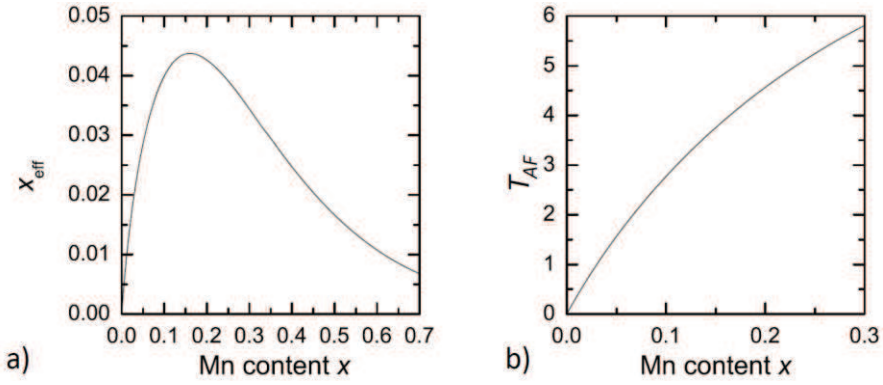

FIGURE 1.10: a) x_{eff} as function of the Mn concentration [28, 29] b) T_{AF} as function of the Mn concentration, image taken from [17]

also with the carriers which in turn are interacting with the magnetic field. In the next Section we will show how to calculate the effect of this coupling.

1.2.4.2 Photoluminescence Zeeman shifts for a light hole and a heavy hole transition

We will show now how to calculate the photoluminescence Zeeman shifts of a light hole and heavy hole exciton in order to compare the experimental values with the theoretical ones.

The coupling between the carriers and the magnetic impurities is a direct exchange interaction and is called sp-d exchange interaction. It involves in fact a ferromagnetic s-d interaction between the s electrons and the 3d states of the Mn atoms and an antiferromagnetic p-d interaction between the p holes and the 3d states of the Mn atoms. The p hole levels result from a pd hybridization with Mn d levels located within the valence band.

The Hamiltonian that describes the sp-d interaction for free carriers (one electron-hole pair) and magnetic impurities (in the presence of an external magnetic field $\vec{B}$) in a bulk crystal, is a Heisenberg like one [17, 30, 31] and can be written as:

$$H_{sp-d} = H_{e-Mn} + H_{h-Mn} = -\alpha \sum_{\vec{R}_i} \delta(r - R_i)\vec{S}_i \cdot \vec{\sigma}_e - \beta \sum_{\vec{R}_i} \delta(r - R_i)\vec{S}_i \cdot \vec{J}_h \qquad (1.17)$$

Where α and $\frac{\beta}{3}$ are the exchange integrals for electron and hole respectively. $\vec{R}_i$ is the position of the magnetic ions characterized by spin operators $\vec{S}_i$. $\vec{\sigma}_{e_i}$ is the electron spin operator and $\vec{J}_{h_i}$ is the hole kinetic momentum operator.

To be able to find an analytical solution for equation 1.17 we have to do some approximations: we will consider a semi-classical treatment. First we consider, for the magnetic impurity spin operator, the value at thermal equilibrium considering it as a classical quantity ($\vec{S}_i \longrightarrow \langle \vec{S}_i \rangle$): this is the so called Mean Field Approximation (MFA). The spin operators for electron and hole will be the quantum ones and they will be described by the following matrix formalism [32]:

$$\sigma_x^e = \begin{pmatrix} 0 & \frac{1}{2} \\ \frac{1}{2} & 0 \end{pmatrix} \quad \sigma_y^e = \begin{pmatrix} 0 & -\frac{i}{2} \\ \frac{i}{2} & 0 \end{pmatrix} \quad \sigma_z^e = \begin{pmatrix} \frac{1}{2} & 0 \\ 0 & -\frac{1}{2} \end{pmatrix} \tag{1.18}$$

$$J_x^h = \begin{pmatrix} 0 & \frac{\sqrt{3}}{2} & 0 & 0 \\ \frac{\sqrt{3}}{2} & 0 & 1 & 0 \\ 0 & 1 & 0 & \frac{\sqrt{3}}{2} \\ 0 & 0 & \frac{\sqrt{3}}{2} & 0 \end{pmatrix} \quad J_y^h = \begin{pmatrix} 0 & -\frac{i\sqrt{3}}{2} & 0 & 0 \\ \frac{i\sqrt{3}}{2} & 0 & -i & 0 \\ 0 & i & 0 & -\frac{i\sqrt{3}}{2} \\ 0 & 0 & \frac{i\sqrt{3}}{2} & 0 \end{pmatrix}$$

$$J_z^h = \begin{pmatrix} \frac{3}{2} & 0 & 0 & 0 \\ 0 & \frac{1}{2} & 0 & 0 \\ 0 & 0 & -\frac{1}{2} & 0 \\ 0 & 0 & 0 & -\frac{3}{2} \end{pmatrix}$$

Where the electron spin matrices are the Pauli ones and the hole kinetic momentum matrices are given in the heavy hole basis $+\frac{3}{2}$, $+\frac{1}{2}$, $-\frac{1}{2}$ and $-\frac{3}{2}$.
At this stage, to describe the Mn atoms distribution and the coupling with the electron-hole pair, it is used the Virtual Crystal Approximation (VCA). The random distribution of magnetic ions and host cations over the cation sublattice is replaced by a periodical structure with artificial cations possessing properties of the host cation and the magnetic ion, averaged using occupation probabilities as weights [30].
We can rewrite equation 1.17 such as:

$$H_{sp-d} = H_{e-Mn} + H_{h-Mn} = -\alpha N_0 x_{eff} \langle \vec{S} \rangle \vec{\sigma}_e - \frac{\beta}{3} N_0 x_{eff} \langle \vec{S} \rangle \vec{J}_h \tag{1.19}$$

We remind that $H_{e-Mn} = -\alpha N_0 x_{eff} \langle \vec{S} \rangle \vec{\sigma}_e$ is defined by a 2×2 matrix while $H_{h-Mn} = -\frac{\beta}{3} N_0 x_{eff} \langle \vec{S} \rangle \vec{J}_h$ by a 4×4 one. For (Cd,Mn)Te, the values $N_0\alpha$=220meV and $N_0\beta$=-880meV are well known [28, 33] (for CdTe $N_0 = \frac{4}{a_0^3} \cong 15\, nm^{-3}$). Their signs highlight that the exchange interaction electron-Mn is ferromagnetic while the hole-Mn one is anti-ferromagnetic. We note that, for (Cd,Mn)Te, the hole-Mn exchange interaction is four times the electron-Mn one.

We can rewrite equation 1.19 by using the definition of magnetization at thermal equilibrium, given by:

$$\langle \vec{M} \rangle = -N_0 x_{eff} g_{Mn} \mu_B \langle \vec{S} \rangle \tag{1.20}$$

having then:

$$H_{sp-d} = H_{e-Mn} + H_{h-Mn} = \frac{\alpha \langle \vec{M} \rangle}{g_{Mn}\mu_B} \vec{\sigma}_e + \frac{\beta \langle \vec{M} \rangle}{3 g_{Mn}\mu_B} \vec{J}_h \tag{1.21}$$

If now we take the z axis, as quantization axis, and a magnetic field applied along this direction, we can deduce the Zeeman splitting for the electron levels and for the heavy hole and the light hole ones:

$$\Delta_e = \alpha \frac{\langle M_z \rangle}{g_{Mn}\mu_B} \tag{1.22}$$

$$\Delta_{hh} = -\beta \frac{\langle M_z \rangle}{g_{Mn}\mu_B} \tag{1.23}$$

$$\Delta_{lh} = \frac{-\beta}{3} \frac{\langle M_z \rangle}{g_{Mn}\mu_B} = \frac{\Delta_{hh}}{3} \tag{1.24}$$

In Figure 1.11 we trace the electron, heavy hole and light hole Zeeman splittings as a function of the magnetic moment $\langle M_z \rangle$

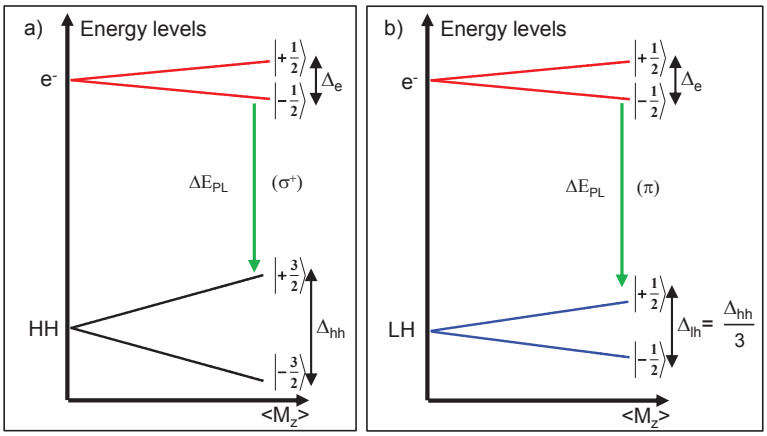

FIGURE 1.11: Giant Zeeman effect of the electron and hole bands as a function of the magnetic moment $\langle M_z \rangle$

Now we have all the ingredients to calculate the photoluminescence Zeeman shift for the fundamental transition of a (Cd,Mn)Te crystal for heavy holes ΔE_{PL}^{hh} and light holes ΔE_{PL}^{lh}. The electron ground state has a spin projection $|-\frac{1}{2}\rangle$, the heavy hole state kinetic momentum $|+\frac{3}{2}\rangle$ and the light hole one $|+\frac{1}{2}\rangle$. Using Figure 1.11, the photoluminescence Zeeman shift for a heavy hole transition will be given by:

$$\Delta E_{PL}^{hh} = \frac{\Delta_e + \Delta_{hh}}{2} \tag{1.25}$$

The photoluminescence Zeeman shift for a light hole transition will be given by:

$$\Delta E_{PL}^{lh} = \frac{\Delta_e + \Delta_{lh}}{2} = \frac{\Delta_e + \frac{\Delta_{hh}}{3}}{2} \tag{1.26}$$

The magnetization at thermal equilibrium is described (as we have already said) by a Brillouin function for a particle with $S = \frac{5}{2}$:

$$\langle M_z \rangle = -M_{sat} \mathrm{B}_{\frac{5}{2}} \left(\frac{g_{Mn} \mu_B B_z S}{k_B (T + T_{AF})} \right) \tag{1.27}$$

With $M_{sat} = g_{Mn} \mu_B S N_0 x_{eff}$.
The Zeeman shift for the fundamental transition (see Figure 1.11) for a heavy hole and a light hole exciton will be given by:

$$\Delta E_{PL}^{hh} = (E_{se} + E_{sh}) \mathrm{B}_{\frac{5}{2}} \left(\frac{g_{Mn} \mu_B B_z S}{k_B (T + T_{AF})} \right) \tag{1.28}$$

$$\Delta E_{PL}^{lh} = \left(E_{se} + \frac{E_{sh}}{3} \right) \mathrm{B}_{\frac{5}{2}} \left(\frac{g_{Mn} \mu_B B_z S}{k_B (T + T_{AF})} \right) \tag{1.29}$$

Where we have defined the Zeeman energies at saturation for electron E_{se} and hole E_{sh} such as:

$$E_{se} = \frac{\alpha N_0 x_{eff} S}{2} \tag{1.30}$$

$$E_{sh} = \frac{-\beta N_0 x_{eff} S}{2} \tag{1.31}$$

Considering a $x_{eff} = 4\%$, the Zeeman energies at saturation for electron and hole are equal to:

$$E_{se} = 11\text{meV} \tag{1.32}$$

$$E_{sh} = 44\text{meV} \tag{1.33}$$

1.3 Studied samples

1.3.1 Review on magnetic and non magnetic II-VI nanostructures

Introduction

In this paragraph we will recall some of the most significant experimental results obtained on magnetic and non magnetic II-VI nanostructures during the last years.
As you will see in Sections 1.4, one of the interest on using Diluted Magnetic Semiconductors materials is the possibility to induce a local ferromagnetic order induced by the exchange interactions between localized exciton and diluted magnetic atoms (Magnetic Polaron state).
Until now, Magnetic Polaron order has been found in systems that are difficult to manipulate: the more recent systems where it has been observed a light-induced ferromagnetic order are nanocrystals [34] or DMS self assembled quantum dots [12, 35]. Unfortunately it is not easy to perform structural analysis on such systems to enhance the theoretical description of the Magnetic Polaron formation process. Moreover, due to the fact that self assembled quantum dots are well embedded in the compound, it is difficult to isolate and manipulate a single self assembled quantum dot and use it to build an optoelectronic device.
Recently the growth of 1D DMS heterostructures (nanowires) has attracted a lot of interest: they are promising candidates to further investigate the Magnetic Polaron formation process. It is possible in fact to incorporate quantum dots inside the nanowire structure offering the possibility to study single object and to manipulate it easily. As you will see in this thesis, it is possible to perform, for example, different types of measurements on the same nanowire. We deposited a nanowire (by using a nanomanipulator, see Section 1.6) on a patterned Si_3N_4 self-suspended membrane that allowed us to retrieve easily its position. By the use of such technique, we did chemical and structural analysis (Energy Dispersive X-ray spectroscopy, Cathodoluminescence spectroscopy, detailed magneto-optical studies, for the details see Chapter 2 and Chapter 3).
In this thesis, it will be shown for the first time the evidence of an Exciton Magnetic Polaron state in a nanowire geometry.

Nanowires

During the last ten years, II-VI nanowires have been intensively studied for various application such as the realization of interesting nanoelectronic and nanophotonic devices [36], nano-pillar solar cells [37] and photodetectors [38].

CdSe quantum dots in ZnSe nanowires

Recently it has been found that CdSe quantum dots inserted in ZnSe can provide an efficient single photon source even at 200K [39]. The same nanowire system has also been improved showing single photon emission properties even at room temperature [40]. In Figure 1.12 we show the antibunching effect, revealing the single photon nature of the CdSe/ZnSe nanowire system, up to 300K.

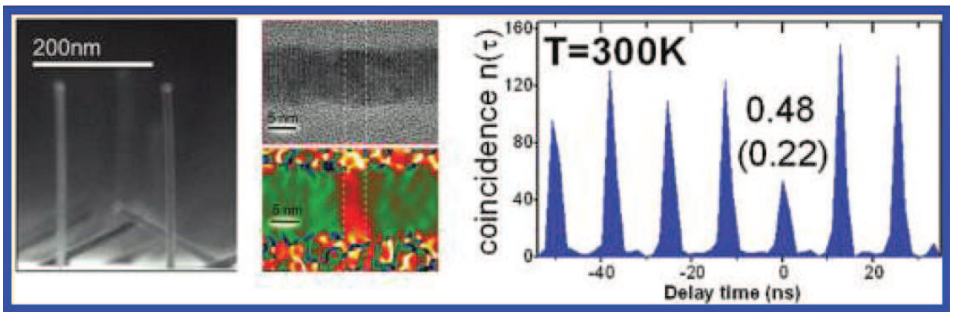

FIGURE 1.12: Antibunching effect, revealing a single photon emission source, of CdSe quantum dots inserted in ZnSe nanowires, image taken from [40]

An efficient single photon source, as the one studied in [40], can bring also other interesting implementation in quantum information processing [41] and quantum cryptography [42].

ZnTe nanowires

ZnTe based nanowires are particularly interesting: they can be easily doped electrically [43] and magnetically [13, 44]. For the incorporation of the Mn atoms it is not necessary to vary the growth temperature leading to more efficient and easy growing procedures compared to III-V semiconductors [45].
In Figure 1.13 we show the result on the Mn doping of ZnTe nanowires that can be found in [13]: the optical properties of (Zn,Mn)Te/(Zn,Mg)Te nanowires (Figure 1.13a) are studied under magnetic field.

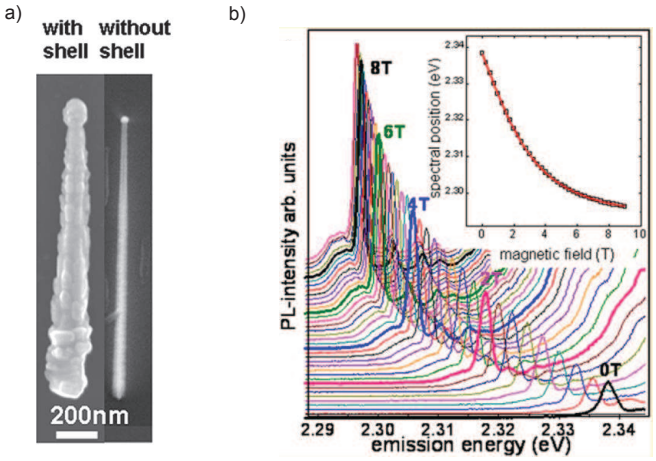

FIGURE 1.13: a) HRSEM image of the (Zn,Mn)Te/(Zn,Mg)Te nanowire b) Exciton Giant Zeeman effect, images taken from [13]

Figure 1.13 shows the near band edge emission variation under magnetic field: the photoluminescence red shift is the so called Giant Zeeman Effect (introduced in the previous Section).
Another interesting property of a nanowire-like system is that it is possible to realize core-shell structures as done in [13]. The (Zn,Mg)Te shell enhances the photoluminescence intensity by surface passivation. As you will see in Chapter 2, it is possible to estimate the gain in the photoluminescence intensity by comparing a system without shell (ZnTe nanowires) with a system surrounded by a (ZnMg)Te shell (ZnTe/(Zn,Mg)Te nanowires). We found that the photoluminescence intensity is 10^4 times higher in the sample covered by a shell.

CdTe quantum dots in ZnTe nanowires

CdTe quantum dot can be easily incorporate in ZnTe nanowires [46]: it is possible to use them as very sensitive optical probe of the spin properties of individual Mn ions [7] and recently, this research field, has been further improved by the successful incorporation of other magnetic impurities (Fe, Co) and it has been called "Solotronics" [8].
A full characterization of CdTe quantum dots inserted in ZnTe nanowires can be found in [17]. This system shows an antibunching effect, even at high temperature (up to 100K), highlighting its efficient single photon source properties (see Figure 1.14).

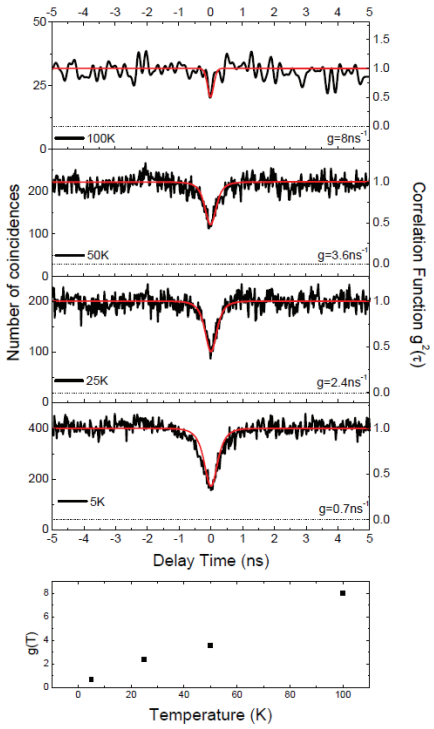

FIGURE 1.14: Antibunching effect of CdTe quantum dots inserted in ZnTe nanowires, images taken from [17]

(Cd,Mn)Te quantum dots

The possibility to incorporate Mn impurities inside CdTe self assembled quantum dots was demonstrated experimentally in [6]. The system are (Cd,Mn)Te quantum dots with different dimensions and few % of Mn atoms inside, inserted in a non magnetic (Zn,Cd)Te layer. In Figure 1.15 we show some of the magneto-optical measurements done in [6].

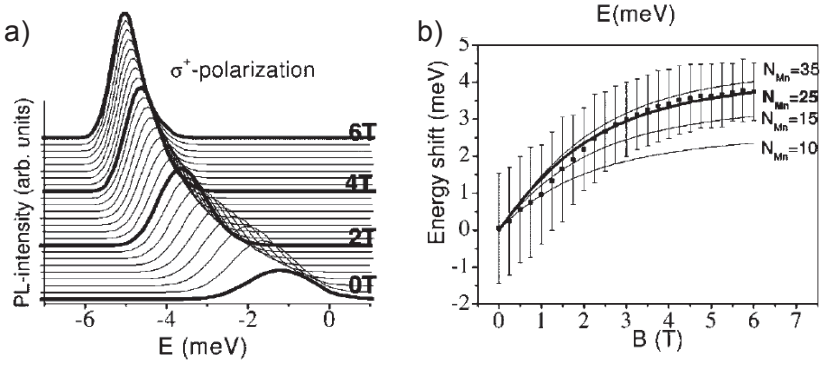

FIGURE 1.15: a) Giant Zeeman Effect of the heavy hole exciton (σ^+ polarization) b) Giant Zeeman shifts fitted by a modified Brillouin function, images have been taken from [6]

In Figure 1.15a is traced the heavy hole exciton photoluminescence spectra under magnetic field. The photoluminescence transition is between the $+\frac{3}{2}$ hole state and the $-\frac{1}{2}$ electron one. The Exciton Giant Zeeman shift is reported in Figure 1.15c and again it is well fitted by a modified Brillouin function (as explained in Section 1.2.4).

(Cd,Mn)Te quantum dots in ZnTe nanowires

In 2015, (Cd,Mn)Te quantum dots were successfully inserted in ZnTe nanowires [47] revealing Giant Zeeman Effect (see Figure 1.16).

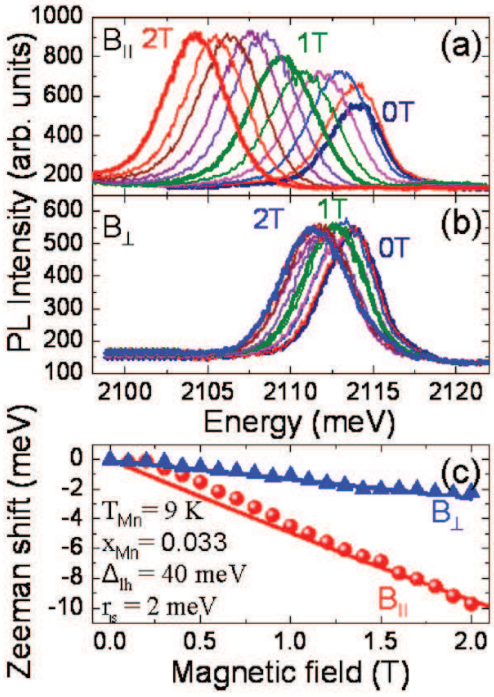

FIGURE 1.16: Giant Zeeman effect of (Cd,Mn)Te quantum dot inserted in ZnTe nanowire with different orientation of the applied magnetic field, images taken from [47]

Figure 1.16 shows the magneto-optical studies done on the system by changing the orientation of the applied magnetic field (parallel and perpendicular to the nanowire growth axis). A strong spin splitting anisotropy has been revealed.

As you have seen, the system formed by (Cd,Mn)Te quantum dot inserted in ZnTe nanowire, has not intensively been studied: the only experimental results are shown in Figure 1.16. The hole ground state has a heavy hole nature with a measured hole anisotropy ΔE=40meV.

This large hole anisotropy remains to be understood: a detailed structural and chemical analysis has to be done to correlate the structural properties with the measured

hole anisotropy. This is the purpose of the first studies done during this PhD work and that could be found in Chapter 2 and in Chapter 3.

1.3.2 Growth of the samples studied in this thesis

In this Section we present the growth of (Cd,Mn)Te quantum dot in ZnTe nanowires done by Pamela Carolina Rueda-Fonseca (Sample 1 and Sample 2, the detailed process can be found in [14]) whereas the Reference sample (CdTe quantum dot in ZnTe) was grown by Marta Orrú. The structures of Sample 1, Sample 2 and the Reference will be given in the following.
The technique used to grow this system is the Molecular Beam Epitaxy (MBE): it consists in the epitaxial growth of materials by sending atomic or molecular fluxes on a heated crystalline substrate under ultra high vacuum (UHV) conditions.
The scheme of the nanowire growth process is shown in Figure 1.17:

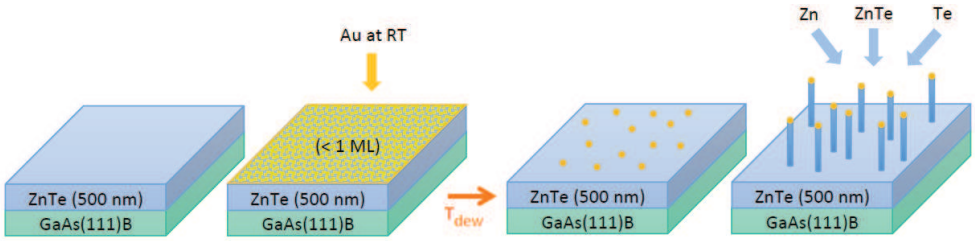

FIGURE 1.17: Scheme of the nanowires growth taken from [14]

The first step (see Figure 1.17) is to grow a ZnTe buffer layer on a GaAs substrate to reduce the defects (stacking faults) resulting from the high difference between the substrate lattice parameter and the nanowire one. After, we deposit a very thin Au layer (less than a monolayer) followed by a dewetting procedure to form Au droplets. The Au droplets act as a catalyst for the growth: the ZnTe elements diffuse from the substrate and they are trapped by the Au particles leading to the nanowire growth.
A typical result of this growth process is shown in Figure 1.18.

Two different types of ZnTe nanowires (see Figure 1.18) can be obtained: one type of nanowires has a cone-shaped form (see Figure 1.18a) with a zinc-blende crystalline structure while the other (see Figure 1.18b) has a cylinder-shaped with a wurtzite crystalline structure [14], [48] (see Figure 1.19).

Without entering too much into the details of the growth processes, the difference in the two types of nanowires is attributed to different values of the diffusion length

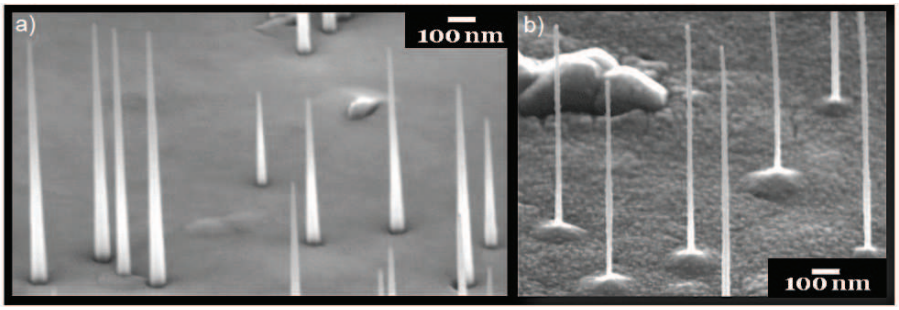

FIGURE 1.18: Tilted HRSEM images of ZnTe nanowires showing a) Cone-Shaped b) Cylinder-Shaped nanowires [14], [48]

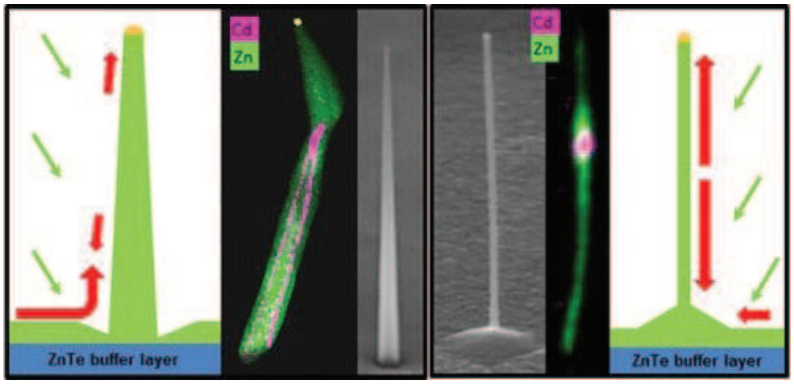

FIGURE 1.19: Different growth mechanisms for ZnTe nanowires, image taken from [14], [48]

along the nanowire sidewalls. For the wurtzite nanowires, the diffusion length along the nanowire is larger than their length, the flux on the top half of the nanowire contributes to the axial growth while the flux on the lower half compensates and exceeds the flux coming from the substrate leading to a cylinder-shaped nanowire with a pyramid at the base. For zinc-blende nanowire, the diffusion length along the nanowire facets is smaller than the nanowire length, the axial growth is due to the flux onto the facets of the top part while the flux from the substrate to the nanowire is smaller than the opposite flux forming a crater at the nanowire base and leading to a cone-shaped nanowire.

We present now the recipe that have been used to grow the (Cd,Mn)Te insertion in ZnTe nanowires covered by a (Zn,Mg)Te shell (**Sample 1**, see Figure 1.20):

Sample 1 has been grown on a II-VI substrate: (Cd,Zn)Te(111)B with 5% of Zn and disoriented of 2°C to avoid the formation of twins. To reduce the number of defects due to the lattice mismatch, a CdTe buffer layer was first grown at 240°C for 10 minutes and after a ZnTe layer at 300°C for almost 1 hour.

A flattening process of the surface was done at 420°C under Te rich atmosphere, Au

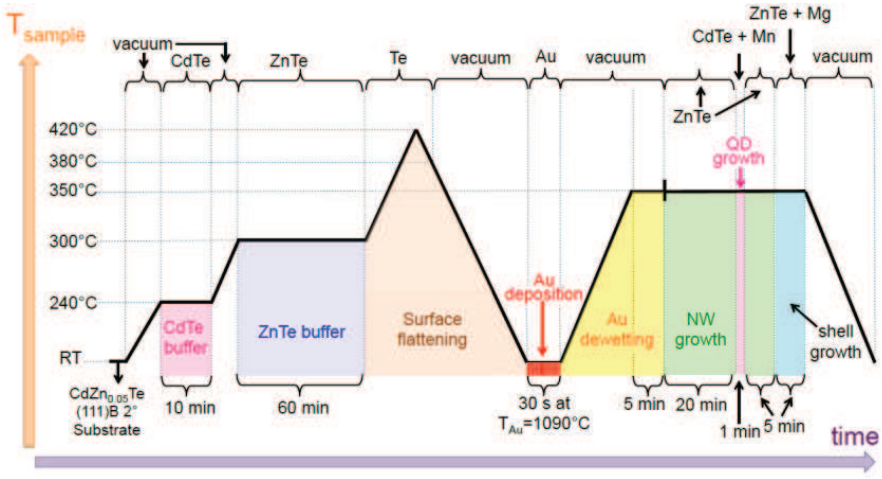

FIGURE 1.20: Sample 1 growth recipe used for the samples discussed in this thesis, taken from [14], [48]

was deposited at 1090°C for 30 seconds and dewetted at 350°C for 5 minutes to form Au nanoparticles. The nanowires were then grown using a ZnTe effusion cell with a unitary Te=Zn ratio at 350°C for 20 minutes and after, for the QD insertion, a CdTe and a Mn effusion cells were used simultaneously for 1 minute. As a final step the (Zn,Mg)Te shell was grown using a ZnTe and a Mg cells keeping the temperature unchanged for 5 minutes. As explained, the aim of the shell is to enhance the photoemitted signal by surface passivation avoiding non radiative recombination processes present at the surface.

Sample 2 has the same structure as Sample 1 but around the (Cd,Mn)Te insertion it was added Mg. The growth recipe is then very similar to the one of Sample 1 but before the (Cd,Mn)Te insertion, (Zn,Mg)Te has been grown for 5 minutes at the same temperature. The final (Zn,Mg)Te shell has been grown for 10 minutes instead of 5 minutes as for Sample 1.

The **Reference** sample consists in CdTe insertion in ZnTe nanowire covered by a (Zn,MgTe) shell. We used a GaAs (111) as a substrate: a ZnTe buffer layer has been grown for 60 minutes at 260°C followed by a flattening of the surface, under Te, at 420°C. As for Sample 1 and 2, we deposited a Au layer at 1090°C for 30 seconds and dewetted at 350°C for 10 minutes. The nanowires have been grown at 350°C: we used first a ZnTe effusion cell with a unitary Te:Zn ratio at 350°C for 40 minutes, after we grew the CdTe insertion for 1 minute and at the end we covered the nanowire by a (Zn,Mg)Te shell using a ZnTe and a Mg cells for 10 minutes.

In this thesis we studied only cone-shaped nanowires (Figure 1.18a) because thanks to their diffusion properties they are bigger and it is simpler to identify them after

the mechanical dispersion on a patterned substrate (the characterization technique is described in Section 1.6).

1.4 Magnetic Polaron formation in II-VI DMS

1.4.1 Review of some significant experimental results

In this Section we will present some of the recent experiments on Magnetic Polarons which can be compared with the ones observed in this manuscript.
First in this Introduction, we will remind what is a Magnetic Polaron and we will recall a bit of the history of their discovery. Mostly of the informations given in the first part of this Section, have been taken from a very nicely written review of papers where the first studies of Magnetic Polaron formation can be found. This review has been done by D.R. Yakovlev and W. Ossau and can be found in [27].
Figure 1.21 shows what is a Magnetic Polaron state.

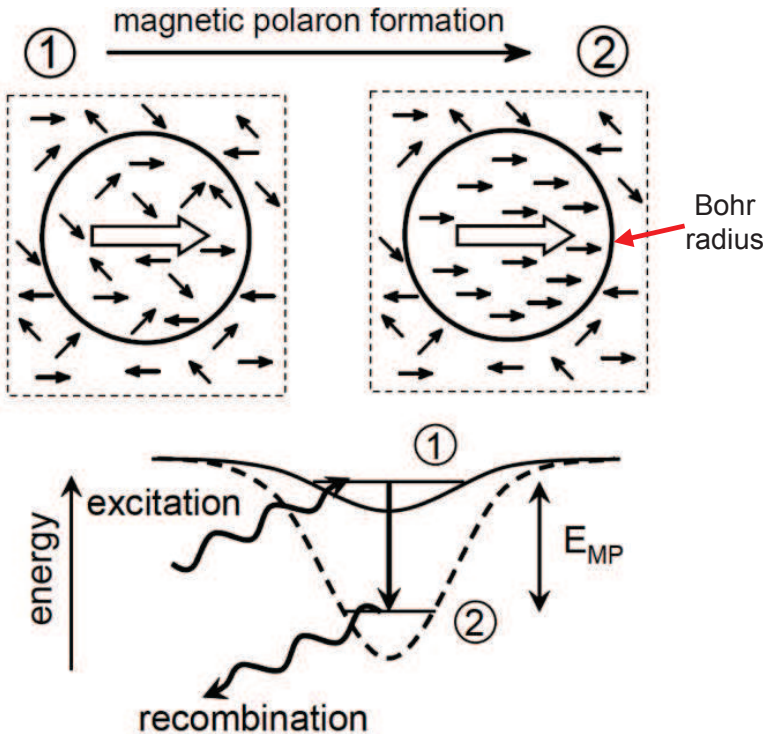

FIGURE 1.21: 1) Scheme of the Magnetic Polaron formation: after the creation of an exciton 2) the exchange interaction with the spins of the Mn atoms polarizes these spins 3) inside an effective volume that takes into account the exciton presence probability, and then decreasing the system energy, image taken from [27]

In DMS compound, the creation of localized exciton (this will be the case of our study but it could be replaced by a charge) starts to polarize locally the spins of the magnetic impurities (in our case Mn) via the sp-d exchange interactions [33] (Figure 1.21): this effect happens in a volume defined by the presence probability of the exciton.

The polarization of the Mn spins lower the total energy of the exciton (the scheme is shown in Figure 1.21) by a quantity E_P.
The "Magnetic Polaron" can be viewed as a quasi-particle state: the cloud of polarized spins can be in fact considered as a magnetic molecule with a total magnetic moment that can be as big as hundreds of Bohr magnetons at very low temperature [49]. Such big values of the total magnetic moment are possible thanks to the high exchange magnetic field ($\sim 1-3$T) that are polarizing a large numbers of Mn spins.
The first experiments, revealing the existence of Magnetic Polarons in magnetic semiconductors, were done by performing transport and magnetization measurements on EuO [50]. Unfortunately from these experiments it was not possible to retrieve detailed informations about the Magnetic Polaron energy and its spin structure.
The interest in Magnetic Polarons grew up after the appearance of II-VI DMS. It is in fact possible to use powerful optical characterization techniques (as you will see in the following) to determine all the Magnetic Polaron parameters: Raman scattering, time resolved photoluminescence spectroscopy and magneto-optical one.

Bound Magnetic Polarons

The first detailed experimental studies, with DMS materials, were done on bound Magnetic Polarons (BMP) with charges (donors) [9, 10].
The samples, n-type (Cd,Mn)Se bulk crystals, were studied by magneto Raman spectroscopy: a Stokes shift is measured and attributed to the BMP caused by spin-flip Raman scattering of the system conduction band. For this system, the Mn spins are polarized by the exchange field created by localized electrons on donors (see Figure 1.22a). The main results (shown in Figure 1.22b) are presented in [10] and they have been explained in [9] (the full model explication can be found in [15]).

The Stokes shifts, shown in Figure 1.22b (red line), at zero magnetic field are generated by the polarization of the Mn spins followed by the formation of the BMP state. The model used to fit the experimental data is based on the calculation of the total free energy: this treatment takes into account the spin fluctuations and can determine the magnitude of the total magnetic moment at any given temperature and at any given value of magnetic field. In Chapter 4 you will see that we will extend this model to analyze the Exciton Magnetic Polaron formation in a nanowire geometry.
Another pioneer work on the Magnetic Polarons can be found in [11]. This group

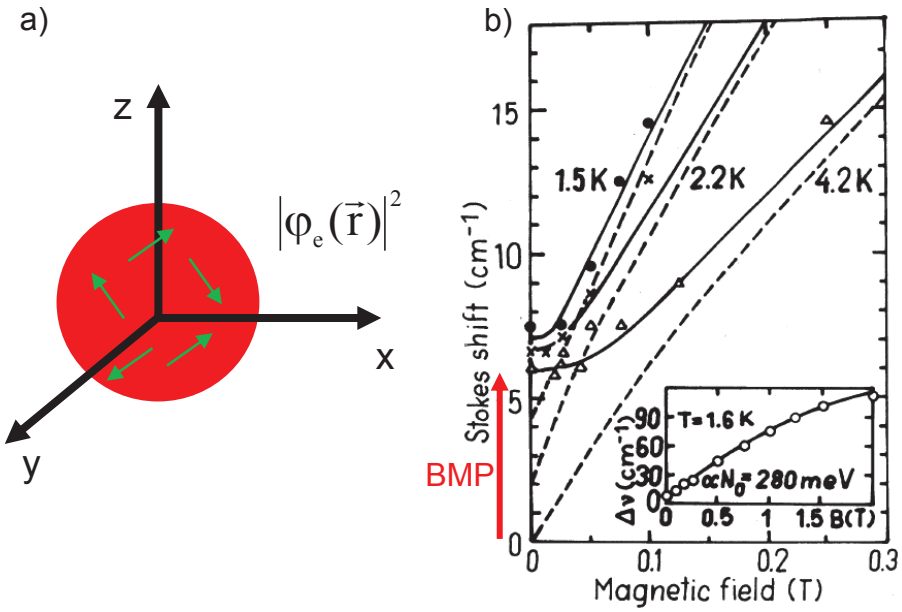

FIGURE 1.22: a) Bound Magnetic Polaron localized on a donor b) Photoluminescence spectra of (Cd,Mn)Se samples , image taken from [9]

studied Bound Magnetic Polaron (BMP) with high-purity p-type (Cd,Mn)Te bulk crystals. The BMP studied in [11] consists in Magnetic Polaron formed on localized acceptors (holes) (see Figure 1.23a): the polarization of the Mn atoms is done by the exchange field with the localized holes.

The photoluminescence line that has been studied is the acceptor one: (e, A^0). They performed detailed photoluminescence studies as function of the temperature for different (Cd,Mn)Te samples (with Mn concentration from 2% to 14%, see Figure 1.23c). We can see that it is possible to observe the characteristic fingerprint of the Magnetic Polaron formation. This fingerprint consists in a red shift of the photoluminescence line as function of the temperature (Figure 1.23c). The variation of the band gap induces a blue shift of the emission energy (dashed line) whereas the Magnetic Polaron formation induces a red shift, at low temperature, which is larger when the Mn concentration is high.
For the highest Mn concentration (Mn=14%) of Figure 1.23c they found a Magnetic Polaron energy of the order $E_P \simeq$50meV at T=5K.

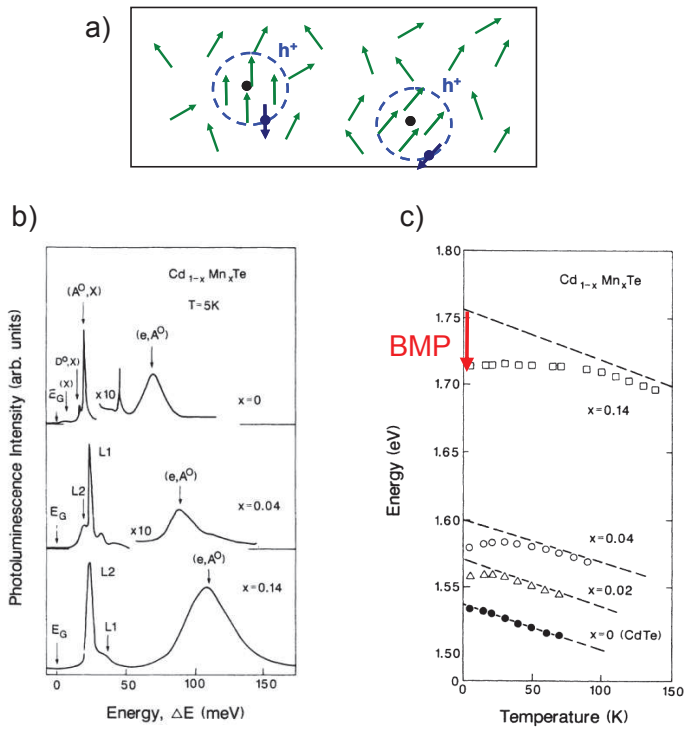

FIGURE 1.23: a) Bound Magnetic Polarons localized on acceptors b) Photoluminescence spectra of (Cd,Mn)Te samples for different Mn concentrations c) Photoluminescence position of the (e, A^0) line as function of the temperature for the different (Cd,Mn)Te samples, images taken from [11]

Exciton Magnetic Polarons

The first experimental results done on Exciton Magnetic Polaron (see Figure 1.24a) can be found in [51]. In this work, bulk crystals of (Cd,Mn)Te were studied by selective excitation of the exciton photoluminescence: this technique uses tunable laser to excite localized exciton states and to measure the Stokes shift of the photoluminescence line associated to the Magnetic Polaron formation.

When we are in presence of an Exciton Magnetic Polaron we could be limited by the exciton recombination lifetime: if the exciton lifetime is smaller than the Magnetic Polaron formation time (τ_f), the magnetic order will not have enough time to take place. For this reason, like in [51], time resolved photoluminescence measurements (see Figure 1.24b) are usually done in order to retrieve the Magnetic Polaron energy without being eventually limited by the exciton recombination time. The creation of an exciton, by the laser excitation at the time $t = 0$, will polarize the Mn spins by direct exchange interaction (see Figure 1.24a). The polarization of the Mn spins will

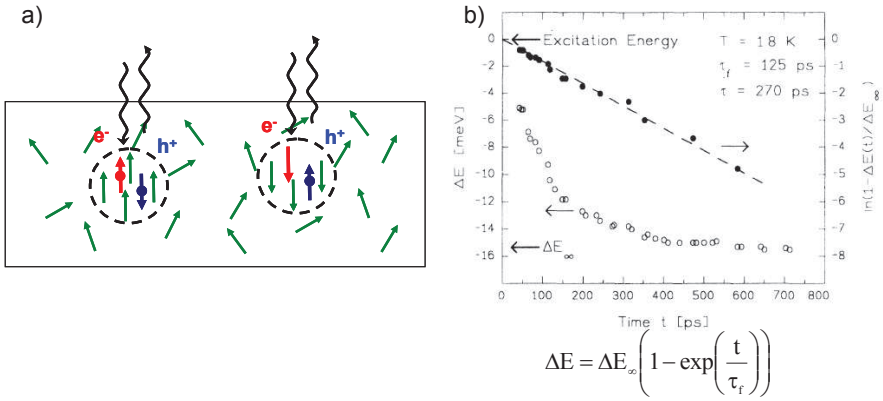

FIGURE 1.24: a) Bound Magnetic Polarons localized on excitons b) Time evolution of the polaron shift ΔE for a sample with Mn=15%, image taken from [51]

decrease the exciton energy and this process can be observed by time resolved photoluminescence experiment.

By fitting the photoluminescence transient energy shift in time (shown in Figure 1.24b) it is possible to retrieve the gain in energy of the exciton transition, i.e. the Magnetic Polaron energy (for this system is around $E_P \approx 15$meV at T=1.8K) and the characteristic formation time τ_f.

We saw that when we are dealing with Exciton Magnetic Polaron, the best experimental technique to retrieve the Magnetic Polaron parameters (the energy E_P and the formation time τ_f) is the time resolved photoluminescence experiment. We used this technique also to characterize our samples and the results, completed by complementary studies such as magneto-optical measurements or temperature dependent micro-PL, will be shown in Chapter 4.

1.4.2 Magnetic Polaron formation in quantum dots

1.4.2.1 Exchange Box Model

In this Section we present the most common model used to describe the Magnetic Polaron formation in quantum dots: it is called "Exchange Box Model". This model has been applied to heavy hole Magnetic Polarons: it is the only type of Magnetic Polaron that has been observed so far experimentally in any II-VI DMS quantum dots. The experimental studies will reveal that (see Chapter 4) we have in our case a light hole Magnetic Polaron. In Section 1.5, we will extend this "Exchange Box Model" to the case of a light hole Magnetic Polaron. Moreover we will summarize the behaviour

of a light hole and a heavy hole Magnetic Polaron for different magnetic field configurations.
Figure 1.25 shows a scheme of our quantum dot system.

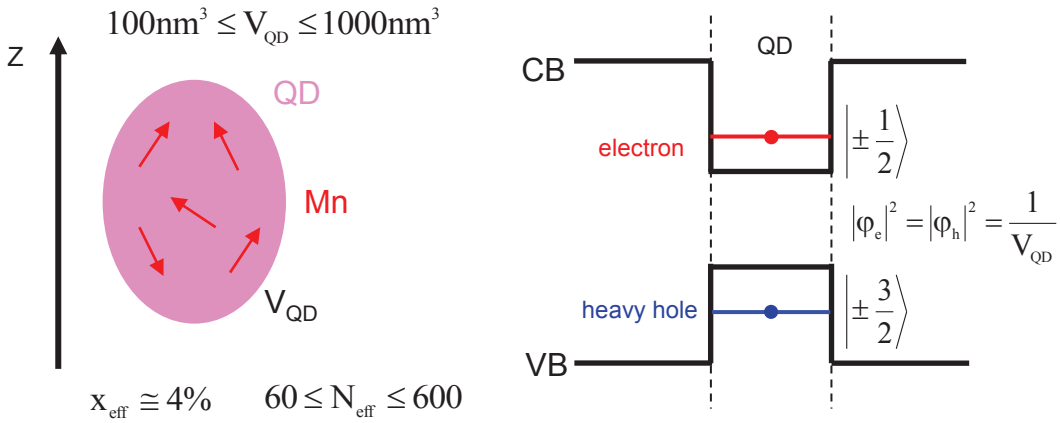

FIGURE 1.25: Scheme of the "Exchange Box Model"

In the presence of a Magnetic Polaron, there are sp-d exchange interactions between the Mn spins and the photocreated excitons. These exchange interactions are described by a Kondo-like Hamiltonian given by:

$$H_{sp-d} = H_{e-Mn} + H_{h-Mn} = -\alpha \sum_{\vec{R}_i} \vec{S}_i \cdot \vec{\sigma}_e |\psi_e(\vec{R}_i)|^2 - \frac{\beta}{3} \sum_{\vec{R}_i} \vec{S}_i \cdot \vec{J}_h |\psi_h(\vec{R}_i)|^2 \tag{1.34}$$

The simplest assumption in order to simplify the calculation is the so-called "Exchange Box Model", used to describe Magnetic Polarons in bulk crystals [52, 53] and then in heterostructures [6, 54–56]. It considers the quantum dot as a rigid box with a volume V_{QD} (see Figure 1.25) in which the envelope functions for electron and hole are $|\psi_e(\vec{R}_i)|^2 = |\psi_h(\vec{R}_i)|^2 = \frac{1}{V_{QD}}$, and in which Mn atoms are distributed homogeneously. This leads to an effective number of Mn spins that interacts with the exciton given by:

$$N_{eff} = N_0 x_{eff} V_{QD} \tag{1.35}$$

Moreover, like in Section 1.2.4, x_{eff} takes into account the Mn atoms that are not coupled by anti-ferromagnetic interactions.
As we did in Section 1.2.4, we can rewrite equation 1.34, by using MFA and VCA approximations, such as:

$$H_{sp-d} = H_{e-Mn} + H_{h-Mn} = -\alpha N_0 x_{eff} \langle \vec{S} \rangle \vec{\sigma}_e - \frac{\beta}{3} N_0 x_{eff} \langle \vec{S} \rangle \vec{J}_h \tag{1.36}$$

We remind that $H_{e-Mn} = -\alpha N_0 x_{eff} \langle \vec{S} \rangle \vec{\sigma}_e$ is defined by a 2×2 matrix and $H_{h-Mn} = -\frac{\beta}{3} N_0 x_{eff} \langle \vec{S} \rangle \vec{J}_h$ by a 4×4 one.
We can rewrite equation 1.38 by using the definition of magnetic moment at thermal equilibrium, given by:

$$\langle \vec{M} \rangle = -N_{eff} g_{Mn} \mu_B \langle \vec{S} \rangle \tag{1.37}$$

having then:

$$H_{sp-d} = H_{e-Mn} + H_{h-Mn} = \frac{\alpha \langle \vec{M} \rangle}{g_{Mn} \mu_B V_{QD}} \vec{\sigma}_e + \frac{\beta \langle \vec{M} \rangle}{3 g_{Mn} \mu_B V_{QD}} \vec{J}_h \tag{1.38}$$

We now consider a heavy hole Magnetic Polaron polarized along the quantization axis z ($\langle M_z \rangle \neq 0, \langle M_x \rangle = \langle M_y \rangle = 0$) with no applied magnetic field ($\vec{B} = 0$). We consider a σ^+ bright exciton composed by an electron in the ground state with spin projection $|-\frac{1}{2}\rangle$ and a heavy hole state with kinetic momentum projection $|+\frac{3}{2}\rangle$.
To retrieve the heavy hole Magnetic Polaron energy we have to calculate the exchange energies for electrons and holes:

$$E_P^{hh} = \langle -\frac{1}{2} | H_{e-Mn} | -\frac{1}{2} \rangle + \langle +\frac{3}{2} | H_{h-Mn} | +\frac{3}{2} \rangle \tag{1.39}$$

The exchange energies are given by:

$$\langle -\frac{1}{2} | H_{e-Mn} | -\frac{1}{2} \rangle = \alpha \frac{\langle M_z \rangle}{2 g_{Mn} \mu_B V_{QD}} \tag{1.40}$$

$$\langle +\frac{3}{2} | H_{h-Mn} | +\frac{3}{2} \rangle = -\beta \frac{\langle M_z \rangle}{2 g_{Mn} \mu_B V_{QD}} \tag{1.41}$$

We note that equation 1.41 has the form of a Zeeman Hamiltonian ($H_{ex} = -\langle M \rangle_z B_{ex}$), we can then define an electron and a heavy hole effective exchange field (along the z quantization axis) by:

$$B_{ex_z}^{ele} = \frac{\alpha}{2g_{Mn}\mu_B V_{QD}} > 0 \tag{1.42}$$

$$B_{ex_z}^{hole} = \frac{-\beta}{2g_{Mn}\mu_B V_{QD}} > 0 \tag{1.43}$$

Then, the heavy hole exciton Magnetic Polaron energy will be given by the sum of electron and hole exchange energies:

$$E_P^{hh} = \langle M_z \rangle \left[B_{ex_z}^{ele} + B_{ex_z}^{hole} \right] \tag{1.44}$$

The magnetic moment $\langle M_z \rangle$ at thermal equilibrium can be expressed as a function of the exchange fields using the modified Brillouin function:

$$\langle M_z \rangle = -M_{sat} B_{\frac{5}{2}} \left(\frac{g_{Mn}\mu_B \left(B_{ex_z}^{ele} + B_{ex_z}^{hole} \right) S}{k_B \left(T + T_{AF} \right)} \right) \tag{1.45}$$

With $M_{sat} = g_{Mn}\mu_B S N_{eff}$. The final expression for the heavy hole Magnetic Polaron energy, considering $\langle M_z \rangle \neq 0$, $\langle M_x \rangle = \langle M_y \rangle = 0$, will be:

$$E_P^{hh}[T] = [E_{se} + E_{sh}] B_{\frac{5}{2}} \left(\frac{g_{Mn}\mu_B \left(B_{ex_z}^{ele} + B_{ex_z}^{hole} \right) S}{k_B \left(T + T_{AF} \right)} \right) \tag{1.46}$$

Where E_{se} and E_{sh} were introduced in Section 1.2.4 and are given by:

$$E_{se} = \frac{\alpha N_0 x_{eff} S}{2} = M_{sat} B_{ex_z}^{ele} \tag{1.47}$$

$$E_{sh} = \frac{-\beta N_0 x_{eff} S}{2} = M_{sat} B_{ex_z}^{hh} \tag{1.48}$$

We trace now the heavy hole Magnetic Polaron energy ($E_P^{hh}[T]$) as a function of the temperature ($T + T_{AF}$) where we have considered the maximum exchange sp-d for a quantum dot with $x_{eff} = 4\%$ and $V_{QD} = 100\text{nm}^3$ (see Figure 1.26).

The energy $E_P^{hh}[T]$ strongly depends on the Mn temperature and then, for the experimental measurements, we chose the lowest laser excitation possible to avoid any

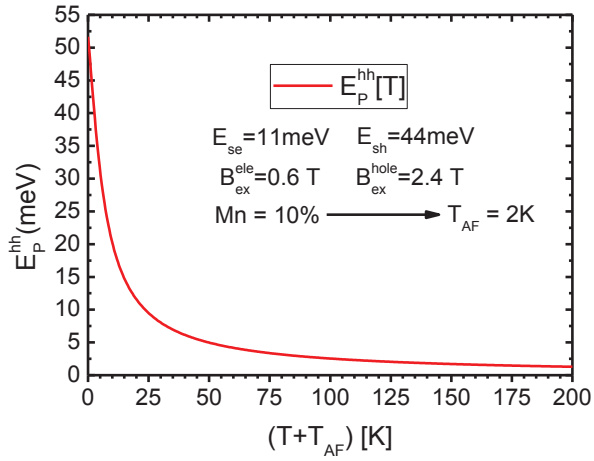

FIGURE 1.26: Variation of the heavy hole Magnetic Polaron energy as a function of the temperature, as calculated in the MFA approximation

heating effect of the Mn atoms.

As you will see in the following Section but also in Chapter 4 it is possible to retrieve the Magnetic Polaron temperature variation by performing micro-PL experiments as a function of the temperature. The photoluminescence energy position is in fact given by:

$$E_{PL}[T] = E_{gap}[T] - E_P^{hh}[T] \tag{1.49}$$

Where $E_{gap}[T]$ is the quantum dot bandgap variation as a function of the temperature.

We conclude this Section by considering what happens when we apply a magnetic field along the z direction. The applied magnetic field is taken into account in the definition of $\langle M_z \rangle$ by shifting the modified Brillouin function by the value of the external magnetic field:

$$\langle M_z \rangle = -M_{sat} B_{\frac{5}{2}} \left(\frac{g_{Mn}\mu_B \left(B_{ex_z}^{ele} + B_{ex_z}^{hole} + B \right) S}{k_B \left(T + T_{AF} \right)} \right) \tag{1.50}$$

The expression that describes the heavy hole Magnetic Polaron Zeeman energy, considering $\langle M_z \rangle \neq 0, \langle M_x \rangle = \langle M_y \rangle = 0$, is:

$$\Delta E_P^{hh}[B,T] = [E_{se} + E_{sh}] B_{\frac{5}{2}} \left(\frac{g_{Mn}\mu_B \left(B_{ex_z}^{ele} + B_{ex_z}^{hole} + B \right) S}{k_B \left(T + T_{AF} \right)} \right) \tag{1.51}$$

In Figure 1.27 we trace equation 1.51 considering the maximum exchange sp-d for a quantum dot with $x_{eff} = 4\%$ and a $T + T_{AF}$=11K.

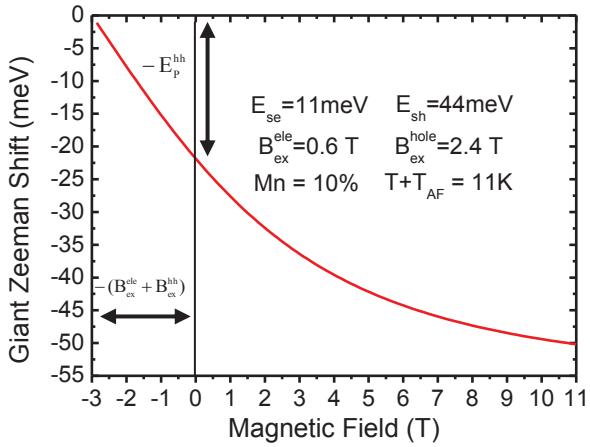

FIGURE 1.27: Giant Zeeman shift of a heavy hole Magnetic Polaron with an applied magnetic field along the z direction

The shifted Brillouin function intersects the horizontal axis at $-(B_{ex_z}^{ele} + B_{ex_z}^{hole})$ and the vertical axis at $-E_P^{hh}$.

1.4.2.2 Magnetic Polaron formation in (Cd,Mn)Te self assembled QDs

The first experiments, done to observe the Magnetic Polaron formation in (Cd,Mn)Te quantum dots (Mn concentration around 7%) can be found in [54]. Photoluminescence measurements recorded at different magnetic fields and temperatures are summarized in Figure 1.28.

Both measurements (temperature and magnetic field ones) can be explained with the "Exchange Box Model" introduced in the previous Section. The photoluminescence energy variations are in fact fitted by a modified Brillouin function where the exchange Magnetic Polaron internal field $B_P = B_{ex_z}^{ele} + B_{ex_z}^{hole}$ has been taken into account. In the present case, the calculated Magnetic Polaron energy is E_P=14meV at T=2K.
A more recent observation of a Magnetic Polaron in a (Cd,Mn)Te quantum dot (with a Mn concentration around 20%) can be found in [12]. The time evolution of the photoluminescence energy has been recorded using a streak camera. The results are shown in Figure 1.29.

By using the "Exchange Box Model", it is possible to retrieve a Magnetic Polaron energy, that in the present case is E_P=13meV at T=8K with a characteristic formation

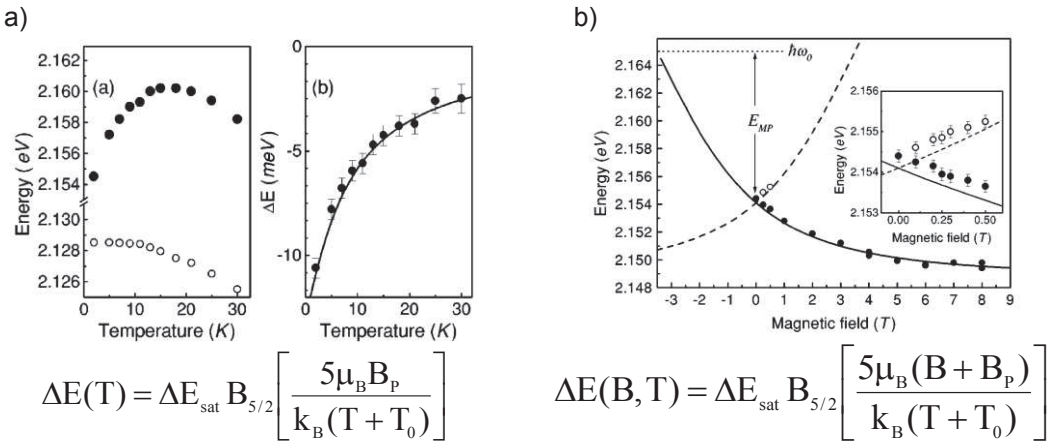

FIGURE 1.28: a) Temperature dependence of the photoluminescence energy for non magnetic (open circles) and magnetic (solid circles) (Cd,Mn)Te QDs b) Magnetic field dependence of the photoluminescence energy for a (Cd,Mn)Te quantum dot (solid symbols is σ^+ polarization and open symbols are σ^- polarized), images have been taken from [54]

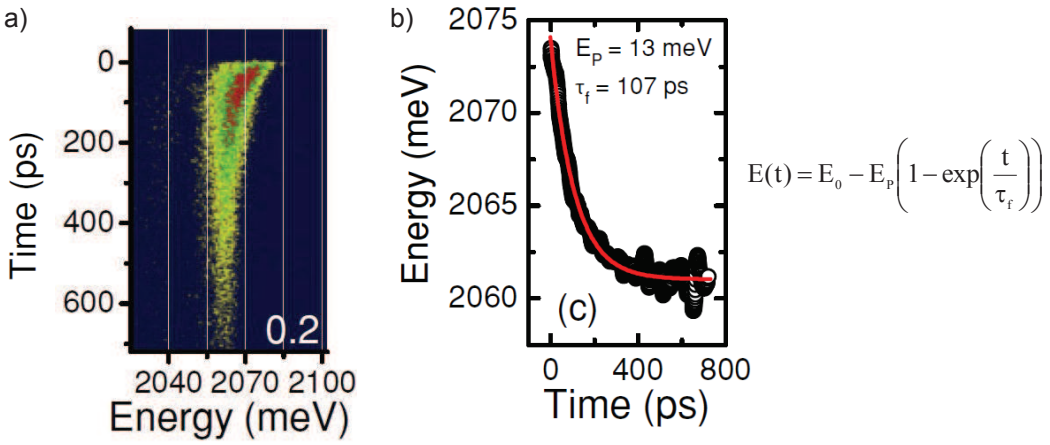

FIGURE 1.29: a) Streak camera images of photoluminescence signal for a (Cd,Mn)Te quantum dot b) Transient photoluminescence energy as function of time, images taken from [12]

time given by τ_f=107ps. These measurements will be compared with the time resolved photoluminescence experiments that we have done on our system in Chapter 4.

A recent work on Magnetic Polaron formation (2015), that goes beyond the "Exchange Box Model" to describe the Magnetic Polaron formation, can be found in [35]. In this paper, Type II quantum dots (the electron is localized in the barrier while the hole is confined inside the quantum dot region) have been studied mainly by time resolved photoluminescence experiments. The studied samples are ZnTe quantum dot in a ZnSe matrix: Mn atoms (Mn concentration around 5%) are incorporated in the matrix (sample 1) or in the quantum dot region (sample 3) (see Figure 1.30a).

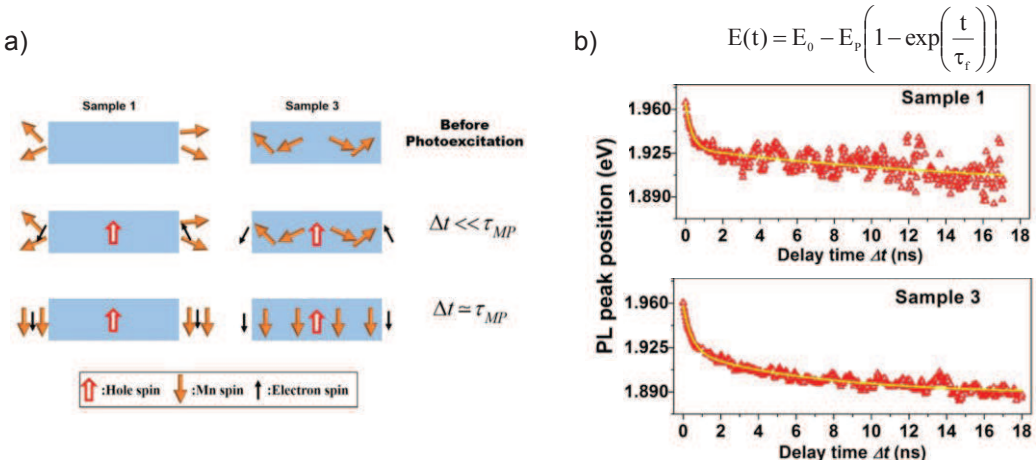

FIGURE 1.30: a) ZnTe quantum dot in (Zn,Mn)Se matrix (sample 1), (Zn,Mn)Te quantum dot in ZnSe matrix (sample 3) b) Transient photoluminescence energy as function of time for the two samples, images taken from [35]

Both samples present a long exciton decay time (Type II quantum dot) with a Magnetic Polaron state (see Figure 1.30). The energies of the Magnetic Polaron are E_P=25.4meV for sample 1 and E_P=34.4meV for sample 3, recorded at T=7K.
A free energy approach, extending what has been done in [9], has been used to deduce the Magnetic Polaron energies and these results will be compared with the ones that we have found at the end of Chapter 4.

1.4.2.3 Charged Magnetic Polaron: beyond the "Exchange Box Model"

Another study of Magnetic Polarons in (Cd,Mn)Te self assembled quantum dots (with Mn concentration around 10%) was done by Petr Stepanov [17], a PhD student responsible for the optical measurements in our group before my arrival.
The main result showing the Magnetic Polaron formation by means of time resolved photoluminescence experiments are shown in Figure 1.31.

The photoluminescence spectrum is composed by an exciton (X) and a charged exciton (X^-) (Figure 1.31a,b). The transients photoluminescence energies as function of the time show a Magnetic Polaron formation for both states with energies E_P=11meV for the exciton and E_P=15meV for the charged one recorded at T=7K.
From Figure 1.31 we can see that in this case time resolved photoluminescence measurements are needed to determine the correct Magnetic Polaron energy: the Magnetic Polaron formation time is in fact higher compared to the exciton lifetime (see Figure 1.31c,d). In a continuous experiment, we would have find a smaller value for the Magnetic Polaron energy.

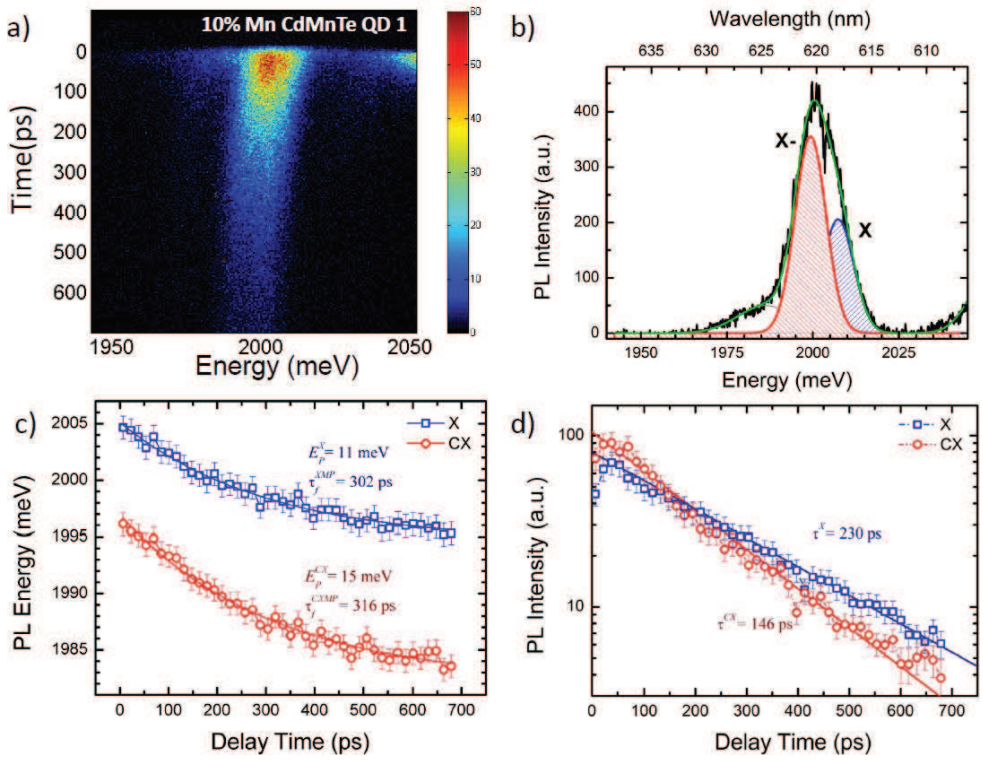

FIGURE 1.31: a) Streak camera measurement of a (Cd,Mn)Te quantum dot b) Photoluminescence spectrum showing the exciton (X) and the charged exciton (X^-) c) Transient photoluminescence energy as function of time d) Transient photoluminescence intensities as function of time, images taken from [17]

1.5 Light hole and heavy hole Magnetic Polaron in anisotropic quantum dot

Introduction

In this Section we extend the "Exchange Box Model" to the case of a light hole Magnetic Polaron in order to calculate the Magnetic Polaron energies for any type of quantum dots (light hole or heavy hole) and for any direction of the applied magnetic field.
As you will see in details in Chapter 2, by playing with the quantum dot shape (the ratio $\frac{L}{D}$ of the length divided by the diameter of the quantum dot) we can have different exciton ground states depending on the hole anisotropy (ΔE). In the presence of an elongated quantum dot, the exciton ground state has a light hole character ($\Delta E > 0$), while for a flat dot the ground state has a heavy hole character ($\Delta E < 0$) (see Figure 1.32).

For simplicity we will consider a quantum dot with a circular symmetry and we restrict the studies to the case of azimuthal angle $\varphi = 0$. The averaged magnetic moment of the dot is given by:

$$\begin{aligned}\langle\vec{M}\rangle(\theta,\phi) &= \langle\vec{M}\rangle[\cos(\theta)\vec{e}_z + \sin(\theta)\cos(\varphi)\vec{e}_x + \sin(\theta)\sin(\varphi)\vec{e}_y] \\ &= \langle\vec{M}\rangle[\cos(\theta)\vec{e}_z + \sin(\theta)\vec{e}_x] = \\ &= \langle M_z\rangle\vec{e}_z + \langle M_x\rangle\vec{e}_x = \langle M\rangle(\theta)\end{aligned} \tag{1.52}$$

We consider a uniaxial hole anisotropy that is described by a diagonal matrix form [57] written in the heavy hole basis ($+\frac{3}{2}$, $+\frac{1}{2}$, $-\frac{1}{2}$ and $-\frac{3}{2}$):

$$H_{an} = \frac{\Delta E}{2}(J_{h_z}^2 - \frac{J(J+1)}{3}) \tag{1.53}$$

Where J_h is the hole kinetic spin operator. For $\Delta E > 0$ the quantum dot ground state has a light hole character while for $\Delta E < 0$ it has a heavy hole one (see Figure 1.32).

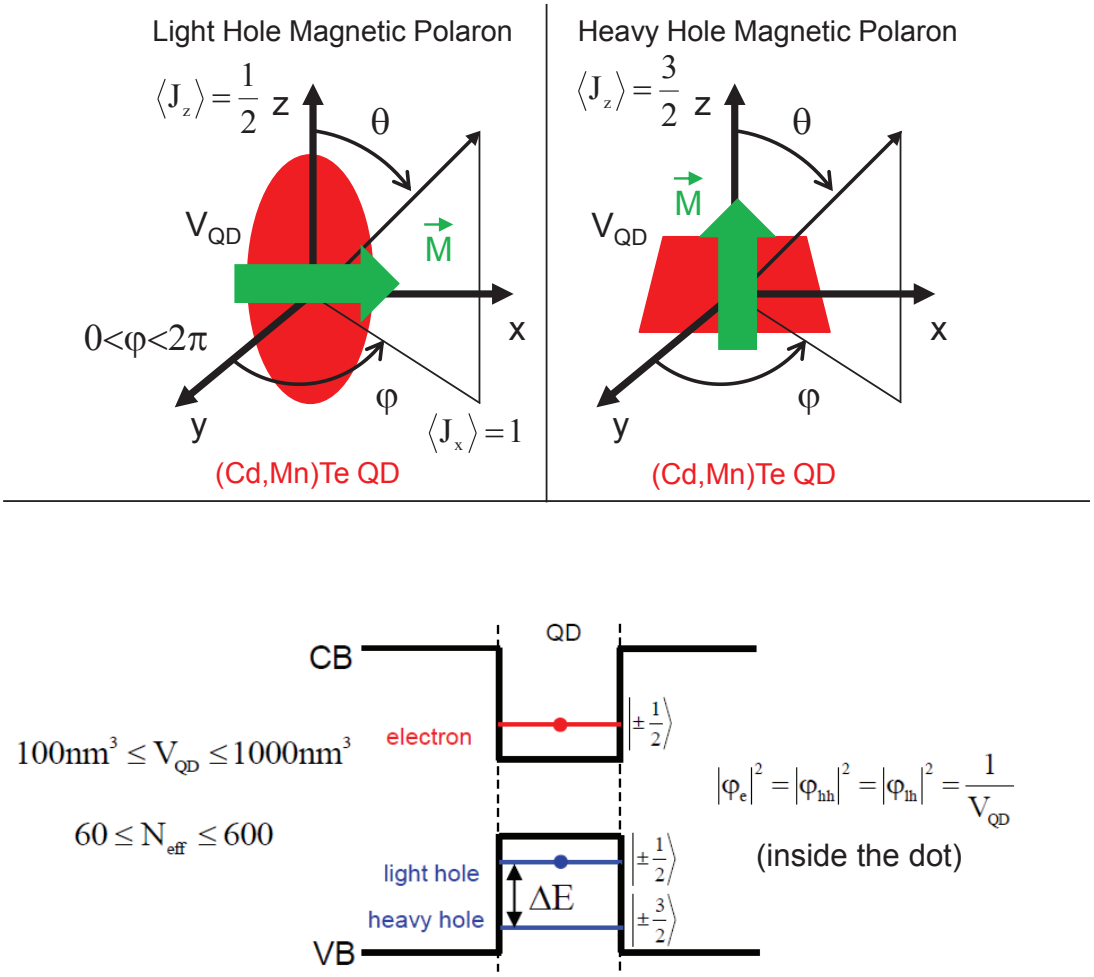

FIGURE 1.32: Light hole and heavy hole exciton Magnetic Polaron

Calculation of heavy hole Magnetic Polaron energy

Following the same treatment used for the "Exchange Box Model" (see Section 1.4.2.1) we now calculate the Magnetic Polaron energy for a pure heavy hole exciton ($\Delta E \longrightarrow -\infty$).

First we calculate the exchange field and Magnetic Polaron energy assuming a non zero magnetic moment oriented with a polar angle θ ($\langle M_x \rangle \neq 0$ and $\langle M_z \rangle \neq 0$). The exchange Hamiltonians for electron-Mn and hole-Mn interactions are given by (see equation 1.38):

$$H_{e-Mn} = \frac{\alpha\left(\langle M_z\rangle \sigma_{e_z} + \langle M_x\rangle \sigma_{e_x}\right)}{g_{Mn}\mu_B V_{QD}}$$
$$H_{h-Mn} = \frac{\beta\left(\langle M_z\rangle J_{h_z} + \langle M_x\rangle J_{h_x}\right)}{3g_{Mn}\mu_B V_{QD}}$$

and hence, by writing the magnetic moment in its matrix form we will have:

$$H_{e-Mn} = \frac{\alpha\langle M\rangle}{g_{Mn}\mu_B V_{QD}}\begin{pmatrix} \frac{\cos(\theta)}{2} & \frac{\sin(\theta)}{2} \\ \frac{\sin(\theta)}{2} & -\frac{\cos(\theta)}{2}\end{pmatrix} \tag{1.54}$$

$$H_{h-Mn} = \frac{\beta\langle M\rangle}{3g_{Mn}\mu_B V_{QD}}\begin{pmatrix} \frac{3\cos(\theta)}{2} & 0 \\ 0 & -\frac{3\cos(\theta)}{2}\end{pmatrix} \tag{1.55}$$

Thanks to the diagonal form of the exchange hole Hamiltonian (H_{h-Mn}), we can retrieve easily the eigenstates ($|\frac{3}{2}\rangle$, $|-\frac{3}{2}\rangle$) and eigenvalues of the hole ($E^{hh}_{\pm} = \frac{\Delta hh}{2}$) where the hole splitting energy is:

$$\Delta_{hh} = \frac{-\beta\langle\vec{M}\rangle\cos(\theta)}{g_{Mn}\mu_B V_{QD}}$$

For the exchange electron Hamiltonian (H_{e-Mn}) we have first to diagonalize the spin matrix leading to two eigenstates given by:

$$|\psi_{e^+}\rangle = \cos(\frac{\theta}{2})\,|+\frac{1}{2}\rangle + \sin(\frac{\theta}{2})\,|-\frac{1}{2}\rangle \tag{1.56}$$
$$|\psi_{e^-}\rangle = -\sin(\frac{\theta}{2})\,|+\frac{1}{2}\rangle + \cos(\frac{\theta}{2})\,|-\frac{1}{2}\rangle \tag{1.57}$$

with eigenvalues $E^{el}_{\pm} = \pm\frac{\Delta e}{2}$, where the electron splitting energy is:

$$\Delta_e = \frac{\alpha\langle\vec{M}\rangle}{g_{Mn}\mu_B V_{QD}} \tag{1.58}$$

Like in Section 1.4.2.1, we can now calculate the Magnetic Polaron energy that is given by the sum of the exchange energies of the electron and hole thermalized in the ground state ($|\psi_{e^-}\rangle$ for the electron and $|+\frac{3}{2}\rangle$ for the hole):

$$\langle\psi_{e^-}|\,H_{e-Mn}\,|\psi_{e^-}\rangle = \frac{\alpha}{g_{Mn}\mu_B V_{QD}}\left[\langle M_z\rangle\,\langle\psi_{e^-}|\,\sigma_{e_z}\,|\psi_{e^-}\rangle + \langle M_x\rangle\,\langle\psi_{e^-}|\,\sigma_{e_x}\,|\psi_{e^-}\rangle\right] \tag{1.59}$$

$$\langle+\frac{3}{2}|\,H_{h-Mn}\,|+\frac{3}{2}\rangle = \frac{\beta}{3g_{Mn}\mu_B V_{QD}}\left[\langle M_z\rangle\,\langle+\frac{3}{2}|\,J_{h_z}\,|+\frac{3}{2}\rangle + \langle M_x\rangle\,\langle+\frac{3}{2}|\,J_{h_x}\,|+\frac{3}{2}\rangle\right] \tag{1.60}$$

By observing that we can rewrite the Hamiltonian as a Zeeman one, we can define an electron magnetic exchange field and a heavy hole one (as we did in Section 1.4.2.1) by:

$$\langle\psi_{e^-}|\,H_{e-Mn}\,|\psi_{e^-}\rangle = -\langle M_z\rangle\,B^{e^-}_{ex_z} - \langle M_x\rangle\,B^{e^-}_{ex_x} \tag{1.61}$$

$$\langle+\frac{3}{2}|\,H_{h-Mn}\,|+\frac{3}{2}\rangle = -\langle M_z\rangle\,B^{hh}_{ex_z} \tag{1.62}$$

The exchange field for the electron will be given by:

$$B^{e^-}_{ex_z} = \frac{\alpha\cos(\theta)}{2g_{Mn}\mu_B V_{QD}} = B^{ele}_{ex}\cos(\theta) \tag{1.63}$$

$$B^{e^-}_{ex_x} = \frac{\alpha\sin(\theta)}{2g_{Mn}\mu_B V_{QD}} = B^{ele}_{ex}\sin(\theta) \tag{1.64}$$

With $B^{ele}_{ex} = \frac{\alpha}{2g_{Mn}\mu_B V_{QD}}$. We observe that for electron, the exchange field will be aligned along the magnetic moment $\langle\vec{M}\rangle$ with $B^{e^-}_{ex} = \frac{\alpha}{2g_{Mn}\mu_B V_{QD}}$ (the electron spin is isotropic). For the heavy hole the exchange field is anisotropic and remains oriented along the z direction having:

$$B^{hh}_{ex_z} = \frac{-\beta cos(\theta)}{2g_{Mn}\mu_B V_{QD}} = B^{hole}_{ex}cos(\theta) \tag{1.65}$$

Where we recall that we have defined $B^{hole}_{ex} = \frac{-\beta}{2g_{Mn}\mu_B V_{QD}}$. We see that the expression for the Magnetic Polaron energy will depend on the angle θ by:

$$-E_P^{hh}[\theta] = \langle M \rangle \left[B_{ex}^{ele} + B_{ex}^{hole} cos(\theta)\right] \tag{1.66}$$

with the total magnetic moment defined as:

$$\langle M \rangle = -M_{sat} B_{\frac{5}{2}} \left(\frac{g_{Mn}\mu_B \left(B_{ex}^{e^-} + B_{ex}^{hh} cos(\theta)\right) S}{k_B \left(T + T_{AF}\right)} \right) \tag{1.67}$$

From equation 1.66 we observe that the maximum Magnetic Polaron energy is for $\theta = 0$ leading to a magnetic moment aligned along the z axis (see Figure 1.32).

Calculation of light hole Magnetic Polaron energy

To calculate the energy of a pure light hole Magnetic Polaron we have to repeat the same procedure but considering the spin kinetic projection J_h associated to the light hole. The exchange Hamiltonian for the electron and hole will be given by:

$$H_{e-Mn} = \frac{\alpha \langle M \rangle}{g_{Mn}\mu_B V_{QD}} \begin{pmatrix} \frac{\cos(\theta)}{2} & \frac{\sin(\theta)}{2} \\ \frac{\sin(\theta)}{2} & -\frac{\cos(\theta)}{2} \end{pmatrix} \tag{1.68}$$

$$H_{h-Mn} = \frac{\beta \langle M \rangle}{3 g_{Mn}\mu_B V_{QD}} \begin{pmatrix} \frac{\cos(\theta)}{2} & \sin(\theta) \\ \sin(\theta) & -\frac{\cos(\theta)}{2} \end{pmatrix} \tag{1.69}$$

As we did before, we have to diagonalize H_{e-Mn} and H_{h-Mn} to find the eigenstates and eigenvalues of the system. For the electron we have the same result as presented before, while for the hole the two eigenstates are:

$$|\psi_{lh^+}\rangle = \cos(\frac{\varepsilon}{2})|+\frac{1}{2}\rangle + \sin(\frac{\varepsilon}{2})|-\frac{1}{2}\rangle \tag{1.70}$$

$$|\psi_{lh^-}\rangle = -\sin(\frac{\varepsilon}{2})|+\frac{1}{2}\rangle + \cos(\frac{\varepsilon}{2})|-\frac{1}{2}\rangle \tag{1.71}$$

Here ε is defined such as: $\tan(\varepsilon) = 2\tan(\theta)$. The eigenvalues for the hole are: $E_{\pm}^{lh} = \pm\frac{\Delta lh}{2}$ where the electron and hole energy splittings are given by:

$$\Delta_e = \frac{\alpha \langle \vec{M} \rangle}{g_{Mn}\mu_B V_{QD}} \tag{1.72}$$

$$\Delta_{lh} = \frac{-\beta \langle \vec{M} \rangle}{3 g_{Mn}\mu_B V_{QD}} \sqrt{\frac{cos^2(\theta)}{4} + sin^2(\theta)} \tag{1.73}$$

As we did for the heavy hole Magnetic Polaron, we calculate the exchange energies of the electron and hole thermalized in their ground states ($|\psi_{e^-}\rangle$ for the electron and $|\psi_{lh^+}\rangle$ for the hole):

$$\begin{aligned} \langle \psi_{e^-} | H_{e-Mn} | \psi_{e^-} \rangle &= \frac{\alpha}{g_{Mn}\mu_B V_{QD}} \left[\langle M_z \rangle \langle \psi_{e^-} | \sigma_{e_z} | \psi_{e^-} \rangle + \langle M_x \rangle \langle \psi_{e^-} | \sigma_{e_x} | \psi_{e^-} \rangle \right] = \\ &= - \langle M_z \rangle B^{e^-}_{ex_z} - \langle M_x \rangle B^{e^-}_{ex_x} \end{aligned} \tag{1.74}$$

$$\begin{aligned} \langle \psi_{lh^+} | H_{h-Mn} | \psi_{lh^+} \rangle &= \frac{\beta}{3 g_{Mn}\mu_B V_{QD}} \left[\langle M_z \rangle \langle \psi_{lh^+} | J_{h_z} | \psi_{lh^+} \rangle + \langle M_x \rangle \langle \psi_{lh^+} | J_{h_x} | \psi_{lh^+} \rangle \right] = \\ &= - \langle M_z \rangle B^{lh}_{ex_z} - \langle M_x \rangle B^{lh}_{ex_x} \end{aligned} \tag{1.75}$$

We can now retrieve the expressions for the electron and light hole exchange fields given by (for the electron we have the same results as for the heavy hole Magnetic Polaron):

$$B^{e^-}_{ex_z} = \frac{\alpha \cos(\theta)}{2 g_{Mn}\mu_B V_{QD}} = B^{ele}_{ex} \cos(\theta) \tag{1.76}$$

$$B^{e^-}_{ex_x} = \frac{\alpha \sin(\theta)}{2 g_{Mn}\mu_B V_{QD}} = B^{ele}_{ex} \sin(\theta) \tag{1.77}$$

$$B^{lh}_{ex_z} = \frac{-\beta \cos(\varepsilon)}{6 g_{Mn}\mu_B V_{QD}} = \frac{B^{hole}_{ex}}{3} \cos(\varepsilon) \tag{1.78}$$

$$B^{lh}_{ex_x} = \frac{-\beta \sin(\varepsilon)}{3 g_{Mn}\mu_B V_{QD}} = \frac{2B^{hole}_{ex}}{3} \sin(\varepsilon) \tag{1.79}$$

We can deduce now the expression for the light hole Magnetic Polaron energy given by:

$$-E_P^{lh}[\theta] = \langle M \rangle [B_{ex}^{ele} + \frac{B_{ex}^{hole}}{3}\cos(\varepsilon)\cos(\theta) + \frac{2B_{ex}^{hole}}{3}\sin(\varepsilon)\sin(\theta)] \tag{1.80}$$

The light hole Magnetic Polaron energy is a function of θ (see equation 1.80). In zero external field the maximum Magnetic Polaron energy is obtained with $\theta = \frac{\pi}{2}$ (x direction). In Figure 1.33 we summarize what we have found so far for the heavy hole and the light hole Magnetic Polaron systems for the cases where the Magnetic Polaron energies are maximum ($\theta = \frac{\pi}{2}$ for the light hole and $\theta = 0$ for the heavy hole).

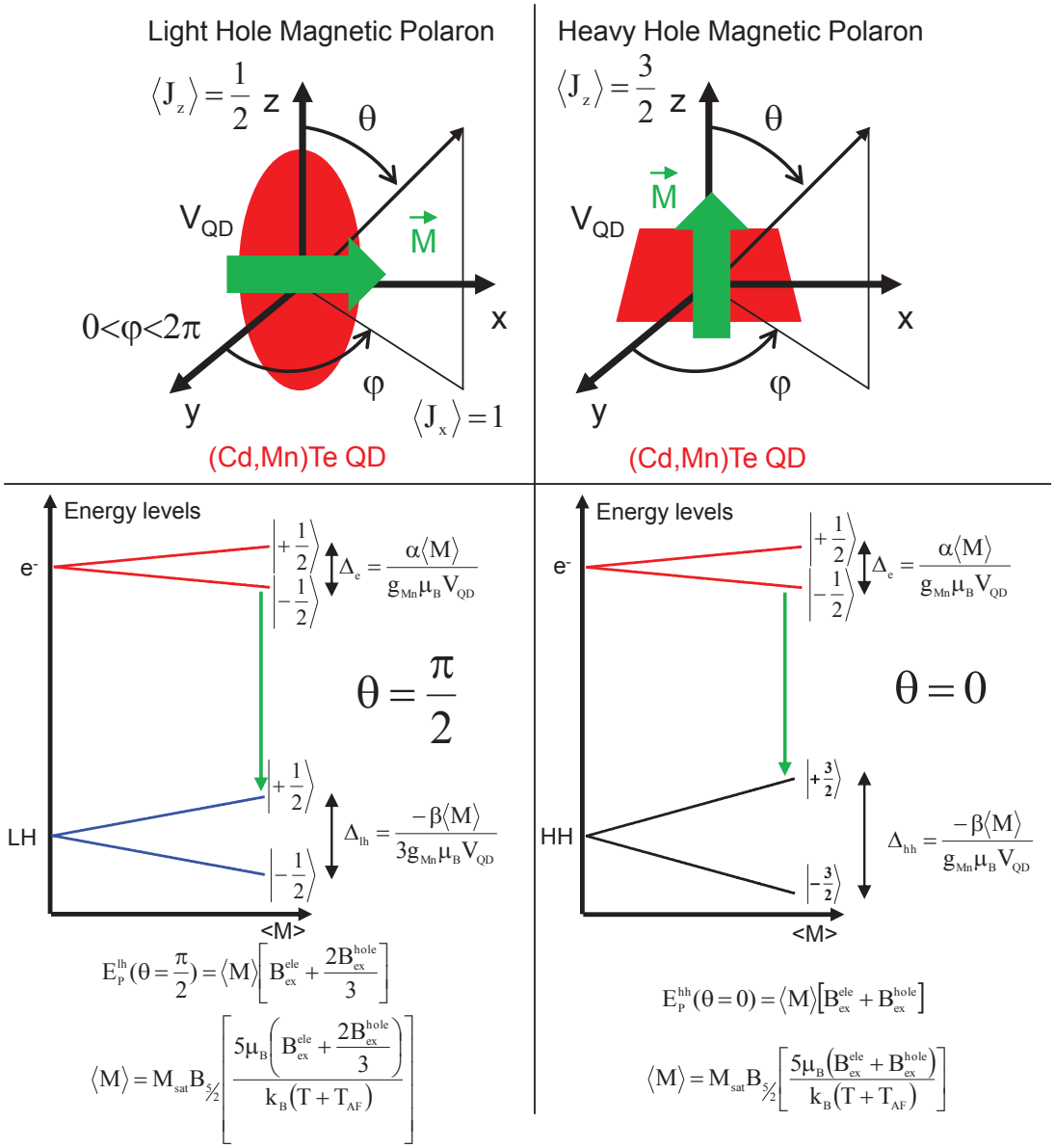

FIGURE 1.33: Light hole and heavy hole exciton Magnetic Polarons

1.5.1 Magnetic Field applied along the easy magnetization axis

In this Section we calculate the Giant Zeeman shift of a light hole and a heavy hole Magnetic Polaron using the equations derived in the previous Section. We consider the case where the magnetic field is applied along an easy magnetization axis: along the x axis for the light hole Magnetic Polaron and along the z axis for the heavy hole one.
We are interested on the fundamental state: for a light hole Magnetic Polaron this is given by one electron in the spin state $-\frac{1}{2}$ and one hole in the kinetic momentum state $+\frac{1}{2}$ while for a heavy hole Magnetic Polaron, the electron state is the same but the hole one is the $+\frac{3}{2}$. To emphasize the exciton Giant Zeeman shift, we plot also, in Figure 1.34, the excited states where we have considered a spin flipping of the electron or the hole after the formation of the Magnetic Polaron in the fundamental state. Anyway we will always focus our attention on the fundamental state and hence we will not consider the excited states in the analysis of the experimental data.

For the calculations, we consider a hole exchange field B_{ex}^{hole}=2.4T and an electron one B_{ex}^{ele}=0.6T. All the parameters used for the simulations are given in the following table.

$T + T_{AF}$=11K	E_{sh}=44 meV	E_{se}=11meV	B_{ex}^{hole}=2.4T	B_{ex}^{ele}=0.6T

The exciton Giant Zeeman energies, calculated using the electron and hole splitting energies are given by:

$$\Delta E_{PL}^{hh} = \pm (E_{se} + E_{sh}) \mathrm{B}_{\frac{5}{2}} \left(\frac{g_{Mn}\mu_B \left(B_z + B_{ex}^{ele} + B_{ex}^{hole}\right) S}{k_B (T + T_{AF})} \right) \tag{1.81}$$

$$\Delta E_{PL}^{lh} = \pm \left(E_{se} \pm \frac{E_{sh}}{3} \right) \mathrm{B}_{\frac{5}{2}} \left(\frac{g_{Mn}\mu_B \left(B_x + B_{ex}^{ele} + \frac{2}{3} B_{ex}^{hole}\right) S}{k_B (T + T_{AF})} \right) \tag{1.82}$$

The behaviour under magnetic field for both light hole and heavy hole Magnetic Polaron, when the magnetic field is applied along the easy magnetization axis, is well explained by a shifted Brillouin function. We will see, in the next Sections, that when the magnetic field is applied perpendicular to the easy magnetization axis we have uncommon situations.

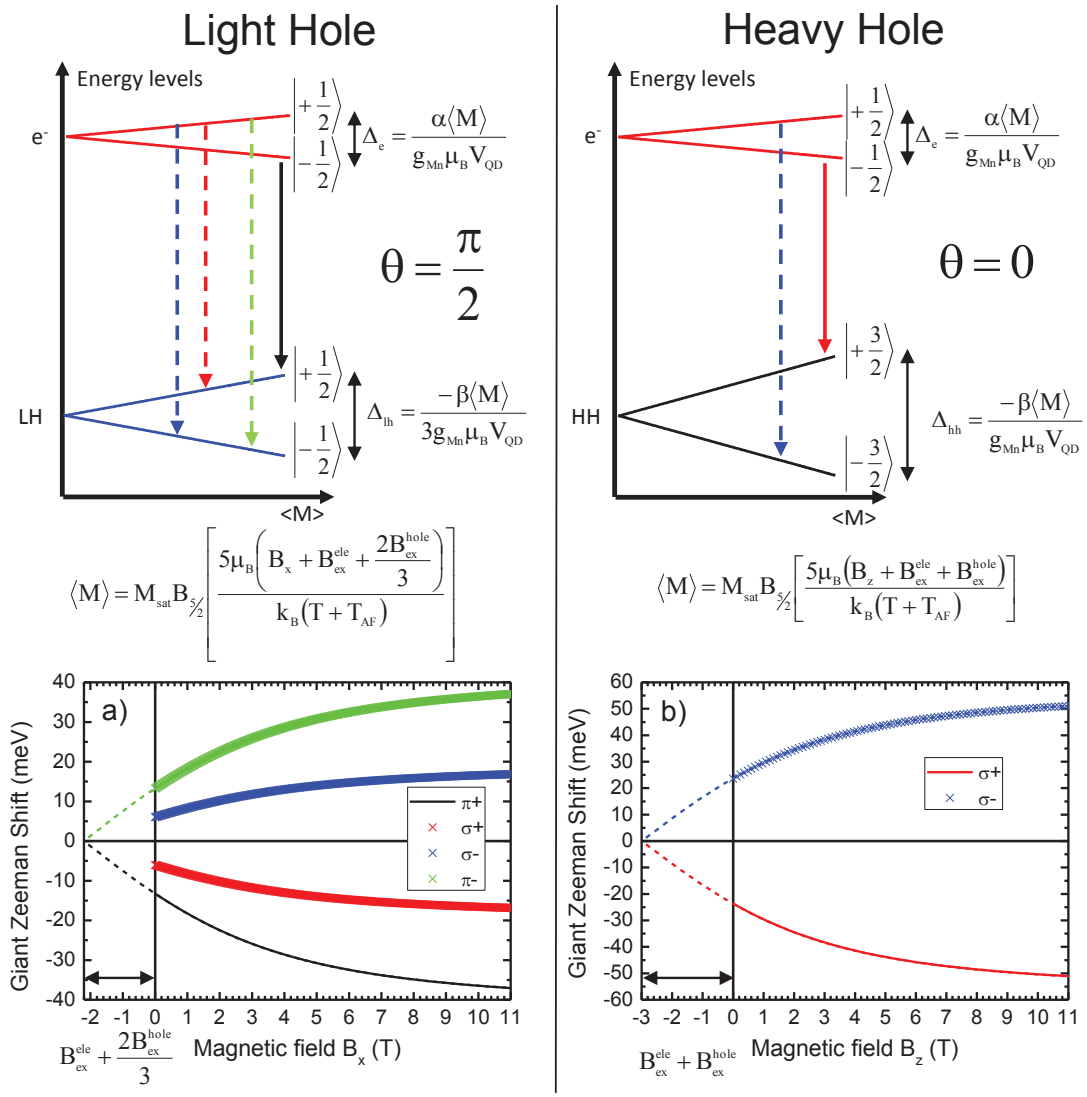

FIGURE 1.34: a) Giant Zeeman Shift for a light hole Magnetic Polaron with an applied magnetic field along the x axis b) Giant Zeeman Shift for a heavy hole Magnetic Polaron with an applied magnetic field along the z axis

1.5.2 Magnetic Field applied perpendicular to the easy magnetization axis

1.5.2.1 The case of a heavy hole Magnetic Polaron

In this paragraph we present the configuration where a magnetic field is applied along the *x* axis for a heavy hole Magnetic Polaron state (see Figure 1.35).

The sp-d interaction Hamiltonian is the sum of the electron and hole exchange Hamiltonian and the Zeeman one, given by (see Figure 1.35):

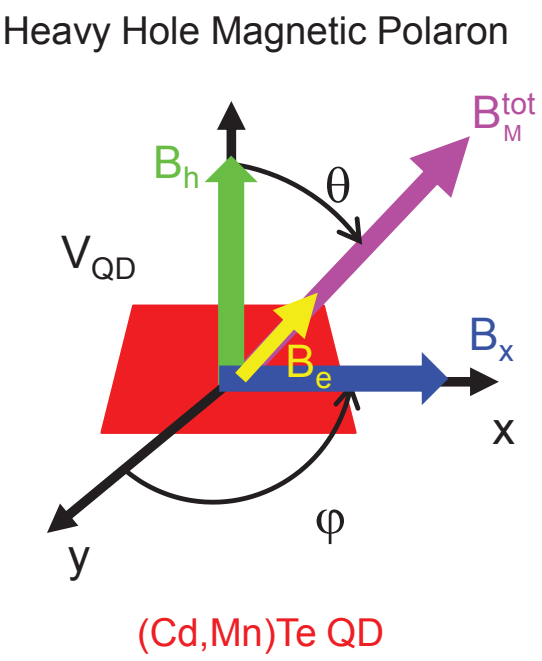

FIGURE 1.35: Heavy hole Magnetic Polaron exchange field in a configuration where the applied magnetic field is along the x axis

$$H_{sp-d} = H_{e-Mn} + H_{h-Mn} - \langle \vec{M} \rangle \cdot \vec{B} = - \langle M \rangle \left[B_{ex}^{ele} + B_{ex}^{hole} \cos(\theta) + B \sin(\theta) \right] \tag{1.83}$$

Where we recall the expression for the electron and hole exchange fields given by:

$$B_{ex}^{ele} = \frac{\alpha}{2 g_{Mn} \mu_B V_{QD}}$$
$$B_{ex}^{hole} = \frac{-\beta}{2 g_{Mn} \mu_B V_{QD}}$$

The projection of all magnetic fields (exchange and external ones) along the magnetic moment $\langle M \rangle$ direction, is given by:

$$B_M^{tot} = B_{ex}^{ele} + B_{ex}^{hole} \cos(\theta) + B \sin(\theta) \tag{1.84}$$

In the MFA approximation, the angle θ, that minimizes the energy corresponds to the direction of the magnetic moment $\langle M \rangle$ that maximizes B_M^{tot}. This is given by:

$$\frac{dB_M^{tot}}{d\theta} = 0 \Longrightarrow \theta = \tan^{-1}\left(\frac{B}{B_{ex}^{hole}}\right) \tag{1.85}$$

Equation 1.85 is plotted in Figure 1.36a. We can see that the magnetic moment $\langle M \rangle$ is smoothly rotating with the increase of the magnetic field, trying to remain aligned along the z direction.
In Figure 1.36b we traced the projection, along the direction of the magnetic moment $\langle M \rangle$, of the hole exchange field B_{ex}^{hole} given by:

$$B_{eff} = B_{ex}^{hole}\cos(\theta) = \frac{B_{ex}^{hole}}{\sqrt{1+\left(\frac{B}{B_{ex}^{hole}}\right)^2}} \tag{1.86}$$

It turns out that the magnetic moment is aligned along the sum of the external field and hole exchange field. Its magnitude is given by a modified Brillouin function shifted by the projection of the total field B_M^{tot} along the $\langle M \rangle$ direction:

$$\langle M \rangle = -M_{sat}\mathrm{B}_{\frac{5}{2}}\left(\frac{5\mu_B\left(B_{ex}^{ele}+\sqrt{B^2+(B_{ex}^{hole})^2}\right)}{k_B\left(T+T_{AF}\right)}\right) \tag{1.87}$$

The normalized magnetic moment $m = \frac{\langle M \rangle}{M_{sat}}$ is traced in Figure 1.36c.

In Figure 1.36c we also trace the two limiting cases when the magnetic moment and the applied magnetic field are parallel to the x axis ($\theta = \frac{\pi}{2}$, red curve) and when the magnetic moment and the applied magnetic field are parallel to the z axis ($\theta = 0$, green curve). These two cases follow shifted Brillouin functions with a total projected field given by $B + B_{ex}^{ele} + B_{ex}^{hole}$ (green curve) and by $B + B_{ex}^{ele}$ (red curve).
In Figure 1.36d we traced the photoluminescence Giant Zeeman shift of the fundamental and excited states. The photoluminescence Giant Zeeman energies are given by:

$$\Delta E_{PL}^{hh} = \pm\left(\frac{1}{2}\Delta_e + \frac{1}{2}\Delta_{hh}\right) = B_{ex}^{ele}\langle M \rangle + B_{ex}^{hole}\langle M \rangle\cos(\theta) \tag{1.88}$$

With $\theta = \tan^{-1}\left(\frac{B}{B_{ex}^{hole}}\right)$. For $B \longrightarrow +\infty$, the angle $\theta \longrightarrow \frac{\pi}{2}$ leading to:

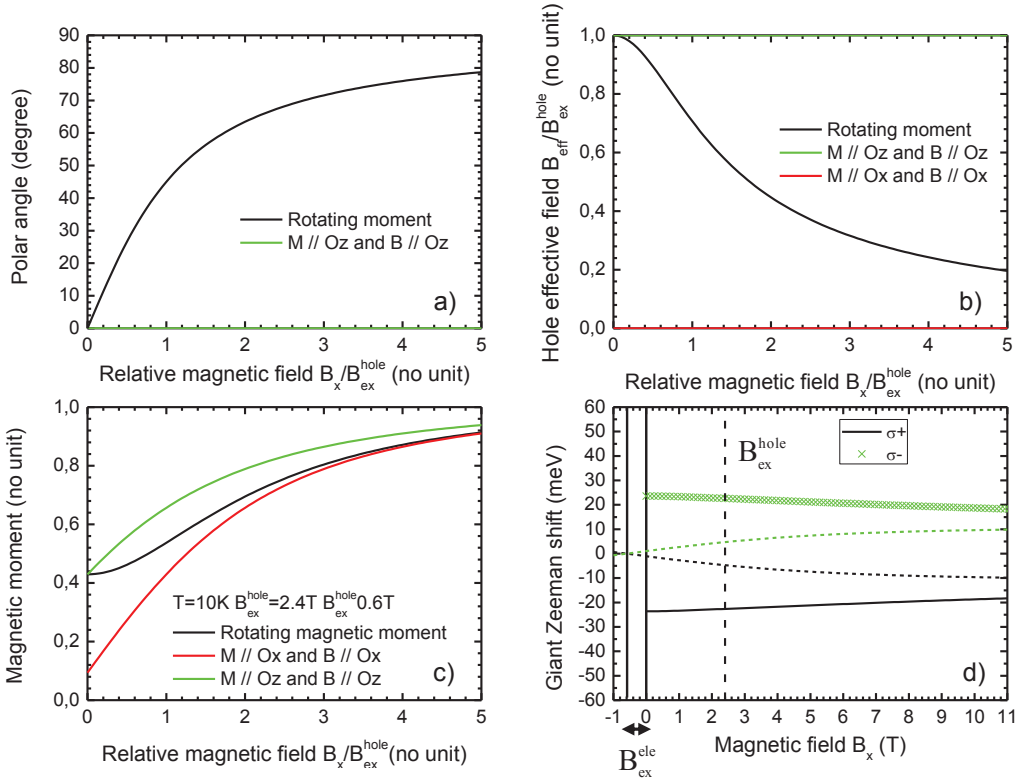

FIGURE 1.36: a) Angle θ as function of the relative magnetic field $\frac{B_{eff}}{B_{ex}^{hole}}$ b) Hole effective relative magnetic field $\frac{B}{B_{ex}^{hole}}$ as function of the relative magnetic field $\frac{B}{B_{ex}^{hole}}$ c) Magnetic moment as function of the relative magnetic field $\frac{B}{B_{ex}^{hole}}$ d) Giant Zeeman Effect of a heavy hole Magnetic Polaron with an applied magnetic field in the z direction

$$\Delta E_{PL}^{hh} = B_{ex}^{ele} \langle M \rangle = \pm E_{se} B_{\frac{5}{2}} \left(\frac{5\mu_B \left(B_{ex}^{ele} + B \right)}{k_B \left(T + T_{AF} \right)} \right) \tag{1.89}$$

We traced the limiting cases for $\theta \longrightarrow \frac{\pi}{2}$ (see equations 1.89) in Figure 1.36d (dashed lines). The Giant Zeeman shift of a heavy hole Magnetic Polaron, under an applied magnetic field perpendicular to the easy magnetization axis, doesn't change a lot being described, at high magnetic field, just by the effect of the electron.
We see in the next Section, that the case of a light hole Magnetic Polaron will be completely different from the heavy hole one.

1.5.2.2 The case of a light hole Magnetic Polaron

In this Section we are going to study the configuration where a magnetic field is applied along the z axis for a light hole Magnetic Polaron quantum dot. In Section 1.5

we showed that in the presence of no magnetic field ($\vec{B} = 0$), the magnetic moment is along the x direction $\langle M_x \rangle \neq 0$, $\langle M_y \rangle = \langle M_z \rangle = 0$, in order to maximize the Magnetic Polaron energy. If we apply a magnetic field along the z direction, we would expect a rotation of the quantum dot magnetic moment.

This situation is more complicated to the one of a heavy hole Magnetic Polaron because we have to consider the two different exchange field projections along z $B_{ex_z}^{lh}$, and along x $B_{ex_x}^{lh}$.

Assuming a magnetic moment $\langle M \rangle$ defined by a polar angle θ, the interaction Hamiltonian is given by the sum of the electron and hole exchange Hamiltonian and the Zeeman one (see equation 1.80):

$$\begin{aligned} H_{sp-d} &= H_{e-Mn} + H_{h-Mn} - \langle \vec{M} \rangle \cdot \vec{B} \\ &= -\langle M \rangle \left[B_{ex}^{ele} + \frac{B_{ex}^{hole}}{3} \cos(\varepsilon)\cos(\theta) + \frac{2B_{ex}^{hole}}{3} \sin(\varepsilon)\sin(\theta) + B\cos(\theta) \right] \end{aligned} \tag{1.90}$$

Where $tan(\varepsilon) = 2tan(\theta)$. For a π emitting light hole exciton, the exchange electron and hole fields are given by:

$$\begin{aligned} B_{ex}^{ele} &= \frac{\alpha}{2g_{Mn}\mu_B V_{QD}} \\ B_{ex}^{hole} &= \frac{-\beta}{2g_{Mn}\mu_B V_{QD}} \end{aligned}$$

The projection of the total exchange magnetic field onto the magnetic moment $\langle M \rangle$ direction, is given by:

$$B_M^{tot} = B_{ex}^{ele} + \frac{B_{ex}^{hole}}{3} \cos(\varepsilon)\cos(\theta) + \frac{2B_{ex}^{hole}}{3} \sin(\varepsilon)\sin(\theta) + B\cos(\theta) \tag{1.91}$$

In the MFA approximation, the angle θ which minimizes the energy corresponds to the one which maximizes B_M^{tot}. This is given by:

$$\frac{dB_M^{tot}}{d\theta} = 0 \Longrightarrow \theta\left(\frac{B}{B_{ex}^{hole}}\right) \tag{1.92}$$

We solved equation 1.92 analytically and we retrieved the expression for the angle θ:

$$tan\theta = \frac{1}{2}\sqrt{\left(\frac{B_{ex}^{hole}}{B}\right)^2 - 1} \tag{1.93}$$

In Figure 1.37a we trace the behaviour of the angle θ, as a function of the magnetic field. We can see that the magnetic moment $\langle M \rangle$ is rotating with the increase of the magnetic field: at $\frac{B}{B_{ex}^{hh}} = 1$ it will be aligned along the z direction.
In Figure 1.36b we traced the projection, on the direction of the magnetic moment $\langle M \rangle$, of the exchange hole field B_{ex}^{hh} given by:

$$B_{eff} = \frac{B_{ex}^{hole}}{3}\left[\cos(\theta)\cos(\varepsilon) + 2\sin(\theta)\sin(\varepsilon)\right] \tag{1.94}$$

The expression for the total magnetic moment $\langle M \rangle$ is given by a modified Brillouin function shifted by the projection of the magnetic moment of the total exchange magnetic field B_M^{tot} along the $\langle M \rangle$ direction. $\langle M \rangle$ is given by:

$$\langle M \rangle = M_{sat} B_{\frac{5}{2}}\left(\frac{5\mu_B\left(B_M^{tot}\right)}{k_B\left(T + T_{AF}\right)}\right) \tag{1.95}$$

Where B_M^{tot} is given by equation 1.91 and $\tan(\varepsilon) = 2\tan(\theta)$. The normalized magnetic moment $m = \frac{\langle M \rangle}{M_{sat}}$ is traced in Figure 1.37c.

In Figure 1.37c we trace the two limiting cases when the magnetic moment and the applied magnetic field are parallel to the x axis ($\theta = \frac{\pi}{2}$, red curve) and when the magnetic moment and the applied magnetic field are parallel to the z axis ($\theta = 0$, green curve). These two cases are described by shifted Brillouin functions with a projected total field given by $B + B_{ex}^{ele} + \frac{2B_{ex}^{hole}}{3}$ (green curve) and by $B + B_{ex}^{ele} + \frac{B_{ex}^{hole}}{3}$ (red curve).
In Figure 1.37d we traced the calculated photoluminescence Giant Zeeman shift of the fundamental state and the three excited states. We can comment about the limiting values. For $\vec{B} \longrightarrow 0$ and $\theta = \frac{\pi}{2}$ the total magnetic moment is described by a modified Brillouin function that is shifted by the quantity $B_{ex}^{ele} + \frac{2B_{ex}^{hole}}{3}$. For $\frac{B}{B_{ex}^{hole}} > 1$ and $\theta = 0$, the total magnetic moment is described by a modified Brillouin function that is shifted by the quantity $B + B_{ex}^{ele} + \frac{B_{ex}^{hole}}{3}$. This limit is given by the dashed line in Figure 1.37d. The case of a light hole Magnetic Polaron, with an applied magnetic field perpendicular to the easy magnetization axis, is very particular. We have in fact

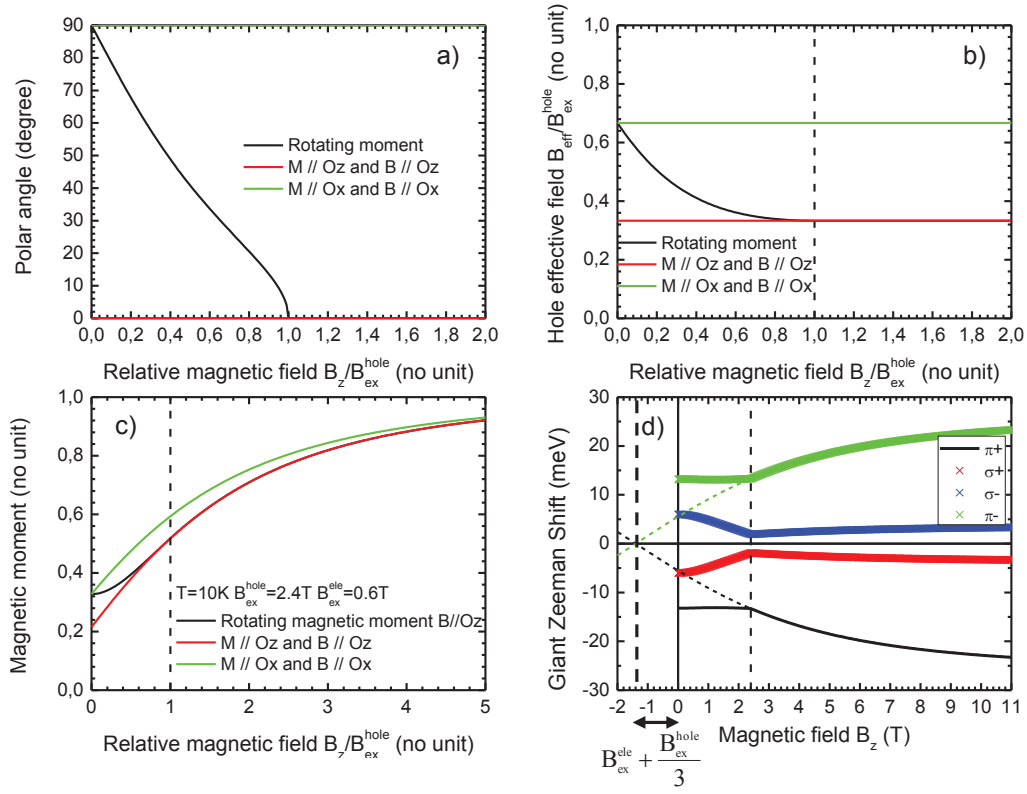

FIGURE 1.37: a) Angle θ as function of the relative magnetic field $\frac{B}{B_{ex}^{hole}}$ b) Hole effective relative magnetic field $\frac{B_{eff}}{B_{ex}^{hole}}$ as function of the relative magnetic field $\frac{B}{B_{ex}^{hole}}$ c) Magnetic moment as function of the relative magnetic field $\frac{B}{B_{ex}^{hole}}$ d) Giant Zeeman Effect of a light hole Magnetic Polaron with an applied magnetic field in the z direction

a complete rotation of the magnetic moment from the easy magnetization axis to the perpendicular one. The rotation ends when the condition $\frac{B}{B_{ex}^{hole}} = 1$ is satisfied. This case is very different from that of the heavy hole Magnetic Polaron one: by applying a magnetic field parallel and perpendicular to the nanostructure quantization axis, we would be able to discriminate the nature of the hole ground state.

1.6 Experimental set-ups and sample preparation

In this Section we describe the set-ups that have been used for the measurements presented in this thesis.

1.6.1 Micro-photoluminescence set-ups

The confocal microphotoluminescence set-up is shown in Figure 1.38 .

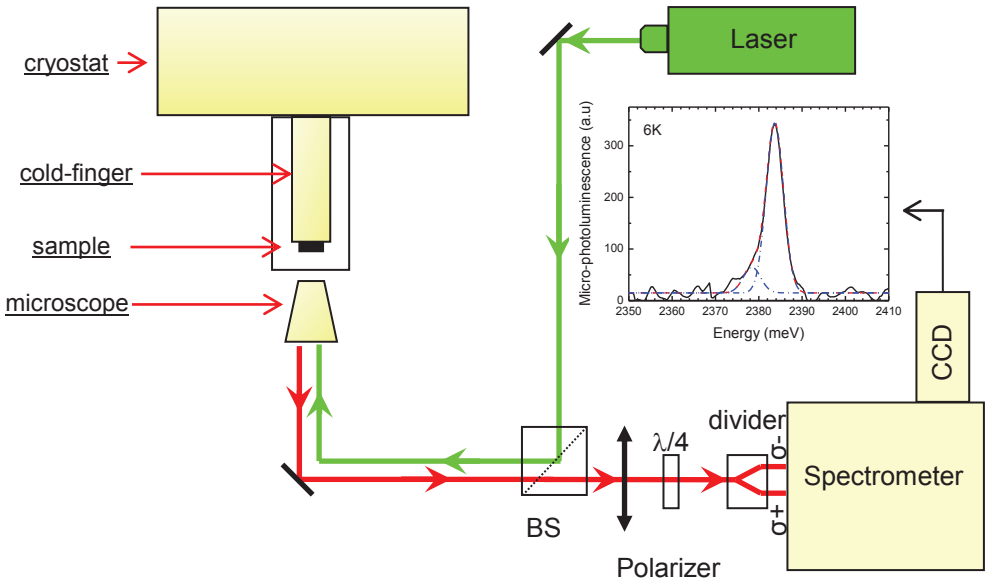

FIGURE 1.38: Micro-PL set-up

In this set-up it is possible to use different types of lasers: continuous laser with different excitation wavelengths (488nm and 405nm laser diodes, a Millennia 532nm solid laser) and a picosecond Spectra Physics Tsunami Ti:Sa pulsed laser with a tunable energy and a repetition rate of f=76MHz. The chosen laser is focused (with a typical spot size around $2\mu m^2$), by means of different optics, through a 100X Mitutoyo magnification microscope with numerical aperture 0.6 and working distance of 12mm, on the sample. The sample is mounted on a cold finger Janis cryostat that allows to chose a working temperature from 300K to 5K by controlling a flow of liquid helium. The light emitted by the sample is collected by the microscope and sent to a 0.46m Jobin-Yvon spectrometer equipped with a CCD camera (1024x256 pixels with a pixel size of $26\mu m$). To be able to characterize nanowires, the sample holder is equipped by a piezoelectric scanner allowing very small displacements with step

around 10nm in the plane (x,y) and in the focal (z) directions.
For the magneto-optical measurements we used the set-up shown in Figure 1.39.

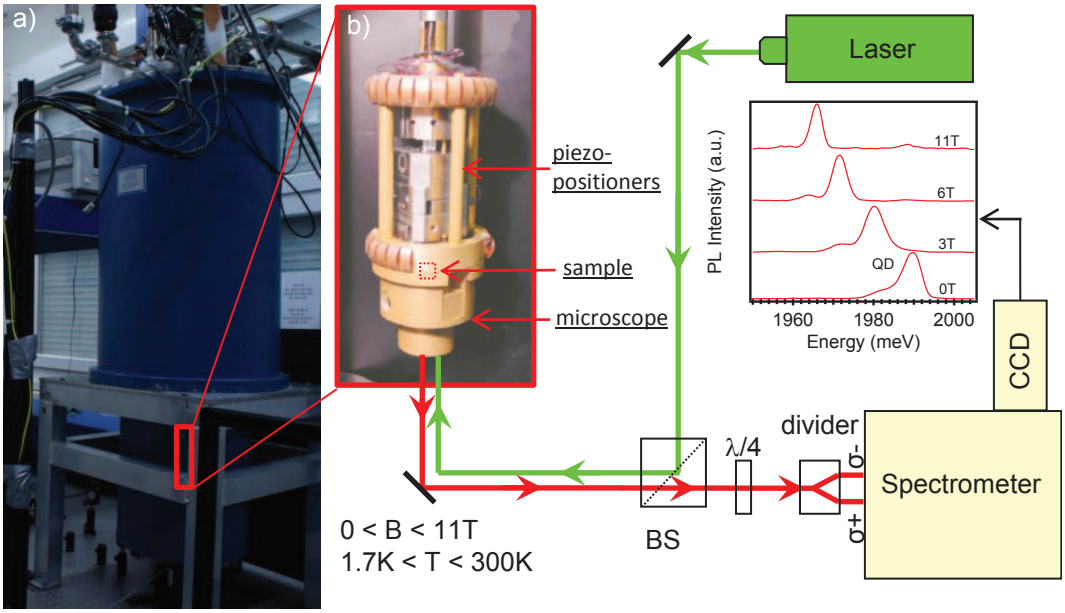

FIGURE 1.39: a) Helium-flow cryostat Oxford Spectromag b) Piezo-controlled sample holder

In this case the sample is mounted on a copper sample-holder that is fixed on a column composed by piezoelectric scanners for the positioning of the laser on the nanowire (see Figure 1.39b). Also in this case the allowed displacement is very small with step around 10nm in the plane (x,y) and in the focal (z) directions. The microscope has a 20X magnification with a numerical aperture around 0.4 and a working distance of 3mm. The column with the piezoelectric scanners is inserted inside the helium-flow cryostat (Oxford Spectromag shown in Figure 1.39a). This cryostat allows to control the temperature from 300K to 4.2K by a constant flow of helium vapors regulated by a valve. It is also possible to directly insert liquid helium inside the sample chamber and to pump it to reach the so called superfluid state: in this case we achieve a temperature of 1.7K. The Oxford Spectromag allows us to apply a magnetic field, up to 11T, in a direction perpendicular to the sample plane. For nanowires deposited on a substrate, the applied magnetic field will be perpendicular to the growth axis while for nanowire on the as-grown sample the magnetic field will be applied parallel to the growth axis. The detection part is the same as the micro-PL set-up (see Figure 1.38).
Both set-ups are also equipped with a white light lamp and a camera that allows to record optical images of the surface and then identify the position of the nanowire.

1.6.2 Cathodoluminescence set-up

In this Section the cathodoluminescence (CL) set-up will be described [58]. It will be shown, later in the thesis, that the cathodoluminescence signal (emission from a sample under electron beam excitation) is a very important hint to identify quantum dot structure inserted in long nanowires. Thanks to the electron beam nanoscale positioning, using a Field Emission Scanning Electron Microscope (FESEM), CL is really a powerful tool for semiconductor nanostructure study. The CL system used in this thesis consists in a FESEM FEI Inspect F50 to ensure a high spatial resolution (down to 1 or 3 nm at 30 keV or 1 keV, respectively) (see Figure 1.40). The electron beam energy goes from 200 eV to 30 keV and the emitted light is collected with an off-axis aluminum parabolic mirror, focused on the entrance slit of a spectrometer via an achromatic optical system using aluminum mirrors.

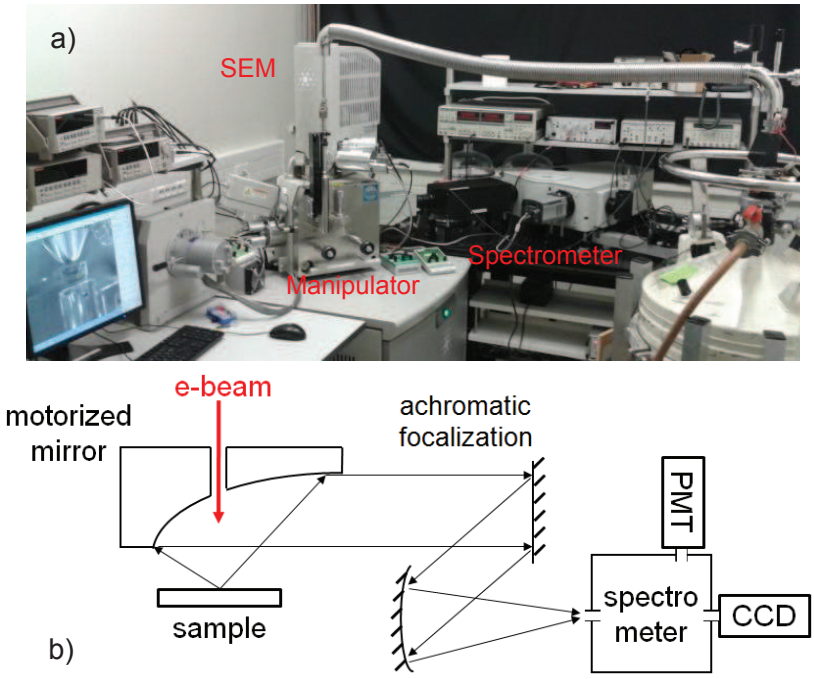

FIGURE 1.40: a) Picture of the cathodoluminescence set-up b) Cathodoluminescence set-up scheme

1.6.3 Sample preparation: patterned substrates and self-suspended membranes

In this Section we will describe the strategy used to characterize single (Cd,Mn)Te quantum dot inserted in ZnTe nanowires. Due to the high density of nanowires on

the as-grown sample (see Figure 1.41a), it is really difficult to study single nanowire. Due to the finite laser spot size of $2\mu m^2$ we excite many nanowires and the spectrum is then composed by many emissions lines (see Figure 1.41b).

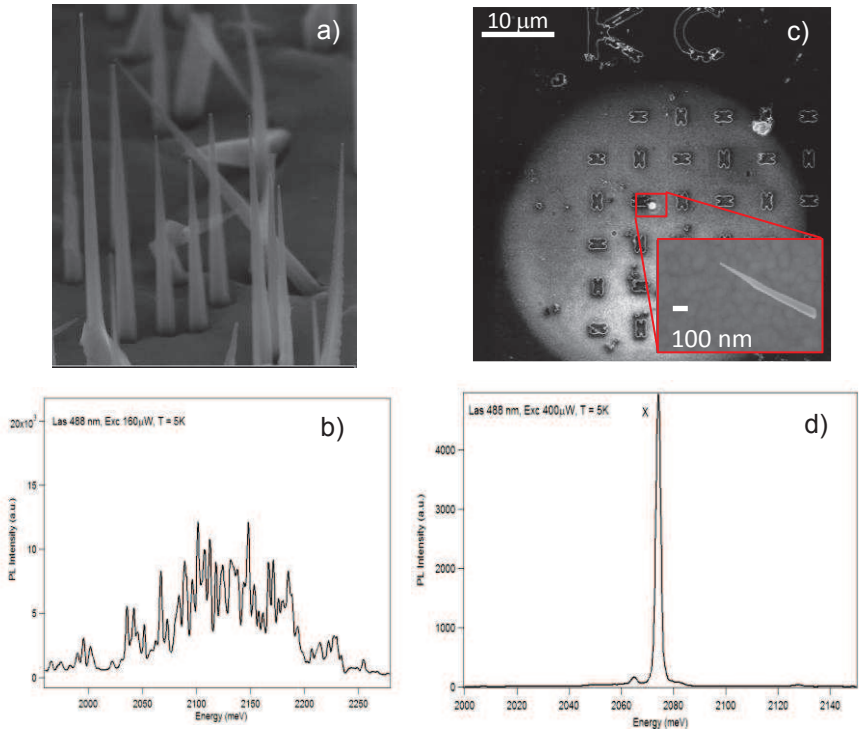

FIGURE 1.41: a) HRSEM image of a typical as grown sample b) Micro-PL spectrum taken directly on the as grown sample (CdTe quantum dot inserted in ZnTe nanowire, see Figure a)) c) Superimposition of a HRSEM image of the silicon substrate used for the nanowire dispersion and the micro-PL signal of the nanowire shown in the inset d) micro-PL spectrum of the nanowire in c)

As described in the following, we used two different types of support in order to be able to analyze the emission of single objects (see Figure 1.41d). We perform systematically optical and HRSEM image to identify well isolated nanowire (see Figure 1.41c). Moreover each support has an Al pattern on the surface used to locate the studied nanowire.

The first and most used type of support is a silicon substrate with an Al_2O_3 pattern on its surface (see Figure 1.41c). We deposited the nanowires mechanically by rubbing the as-grown sample (see Figure 1.41a) with the silicon support surface. This is a destructive method and a lot of nanowires are crashed but it is still possible to find many nanowires on the silicon surface that are not broken. We preferred this method compare to the chemical deposition one because it is easier to control.

The second type of substrate that we have used, is a Si_3N_4 membrane (see Figure 1.42).

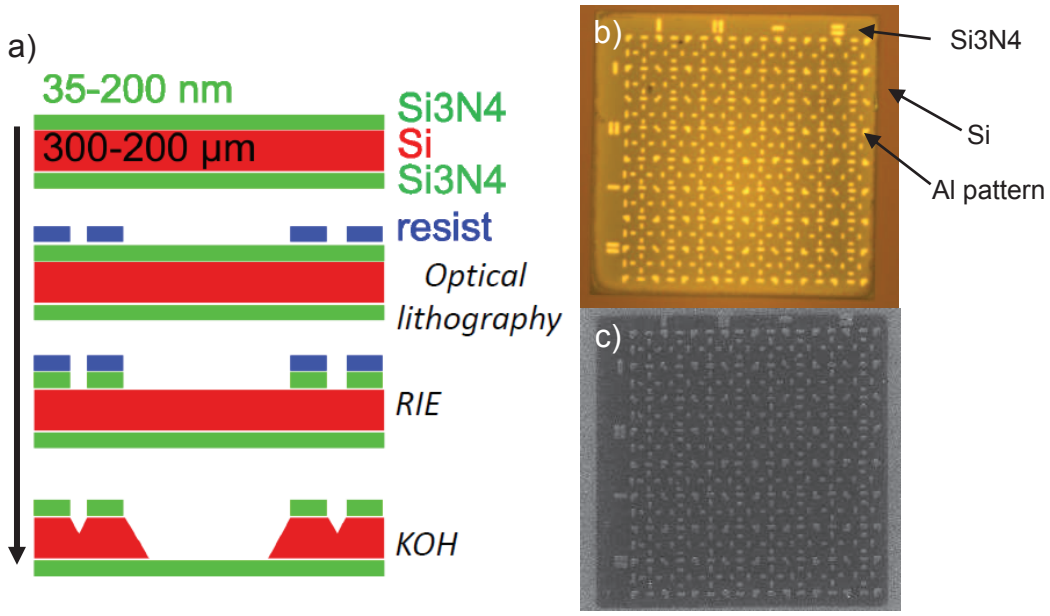

FIGURE 1.42: a) Membrane's fabrication scheme b) Optical image of a membrane c) HRSEM image of a membrane

The membranes have been realized by lithography processes described in Figure 1.42a: this process has been previously developed by Martien den Hertog (Institut Néel) and i did the fabrication of these supports in the CNRS Nanofab. The first step consists in the coating of a $Si_3N_4/Si/Si_3N_4$ substrate: the Si_3N_4 layer has thickness of (50nm) that the membrane will have at the end of the process while the thickness of the Si will define its lateral dimensions. By UV lithography we impress the resist using a mask designed for the membrane. After we etch the sample to remove the Si_3N_4 layer on the top part in order to be able to remove the Si by a KOH solution. The KOH solution remove the Si along the ⟨100⟩ plane producing a characteristic anisotropic V-etch with sidewalls that form a 54.7° angle with the surface (for this reason the thickness of the Si will affect the later dimensions of the membrane). The whole fabrication process took some months of work because membranes are really fragile and their manipulation needs attention: in such a process with many different steps, without a strong lithography experience, it is really easy to break them.
At this stage the membranes are ready and we can deposited a pattern of Al on the surface to retrieve easily the nanowire after its deposition (see Figure 1.42b,c). Due to the fragility of the membranes, the nanowires from the as-grown sample were transferred, using a dual beam FIB/SEM machine (Zeiss NVision 40 DualBeam) equipped with a micromanipulator [59] by Jean-François Motte (Institut Néel, see Figure 1.43).

The interest to use such a support is that it permits to perform different type of measurements on the same object like: micro-PL under magnetic field, TEM and EDX

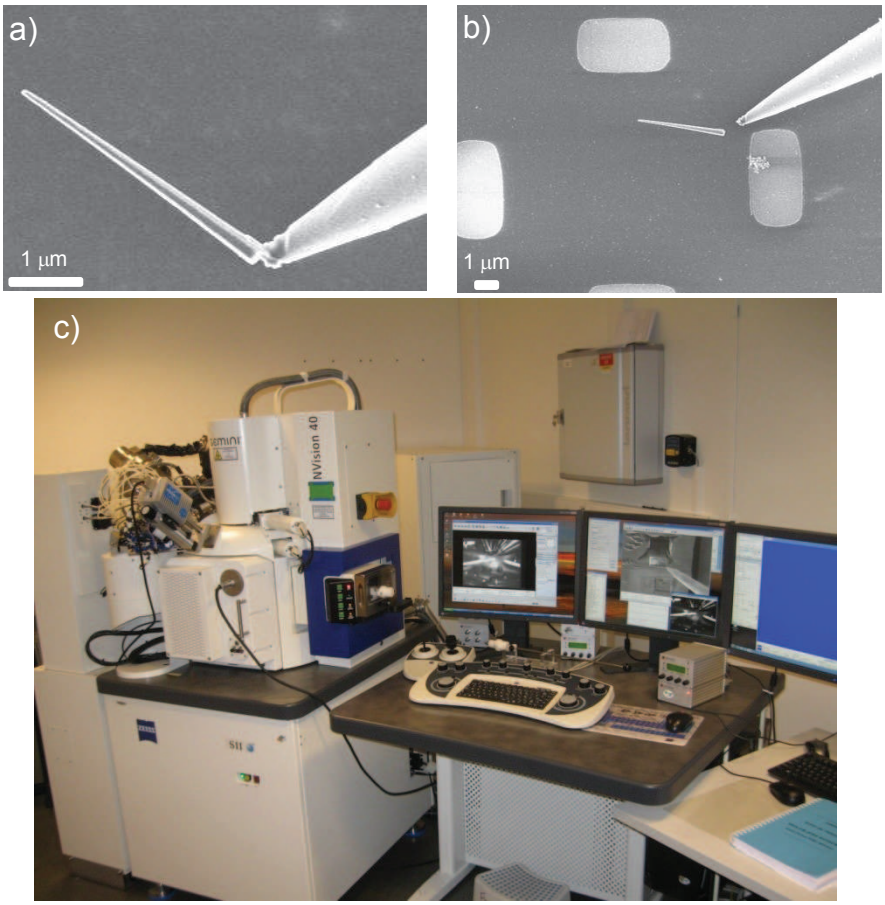

FIGURE 1.43: a) HRSEM image of a nanowire taken with the nanomanipulator's tip b) HRSEM image of the nanowire deposited on the membrane c) Zeiss NVision 40 DualBeam micromanipulator set-up [59]

characterizations and Cathodoluminescence imaging. This is a really key point, as you will see later on in the thesis, because it allows to retrieve important information such as the quantum dot structural and chemical composition and to use them to analyze the optical measurements.

1.7 Conclusions

We showed how to calculate the electron and hole exchange fields and the Magnetic Polaron energies for a light hole and a heavy hole Magnetic Polaron. We extended the "Exchange Box Model" to any hole character and in any configuration of applied magnetic field (we focused our attention to the two cases where the field is applied parallel and perpendicular to the quantization axis).

When the magnetic field is applied along the easy magnetization axis, the Giant Zeeman shift of the fundamental state (for a light hole Magnetic Polaron the electron is in the spin state $|-\frac{1}{2}\rangle$ and hole has kinetic momentum $|+\frac{1}{2}\rangle$ while for a heavy hole Magnetic Polaron, the electron state is the same but the hole state is the $|+\frac{3}{2}\rangle$) is described by shifted Brillouin functions:

$$\Delta E_{PL}^{hh} = -\left(E_{se}+E_{sh}\right)\mathrm{B}_{\frac{5}{2}}\left(\frac{g_{Mn}\mu_B\left(B_z+B_{ex}^{ele}+B_{ex}^{hole}\right)S}{k_B\left(T+T_{AF}\right)}\right)$$
$$\Delta E_{PL}^{lh} = -\left(E_{se}+\frac{E_{sh}}{3}\right)\mathrm{B}_{\frac{5}{2}}\left(\frac{g_{Mn}\mu_B\left(B_x+B_{ex}^{ele}+\frac{2}{3}B_{ex}^{hole}\right)S}{k_B\left(T+T_{AF}\right)}\right)$$

Where we recall the electron and hole exchange fields:

$$B_{ex}^{ele} = \frac{\alpha}{2g_{Mn}\mu_B V_{QD}}$$
$$B_{ex}^{hole} = \frac{-\beta}{2g_{Mn}\mu_B V_{QD}}$$

When the magnetic field is apply along the hard magnetization axis, the light hole and heavy hole Magnetic Polaron behave really differently. We have a rotation of the magnetic moment that is described by the angle θ (defined respect to the growth axis). For the two cases we calculated the analytical formula for the angle that is given by:

$$\theta^{hh} = \tan^{-1}\left(\frac{B}{B_{ex}^{hole}}\right)$$
$$tan\theta^{lh} = \frac{1}{2}\sqrt{\left(\frac{B_{ex}^{hole}}{B}\right)^2 - 1}$$

For the Giant Zeeman shift of the fundamental state, if we consider, for example, the limiting case of high magnetic field ($B \longrightarrow +\infty$), we have:

$$\Delta E_{PL}^{hh} = -E_{se} B_{\frac{5}{2}}\left(\frac{5\mu_B\left(B_{ex}^{ele} + B\right)}{k_B\left(T + T_{AF}\right)}\right)$$
$$\Delta E_{PL}^{lh} = -\left(E_{se} + \frac{E_{sh}}{3}\right) \mathrm{B}_{\frac{5}{2}}\left(\frac{g_{Mn}\mu_B\left(B + B_{ex}^{ele} + \frac{1}{3}B_{ex}^{hole}\right)S}{k_B\left(T + T_{AF}\right)}\right)$$

We see that the Giant Zeeman shift of the heavy hole fundamental state is small and, at high magnetic field, is described just by the exchange field of the electron. The Giant Zeeman shift of the light hole is larger and can be described by a shifted Brillouin function where the shift is given by $B_{ex}^{ele} + \frac{1}{3}B_{ex}^{hole}$.

We can conclude that one way to discriminate experimentally a light hole or a heavy hole emission, is to perform magneto-optical measurements with magnetic fields applied parallel and perpendicular to the nanowire growth axis. For this reason, in Chapter 3 we present optical studies where we changed the orientation of the magnetic field respect to the nanowire growth axis.

Chapter 2

Micro-photoluminescence at zero magnetic field

2.1 Introduction

In this Chapter we are going to discuss all the nanowires optical properties that are magnetic field independent. First we will present the studied samples and for one of them (Sample 1) we will show a detailed structural and chemical characterization.
We continue by discussing the effect of elastic strain, that is really strong in such heterostructures, and we will show how it affects their optical emission properties.
In the second part of the Chapter, we present power dependence photoluminescence measurements to determine the fine structure of the quantum dots and cathodoluminescence ones to spatially localize them in the nanowire.
In the last part of the Chapter, we show time dependent photoluminescence experiments to check the single photon properties of the quantum dot and to highlight its confinement properties.
We conclude by showing an original study, based on Fourier microscopy, to reveal the fine structure of an emitter (in our case a quantum dot inserted in a nanowire).

2.1.1 Studied sample and structural analysis

Figure 2.1 shows the three samples more largely studied and characterized during this thesis.

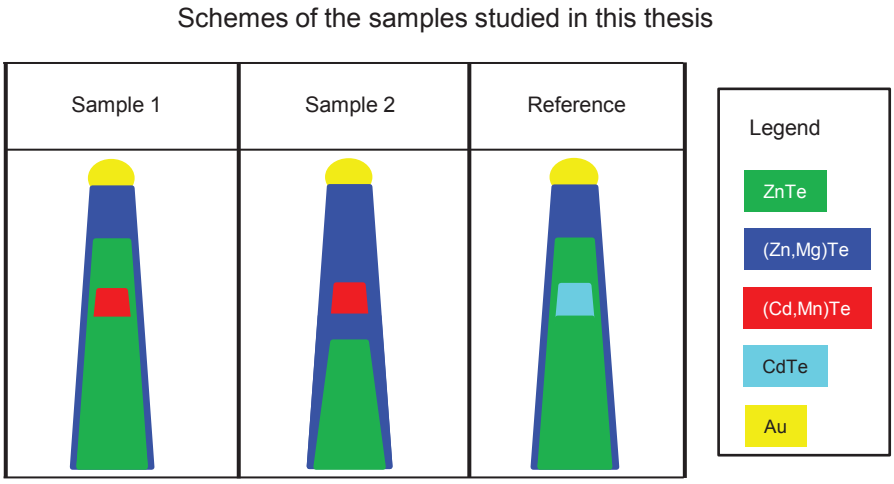

FIGURE 2.1: Scheme of the samples studied in this thesis: Sample 1 is a ZnTe nanowire with a (Cd,Mn)Te quantum dot and a (Zn,Mg)Te shell (nanowires NW1, NW2, NW3), Sample 2 is a a ZnTe nanowire with a (Cd,Mn)Te quantum dot surrounded by a (Zn,Mg)Te shell (nanowire MP1), Reference is a ZnTe nanowire with a CdTe quantum dot and a (Zn,Mg)Te shell (nanowire RH1)

The Reference sample is composed by a CdTe quantum dot inserted in a ZnTe nanowire passivated by a (Zn,Mg)Te shell. The growth process was described in Chapter 1. We studied the Reference sample to check the good quality of the quantum dot: we perform power dependence studies to retrieve the typical quantum dot cascade and autocorrelation measurements to check the single photon emission property of the quantum dot.
Sample 1 presents the same composition properties as those of the Reference sample but we insert Mn atoms inside the quantum dot.
In Sample 2 all the growth parameters used for Sample 1 were kept identical but to achieve a stronger hole wavefunction confinement, Mg was added all around the quantum dot.
We will analyze and discuss the optical properties of 5 nanowires: 3 nanowires from Sample 1 (NW1, NW2 and NW3), 1 nanowire from Sample 2 (MP1) and 1 from the Reference sample (RH1). To avoid confusion, we collect HRSEM images of the 3 nanowires of Sample 1 in Figure 2.2, we will discuss the optical properties of MP1 in Chapter 4 and the ones of RH1 in Section 2.3.2.1.

Figure 2.2a shows the so called NW1: it is a nanowire deposited on a patterned Si_3N_4 membrane, as described in Chapter 1. The SEM tip used to mechanically grab the nanowire is visible in the upper right corner of Figure 2.2a.
Figure 2.2b presents NW2: this nanowire was mechanically deposited on a Si patterned substrate by putting it in contact with the as-grown sample.

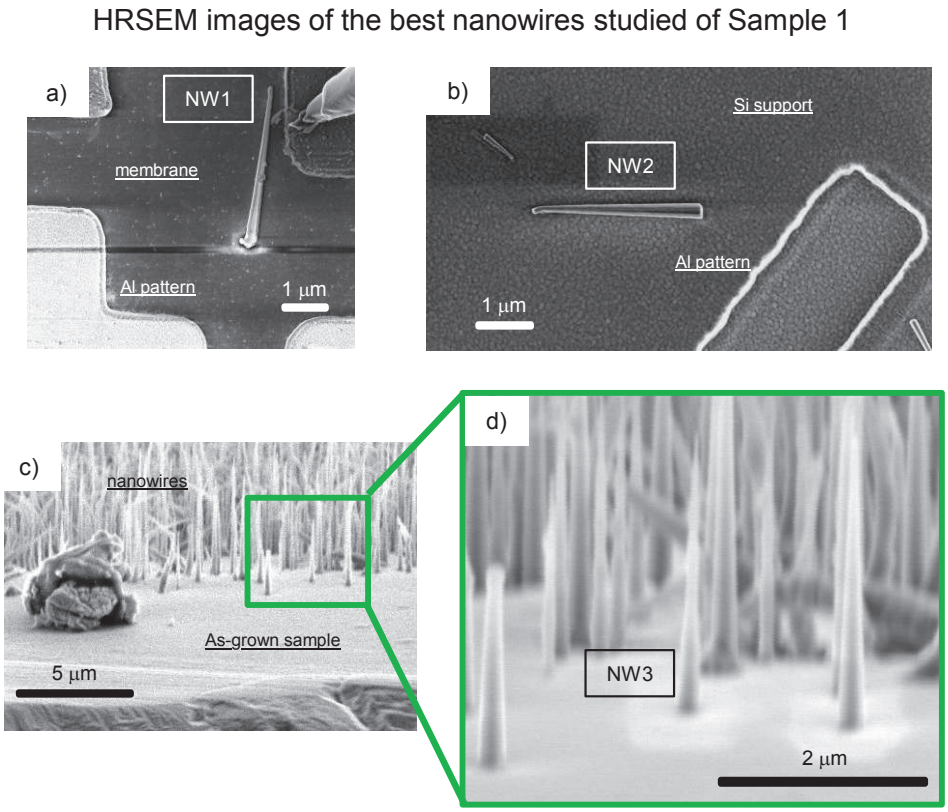

FIGURE 2.2: HRSEM images of the nanowires of Sample 1 that are going to be discussed a) NW1 is deposited on a patterned Si_3N_4 membrane b) NW2 is deposited on a patterned silicon substrate c) Tilted HRSEM showing Sample 1 d) Image of NW3 showing its position on Sample 1

Figure 2.2d shows NW3: while NW1 and NW2 were deposited on a substrate, NW3 was directly measured on the as-grown sample (see Figure 2.2c). NW3 is a nanowire that is close to the edge of the sample (see Figure 2.2c). In this case there is no Al pattern but it was relatively easy to retrieve its position thanks to the presence of a big defect nearby (see Figure 2.2c).

We are interested in the study of the optical properties of quite complicated heterostructures. We have to consider how the elastic strain (originated by the lattice mismatch) affects the emission properties of the quantum dots. We will present calculations to determine the hole anisotropy ΔE.

2.1.1.1 Quantum dot shape determination

Nanowire NW1 has been deposited on a Si_3N_4 membrane. The use of a 50nm thick membrane allowed us to perform different characterization techniques: micro-PL, TEM, EDX, CL and magneto-optical measurements.
In this Section and the following one, we analyze the EDX hypermaps that we acquired on NW1. Figure 2.3 shows the element maps around the quantum dot region (localized at the tip of the nanowire).

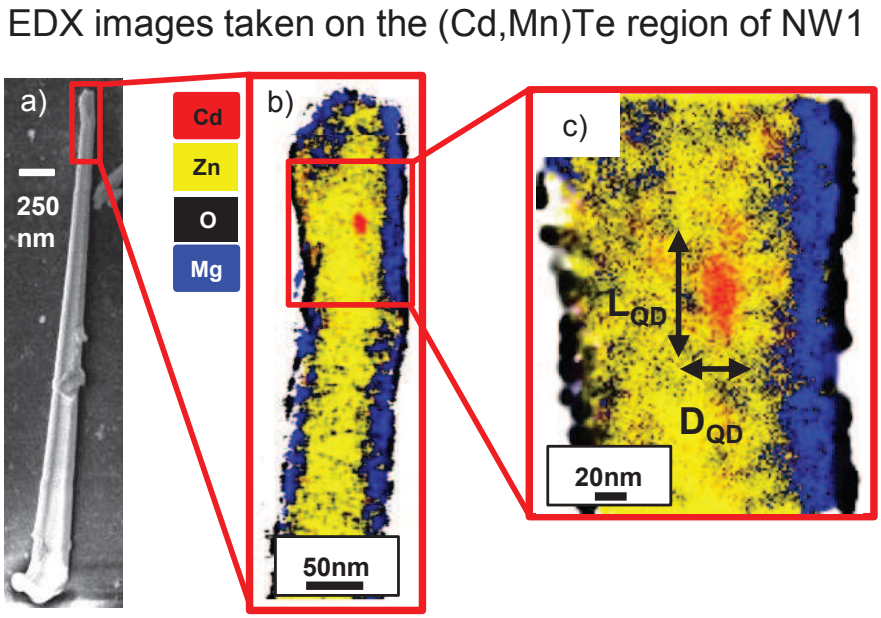

FIGURE 2.3: a) HRSEM image of NW1 b) EDX image of the NW1 tip c) Zoom of the EDX image showing the (Cd,Mn)Te quantum dot

The EDX technique is a really powerful tool for chemical and compositional analysis: a high energy electron beam is used to scan the sample and the emitted photons are collected by an analyzer. By the analysis of the X-ray emitted spectrum, it is possible to determine which element has been excited and then reconstruct a map as shown in Figure 2.3b.
Thanks to the high resolution of the TEM hypermaps, it is possible to determine the shape and the size of the quantum dot (see Figure 2.3c). In the present case it is a very small object. From the EDX analysis we get the following quantum dot dimensions:

TABLE 2.1: (Cd,Mn)Te typical dimensions

D_{QD} = 8nm	L_{QD} = 15nm

The presented measurements reveal something that will be really important in the following: the quantum dot presents an uncommon shape. The dot is elongated along the nanowire growth axis with an aspect ratio of $\frac{L}{D} \cong 2$.

2.1.1.2 Determination of the Mn concentration

From EDX hypermaps, it is possible to trace different chemical profiles and then retrieve quantitative informations about the composition. We traced a profile at the quantum dot position in Figure 2.4a and the composition of the most relevant elements Cd and Mn are shown in Figure 2.4b.

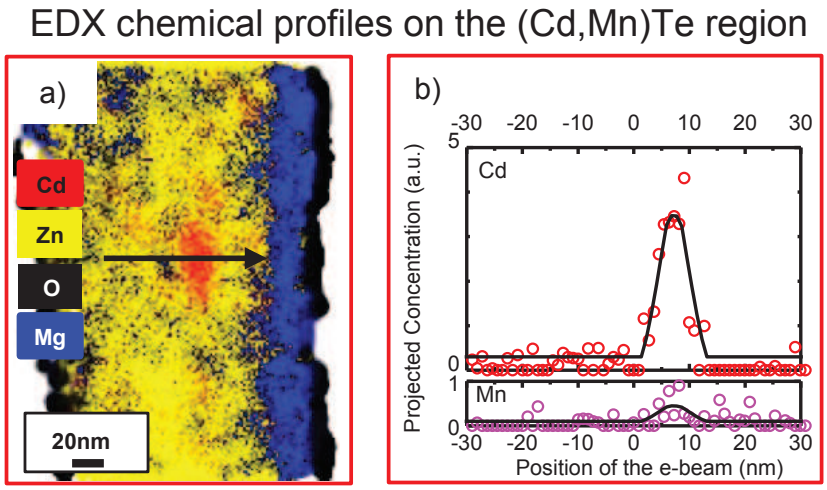

FIGURE 2.4: a) EDX image showing the (Cd,Mn)Te quantum dot b) Chemical composition of the (Cd,Mn)Te quantum dot region showing the Cd and the Mn concentration

To determine the correct concentration of each element, we built a model that uses a set of five ellipses to reconstruct the quantum dot insertion. The software has been developed by E. Robin while the fitting procedure has been developed by P. Rueda Fonseca, J. Cibert and E. Robin [14]. Without entering into the details, the model consists in the changing of the ellipses concentration (Zn, Mg, Cd, Mn, Te and O) and their dimensional parameters to best reproduce the corresponding projected EDX profile. The best fitting parameters leads to the following chemical concentrations:

TABLE 2.2: (Cd,Mn)Te chemical composition

Mn = 10% ± 2%	Cd = 90%	Zn = 0%

This analysis reveals pure (Cd,Mn)Te (there is no presence of Zn) and high Mn concentrated quantum dot. If we consider the empirical law, shown in Chapter 1, a Mn = 10% concentration means that the effective Mn concentration is x_{eff} = 4% which denotes almost the maximum density of isolated spins for a DMS system (see Chapter 1).

2.2 Theoretical Models

2.2.1 Elastic strain in core-shell nanowires and quantum dots

The nanowires have a core-shell structure with a (Cd,Mn)Te quantum dot embedded in it. Moreover the chemical composition of the core is different from the composition of the shell and from the composition of the dot, leading to different lattice mismatches that produce elastic strain in the core and in the quantum dot.
The strain affects the electronic properties of the system: the band edge emission has a high sensitivity to the strain and the exciton emission is strain dependent. In this Section we analyze the effect of the elastic strains induced by the shell.
In the first part of the Section, we analyze how the electronic emission properties of a ZnTe core are affected by a (Zn,Mg)Te outer shell.
In the second part we calculate how the elastic strain affects the excitonic emission of a CdTe quantum dot and moreover, at the end, we include the exact shape of the quantum dot, revealed by the EDX measurements done on NW1.

2.2.1.1 Core-shell nanowires

We start by considering the effect of elastic strain in a core-shell structure. The system is described in Figure 2.5: we can define r_c as the inner core radius and r_s as the outer radius of shell one.

The general solution consists in the calculation of the displacement field $\mathrm{u}(\vec{r})$ which relates the position of any point $\vec{r}$ in the strain material to its value in the unstrained system [57]. The displacement field $\mathrm{u}(\vec{r})$ is the solution of the Lamé-Clapeyron-Navier equation that is given by:

$$\sum_{i,j,k} c_{ijkl} \frac{\partial}{\partial x_j} \left(\frac{\partial \mathrm{u}_k}{\partial x_l} + \frac{\partial \mathrm{u}_l}{\partial x_k} \right) = 0 \tag{2.1}$$

for the three directions x, y, z. The parameter c_{ijkl} defines the stiffness tensor which links the stress tensor σ_{ij} to the strain tensor ε_{ij} through the Hooke's law:

$$\sigma_{ij} = \sum_{k,l} c_{ijkl} \varepsilon_{k,l} \tag{2.2}$$

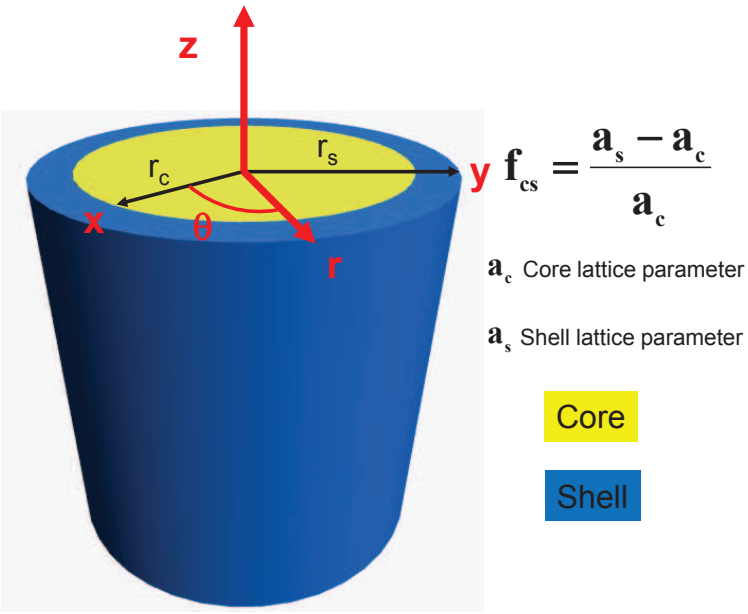

FIGURE 2.5: Core-shell nanowire structure

the stiffness tensor c_{ijkl} depends on the symmetry of the system. In the next Section we show how to solve equation 2.1 considering two isotropic materials for the core-shell structure.

If we take into account the translational invariance, typical of a cylindrical core-shell structure, we can simplify the expression for the displacement field $\mathrm{u}(\vec{r})$. All the derivatives of $\mathrm{u}(\vec{r})$ are independent of z: $\frac{\partial}{\partial x_j}\left(\frac{\partial u_i}{\partial z}\right) = 0$ and hence $\frac{\partial \mathrm{u}_i}{\partial z} = \mathrm{C}$ is a constant independent of $\vec{r}$. The general form of the displacement field will be given then:

$$\mathrm{u}_i(\vec{r}) = \mathrm{C}z + \mathrm{D} + \mathrm{u}_i(x, y) \tag{2.3}$$

2.2.1.1.1 The isotropic case

We start by considering the case where the core and the shell are considered as isotropic materials: this system is well known in the literature [60]. The displacement field $\vec{\mathrm{u}}(\vec{r})$ is the solution of the Lamé-Clapeyron-Navier equation given by:

$$\mu \sum_j \frac{\partial^2 \mathrm{u}_i}{\partial x_j^2} + (\lambda + \mu) \sum_j \frac{\partial^2 \mathrm{u}_j}{\partial x_i \partial x_j} = 0 \tag{2.4}$$

which contains three equations for $x_i = x, y, z$. If now we consider a core-shell structure we can rewrite equation 2.4 including the invariance by translation:

$$\begin{cases} \mu\left(\frac{\partial^2}{\partial y^2}+\frac{\partial^2}{\partial x^2}\right)\mathrm{u}_x+(\lambda+\mu)\frac{\partial}{\partial x}\left(\frac{\partial \mathrm{u}_x}{\partial x}+\frac{\partial u_y}{\partial y}\right)=0 \\ \mu\left(\frac{\partial^2}{\partial y^2}+\frac{\partial^2}{\partial x^2}\right)\mathrm{u}_y+(\lambda+\mu)\frac{\partial}{\partial y}\left(\frac{\partial \mathrm{u}_x}{\partial x}+\frac{\partial \mathrm{u}_y}{\partial y}\right)=0 \\ \mu\left(\frac{\partial^2}{\partial y^2}+\frac{\partial^2}{\partial x^2}\right)\mathrm{u}_z=0 \end{cases} \tag{2.5}$$

It is possible to define the displacement field taking into account the cylindrical symmetry [57] having:

$$\begin{cases} \mathrm{u}_x=\mathrm{u}_r(r)cos\theta \\ \mathrm{u}_y=\mathrm{u}_r(r)sin\theta \end{cases} \tag{2.6}$$

Finally if we rewrite the Lamé-Clapeyron-Navier equation, in cylindrical coordinates we have:

$$\begin{cases} \frac{d^2}{dz^2}\mathrm{u}_z(z)=0 \quad \Longrightarrow \quad \mathrm{u}_z(z)=Cz+\mathrm{D} \\ \frac{d^2}{dr^2}\mathrm{u}_r(r)+\frac{1}{r}\frac{d}{dr}\mathrm{u}_r(r)-\frac{1}{r^2}\mathrm{u}_r(r) \quad \Longrightarrow \quad \mathrm{u}_r(r)=Ar+B\frac{r_c^2}{r} \end{cases} \tag{2.7}$$

The parameters A,B,C,D have to be determined for each material. In cylindrical coordinates (r,θ,z) the strain tensor components is given by:

$$\begin{cases} \varepsilon_{zz}=\frac{du_z}{dz}=C & \text{axial strain} \\ \varepsilon_{rr}=\frac{du_r}{dr}=A-B\frac{r_c^2}{r^2} & \text{radial strain} \\ \varepsilon_{\theta\theta}=\frac{u_r}{r}=A+B\frac{r_c^2}{r^2} & \text{local angular strain} \end{cases} \tag{2.8}$$

The different strain components (see equations 2.10) are calculated by determining A,B,C,D with the proper boundary conditions, of the core-shell structure, given by:

$$\begin{cases} \varepsilon_{zz}^c-\varepsilon_{zz}^s=f_{cs} & \text{continuity at the interface} \\ \varepsilon_{\theta\theta}^c-\varepsilon_{\theta\theta}^s=f_{cs} & \text{continuity at the interface} \\ \sigma_{rr}^c(r_c)-\sigma_{rr}^s(r_c)=0 & \text{equilibrium at the interface} \\ \sigma_{rr}^s(r_s)=0 & \text{equilibrium at the sidewall} \\ \pi r_c^2\sigma_{zz}^c+\pi(r_s^2-r_c^2)\sigma_{zz}^s=0 & \text{equilibrium along z} \end{cases} \tag{2.9}$$

We have then for the core strain components:

$$\begin{cases} \varepsilon^c_{zz} = \left(1 - \frac{r_c^2}{r_s^2}\right) f_{cs} \\ \varepsilon^c_{rr} = \varepsilon_{\theta\theta} = -\left(1 - \frac{r_c^2}{r_s^2}\right) f_{cs} \left(\frac{1}{2} - \frac{2\mu}{\lambda+2\mu}\right) \end{cases} \tag{2.10}$$

It is interesting to define the following strain components for the core:

$$\begin{cases} \sqrt{6}\varepsilon^c_{axial} = [\varepsilon_{rr} + \varepsilon_{\theta\theta} - 2\varepsilon_{zz}] \\ \sqrt{3}\varepsilon^c_{hydro} = [\varepsilon_{rr} + \varepsilon_{\theta\theta} + \varepsilon_{zz}] \end{cases} \tag{2.11}$$

The new defined strain components describe the change of volume (ε_{hydro}) and a shear strain coupling the z axis and the xy-plane (ε_{axial}): these are the only terms that influence the electronic properties of the core. In fact ε_{hydro} and ε_{axial} allow to calculate the effect on the excitonic emission. The symmetrical component ε_{hydro} shifts the conduction and the valence band while the ε_{axial} determines the light hole-heavy hole splitting (ΔE_{LH}).

The coupling of carriers to strain is described by the Bir-Pikus Hamiltonian. For the holes, the 4×4 Hamiltonian, for the core with $< 111 >$ direction, is diagonal and in the hole states basis $|\frac{3}{2}\rangle$, $|\frac{1}{2}\rangle$, $|-\frac{1}{2}\rangle$, $|-\frac{3}{2}\rangle$ is given by:

$$\mathrm{H_{BP}} = \begin{pmatrix} P_v + Q & 0 & 0 & 0 \\ 0 & P_v - Q & 0 & 0 \\ 0 & 0 & P_v - Q & 0 \\ 0 & 0 & 0 & P_v + Q \end{pmatrix} \tag{2.12}$$

P_v is proportional to the hydrostatic strain (ε_{hydro}) and shifts the conduction and the valence band. Q is proportional to ε_{axial} and splits the valence band (light hole-heavy hole splitting, ΔE_{LH}).

More quantitatively, for the hole we have:

$$\begin{cases} Q = \frac{d\sqrt{6}}{2\sqrt{3}} \varepsilon_{axial} \\ P_v = -a_v \sqrt{3} \varepsilon_{hydro} \end{cases} \tag{2.13}$$

Instead for the electron we have:

$$\mathrm{H_c} = \begin{pmatrix} P_c & 0 \\ 0 & P_c \end{pmatrix} \tag{2.14}$$

With P_c given by:

$$P_c = -a_c\sqrt{3}\varepsilon_{hydro} \tag{2.15}$$

Where a_v (a_c) describes the hydrostatic deformation potential of the valence band (conduction band) and d is the shear deformation potential in the < 111 > direction. The exciton emission energy, for a heavy hole exciton, is then given by:

$$E^X_{HH} = E^X_{bulk} + P_c - P_v - Q = E^X_{bulk} - a\sqrt{3}\varepsilon_{hydro} - \frac{d\sqrt{6}}{2\sqrt{3}}\varepsilon_{axial} \tag{2.16}$$

Where we have defined $a = a_c - a_v$.
For a light hole exciton we have:

$$E^X_{LH} = E^X_{bulk} + P_c - P_v + Q = E^X_{bulk} - a\sqrt{3}\varepsilon_{hydro} + \frac{d\sqrt{6}}{2\sqrt{3}}\varepsilon_{axial} \tag{2.17}$$

Where the light hole-heavy hole splitting ΔE_{LH} is given by:

$$\Delta E_{LH} = \frac{d}{\sqrt{3}}\sqrt{6}\varepsilon_{axial} = 2Q \tag{2.18}$$

The two quantities $\sqrt{3}\varepsilon_{hydro}$ and $\sqrt{6}\varepsilon_{axial}$ are defined by equations 2.10 and 2.11:

$$\sqrt{3}\varepsilon^c_{hydro} = \left(1 - \frac{r_s^2}{r_c^2}\right) f_{cs}\frac{4\mu}{\lambda + 2\mu} = \left(1 - \frac{r_s^2}{r_c^2}\right) f_{shear}\frac{8\mu}{3\lambda + 2\mu}$$

$$\sqrt{6}\varepsilon^c_{axial} = \left(1 - \frac{r_s^2}{r_c^2}\right) f_{cs}\frac{3\lambda + 2\mu}{\lambda + 2\mu} = \left(1 - \frac{r_s^2}{r_c^2}\right) 2 f_{shear}$$

Where we have defined $f_{shear} = f_{cs}\frac{1}{2}\frac{3\lambda+2\mu}{\lambda+2\mu}$. The expression for the excitonic emission energy of the core for a core-shell nanowire oriented in the < 111 > direction is:

$$\begin{aligned} E_X^{NW} &= E_X^{bulk} - a\left(1-\frac{r_c^2}{r_s^2}\right) f_{cs}\frac{4\mu}{\lambda+2\mu} \pm \frac{d}{2\sqrt{3}}\left(1-\frac{r_c^2}{r_s^2}\right) f_{cs}\frac{3\lambda+2\mu}{\lambda+2\mu} \\ &= E_X^{bulk} - a\left(1-\frac{r_c^2}{r_s^2}\right) f_{shear}\frac{8\mu}{3\lambda+2\mu} \pm \frac{d}{2\sqrt{3}}\left(1-\frac{r_c^2}{r_s^2}\right) f_{shear} \end{aligned} \tag{2.19}$$

Equation 2.19 is for isotropic materials and when the elastic properties of the compounds are identical. In the next Section we will extract a more general equation compared to the one 2.19 that will take into account the different elastic properties of the materials, with different crystal structures, described by the stiffness tensor.

2.2.1.1.2 Calculation considering the elastic anisotropy

It is possible to calculate equation 2.1, taking into account the symmetry of the crystal structure of the core-shell materials, as explained in [57]. The crystal structure of the semiconductors is described by the stiffness tensor c_{ijkl} with the appropriate symmetry. In the case of cubic symmetry, as for the studied nanowires, we have for the stiffness matrix:

$$c_{ij} = \begin{pmatrix} c_{11} & c_{12} & c_{12} & 0 & 0 & 0 \\ c_{12} & c_{11} & c_{12} & 0 & 0 & 0 \\ c_{12} & c_{12} & c_{11} & 0 & 0 & 0 \\ 0 & 0 & 0 & c_{44} & 0 & 0 \\ 0 & 0 & 0 & 0 & c_{44} & 0 \\ 0 & 0 & 0 & 0 & 0 & c_{44} \end{pmatrix} \tag{2.20}$$

Where the anisotropy is characterized by the parameter $(c_{11} - c_{12} - 2c_{44})$. By solving the new set of Lamé-Clapeyron-Navier equations (see equations 2.1) we can retrieve the new expressions for ε^c_{hydro} and ε^c_{axial} [57] for a cubic nanowire along <111>:

$$\sqrt{3}\varepsilon^c_{hydro} = \left(1-\frac{r_s^2}{r_c^2}\right) f_{cs}\frac{c_{11}-c_{12}+6c_{44}}{c_{11}+c_{12}+2c_{44}}$$

$$\frac{\sqrt{6}}{2}\varepsilon^c_{axial} = \left(1-\frac{r_s^2}{r_c^2}\right) f_{cs}\frac{c_{11}+2c_{12}}{c_{11}+c_{12}+2c_{44}}$$

The expression for the excitonic emission energy is then:

$$E_X^{NW} = E_X^{bulk} - a\left(1-\frac{r_s^2}{r_c^2}\right) f_{cs}\frac{c_{11}-c_{12}+6c_{44}}{c_{11}+c_{12}+2c_{44}} \pm \frac{d}{\sqrt{3}}\left(1-\frac{r_s^2}{r_c^2}\right) f_{cs}\frac{c_{11}+2c_{12}}{c_{11}+c_{12}+2c_{44}} \quad (2.21)$$

Note that for an isotropic crystal: $c_{11}-c_{12}=2c_{44}=2\mu$ and $c_{11}=\lambda+2\mu$ retrieving the equation 2.19 of the previous Section.
For the ZnTe we can use the deformation potentials and stiffness coefficients that can be found in [61–63], summarized in the following tables:

TABLE 2.3: ZnTe deformation potentials

$a = 5.3$eV	$\frac{d}{\sqrt{3}} = 2.5$eV

TABLE 2.4: ZnTe stiffness coefficients

$c_{11} = 73.7$GPa	$c_{12} = 42.3$GPa	$c_{44} = 32.1$GPa

It is then possible to calculate the excitonic emission (in meV), using equation 2.21, for a cubic ZnTe nanowire with a heavy hole ground state:

$$E_X^{HH} = 2381 - 88\left(1-\frac{r_s^2}{r_c^2}\right) f_{cs} \quad (2.22)$$

and for a light hole ground state:

$$E_X^{LH} = 2381 - 44\left(1-\frac{r_s^2}{r_c^2}\right) f_{cs} \quad (2.23)$$

As we have extracted the equations to calculate the excitonic emission energy for a ZnTe nanowire, we can compare them with the value found in the literature: a work done by P. Wojnar et al. [13, 46]. If we consider the structural properties of their nanowires we have $D_c = 70$nm, $D_s = 130$nm and $f_{cs} = 1.04\%$ which corresponds to the lattice mismatch between a ZnTe core and a $Zn_{0.8}Mg_{0.2}Te$ outer shell. We obtain an exciton emission energy of 2.31eV corresponding to a heavy hole ground state, in agreement with the experimental value [13].
We will use equation 2.21 to calculate the theoretical exciton emission energy for a ZnTe core in a (Zn,Mg)Te shell as function of the averaged Mg concentration in the shell ($x_{Mg}\left(1-\frac{r_s^2}{r_c^2}\right)$) and we will compare it to our experimental results in Section 2.3.1.3.

2.2.1.2 Quantum dots

2.2.1.2.1 Circular approximation for elongated quantum dots

A first approximation, to calculate the strain in a (Cd,Mn)Te quantum dot inserted in a ZnTe nanowire, is to assume that we have a core-shell structure with a circular symmetry. It corresponds to an infinitely long cylindrical quantum dot of (Cd,Mn)Te as a core surrounded by a ZnTe shell and a (Zn,Mg)Te outer shell (see Figure 2.6).

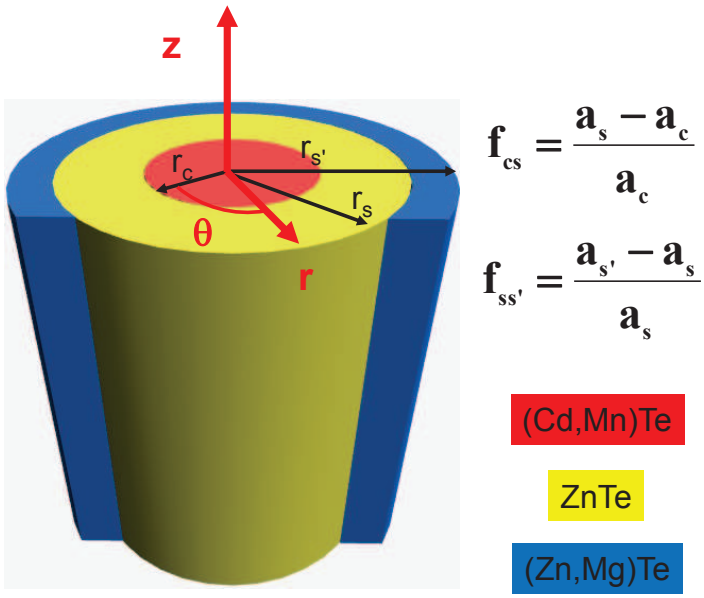

FIGURE 2.6: Core-shell nanowire structure

It is possible then to use the same formalism, shown in the previous Section, to calculate the excitonic emission energy for the core. We made an approximation to simplify the calculation: we took the same stiffness tensor in the whole structure:

$$c_{ijkl}^{core} = c_{ijkl}^{shell} = c_{ijkl}^{shell'} = c_{ijkl}^{ZnTe} \tag{2.24}$$

$$\begin{cases} \varepsilon^c_{zz} - \varepsilon^s_{zz} = f_{cs} & \text{continuity at the interface} \\ \varepsilon^s_{zz} - \varepsilon^{s'}_{zz} = f_{ss'} & \text{continuity at the interface} \\ \varepsilon^c_{\theta\theta} - \varepsilon^s_{\theta\theta} = f_{cs} & \text{continuity at the interface} \\ \varepsilon^s_{\theta\theta} - \varepsilon^{s'}_{\theta\theta} = f_{ss'} & \text{continuity at the interface} \\ \sigma^c_{rr}(r_c) - \sigma^s_{rr}(r_c) = 0 & \text{equilibrium at the interface} \\ \sigma^s_{rr}(r_s) - \sigma^{s'}_{rr}(r_s) = 0 & \text{equilibrium at the interface} \\ \sigma^{s'}_{rr}(r_{s'}) = 0 & \text{equilibrium at the sidewall} \\ \pi r_c^2 \sigma^c_{zz} + \pi(r_s^2 - r_c^2)\sigma^s_{zz} + \pi(r_{s'}^2 - r_s^2)\sigma^{s'}_{zz} = 0 & \text{equilibrium along z} \end{cases} \tag{2.25}$$

By solving numerically equation 2.7 with the proper boundary conditions given by equations 2.25, it is possible to retrieve ε_{rr}, $\varepsilon_{\theta\theta}$, ε_{zz} and then the corresponding strain values ε_{hydro}, ε_{axial}, ε_{shear}, for the inner core and the shell. Using these values we have:

$$\text{Core} \begin{cases} \sqrt{6}\varepsilon^c_{axial} = \left[\varepsilon^c_{rr} + \varepsilon^c_{\theta\theta} - 2\varepsilon^c_{zz}\right] = Q_c \\ \sqrt{3}\varepsilon^c_{hydro} = \left[\varepsilon^c_{rr} + \varepsilon^c_{\theta\theta} + \varepsilon^c_{zz}\right] = P_c \end{cases}$$

$$\text{(ZnTe)Shell} \begin{cases} \sqrt{6}\varepsilon^s_{axial} = \left[\varepsilon^s_{rr} + \varepsilon^s_{\theta\theta} - 2\varepsilon^s_{zz}\right] = Q_s \\ \sqrt{3}\varepsilon^s_{hydro} = \left[\varepsilon^s_{rr} + \varepsilon^s_{\theta\theta} + \varepsilon^s_{zz}\right] = P_s \\ \sqrt{2}\varepsilon^s_{shear} = \left[\varepsilon^s_{rr} - \varepsilon^s_{\theta\theta}\right] = R \end{cases} \tag{2.26}$$

We can calculate the values $\varepsilon^{c,s}_{hydro}$, $\varepsilon^{c,s}_{axial}$, ε^s_{shear} for the two different configurations with CdTe/ZnTe/(Zn,Mg)Te and (Cd,Mn)Te/ZnTe/(Zn,Mg)Te (see Figure 2.7).

We have considered a inner core radius of 5nm, a radius of 50nm for the ZnTe and a radius of 20nm for the (Zn,Mg)Te outer shell.
For the shell, close to the interface with the core, ε^s_{rr} and $\varepsilon^s_{\theta\theta}$ don't compensate leading to $\varepsilon^s_{shear} \neq 0$. The Bir-Pikus Hamiltonian (written in the hole basis $|+\frac{3}{2}\rangle, |+\frac{1}{2}\rangle, |-\frac{1}{2}\rangle, |-\frac{3}{2}\rangle$) is not anymore diagonal and is given by:

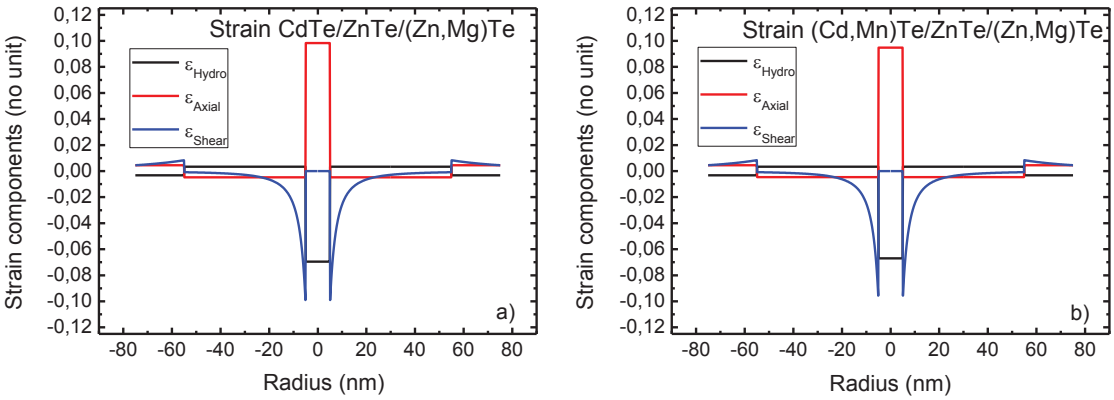

FIGURE 2.7: a) $\varepsilon_{hydro}, \varepsilon_{axial}, \varepsilon_{shear}$ for a CdTe/ZnTe/(Zn,Mg)Te nanowire b) ε_{hydro}, $\varepsilon_{axial}, \varepsilon_{shear}$ for a (Cd,Mn)Te/ZnTe/(Zn,Mg)Te nanowire

$$\begin{pmatrix} P_v+Q & -S & R & 0 \\ -S^* & P_v-Q & 0 & R \\ R^* & 0 & P_v-Q & S \\ 0 & R^* & S^* & P_v+Q \end{pmatrix} \tag{2.27}$$

The non diagonal term R and S, are responsible for the mixing between the different hole states. The R term mixes the hole state $|\pm\frac{3}{2}\rangle$ with the state $|\mp\frac{1}{2}\rangle$ while the term S mixes the hole state $|\pm\frac{3}{2}\rangle$ with the state $|\pm\frac{1}{2}\rangle$.
Having the values of the strain, it is possible to determine the heavy hole-light hole splitting ΔE_{LH}, in the core and in the shell, and the mixing term ΔE_{mix} in the shell defined by:

$$\text{Core}\begin{cases} \frac{\Delta E^c_{LH}}{2} = \frac{d}{\sqrt{3}}\sqrt{6}\varepsilon^c_{axial} = Q_c \\ \Delta E^c_{mix} = 0 \end{cases} \quad \text{(ZnTe)Shell}\begin{cases} \frac{\Delta E^s_{LH}}{2} = \frac{d}{\sqrt{3}}\sqrt{6}\varepsilon^s_{axial} = Q_s \\ \Delta E^s_{mix} = \left[\frac{2d}{\sqrt{3}} + b\right]\frac{\sqrt{2}\varepsilon^s_{shear}}{3} = R \\ S = 0 \end{cases} \tag{2.28}$$

In Figure 2.8 are traced the two quantities Q and R for a CdTe/ZnTe/(Zn,Mg)Te nanowire.

Without entering too much into the details, the strain component R is proportional to $\frac{1}{r^2}e^{-2i\theta}$ and is traced in blue in Figure 2.7a,b. We will discuss the importance of this term in Section 2.2.2. The parameters used for the calculation are given in the following tables:

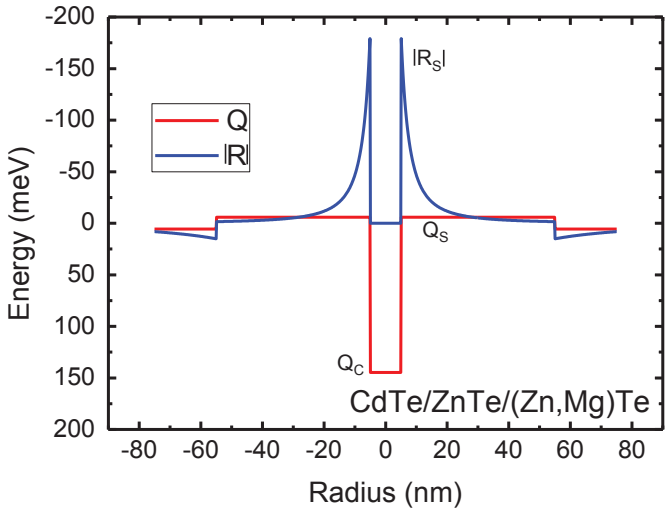

FIGURE 2.8: Strain Hamiltonian parameters for a CdTe/ZnTe/(Zn,Mg)Te nanowire

TABLE 2.5: ZnTe potentials

$a_V = 0.79\text{eV}$	$d = -4.3\text{eV}$	$b = -1.3\text{eV}$	$a = -5.48\text{eV} = a_C - a_V$

TABLE 2.6: CdTe potentials

$a_V = 0.55\text{eV}$	$d = -5.1\text{eV}$	$b = -1.15\text{eV}$	$a = -3.85\text{eV} = a_C - a_V$

From Figure 2.8 it is possible to extract the expected values for the heavy hole-light hole splitting ΔE_{LH} without considering the mixing term. In the core we expect a light hole exciton ground state with a light hole-heavy hole splitting of $2Q_c = \Delta E_{LH} = 300\text{meV}$. In the shell the exciton ground state is a heavy hole with a much smaller splitting equal to $2Q_s = \Delta E_{LH} = -12\text{meV}$.

2.2.1.2.2 Strain effect considering an ellipsoidal shape quantum dot

Even though (as you will see in the following) the calculation done in the previous Section will be very useful to interpretate the experimental results, the quantum dot shape is not infinitely long according to the EDX results.
In this Section we calculate the strain effect taking into account the real shape of the CdTe quantum dot. To simplify a bit the calculation, we will consider the isotropic approximation like in Section 2.2.1.1.1 and an ellipsoidal quantum dot shape in a infinite nanowire. This is a well known case and the elastic strain components that affects the quantum dot have been calculated by J.D. Eshelby [64] (inside an ellipsoidal inclusion) and [65] outside.

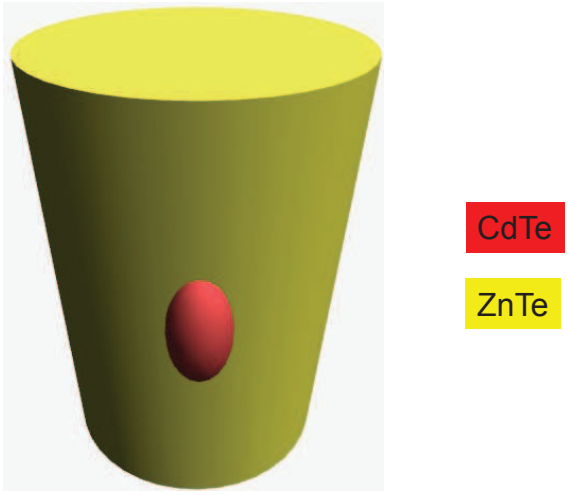

FIGURE 2.9: Core-shell nanowire structure

The deformation of an ellipsoid is uniform. It depends on f_{cs} and on a shape factor $\varphi\left(\frac{L}{D}\right)$, where L is the length and D the diameter of the quantum dot. The shape factor function $\varphi\left(\frac{L}{D}\right)$ is given by the analytical formula:

$$\begin{cases} \varphi(x) = 1 - \dfrac{1 - \frac{x}{\sqrt{1-x^2}}\cos^{-1}x}{1-x^2} & \text{when} \quad x < 1 \\ \varphi(x) = 1 + \dfrac{1 - \frac{x}{\sqrt{x^2-1}}\cosh^{-1}x}{x^2-1} & \text{when} \quad x > 1 \end{cases} \tag{2.29}$$

The strain components, in cylinder coordinates, for the quantum dot is given by:

$$\text{Quantum Dot} \begin{cases} \varepsilon_{rr} = \varepsilon_{\theta\theta} = f_{cs} - f_{shear}\varphi\left(\frac{L}{D}\right) \\ \varepsilon_{zz} = f_{cs} + 2f_{shear}\left[\varphi\left(\frac{L}{D}\right) - 1\right] \end{cases} \tag{2.30}$$

Where the quantity f_{shear} was introduced in the previous Section:

$$f_{shear} = f_{cs}\frac{1}{2}\frac{3\lambda + 2\mu}{\lambda + 2\mu} \tag{2.31}$$

Then, we can trace how the strain tensor changes as function of the aspect ratio $\frac{L}{D}$, from a $2D$ layer to a core-shell structure:

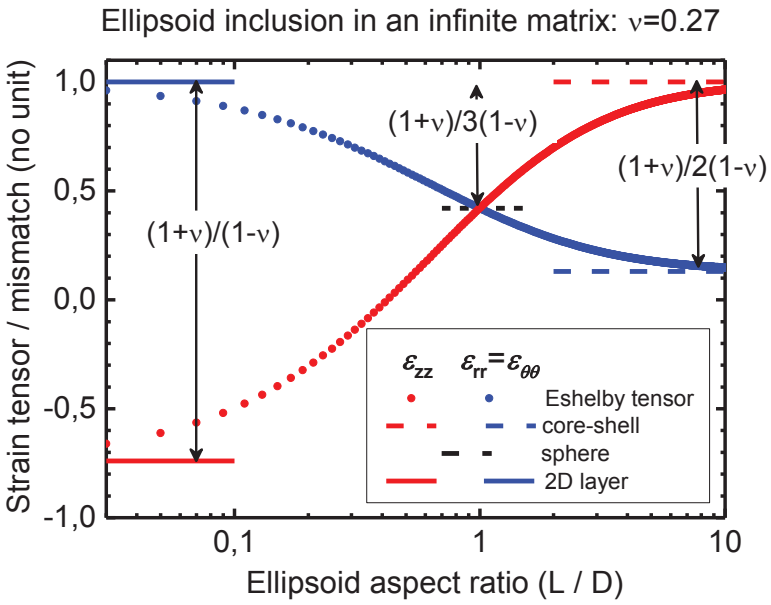

FIGURE 2.10: Strain Tensor as a function of the aspect ratio $\frac{L}{D}$

It is interesting to look at what happens in the limit cases: for $\frac{L}{D} >> 0$ (infinitely long quantum dot case) we have (cylinder limit):

$$\begin{cases} \varepsilon_{rr} = \varepsilon_{\theta\theta} = f_{cs} - f_{shear} \\ \varepsilon_{zz} = f_{cs} \end{cases} \tag{2.32}$$

For $\frac{L}{D} \approx 0$, finite long quantum dot case (quantum well limit):

$$\begin{cases} \varepsilon_{rr} = \varepsilon_{\theta\theta} = f_{cs} \\ \varepsilon_{zz} = f_{cs} - 2f_{shear} \end{cases} \tag{2.33}$$

For $\frac{L}{D} = 1$, the spherical case:

$$\varepsilon_{rr} = \varepsilon_{\theta\theta} = \varepsilon_{zz} = f_{cs} - \frac{2}{3} f_{shear} \tag{2.34}$$

As we have calculated the strain components ε_{rr}, $\varepsilon_{\theta\theta}$ and ε_{zz} for the ellipsoid quantum dot, we can derive the expressions for ε^c_{hydro} and ε^c_{axial}. Moreover, we can deduce the strain components for the shell just at the interface with the quantum dot

using the boundary conditions (the calculation of the strain in the shell, far from the dot, is more complicated). We have then:

$$\text{Quantum dot}\begin{cases}\frac{\Delta E^c_{LH}}{2} = \frac{d}{\sqrt{3}}\sqrt{6}\varepsilon^c_{axial} = Q_c \\ \Delta E^c_{mix} = 0\end{cases}$$

$$\text{Shell}\begin{cases}\frac{\Delta E^s_{LH}}{2} = \frac{d}{\sqrt{3}}\sqrt{6}\varepsilon^s_{axial} = Q_s \\ \Delta E^s_{mix} = \left[\frac{2d}{\sqrt{3}} + b\right]\sqrt{2}\frac{\varepsilon^s_{shear}}{3} = R_s\end{cases} \tag{2.35}$$

Using equation 2.35 it is possible to trace the two parameters Q and R for the quantum dot and for the shell as function of the ratio $\frac{L}{D}$. The results are shown in Figure 2.11.

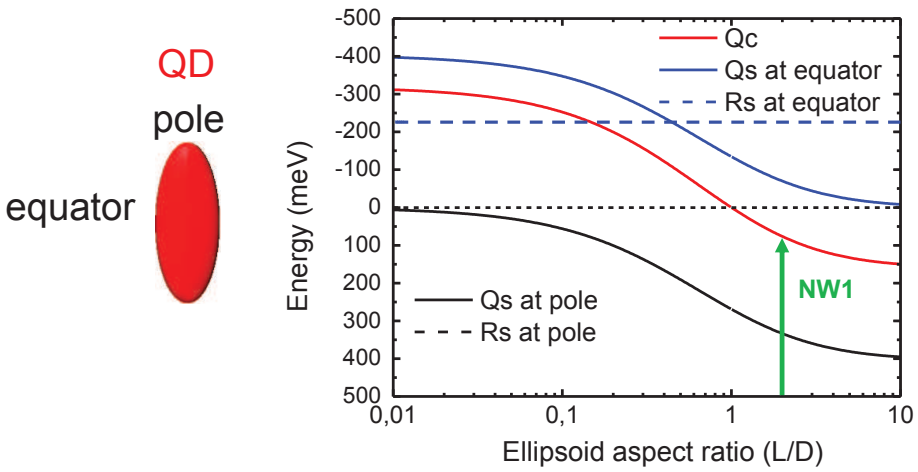

FIGURE 2.11: Strain Hamiltonian parameters for a CdTe ellipsoidal quantum dot in a ZnTe nanowire, the potentials are given in Table 2.7

TABLE 2.7: CdTe/ZnTe potentials

CdTe	$d = -5.1$eV	$b = -1.15$eV
ZnTe	$d = -4.3$eV	$b = -1.3$eV

From Figure 2.11 we can see that for an infinite core $\frac{L}{D} \cong 10$ we retrieve the value of $\Delta E_{LH} = 2Q_c = 300$meV that we have calculated in the previous Section. For flat quantum dots $\frac{L}{D} \cong 0.01$, we have $\Delta E_{LH} << 0$. This means that we have a heavy hole exciton as a ground state, with a very far light hole excited state ($\Delta E_{LH} = -600$meV). This is what is observed for self assembled quantum dots. We can try to estimate

what we could expect for NW1, the nanowire where we have performed EDX mapping and that has been presented in Section 2.1.1.1. From Figure 2.11, using $\frac{L}{D} \cong 2$, one can predict an exciton ground state with a light hole character and with a light hole-heavy hole splitting $\Delta E_{LH} \cong 140$meV.
The change on the hole character, depending on the aspect ratio $\frac{L}{D}$, has been calculated also for III-V materials (InAs quantum dot inserted in InP nanowire) and can be found in [66].
By performing photoluminescence experiments under magnetic field, we can determine the experimental value of ΔE_{LH} and we will check if it is in agreement with the calculated one.

2.2.2 Discussion of LH-HH splitting and transition from Type I to Type II quantum dots

In this Section we summarize the results obtained with the different theoretical models that have been explained in Section 2.2.1.2. These considerations will be very useful to understand all the experimental results discussed in the following.
We start by considering the valence band-conduction band profiles for a (Cd,Mn)Te quantum dot inserted in a ZnTe nanowire without the presence of strain (see Figure 2.12).

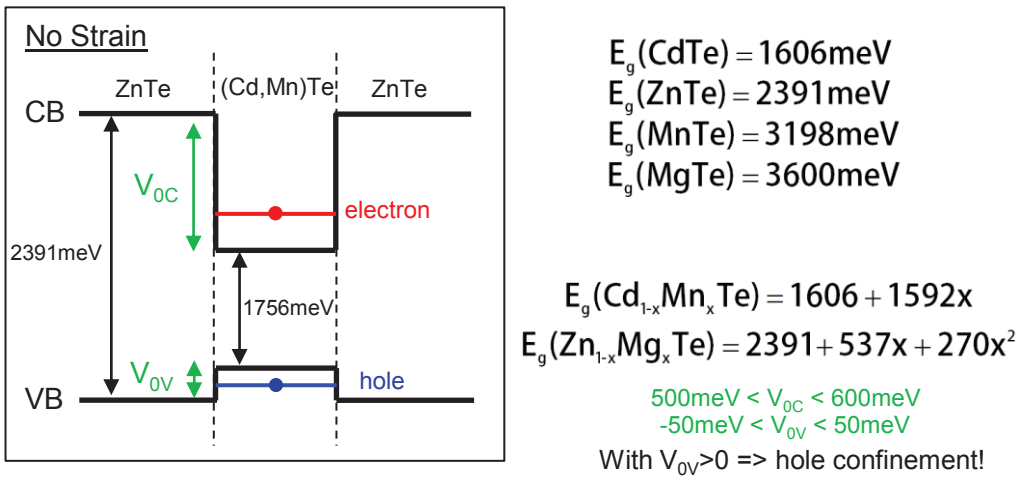

FIGURE 2.12: Band profiles for an unstrained (Cd,Mn)Te quantum dot in a ZnTe nanowire

The value of the band offsets of the systems CdTe/ZnTe is not very well known: only the gap difference $\Delta E_g = E_g(\text{ZnTe}) - E_g(\text{CdTe}) = V_{0C} + V_{0V}$ is known.

We can however discuss values of V_{0C} and V_{0V} using what have been reported in the literature [17]. V_{0C} is quite large (500meV < V_{0C} < 600meV) leading to a fully confined electron. For the valence band −50meV < V_{0V} < 50meV leading to at best a not so strong confinement potential for the holes. For a high Mn concentration in the quantum dot (Mn > 8%), it has been calculated in [17], that $V_{0V} \longrightarrow 0$: the confinement is governed just by the Coulomb interaction with the electron.
We will summarize now how the elastic strain affects the electronic properties of the (Cd,Mn)Te quantum dot for the two limiting case: V_{0V} = 50meV (confined hole, Mn = 1%) and V_{0V} = −50meV (hole not confined) . The main results of the two different approximations described in Section 2.2.1.2 are shown in Figure 2.13.

	Core	Shell
Cylindrical approximation	ΔE_{LH}= 300meV	ΔE_{LH}= -12meV
Ellipsoidal Quantum dot	ΔE_{LH}= 140meV	Pole ΔE_{LH}= +660meV Equator ΔE_{LH}= -140meV

FIGURE 2.13: Summary of the main results of Section 2.2.1.2

For both approximations, when the exciton is well confined in the quantum dot (V_{0V} = 50meV, Type I quantum dot), the expected ground state has a light hole nature with a quite large heavy hole-light hole splitting: ΔE_{LH}^{ell} = 140meV and ΔE_{LH}^{cyl} = 300meV.
The situation is more complicated in the case of a not fully confined exciton (V_{0V} = −50meV, Type II quantum dot): for the cylinder model, if we neglect mixing, the ground state has a heavy hole nature with a rather small heavy hole-light hole splitting ΔE_{LH}^{cyl} = −12meV. In the case of an ellipsoidal quantum dot, we have two different cases: if the hole (the electron wavefunction is supposed to be fully confined) is localized at the pole of the quantum dot, the ground state is a light hole exciton with a ΔE_{LH}^{ell} = 660meV. If the hole is localized at the equator, the ground state is a heavy hole exciton with ΔE_{LH}^{ell} = −140meV.
You will see, when we will analyze the experimental results, that there are nanowires having a heavy hole exciton ground state with a small ΔE_{LH} around 10meV (Sample 1, NW1 and NW2) showing probably a partially delocalized hole wavefunction around the quantum dot. Other nanowires will have a light hole exciton ground state

with a ΔE_{LH} around 20 meV (NW3 of Sample 1 and MP1 of Sample 2) leading to a more confined hole in the dot.

2.3 Experimental results

2.3.1 Nanowire emission spectrum

In this Section we will present all the experimental results obtained on pure ZnTe and ZnTe/(Zn,Mg)Te core-shell nanowires.
First we performed micro-photoluminescence experiments on pure ZnTe nanowires to check their good optical quality. We analyze the emission properties of the nanowires and we show, for the first time, the exciton emission from ZnTe nanowires. We conclude this part showing that it is necessary to cover the nanowire with a (Zn,Mg)Te shell because although the ZnTe nanowire has a good crystalline quality and presents an excitonic emission, the photoluminescence intensity is rather weak.
In the second part we show the microphotoluminescence studies done on ZnTe/(Zn,Mg)Te core-shell nanowires. We analyze the excitonic emission position and we will discuss the effect of the elastic strain on the optical properties.

2.3.1.1 ZnTe nanowire

In this Section we present the main results obtained with pure ZnTe nanowires [16].

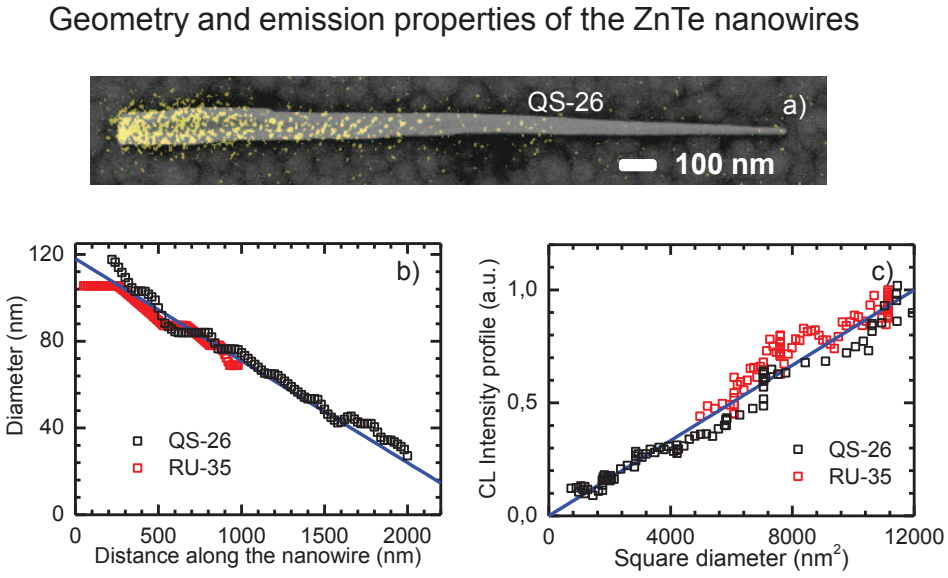

FIGURE 2.14: a) Superimposition of the HRSEM image of a ZnTe nanowire and the CL image (yellow pixels) recorded at 6K b) Nanowire diameter as a function of the position along the nanowire axis c) Cathodoluminescence intensity (integrated over a 12nm × 120nm) as a function of the square of the nanowire diameter

Figure 2.14a is a HRSEM image of a typical ZnTe nanowire that has been deposited on a patterned silicon substrate (see Chapter 1). Moreover, in Figure 2.14a, we superimpose the cathodoluminescence image obtained on this nanowire (yellow pixels) on the HRSEM one. For cone-shaped nanowires [14, 48] (see Figure 2.14b) the cathodoluminescence intensity is high at the base of the nanowire and becomes smaller and smaller when we move towards the tip of the nanowire. If we trace the cathodoluminescence intensity (integrated over a rectangle wider than the nanowire diameter) as a function of the square of the nanowire diameter (see Figure 2.14c) we see that the CL signal is proportional to D^2. This suggests that the radiative efficiency remains constant along the nanowire, with a CL intensity determined by the excitation density which is proportional to D^2.

We performed micro-photoluminescence studies on the nanowire (shown in Figure 2.14a). The main results are plotted in Figure 2.15.

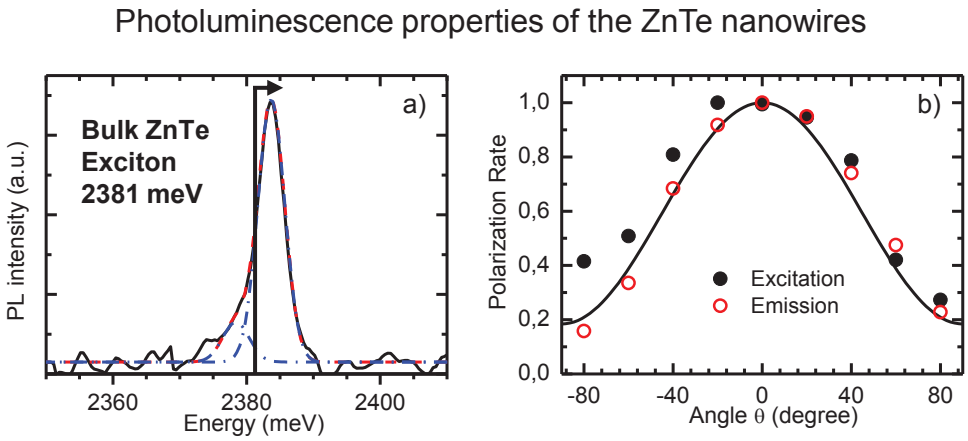

FIGURE 2.15: a) Micro-PL spectrum of the nanowire shown in Figure 2.14a b) Dependence of the PL intensity on the angle θ between the nanowire axis and the direction of the linear polarization of the laser excitation (closed circles) or the emitted light (open circles)

The micro-PL spectrum is dominated by a single emission peak close to the ZnTe exciton band edge. We fit the spectrum by two Gaussian functions having a full width at half maximum equal to 4meV. The main peak is located at 2383.7meV: it is blue shifted compared to the ZnTe excitonic emission expected at 2381meV (for the bulk exciton) [62, 67]. The small satellite peak observed 5meV below the main peak is attributed to bound excitons. These results are apparently in contrast with the studies performed on ZnTe nanowires with a (Zn,Mg)Te shell [13] presented in Section 2.2.1.1.2. This will be clarified at the end of this Section.

In Figure 2.15b, we plot the variation of the intensity of the band-edge emission peak by changing the linear polarization of the laser excitation (closed circles) or of the

detection (open circles). The maximum of the emission intensity is reached when the polarization is parallel to the nanowire axis ($\theta = 0$). Polarization rates of about 70% are observed for emission and detection, in agreement with the value reported with III-V standing nanowires [68]. These effects result from the dielectric screening induced by the characteristic aspect ratio of the nanowires [69].
We showed that the ZnTe nanowires have a good crystalline quality presenting an excitonic band edge emission. But the intensity of the emission is rather weak and you will see, in the next Section, that covering the ZnTe nanowires by a (Zn,Mg)Te shell enhances the photoluminescence intensity.

2.3.1.2 ZnTe/(Zn,Mg)Te core-shell nanowire

In this Section we present the experimental results obtained on ZnTe nanowires covered by a (Zn,Mg)Te shell (the scheme is shown in Figure 2.16a).

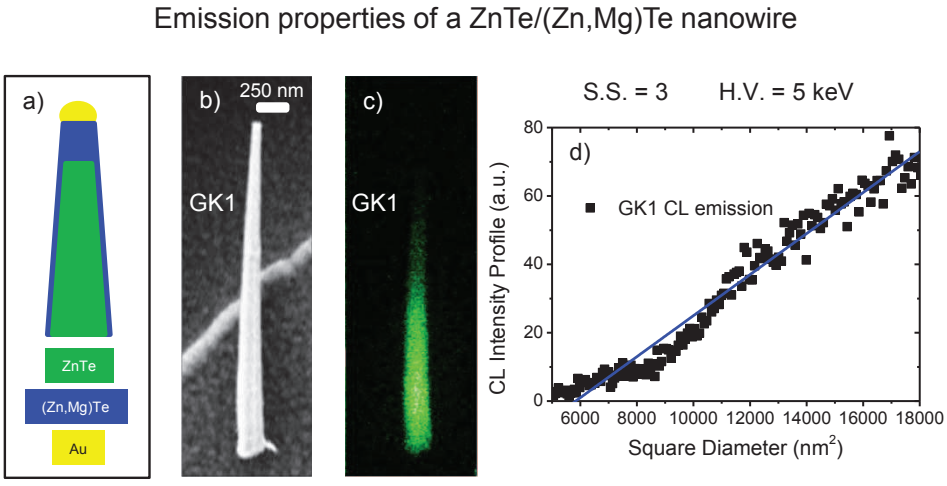

FIGURE 2.16: a) Scheme of the studied nanowire called GK1 b) HRSEM image of GK1 c) Monochromatic cathodoluminescence image recorded at the excitonic emission energy d) Integrated cathodoluminescence intensity as a function of the square of the nanowire diameter

The most studied nanowire has been called GK1 and its HRSEM image is shown in Figure 2.16b. Figure 2.16c presents the monochromatic cathodoluminescence image recorded at the excitonic band edge emission (see Figure 2.17a). As for the pure ZnTe nanowire, the CL intensity is locally uniform and it depends on the nanowire diameter (also in this case we have a cone-shaped nanowire and the CL intensity is a function of D^2, see Figure 2.17d).

We performed also micro-PL experiments on GK1. The results are traced in Figure 2.17.

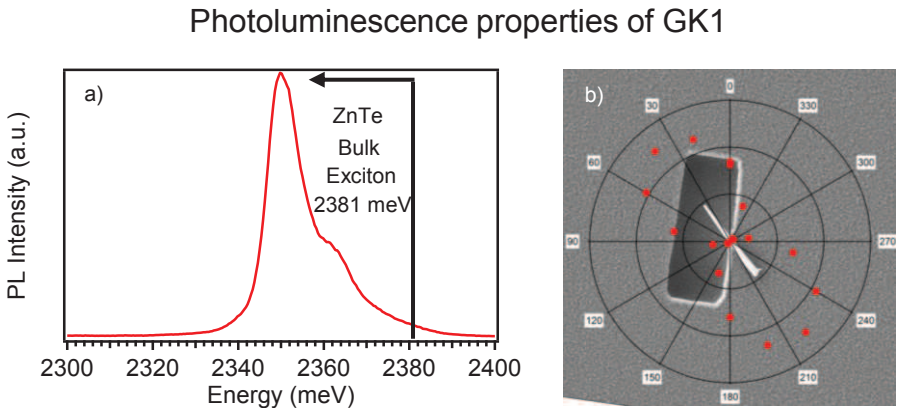

FIGURE 2.17: a) Micro-PL spectrum showing the excitonic line of GK1 b) Superimposition of the HRSEM image of GK1 and the polarization diagram of the excitonic line

The PL spectrum is traced in Figure 2.17a: the excitonic emission is red shifted compared to the ZnTe band edge emission. The main peak is located at 2350meV: this value is really different from what we observed for pure ZnTe nanowire where we found 2383.7meV. This apparent discrepancy will be clarified in the next Section.
In Figure 2.17b we traced the superimposition between the polarization rate of the PL emission (Figure 2.17a) and the HRSEM image of GK1. Like for the pure ZnTe nanowires, the maximum of the emission intensity is reached when the polarization is parallel to the nanowire axis. We observed polarization rates of about 80% for the detection (in this case we didn't performed polarization resolved measurements for the excitation).

To conclude this Section we present a last Figure to show how, by adding a shell around the nanowire, we enhance its photoluminescence emission properties (Figure 2.18). Figure 2.18 shows the micro-PL spectra of pure ZnTe nanowire and ZnTe nanowire covered by a (Zn,Mg)Te shell. The two spectra have been recorded in the same conditions: we acquired them at 5K using the same excitation power and both nanowires were deposited on a patterned silicon substrate. The passivation of the surface, done by the (Zn,Mg)Te shell, increase the photoluminescence emission intensity of about 10^4 times.

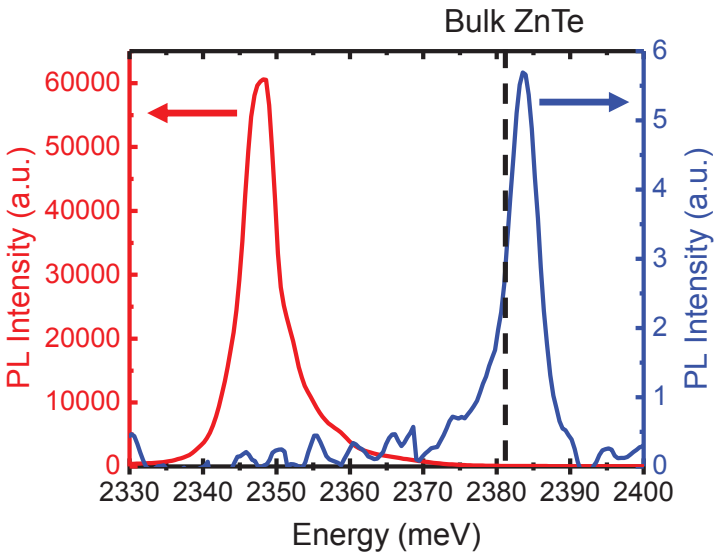

FIGURE 2.18: Comparison between the micro-PL spectra of pure ZnTe nanowire (blue) and ZnTe nanowire with a (Zn,Mg)Te shell (red) acquired with the same excitation power ($100\mu W$) and at 5K

2.3.1.3 Determination of the strain in ZnTe and core-shell nanowires

It is possible to trace the expected excitonic emission energy for a ZnTe nanowire covered by a (Zn,Mg)Te shell using equation 2.21. In Figure 2.19, the excitonic emission energy is plotted as a function of the averaged Mg concentration expressed by $x_{Mg}(1-\frac{r_c^2}{r_s^2})$.

Figure 2.19 shows the good agreement between the calculation and the experimental points. The black circled points are taken from [46] (Wojnar Ref 2 on the Figure), the green square point is taken from [13] (Wojnar Ref 1 on the Figure) while the red square point is what we have found and shown in Section 2.3.1.2 (the horizontal error bar is caused by the incertitude in the determination of the Mg concentration). From the Figure it is clear that the exciton emission energy strongly depends on the averaged Mg concentration but in all the cases the exciton ground state has a heavy hole nature.

For pure ZnTe nanowires the situation is different. If we look at the Figure 2.19, we see that the blue shift (exciton emission energy equal to 2383.7meV) observed in pure ZnTe nanowires, could be attributed to a light hole exciton ground state. This is possible if the ZnTe core is under a small compressive strain induced by a shell. TEM measurements, done on some ZnTe nanowires, reveal the presence of a thin oxide shell that could be responsible for the compression of the core part [16].

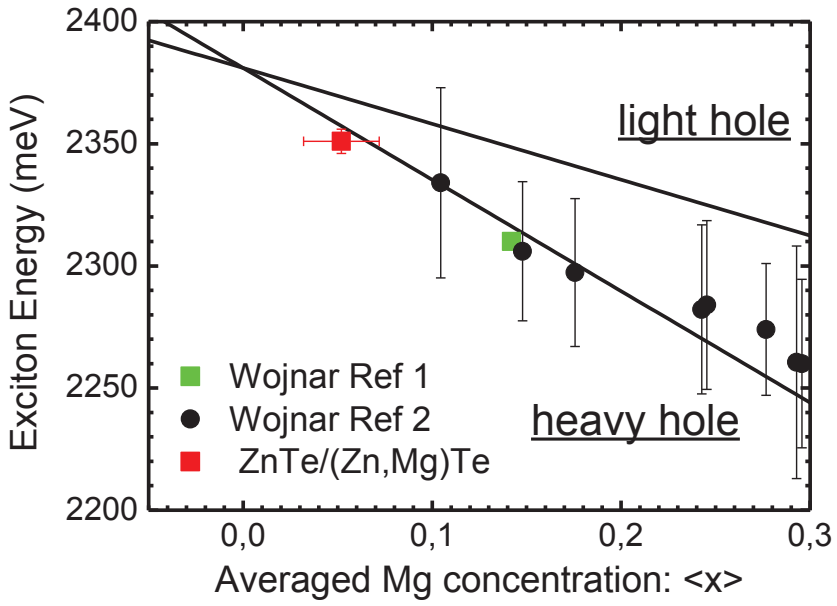

FIGURE 2.19: Exciton emission energy of a ZnTe/(Zn,Mg)Te nanowire as a function of the averaged Mg concentration along the nanowire. The vertical error bars are defined by the emission energy linewidth

2.3.2 CdTe quantum dot emission spectrum

2.3.2.1 Exciton fine structure of the Reference sample

In this Section we present the analysis done on a CdTe quantum dot inserted in a ZnTe nanowire called RH1. Before inserting Mn atoms inside the quantum dots, our motivation was to check the good quality of a pure CdTe quantum dot. RH1 is shown in Figure 2.20b while a HRSEM image of the as-grown sample is shown in Figure 2.20a.

To characterize the quantum cascade of a quantum dot, we performed micro-PL experiments on RH1: the results are shown in Figure 2.21. The spectrum at low power (see Figure 2.21b) is composed by three components: L_1, L_2 and L_3 identified by a Gaussian fit. To study the nature of these emitting states, we performed power dependence photoluminescence studies.
The evolution of the three components is shown in Figure 2.21c. From the Figure we can see that the two components L_1 and L_2 have a quite similar linear dependence with the laser power ($P^{1.1}$ and P^1). Due to the proximity in energy of the two components (the splitting is around 3meV) we cannot analyze properly each line.
Nevertheless we can do another consideration: L_1 saturates at high excitation power

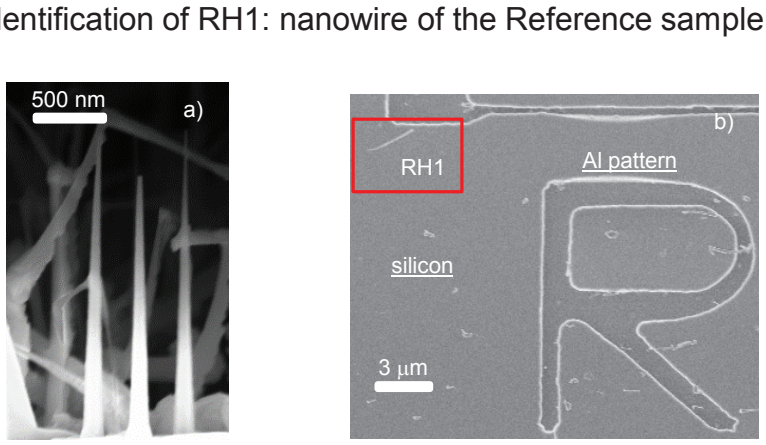

FIGURE 2.20: a) HRSEM image of the as-grown sample b) HRSEM image of RH1 deposited on the patterned silicon substrate

leading to the conclusion that this could be attributed to the exciton state [17]. L_2 could be then attributed to a charged excitonic state (the line is in fact also located at lower emission energy).
The other two components L_3 and L_4 have superlinear dependencies ($P^{1.45}$ and $P^{2.3}$) with the excitation power: we could attribute L_3 to the biexcitonic state while L_4 is the triexciton state.
The separation in energy between the exciton (L_1) and the possible biexcitonic state (L_3) is around 6meV: it is the same value found in [17] showing a comparable quantum confinement. A complete overview of the CdTe quantum dot inserted in ZnTe nanowires could be found on the thesis [17].

To conclude this Section we can make some considerations also on the L_1, L_2, L_3 and L_4 linewidths. These are reported in the table:

TABLE 2.8: CdTe quantum dot linewidths

$L_1 = 3.2$meV	$L_2 = 3.6$meV	$L_3 = 3.6$meV

If we consider the linewidth of the excitonic state FWHM = 3.2meV we see that is much bigger than in CdTe self assembled quantum dots where it is possible to find linewidths between 10μeV to 50μeV (moreover linewidths can be even smaller than 10μeV but they are limited by the resolution of the spectrometer). The broadening of the line, in the case of nanowires, is usually attributed to the spectral diffusion which results from Stark shift of the excitonic line due to the presence of surface charges [70]. This broadening, for self assembled quantum dot, is suppressed thanks to the presence of a capping layer that keeps the charges far from the quantum dots.

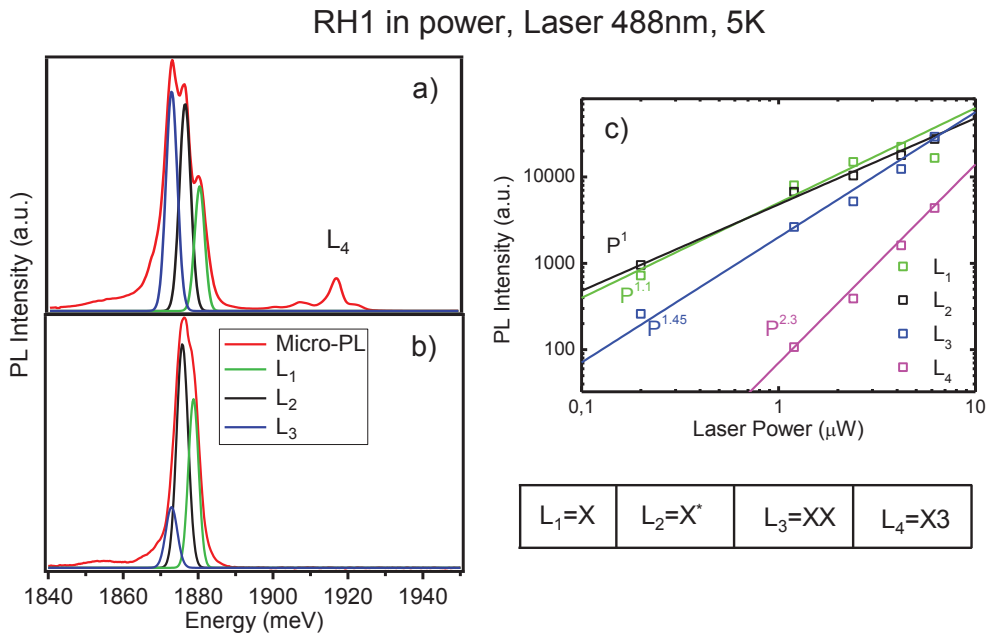

FIGURE 2.21: a) Photoluminescence spectrum of RH1 at high laser excitation $6.7\mu W$ b) Photoluminescence spectrum of RH1 at low laser excitation $0.2\mu W$ c) Photoluminescence intensities as function of the laser excitation power for the four components L_1, L_2, L_3 and L_4

2.3.2.2 QD spatial localization using CL experiment

We perform also cathodoluminescence experiments to spatially localized the CdTe emission on RH1. The results are shown in Figure 2.22. Due to the lower resolution of the CL set-up, it was not possible to resolve the three different components (see Figure 2.22d) identified by the micro-PL studies, shown in the previous Section. We acquired then a monochromatic cathodoluminescence image integrating all the signal of the CdTe emission as shown in Figure 2.22c. From Figure 2.22c, it is clear that the emitted light is spatially localized and it is located at a position corresponding to $\frac{2}{3}$ of the nanowire length.
We acquired also a monochromatic cathodoluminescence image at the energy of the ZnTe emission (see Figure 2.22b). In contrast to the CdTe emission, the ZnTe one is coming from all the nanowire, as expected (the CL signal at the tip is lower due to the smaller diameter and hence a lower excitation efficiency).

In the next Section we present a simplified model to extract the characteristic diffusion lengths of excitons in the nanowire.

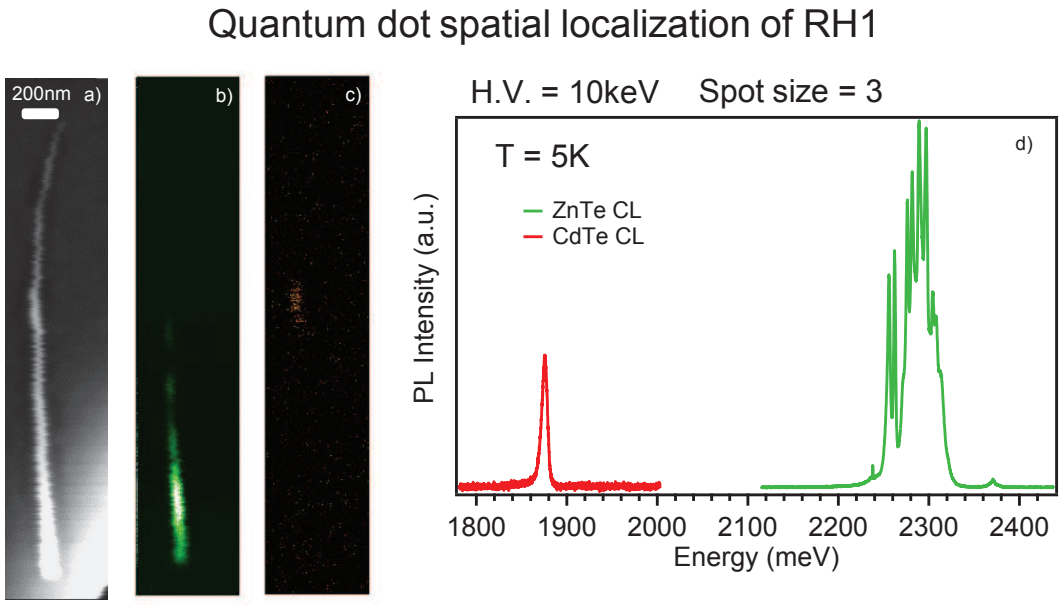

FIGURE 2.22: a) HRSEM image of RH1 b) Monochromatic Cathodoluminescence image recorded at the ZnTe emission energy (2300meV) c) Monochromatic Cathodoluminescence image recorded at the exciton emission energy (1880meV) d) CL spectrum showing the ZnTe emission and the CdTe signal

2.3.2.2.1 Model to extract the diffusion lengths

In this Section we explain how we fit the quantum dot emission profile using the diffusion equation [71]. Figure 2.23a shows the diffusion model scheme while Figure 2.23b shows the intensity profile.

We consider a $1D$ model for the diffusion along x using the intensity integrated perpendicularly to x. The scheme of the system is shown in Figure 2.23a. We excite the nanowire at $x = 0$ with the electron beam: the carriers diffuse along the nanowire and they are trapped in the quantum dot region (having a trapping extension $2x_t$). When the carriers reach the quantum dot they recombine and emit a photon.
The goal is to calculate the cathodoluminescence intensity profile that it is given by the following equation:

$$\widetilde{I}_{QD}(x_0) = \int I_{QD}(x)\phi_{beam}(x_0 - x)dx \tag{2.36}$$

Where $\phi_{beam}(x_0) = \frac{\phi_0}{\sqrt{2\pi}\sigma} e^{-\frac{x_0^2}{2\sigma^2}}$ is a Gaussian function that describes the electron beam and $I_{QD}(x)$ is the solution to the diffusion equation and given by:

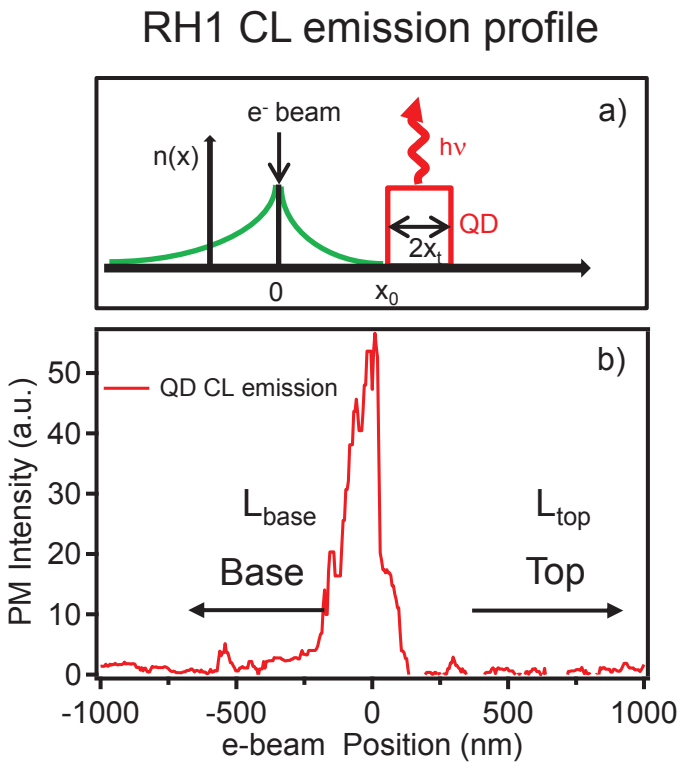

FIGURE 2.23: a) CL model scheme b) RH1 integrated cathodoluminescence excitonic emission profile recorded using a photomultiplier (PM) detector

$$\begin{cases} I_{QD}(x) = \phi_0 e^{\frac{-|x_0-x_t|}{L_{base}}} & x < -x_t \\ I_{QD}(x) = \phi_0 e^{\frac{-|x_0-x_t|}{L_{top}}} & x > x_t \\ I_{QD}(x) = \phi_0 & -x_t <\mid x \mid < x_t \end{cases} \tag{2.37}$$

L_{base} and L_{top} are the exciton diffusion lengths for $x < -x_t$ and $x > x_t$.
The derivation of equation 2.37 is presented in Appendix C.

2.3.2.2.2 Fitting the CL profile

We used equation 2.36 to fit the RH1 cathodoluminescence profile, the result is shown in Figure 2.24.

The parameters used for the fit are given in Table 2.9.

TABLE 2.9: CdTe quantum dot diffusion lengths

$L_{top} = 35$nm	$L_{base} = 90$nm	$e-beam(FWHM) = 80$nm	$2x_t = 10$nm

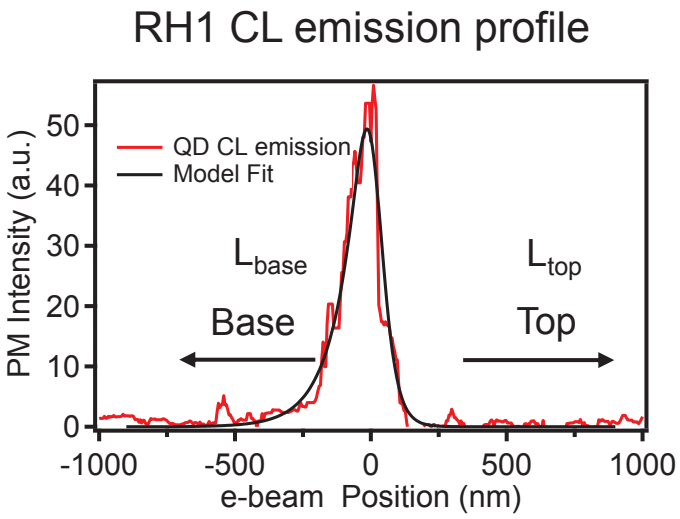

FIGURE 2.24: a) RH1 integrated cathodoluminescence excitonic emission profile with the model fit (in black)

We see that for RH1 we have an asymmetrical profile leading to two different diffusion lengths L_{top} and L_{base}. We have the biggest diffusion length L_{-} for excitons that recombine towards the base of the nanowire. This could result from a more efficient radiative recombination that is linked to the higher thickness of the nanowire. If we look at the HRSEM image of RH1 we see in fact that it has a cone-shape form, like all the nanowire that have been studied (see Chapter 1).

2.3.3 (Cd,Mn)Te quantum dot emission spectrum

In this Section we present the analysis done to characterize the emission properties of the (Cd,Mn)Te quantum dot inserted in ZnTe nanowires. Moreover we show how we spatially localize the quantum dots using cathodoluminescence measurements (NW1 and NW3) or photoluminescence ones (NW2). The fundamental state, the more intense at low excitation power, is always called L_1: this is the exciton state. The excited states are denoted from L_2 up to L_5: for these states the assignment of the emission nature is not always clear and hence from nanowire to nanowire, the same labeling may not denote the same excited state.

2.3.3.1 Doublet emission lines broaded by magnetic fluctuations

2.3.3.1.1 NW1

We performed power dependence photoluminescence studies on all the nanowires studied in this thesis, to determine the typical quantum cascade of the quantum dot. Figure 2.25 shows the micro-PL results of NW1.

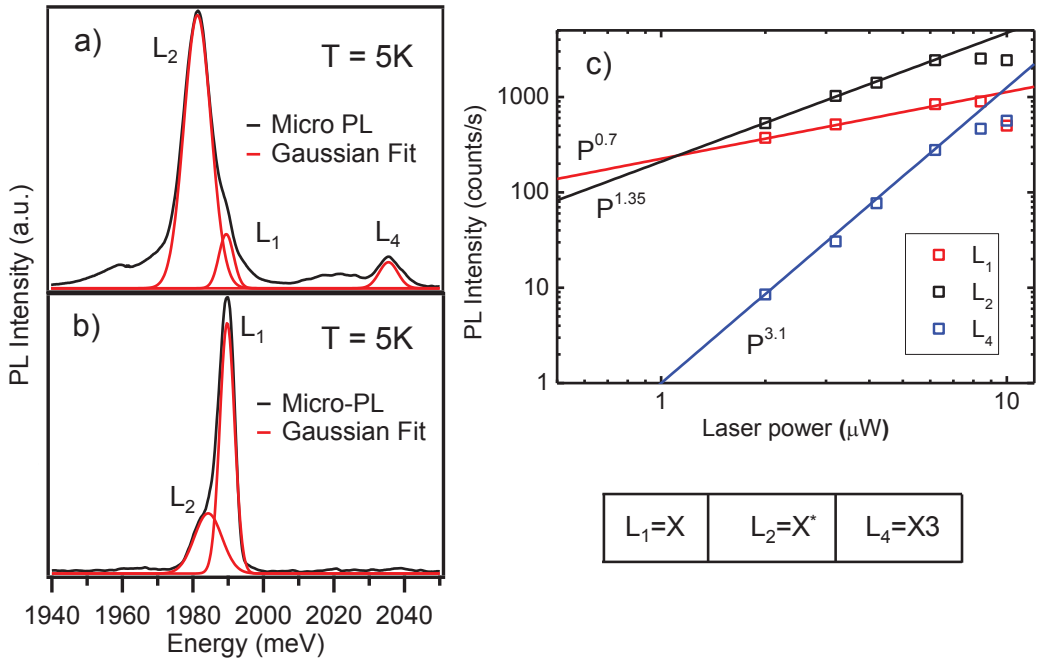

FIGURE 2.25: a) NW1 quantum dot emission at higher power where it is visible the multi-excitonic line b) NW1 quantum dot emission spectrum taken at very low power c) PL intensities of the main lines versus the excitation power (the component L_3 will appear when we will show the magneto-optical measurements done on this nanowire, see Chapter 3)

The spectrum at very low power (see Figure 2.25b) is dominated by a doublet: we identified the two components L_1 and L_2 by a Gaussian fit. At higher laser power (see Figure 2.25a) an excited state L_4 starts to be populated. If we trace the photoluminescence intensity as function of the excitation power (see Figure 2.25c) we see that the L_1 component has a nearly linear dependency with the laser power: we can then suppose that L_1 is the excitonic state X. The L_2 component has a superlinear dependency with the excitation power and could be attributed to the charged excitonic state CX or could even be the biexcitonic one XX.

It is not easy to determine what could be the state described by L_5: its dependency on the laser power reveals an excited nature. If we look at what we measured for the

pure CdTe quantum dot (RH1, Section 2.3.2.1) we could attribute the state L_5 to the X3 (Triexciton).
In the following table we present the typical linewidth of a (Cd,Mn)Te quantum dot.

TABLE 2.10: (Cd,Mn)Te quantum dot linewidths

$L_1 = 6$meV	$L_2 = 9.2$meV

If we compare these values with what we found for pure CdTe quantum dot (RH1, Section 2.3.2.1) we see that the lines are broader. This extra broadening is expected from the thermal fluctuations of Mn spins [72]. A full study on the fine structure properties of self assembled (Cd,Mn)Te can be found here [17]. Figure 2.26 shows the variation of the excitonic linewidth as function of the Mn atoms concentration.

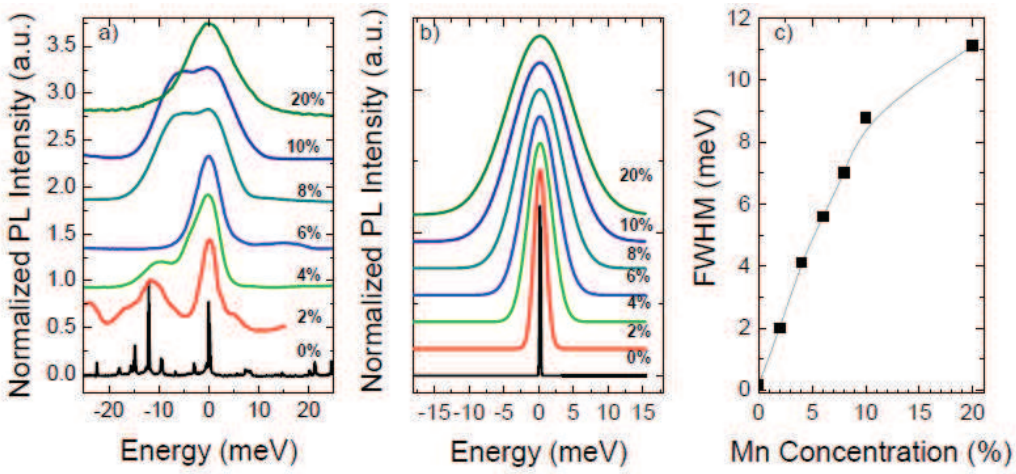

FIGURE 2.26: a) Experimental spectra of (Cd,Mn)Te QDs with different Mn concentration recorded at 6K b) Fitted exciton emission lines of samples with different Mn concentration c) Full width at half maximum of emission line as a function of Mn concentration, images taken from [17]

From Figure 2.26 it is clear that the observed increase in linewidth follows the increase of Mn concentration. From Figure 2.26c, considering the experimental error, we see that considering 7% < Mn < 10% the linewidth fluctuates in a range of 5meV<FWHM<8meV that is in agreement whit the value found for NW1 (From the EDX measurements done on NW1 we found that the typical Mn concentration for Sample 1 is around $10\% \pm 2\%$).

2.3.3.1.2 NW2

We studied also the fine structure of NW2 with a detailed power dependence characterization. The results are shown in Figure 2.27.

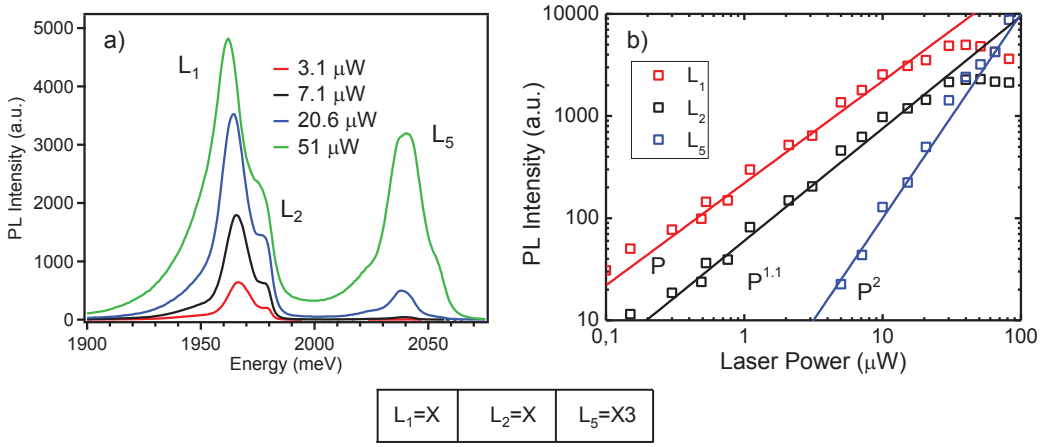

FIGURE 2.27: a) NW2 quantum dot emission spectrum taken at different excitation powers b) PL intensities of the main lines versus the excitation power (the components L_3 and L_4 will appear when we will show the magneto-optical measurements done on this nanowire, see Chapter 3)

Like for NW1, at very low excitation power (Figure 2.27a), the spectrum is dominated by a doublet that can be fitted by two Gaussian components L_1 and L_2. With the increase of the laser power, both L_1 and L_2 show a linear dependence and they saturates at the same laser power: we can't then conclude about the nature of both lines. We decided then to do time resolved measurements, as you will see in Section 2.3.4, to clarify the nature of this doublet.
Like for NW1, at high laser power, we can identify an excited state L_5 that has a superlinear dependency with the excitation power and could be attributed to the X3 (Triexciton).

2.3.3.1.3 NW3

Figure 2.28 shows the results concerning the fine structure of NW3.

At low excitation power (see Figure 2.28a) the spectrum is dominated by a multi-peak structure where we can identify two main components L_1 and L_2 by a Gaussian fit. With the increase of the laser power (see Figure 2.28b) L_1 increases linearly with the laser power and then may be attributed to the exciton X. L_2 grows superlinearly with the excitation power and we can associate this state to an excited state called X^*. The

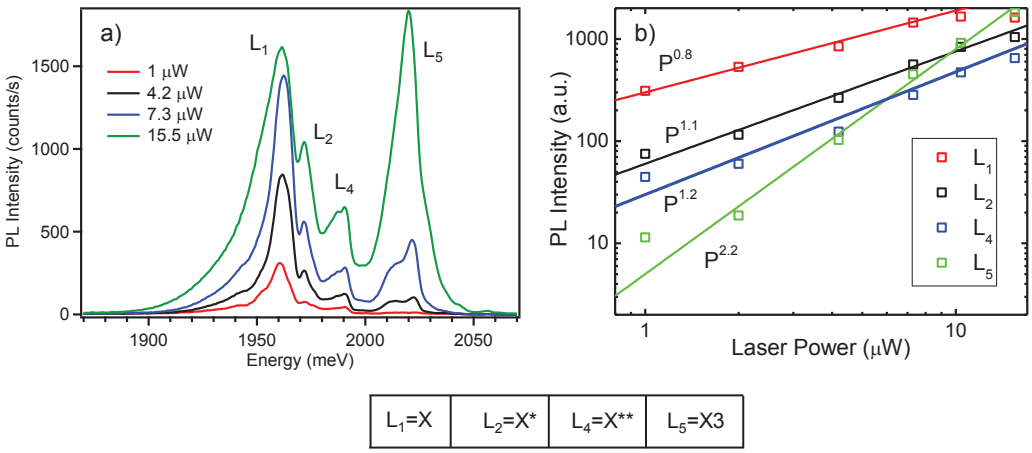

FIGURE 2.28: a) NW3 quantum dot emission spectra at different excitation powers b) PL intensities of the main lines versus the excitation power (the component L_3 will appear when we will show the magneto-optical measurements done on this nanowire, see Chapter 3)

identification of the nature of these two components will be done at the end of this Chapter, when we will present the polarized resolved Fourier imaging.

When the laser power is increased, the fine structure of NW3 becomes more complex compared to the one of NW1 and NW2 but it is still possible to identify an excited state L_5, similar to the one of the other nanowires, that can be attributed to X3 (Triexciton). There is also a presence of another excited state called L_4 whose nature is not clear.

The more complicated identification of the photoluminescence lines could be attributed to the fact that NW3 has been directly measured on the as-grown sample: some of the extra components in the spectrum, like the low energy tale that affects the L_1 transition, could be associated to another nanowire. In this manuscript we are interested to the excitonic state (L_1) and we will not push further the analysis on the other photoluminescence transitions.

2.3.3.2 QD Spatial localization using CL experiment

2.3.3.2.1 NW1

We performed cathodoluminescence measurements (see Figure 2.29), to spatially identify the quantum dot emission.

Figure 2.29a shows the HRSEM image of NW1 while Figure 2.29b,c are the monochromatic cathodoluminescence images showing, respectively, the (Cd,Mn)Te quantum

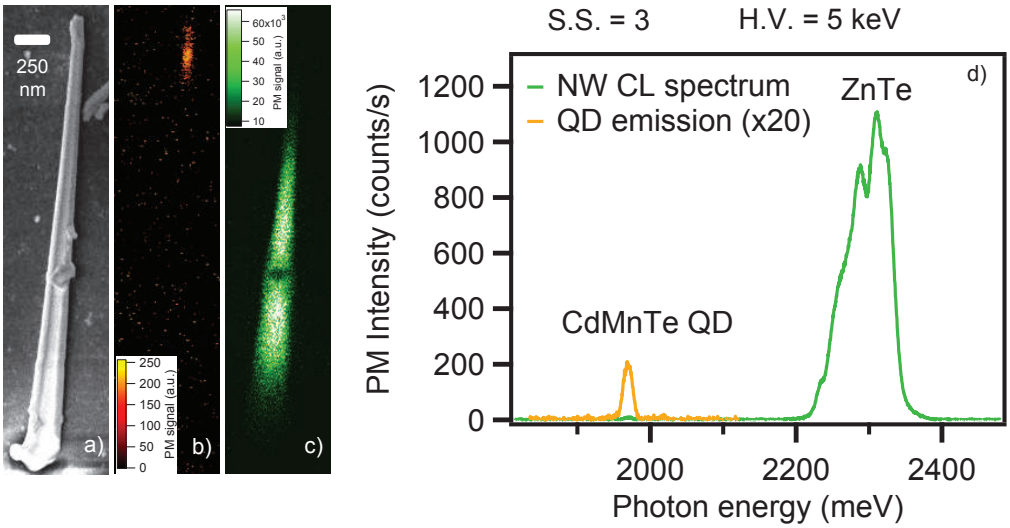

FIGURE 2.29: a) HRSEM of NW1 b) Monochromatic CL image recorded at the (Cd,Mn)Te emission c) Monochromatic CL image recorded at the ZnTe emission d) CL spectrum showing the ZnTe emission and the (Cd,Mn)Te signal

dot emission and the ZnTe one. Thanks to the use of the spectrometer mounted in the set-up, we were able to record monochromatic cathodoluminescence images (see Figure 2.29b,c) at the (Cd,Mn)Te and ZnTe emission energy. The emission spectrum is shown in Figure 2.29d.

From Figure 2.29 we can see that the quantum dot emission is spatially localized and is coming from the a region close to the tip of the nanowire. In contrast the ZnTe emission is coming homogeneously from all the nanowire.

2.3.3.2.2 Fitting the CL profile

Having the characteristic emission map of the quantum dot (see Figure 2.29b) we can determine the typical diffusion length of this structure L_D. We used equation 2.36 to fit, as for RH1, the integrated CL emission profile and the results is shown in Figure 2.30b.

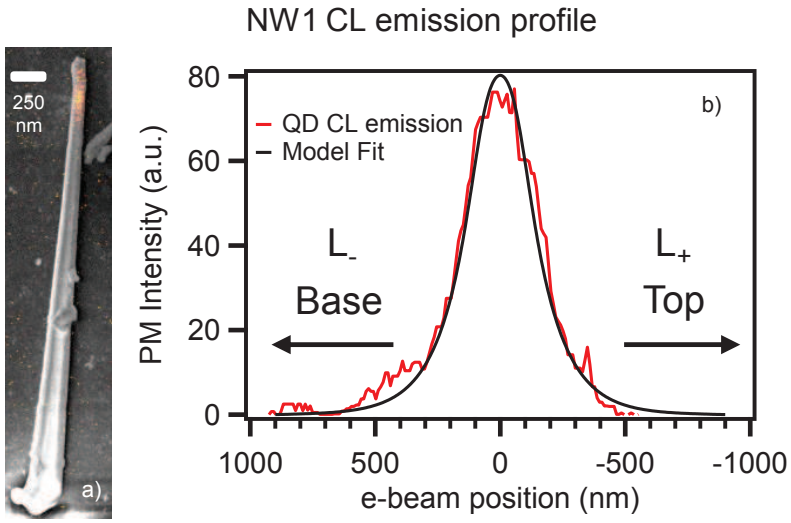

FIGURE 2.30: a) Superimposition of the monochromatic CL image recorded at the (Cd,Mn)Te emission and the HRSEM image of the nanowire b) CL profile of the (Cd,Mn)Te emission with the fit discussed above

The parameters that we have used for the fit are written in the following table:

TABLE 2.11: (Cd,Mn)Te quantum dot diffusion lengths

$L_{top} = L_{base} = 120$nm	$e-beam = 100$nm	$2x_t = 120$nm

We can notice that in this case the CL emission profile is almost symmetrical leading to the same diffusion length for the top and the base of the nanowire ($L_{top} = L_{base} =$ 120nm). The diffusion length is larger compared to RH1 ($L_{base} = 90$nm): this could be attributed to the larger diameter of NW1 (around 100nm for NW1 and 68nm for RH1) that enhances the diffusion process.
Also the trapping region x_t is much higher compared to RH1. The reason is unclear: it could reveal bigger quantum dot dimensions or trapping section for NW1 but unfortunately it was impossible to perform EDX measurements on RH1 because it has been deposited on a patterned silicon substrate.

2.3.3.2.3 NW2

We used the micro-PL set-up to spatially localized the quantum dot emission for NW2.

Figure 2.31a,b shows the superimposition of the HRSEM image of NW2 and the monochromatic photoluminescence image recorded at the quantum dot emission (see Figure 2.31a) and at the ZnTe one (see Figure 2.31b) using two different energy filters (Filter

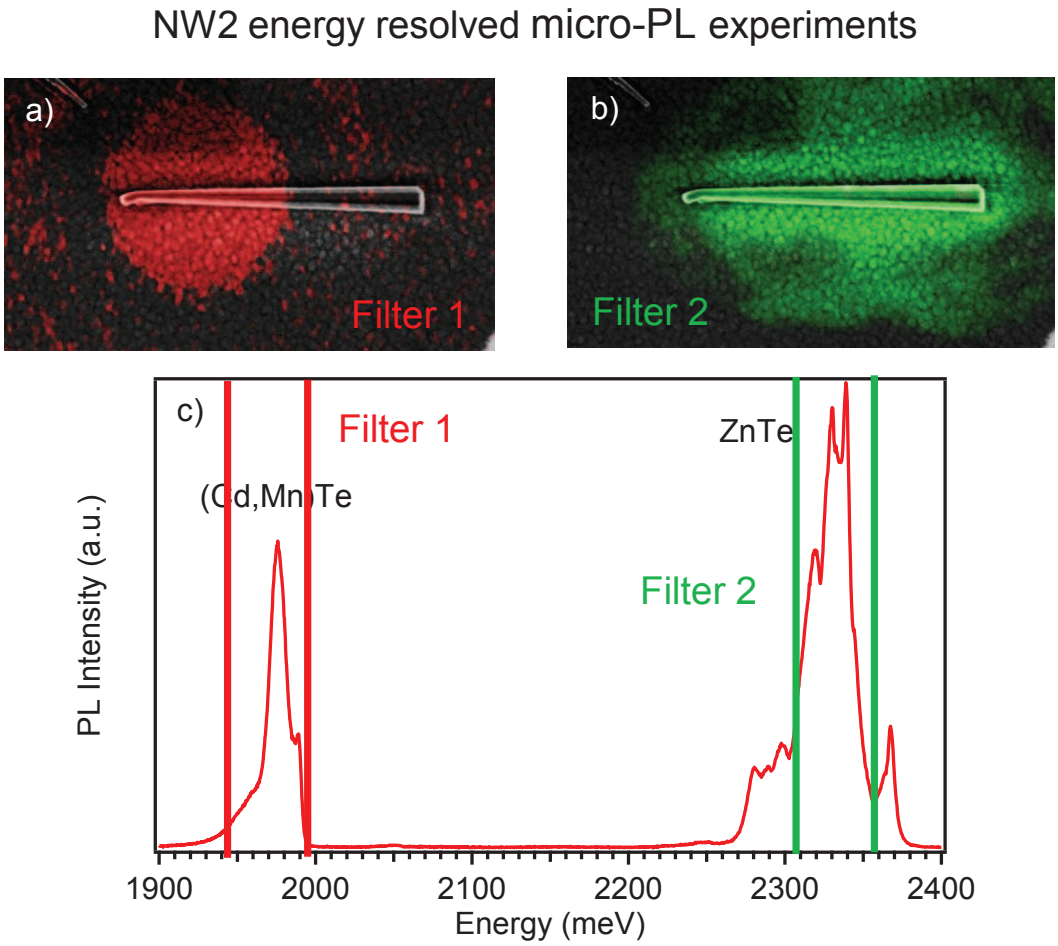

FIGURE 2.31: Superimposition of the HRSEM image of NW2 and its monochromatic photoluminescence image, recorded at a) the quantum dot emission energy using Filter 1 b) the ZnTe emission energy using Filter 2 c) PL emission spectrum of NW2 recorded at 5K

1 and Filter 2 in the Figure).

Thanks to the use of a white light lamp and a high sensitivity camera, it was possible to easily identify the NW2 position on the patterned silicon substrate and then collect high quality images of the photoemitted light.

We can see from Figure 2.31a that the quantum dot emission is spatially localized and coming from the tip of the nanowire (like for NW1). The ZnTe emission is instead coming from all the nanowire as expected (see Figure 2.31b).

Clearly by using photons (photoluminescence) instead of electrons (cathodoluminescence) we are limited in the resolution, but nevertheless, as we have shown, with a good micro-PL set-up it is possible to discriminate between a spatially and not spatially localized emission.

2.3.3.2.4 NW3

NW3 was directly measured on the as-grown sample (without the presence of a patterned surface) it was possible to identify its position thanks to the presence of a big defect nearby. Due to the fact that it is a vertical nanowire, it is not possible to use the micro-PL set-up, like for NW2, to spatially identify the emission for different energies. We performed then tilted cathodoluminescence measurements. Thanks to the proximity of NW3 to the edge of the sample, it was possible to acquire monochromatic cathodoluminescence images (see Figure 2.32) without being too much influenced by the presence of the nanowires nearby.

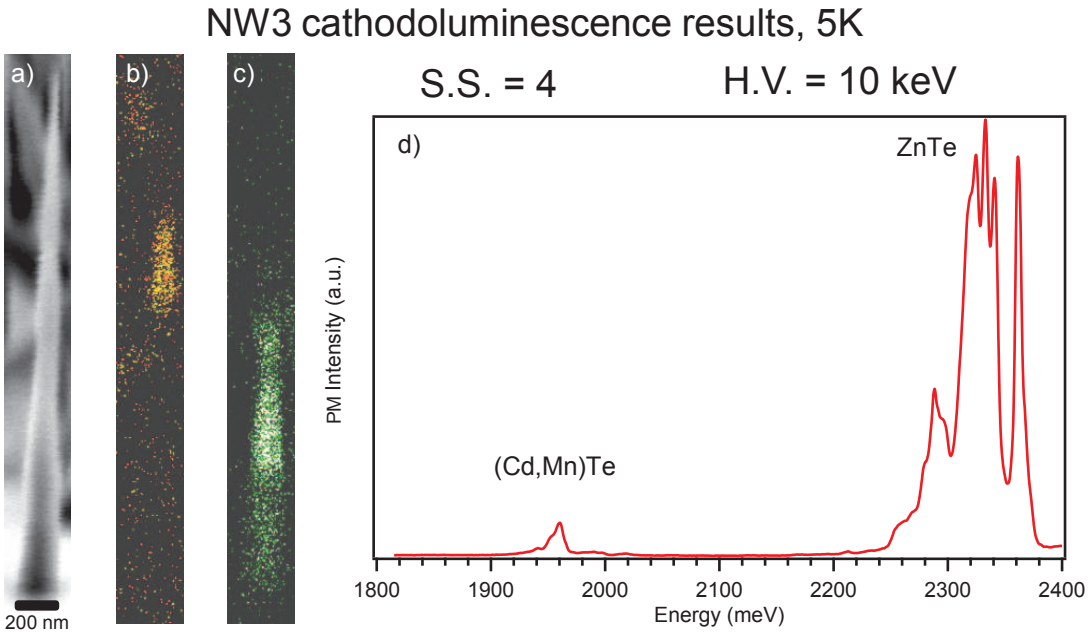

FIGURE 2.32: a) HRSEM image of NW3 b) Monochromatic CL image recorded at the quantum dot emission c) Monochromatic CL image recorded at the ZnTe emission d) NW3 cathodoluminescence spectrum recorded at 5K

We recorded different images at the quantum dot emission energy (see Figure 2.32b) and at the ZnTe one (see Figure 2.32b). Like for NW1 and NW2 we see that the quantum dot emission is spatially localized while the ZnTe one is coming from all the nanowire.

2.3.3.2.5 Fitting the CL profile

We used equation 2.36 to fit, as for RH1 and NW1, the integrated CL emission profile and the result is shown in Figure 2.33b.

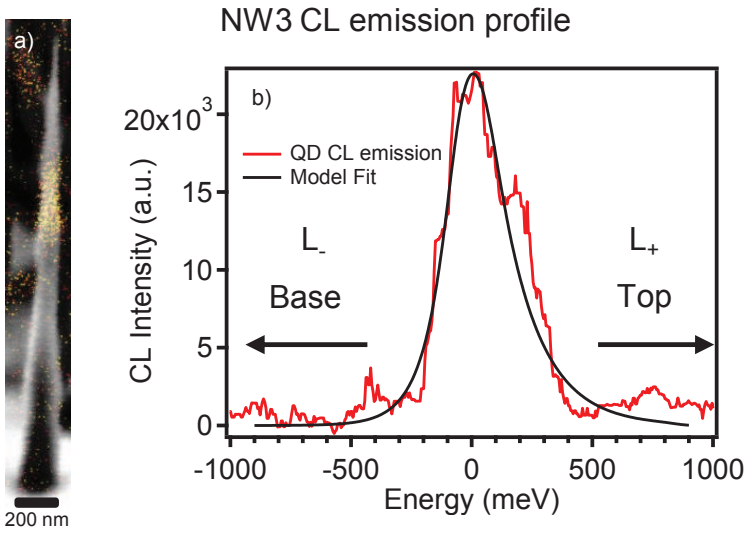

FIGURE 2.33: a) Superimposition of the HRSEM image of NW3 and the monochromatic CL image recorded at the quantum dot emission b) CL profile of the (Cd,Mn)Te emission with the model fit discussed above

The parameters that we have used for the fit are written in the following table:

TABLE 2.12: (Cd,Mn)Te quantum dot diffusion lengths

$L_{top} = 160$nm	$L_{base} = 90$nm	$e-beam = 100$nm	$2x_t = 100$nm

In this case the CL emission profile is asymmetrical with, in contrast to RH1, a bigger diffusion length for the top of the nanowire ($L_{top} = 160$nm). We can notice that the diffusion length is comparable to NW1 ($L_{top} = L_{base} = 120$nm): NW1 and NW3 have similar diameters, they are coming in fact from the same sample (Sample 1).
Also the trapping region $2x_t = 100$nm is similar compared to NW1 ($2x_t = 120$nm): this could reveal similar quantum dot dimensions.

2.3.4 Time resolved photoluminescence experiments: Type II quantum dot

In this Section we present the time resolved photoluminescence measurements. We used the set-up shown in Figure 2.34.

A Tsunami Ti:Sa pulsed laser, at 890nm doubled by a non-linear BBO crystal, is focused by a microscope and sent onto the samples that are mounted on a cold finger cryostat allowing to measure and cool down to 5K. The repetition frequency of pulses is 76MHz. The micro-PL signal is then collected by the microscope and analyzed by

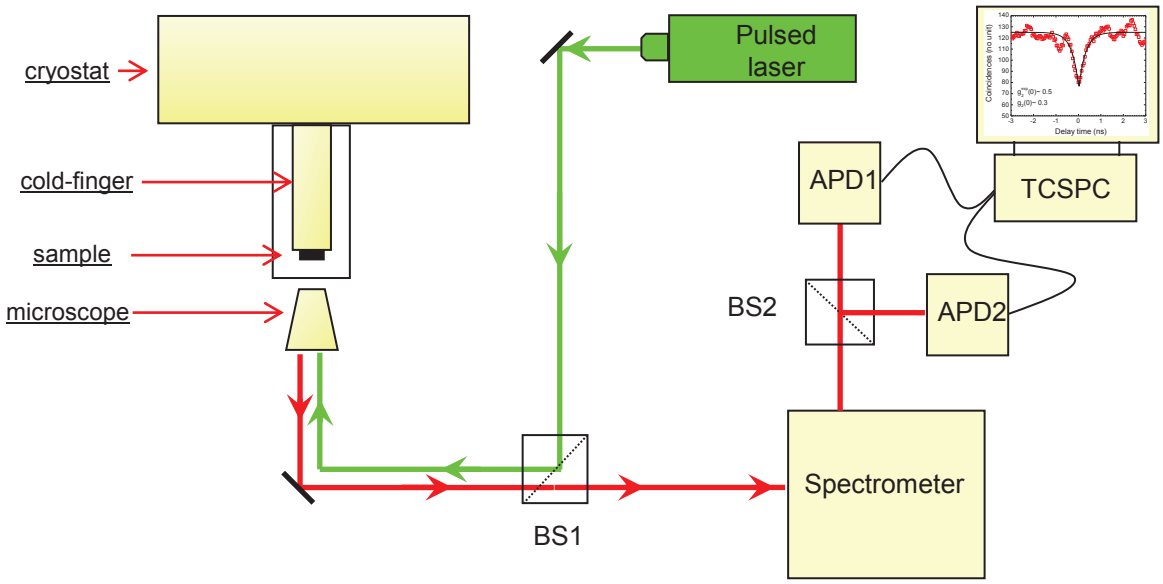

FIGURE 2.34: Micro-PL set-up used for the microphotoluminescence time resolved measurements

a spectrometer. The spectrometer is equipped with a CCD camera and two APD to be able to perform time resolved measurements. The statistics of the detection time is realized by using a counting card: a photo-diode detects the laser pulses and gives a start of counting while the stop is when the APD measures the arrival of a photon. To detect the transient of the photoluminescence emission we used a fast APD with a temporal resolution of about 50ps, smaller than the expected exciton lifetime.
With the set-up described in Figure 2.34 it is possible also to perform autocorrelation measurements. The working principle is the one of a Handbury-Brown Twiss set-up [73]: one APD triggers the chronometer to start the time counting, which is stopped by the detection of a photon by the second APD providing a coincidence. The time τ between two emitted photons is measured by an acquisition card. The number of coincidences plotted as a function of the delay time characterizes the autocorrelation curve.

2.3.4.1 Exciton lifetime and hole confinement

The photoluminescence intensity decay of RH1 is shown in Figure 2.36.

The photoluminescence intensity of the excitonic line is proportional to the population of the exciton $n_X(\tau)$. We can then fit the transient of the photoluminescence intensity (see Figure 2.36b) by a mono-exponential law with the form of: $\alpha \exp^{\frac{-t}{\tau_x}}$.

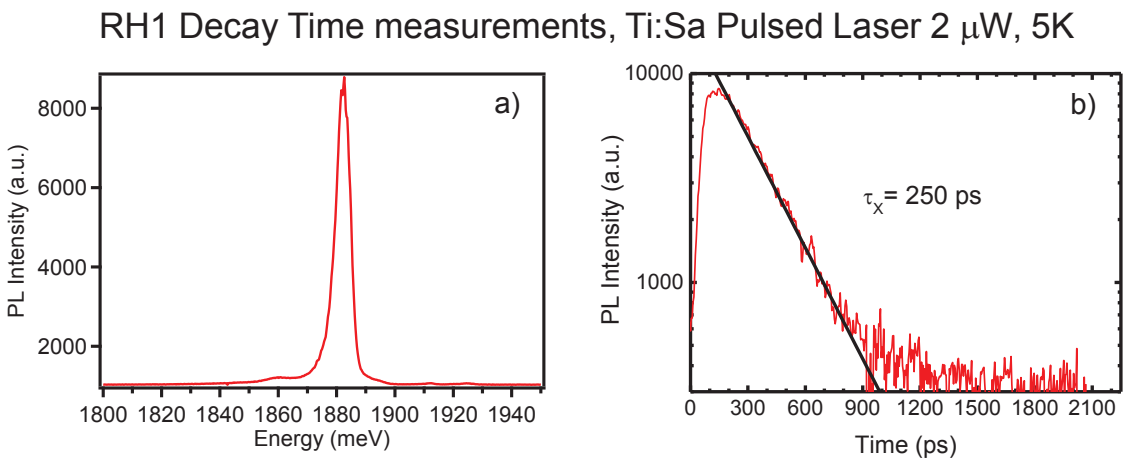

FIGURE 2.35: a) RH1 photoluminescence spectrum recorded at 5K b) Decay time measurements

The characteristic exciton lifetime in II-VI self assembled semiconductor quantum dot is between 200ps to 300ps both for CdSe/ZnSe [74, 75] and CdTe/ZnTe [76]. For RH1 the exciton lifetime is around 250ps: this value is in agreement with what has been observed and reveals a Type I quantum dot character.
Figure 2.36 shows the time resolved measurements done on NW2.

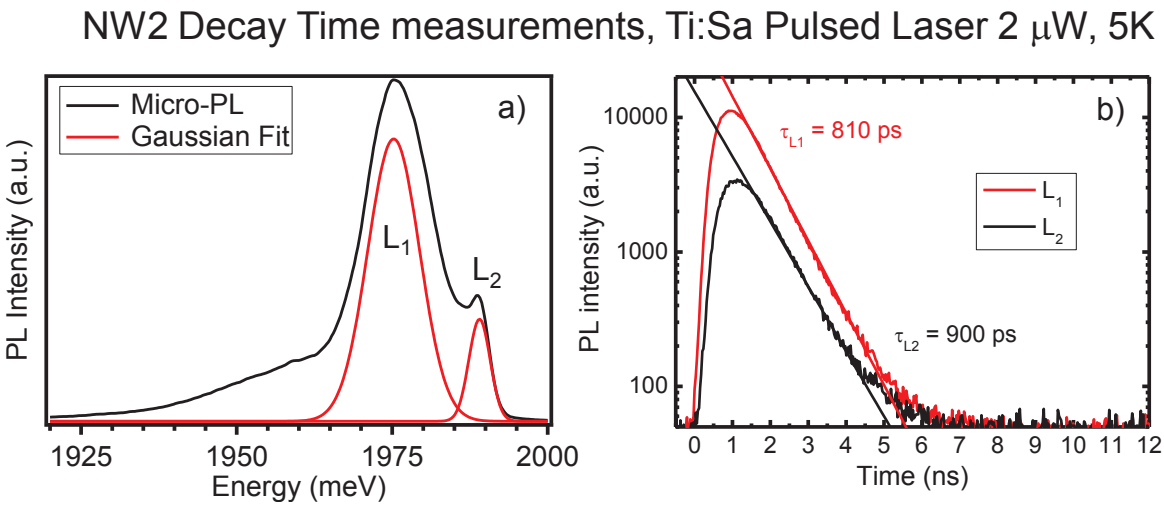

FIGURE 2.36: a) NW2 photoluminescence spectrum recorded at 5K b) Decay time measurements done on L_1 and L_2

We fit the two components with two mono-exponential laws with different decay times: for L_1 we found $\tau_{L_1} = 810$ps while for L_2 we found $\tau_{L_2} = 900$ps. This suggests that the quantum dot has a more Type II character with a partial delocalization of the hole wavefunction in the barrier due to a weaker quantum confinement. Moreover the two components L_1 and L_2 have different decay times: we observe a longer decay time for L_2. This state may not correspond to a quantum dot excited state: in fact we

saw from the power dependence studies that L_1 and L_2 have a linear dependence on the excitation power. We can then suppose that the L_2 state describes another exciton state that is more delocalized (compare to L_1) around the quantum dot.
We performed decay time measurements also directly on the as-grown sample for NW3 (see Figure 2.37).

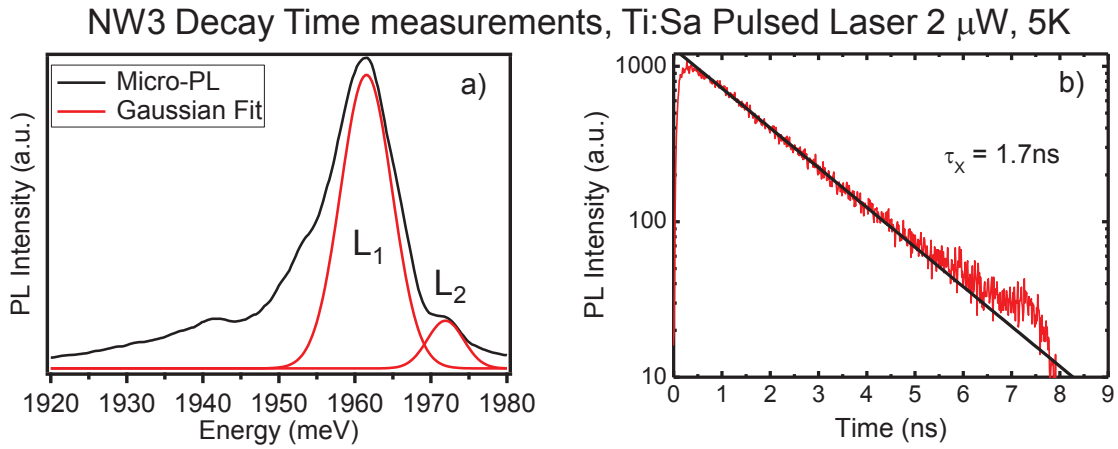

FIGURE 2.37: a) NW3 photoluminescence spectrum recorded at 5K b) Decay time measurements done on L_1

In this case we are maybe in the presence of a even more pronounced Type II quantum dot: the typical measured decay time is in fact around $\tau_X = 1.7$ns showing a weaker quantum confinement compared to NW2.
The decay time measurements give important informations on the hole confinement but it does not allow us to determine the light hole or heavy hole character of the hole involved in the recombination process. This kind of analysis will be done in the next Chapter when we will present and discuss the micro-PL experiments done under an applied magnetic field.

2.3.4.2 Single photon emission

To determine the 0D confinement of a quantum dot, time resolved correlation measurements have recently attracted a significant attention. In the case of II-VI semiconductor quantum dot inserted in nanowires, it is particularly interesting to consider the second order of the normalized intensity of the correlation function [17, 18]:

$$g^{(2)}(t,\tau) = \frac{\langle \hat{a}^\dagger(t)\hat{a}^\dagger(t+\tau)\hat{a}(t)\hat{a}^(t+\tau)\rangle}{\langle \hat{a}^\dagger(t)\hat{a}(t)\rangle \langle \hat{a}^\dagger(t+\tau)\hat{a}(t+\tau)\rangle} \tag{2.38}$$

Where $\hat{a}^{\dagger}$ and $\hat{a}$ are the photon creation and annihilation operators for the mode evaluated at time t and $t+\tau$, respectively. The correlation function $g^{(2)}(t,\tau)$ quantifies how the detection of one photon from a light source influences the probability to detect another one. It is interesting to evaluate the correlation function at $\tau = 0$. In the case of $g^{(2)}(t,0) > 1$ we have a thermal light emission while for $g^{(2)}(t,0) = 1$ we have a coherent and for $g^{(2)}(t,0) < 1$ a quantum one. Only the second order correlation function can reveal the photon anti-bunching and prove the presence of a single photon source and hence a $0D$ quantum confinement [18].
To measure the $g^{(2)}(t,\tau)$ correlation function we used the set-up [73] shown in Figure 2.34. The principle behind this technique is the following: the time counter starts when the detector $APD1$ detects a photon and it stops when the $APD2$ reveals a photon. In this way, it is possible to measure the time τ between two emitted photons by the quantum dot. By tracing the histogram of such events as a function of the time τ, it is possible to obtain the curve of the number of coincidences as a function of τ. This curve represents the probability to detect a photon at time τ knowing that a photon has been detected at time 0. We can introduce the conditional probability $P(t+\tau|t)$ to detect a photon at time $t+\tau$ after the detection of a photon at the time t. The second order correlation function is given by:

$$g^{(2)}(\tau) = \frac{P(t+\tau|t)P(t)}{P(t)^2} = \frac{P(t+\tau|t)}{P(t)} \tag{2.39}$$

Equation 2.39 tells us that by measuring a photon at the time τ, after having detected one at time 0, we measure directly the autocorrelation function of the second order.

2.3.4.2.1 RH1

In Figure 2.38b we trace the experimental second order autocorrelation function of RH1.

This curve reveals the characteristic anti-bunching effect expected for a quantum dot: this is in fact the feature that characterized a single photon source and hence 0D quantum confinement. The experimental value of the second order correlation function is $g^{(2)}_{exp}(0) = 0.5$. This has to be corrected by taking into account the temporal resolution of the APDs detectors and so the real value for the second order correlation function is $g^{(2)}_{real}(0) = 0.3$. It is not the aim of this thesis to enter too much into details

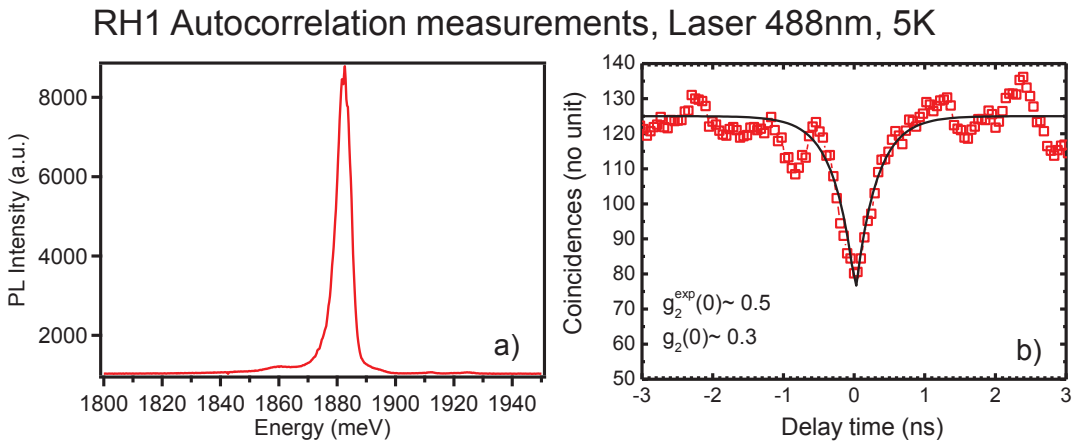

FIGURE 2.38: a) RH1 PL spectrum recorded at 5K b) Exciton autocorrelation curve

concerning the study of the quantum confinement: a complete characterization on CdTe quantum dots inserted in ZnTe nanowires can be found in [17].

2.3.4.2.2 NW2

In this Section we show the time resolved measurements performed on NW2. Using the set-up shown in Figure 2.34 we observed the second-order correlation function $g^{(2)}(0)$ under pulsed excitation and we plot it in Figure 2.39b.

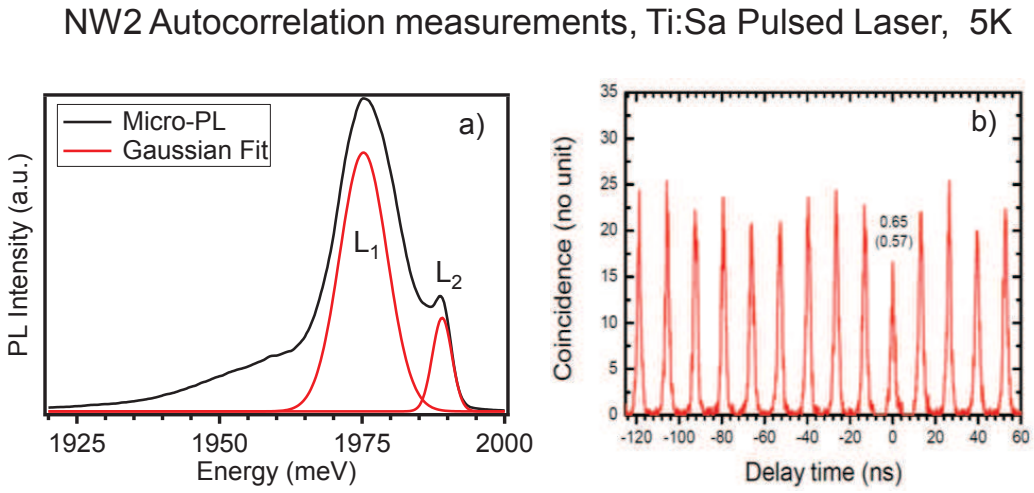

FIGURE 2.39: a) NW2 PL spectrum recorded at 5K b) Exciton antibunching curve acquired at L_1 emission energy

Figure 2.39b shows an experimental corrected correlation function $g^{(2)}(0) = 0.57$, done on the excitonic peak L_1. Unfortunately, due to presence of Mn atoms that enlarge the linewidths, it is difficult to perform time resolved measurements just on

a well isolated emitting state. Moreover we see, from Figure 2.39a, that the fine structure of NW2 is quite complicated. The spectrum in fact is composed by other components beyond the L_1 and L_2 states that could merge into the time resolved measurements, decreasing then the value of second order correlation function $g^{(2)}(0)$. To assert then without any doubts, that we are in the presence of a single photon emitting quantum dot, it will be necessary to perform further time resolved experiments.

2.3.5 Light Hole exciton identification using polarized emission diagrams

In the case of nanostructures, the directionality of the emitting light plays a key role in the realization of efficient sources. The control of this property will improve the performance of such light emitting objects such as light-emitting diodes, nanolasers or single photon emitters [77]. Moreover from the analysis of the directionality of the emitting photons, it is possible to properly understand the emitting exciton fine structure.
In this Section we present the emission resolved analysis done on NW3. These measurements were performed by Mathieu Jeannin, myself, Gilles Nogues and David Ferrand.
The technique that we have used is the Fourier microscopy: this is based on the Fourier transform properties of lenses to obtain the emission pattern of an object in the reciprocal space (see Figure 2.40).

In a conventional micro-PL set-up (see Figure 2.40), the sample is imaged by an optical microscope (focal distance f): the signal (parallel beam) is then sent, by means of optics, on an optical lens that focused it (focal distance f') on the CCD camera. In this configuration, it is the real image of the sample that is collected.
In Fourier microscopy, an extra lens (focal distance f'') is added to the conventional micro-PL set-up. The Fourier lens images the back focal plane of the microscope and sends it to the focusing lens (focal distance f') that sends the signal on the CCD camera. Each point acquired by the CCD camera correspond to all the photons emitted with a precise wave vector $\vec{k}$. In fact, a wave collected by an objective lens can be decomposed into individual plane waves, each focusing at a unique position on the back focal plane of the objective. This plane is imaged by this extra lens (Fourier lens) onto the CCD detector [77, 78]. In such a way it is possible to determine the directionality of the emitted light.

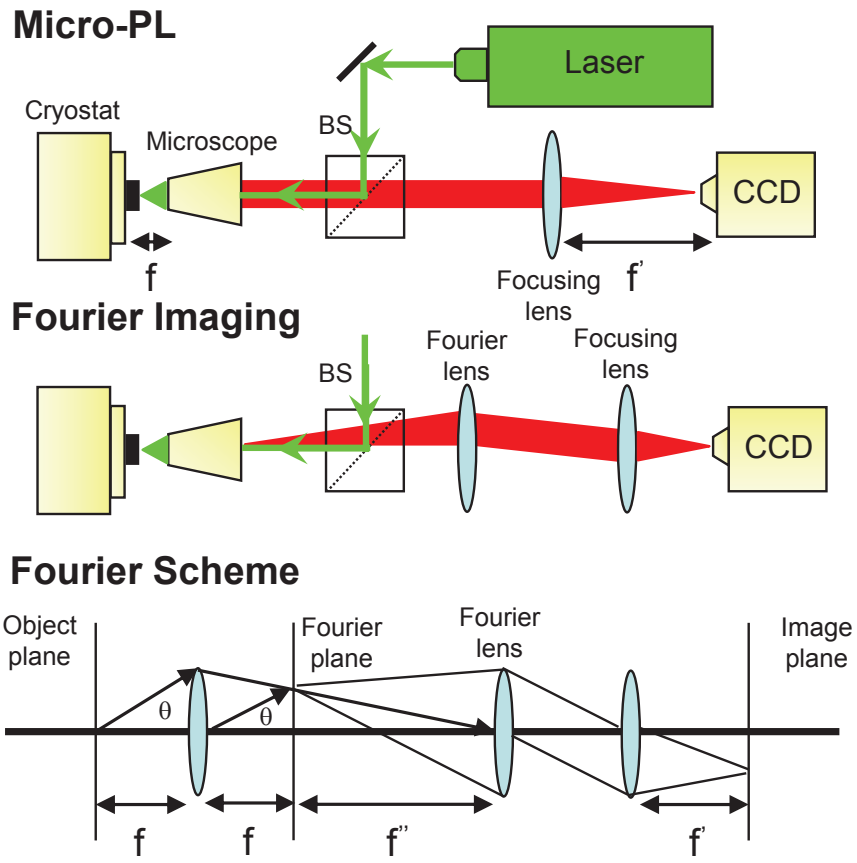

FIGURE 2.40: Fourier imaging scheme

2.3.5.0.3 Experimental determination of the hole character

The Fourier images of NW3 recorded with the ZnTe emission are shown in Figure 2.41 while the ones recorded with the (Cd,Mn)Te quantum dot emission are presented in Figure 2.42. The images are traced in polar coordinates. We have acquired also linearly polarized images in two arbitrary pairs of orthogonal directions I_0, I_{90} and I_{45}, I_{135} rotated by 45 degrees. Thanks to the different linearly polarized images we were able to calculate maps of the two Stokes parameters S_1 and S_2 [79] that are given by:

$$S_1 = \frac{I_0 - I_{90}}{I_0 + I_{90}}$$

$$S_2 = \frac{I_{45} - I_{135}}{I_{45} + I_{135}} \tag{2.40}$$

and are shown on the right side of Figures 2.41 and 2.42.

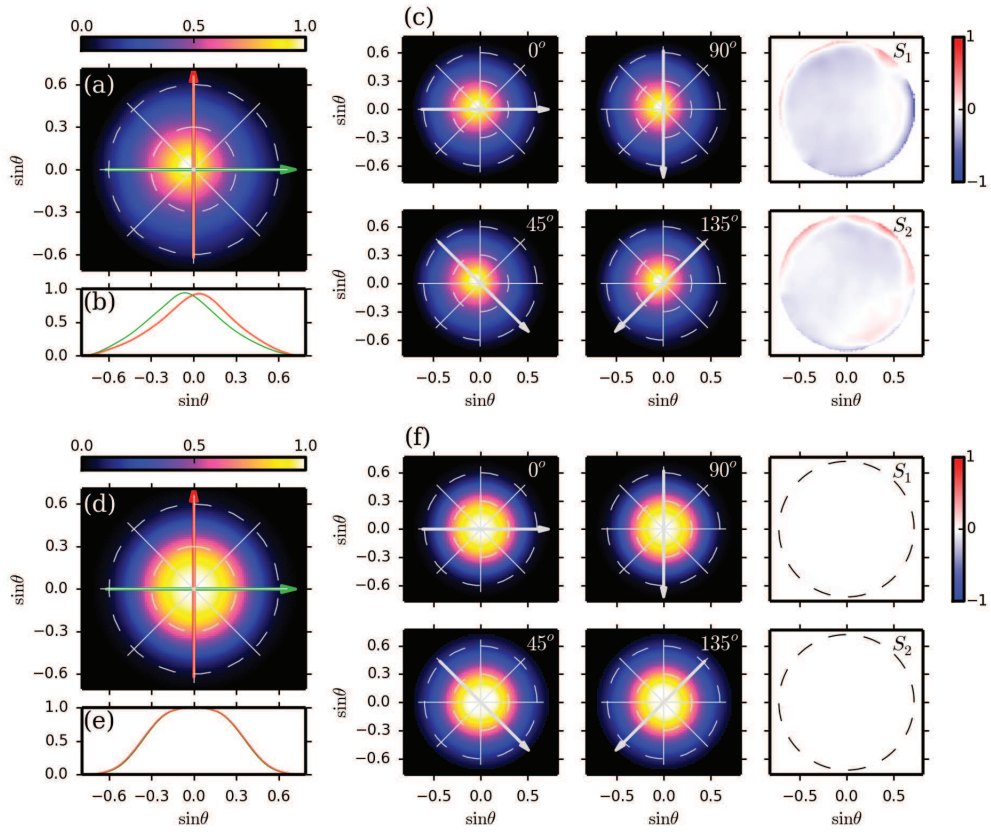

FIGURE 2.41: a) Normalized experimental Fourier plane image of the ZnTe emission line b) Orthogonal cross-sections in the Fourier plane c) Linearly polarized Fourier plane normalized intensity map of the ZnTe emission line along two sets of orthogonal axis 0°; 90° and 45°; 135° indicated by the arrow direction, and the corresponding Stokes parameters d) Normalized simulated Fourier plane image of the ZnTe emission line e) Orthogonal cross-sections in the Fourier plane f) Linearly polarized Fourier plane normalized intensity map of the ZnTe emission line along two sets of orthogonal axis 0°; 90° and 45°; 135° indicated by the arrow direction, and corresponding Stokes parameters, images realized by PhD M. Jeannin

We first consider Figure 2.41 with the Fourier analysis of the ZnTe emission. The polarization resolved Fourier images show no dependence respect to the linear detection axis, indicating that there is no preferential polarization axis orthogonal to the nanowire axis.

If we look now at the results concerning the (Cd,Mn)Te quantum dot emission (see Figure 2.42) we see that the radiation pattern shows an azimuthal modulation correlated with the analyzer orientation.

To fully understand the radiation properties of NW3, it is better to recall all the possible transitions for a (Cd,Mn)Te quantum dot as shown in Figure 2.43.

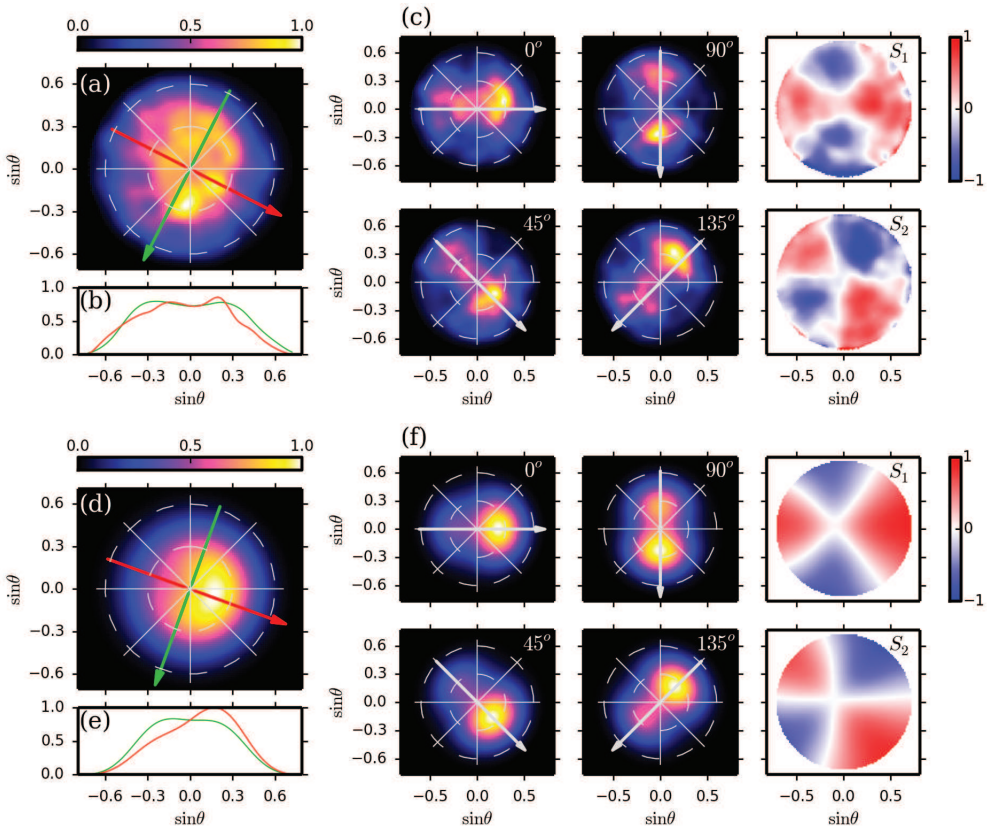

FIGURE 2.42: a) Normalized experimental Fourier plane image of the (Cd,Mn)Te emission line b) Orthogonal cross-sections in the Fourier plane c) Linearly polarized Fourier plane normalized intensity map of the (Cd,Mn)Te emission line along two sets of orthogonal axis 0°; 90° and 45°; 135° indicated by the arrow direction, and the corresponding Stokes parameters d) Normalized simulated Fourier plane image of the (Cd,Mn)Te emission line e) Orthogonal cross-sections in the Fourier plane f) Linearly polarized Fourier plane normalized intensity map of the (Cd,Mn)Te emission line along two sets of orthogonal axis 0°; 90° and 45°; 135° indicated by the arrow direction, and corresponding Stokes parameters, images realized by PhD M. Jeannin

I will explain in the following how it is possible to determine the type of the emitting state by just looking at the polarized resolved Fourier images.

The polar color maps of $I(\theta)$ shows the emitted field that has been transformed, by the optical objective, into a polarized "projected" state in the (x, y) plane (green curves in Figure 2.43c,d) that follows the electric field vector $E(\theta)$.

For a pure σ polarized emission (see Figure 2.43c), the projected state, from the top view (z axis), has a spherical precession: the σ polarized light will be then not dependent on the rotation of a polarizer. If we look at what we found for the ZnTe emission (see Figure 2.41) we understand then that we are in the presence of a σ polarized emission.

For a pure π polarized emission (Figure 2.43d), the projected state, from the top view

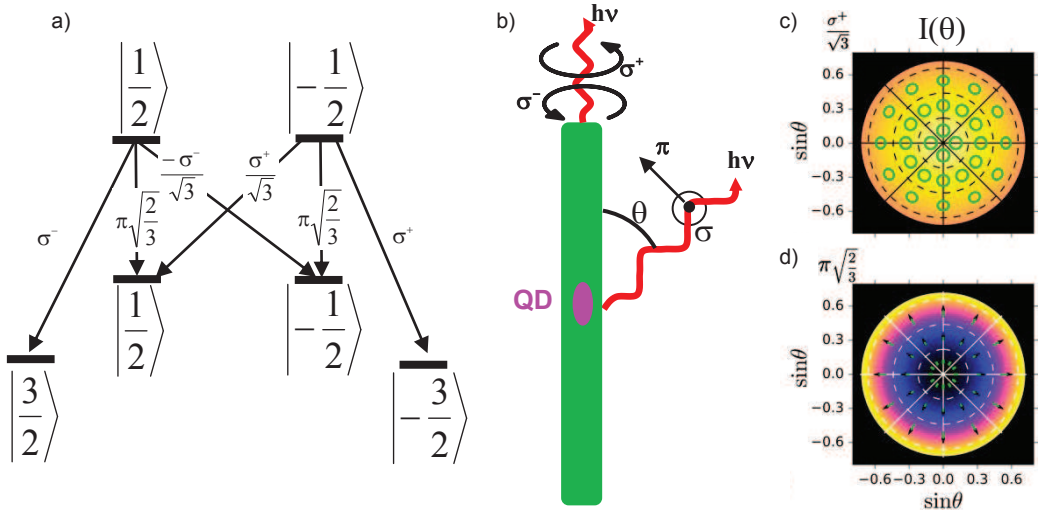

FIGURE 2.43: a) Fine structure scheme showing the optically allowed transitions b) Emission scheme of the allowed optical transitions c) Top view of the Fourier emission showing the intensity color map ($I(\theta)$) for a σ polarized emission (Courtesy of Mathieu Jeannin, Gilles Nogues) d) Top view of the Fourier emission showing the intensity color map ($I(\theta)$) for a π polarized emission (Courtesy of Mathieu Jeannin, Gilles Nogues)

(z axis), has a linear polarization: the π polarized light will be then sensitive to the rotation of a polarizer. Figure 2.42 shows then an emission that is π polarized: the Fourier emission follows in fact the rotation of the polarizer.

To model the emission diagram of NW3 we assumed a distribution of dipoles along the nanowire axis and weighted by the intensity of the corresponding cathodoluminescence intensity presented in Section 2.3.3.2.4. The full complex electric field propagated to the farfield is extracted and recreated by post-processing dipolar emission with all possible linear and circular polarizations within the experimental numerical aperture of the microscope.

The simulations results for the ZnTe emission (see Figure 2.41) confirm a pure heavy hole exciton ground state, induced by the strain that splits the valence band, as expected by the consideration on the strain in a core-shell structure (see Section 2.2.1.1.2 and 2.3.1.3).

By using the same numerical simulation procedure, it is possible to analyze the (Cd,Mn)Te radiation diagram. The quantum dot is modelled as an electric dipole and placed at the position of maximum cathodoluminescence intensity along the NW axis. All polarization states are computed, and the Fourier plane intensity and Stokes parameters maps are retrieved. Following the previous theoretical derivations, band mixing is detected through superposition of circularly polarized emission ($\sigma^{\pm}$ photons, Figure 2.43) and linearly polarized emission along the z axis (π_z photons, Figure 2.43).

Considering such a superposition of dipoles, the simulation allows to reproduce the optical measurements (Figures 2.41 and 2.42) leading to a light hole exciton ground state mixed with a heavy hole one (20% mixing).
This result is in agreement with the consideration concerning how the strain of a such core-shell structure affects the emission properties of an ellipsoidal quantum dot (see Section 2.2.1.2.2). In fact, the expected fundamental state is a light hole exciton, as found experimentally but the measured hole anisotropy $\Delta E_{LH} \cong$18meV is smaller compared to the calculated one $\Delta E_{LH} \cong$140meV.

2.4 Conclusions

This Chapter describes the knowledge acquired on different configurations, which are independent of the magnetic properties. To make it simple, three configurations have been considered: ZnTe/(Zn,Mg)Te, CdTe/ZnTe, (Cd,Mn)Te/(Zn,Mg)Te. All are either core-shell nanowires or elongated quantum dots with an aspect ratio ($\frac{L}{D}$) of the order of 2. Simple analyzes of the strain configuration due to the lattice mismatch concludes to a heavy hole character of the confined holes in ZnTe/(Zn,Mg)Te. In the three other cases the strain configuration tends to favor a light-hole character but the valence band offset is small and poorly known, so that the confinement in the dot is not guaranteed, particularly in the case of (Cd,Mn)Te/ZnTe

Complementary characterization (including multiple characterizations performed on the same nanowire) confirms some characteristic parameters and common features:

- elongated morphology of the quantum dot, diameter of the order of 8nm, presence of 10% Mn, negligible Zn concentration;
- confirmation of the origin of the luminescence ascribed by the quantum dot by two different methods:
    1. correlation data confirming the single-photon emission in the CdTe/ZnTe (less pronounced in a (Cd,Mn)Te quantum dot);
    2. transfer of the excitation to the quantum dot, with characteristic diffusion length values around 100nm

Several configurations provide clear-cut results!

- The ZnTe/(Zn,Mg)Te core-shell configuration gives rise to a heavy hole exciton, with a noticeable effect of the shell on the PL yield ($\times 10^4$) and a quantitative interpretation of the energy shift and hence light hole/heavy hole splitting;
- The (Cd,Mn)Te/ZnTe configuration in one of the nanowire (NW3) gives rise to a light hole exciton, as expected; however there is a significant light hole/heavy hole mixing, and the lifetime is long, which suggests at least a partial delocalization into the shell. This will be further studied by magneto-optical spectroscopy

Our results on the (Cd,Mn)Te/ZnTe configuration (the other two nanowires NW1 and NW2) are less conclusive at this point: here also the magneto-optical spectroscopy will bring complementary results, suggesting a mainly heavy hole character. This is the subject of the following Chapter.

Chapter 3

Hole spin anisotropy studied by magneto-optical measurements

3.1 Introduction

In this Chapter we discuss the hole spin anisotropy (heavy hole-light hole splitting noted ΔE) of (Cd,Mn)Te quantum dots inserted in ZnTe nanowires (see Figure 3.1). The growth of such a system is described in Chapter 1. A (Zn,Mg)Te shell has been added to have a good surface passivation and enhance the photoluminescence signal (see Chapter 1 and Chapter 2, [13]).

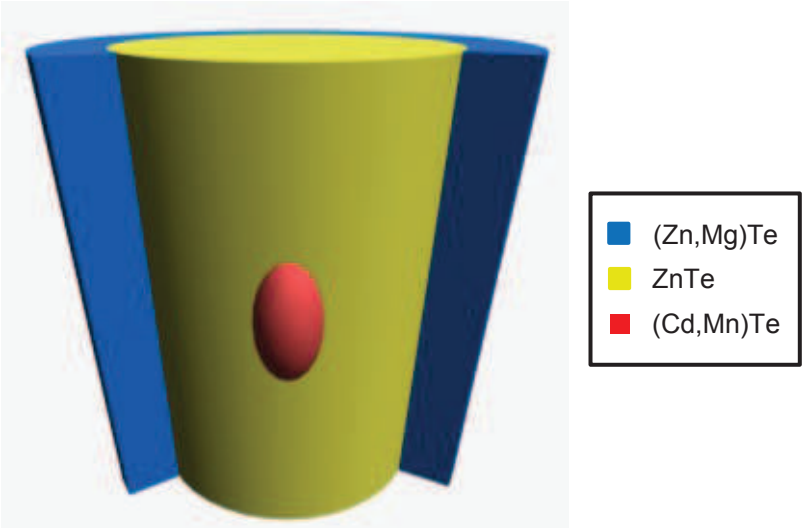

FIGURE 3.1: Scheme of the sample studied in this chapter

The magneto optical studies performed on three different nanowires (NW1, NW2 and NW3) are shown. NW1 is deposited on a Si_3N_4 membrane, NW2 is dispersed on a patterned silicon substrate and NW3 is studied directly on the as-grown sample, the three nanowires were presented in Chapter 2.
NW1 and NW2 were studied in a configuration where the magnetic field is applied perpendicular to the nanowire growth axis while for NW3 the magnetic field was applied parallel to the nanowire growth axis. All the measurements, presented in this Chapter, were done using a micro-PL set-up equipped with an helium-flow cryostat (Oxford Spectromag) described in Chapter 1.
For the three nanowires presented in this Chapter, a power dependence study has permitted to assign the nature of the emitting lines and this has been presented in Chapter 2. Moreover this power dependence study is also important to identify the heating of the Mn atoms induced by the laser: for the magneto-optical studies, in fact, the smallest excitation power was chosen to avoid this heating effect [80]. The motivations to do such detailed magneto-optical characterizations, with different applied magnetic field orientations, are to quantify the sp-d exchange coupling between carriers and Mn spins (see Chapter 1) and to study the hole anisotropy ΔE (see Chapter 2). It will be shown in fact that from the fit of the photoluminescence positions versus magnetic field it is possible to extract the magnitude of the light hole-heavy hole splitting ΔE and its sign: if the sign of ΔE is positive (negative) the ground state has a light hole (heavy hole) nature. Moreover, thanks to the EDX measurements done on the nanowire deposited on the membrane (NW1), shown in Chapter 2, we can calculate the expected value for ΔE in this sample. In the case of the (Cd,Mn)Te quantum dot, considering the geometry and the composition of the quantum dot, given in Chapter 2 by the EDX map, a light hole ground state is expected with a quite large value of ΔE around 140meV. In the last part of the Chapter we will compare the experimental ΔE value, deduced from the magneto-optical studies, with the theoretical one.
From the EDX images we have also another important information: we can evaluate the concentration of the Mn atoms inside the (Cd,Mn)Te quantum dot. Having the Mn concentration, it is possible to calculate the Mn effective concentration x_{eff} and so the real number of Mn atoms that are coupled to the exciton (see Chapter 1). x_{eff} is a very important quantity: it constraints the amplitude of the Zeeman shift at saturation (defined by E_{se} and E_{sh}, see Chapter 1) and we will consider it when discussing the magneto-optical studies in the Experimental Section 3.3.2 of this Chapter.

In Section 3.2 all the magneto-optical experimental results on NW1,NW2 and NW3

are presented: for the three nanowires, the excitonic Giant Zeeman effect is shown for different temperatures.

In Section 3.3 a theoretical model that takes into account the hole anisotropy ΔE is explained and used to fit the experimental data. The importance of such detailed magneto-optical studies will be clear: it is possible to determine the value of the magnetic anisotropy ΔE of the (Cd,Mn)Te quantum dot and reveal the nature of the emission (if it has a light hole or heavy hole character depending on the sign of ΔE).

3.2 Experimental results

In this Section we present all the magneto-optical studies done on NW1, NW2 and NW3. From the power dependent photoluminescence studies, we ascribe the emission line L_1 (the more intense emission at low excitation power) to the exciton state X and in all the analysis we focus our attention just on this state. For the excited states, we call them from L_2 up to L_5: without complementary studies we can't determine the nature of these emissions so for example, two components L_2 present in two different nanowires can be related to different exciton excited state.

3.2.1 Magnetic field applied perpendicular to the nanowire growth axis

In this Section we show the results obtained on NW1 and NW2.
As mentioned in Chapter 1, the exchange interaction between Mn spins and the kinetic moments of the electron-hole pair reveals itself in the photoluminescence spectra through the Excitonic Giant Zeeman effect which is a unique feature of diluted magnetic semiconductors (DMS). The objective of this Section is to characterize the exchange interaction between the exciton and the Mn spins by performing micro photoluminescence experiments under magnetic field and at different temperatures.
NW1 and NW2 were presented in Chapter 2: NW1 is the nanowire that has been deposited on Si_3N_4 membrane while NW2 has been deposited on patterned silicon substrate. The spectra have been recorded in a Faraday configuration: the excitation and the detection are parallel to the magnetic field, which is applied perpendicular to the NW's growth axis.
The emission spectra of the two nanowires present different emission lines: the identification of these emission lines was done in Chapter 2 but it will be shortly reminded in the different Sections when the different magneto optical studies are discussed.

3.2.1.1 NW1

NW1 (see Figure 3.2) is a nanowire deposited onto a Si_3N_4 membrane that allowed us to perform different characterization techniques such as: EDX chemical analysis (see

Chapter 2), cathodoluminescence experiment (see Chapter 2) and magneto-optical measurements (this Chapter). Figure 3.3 shows the photoluminescence spectra evolution with an applied magnetic field from 0T up to 11T with a step of 0.5T. The spectra are dominated by a doublet composed by two lines called L_1 and L_2.

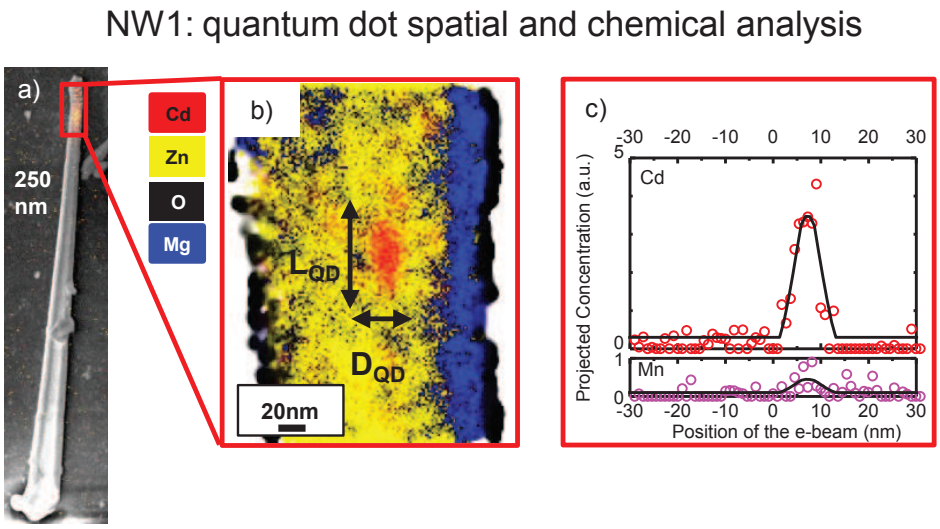

FIGURE 3.2: a) Superimposition of the (Cd,Mn)Te signal and the HRSEM image of NW1 b) EDX map of the (Cd,Mn)Te region c) EDX composition profiles for the Cd and Mn elements

The two components L_1 and L_2 were identified in Chapter 2 by a detailed power dependence study. We attribute L_1 to the excitonic state (its intensity is linearly dependent on the laser power), with just an electron-hole pair inside the quantum dot, while L_2 could be related to a charged excitonic state, with an electron-hole pair inside the quantum dot and a charge particle (its dependence on the laser power is slightly superlinear $\propto P^{1.35}$).

From Figure 3.3a, it is clear that the emission energy of the exciton L_1 and charged exciton L_2 are decreasing with the increase of the magnetic field. This red shift under magnetic field is the fingerprint of the so called Giant Zeeman Effect. Both lines L_1 and L_2 are reaching a saturation value of about 24meV at 11T. For the complete overview of the Mn coupling with the excitonic state, more studies were done under magnetic field and at different temperature: 6K, 13K, 24K, 34K (see Figure 3.3). When the temperature is increased (see Figure 3.3b,c,d) the Giant Zeeman shift decreases for both states L_1 and L_2: the amplitude of the Zeeman shift goes from 24meV at 6K to almost 10meV at 34K. With the increase of the temperature, the magnetic moment of the Mn atoms, under magnetic field, is reduced leading to a smaller amplitude of the Zeeman shift.

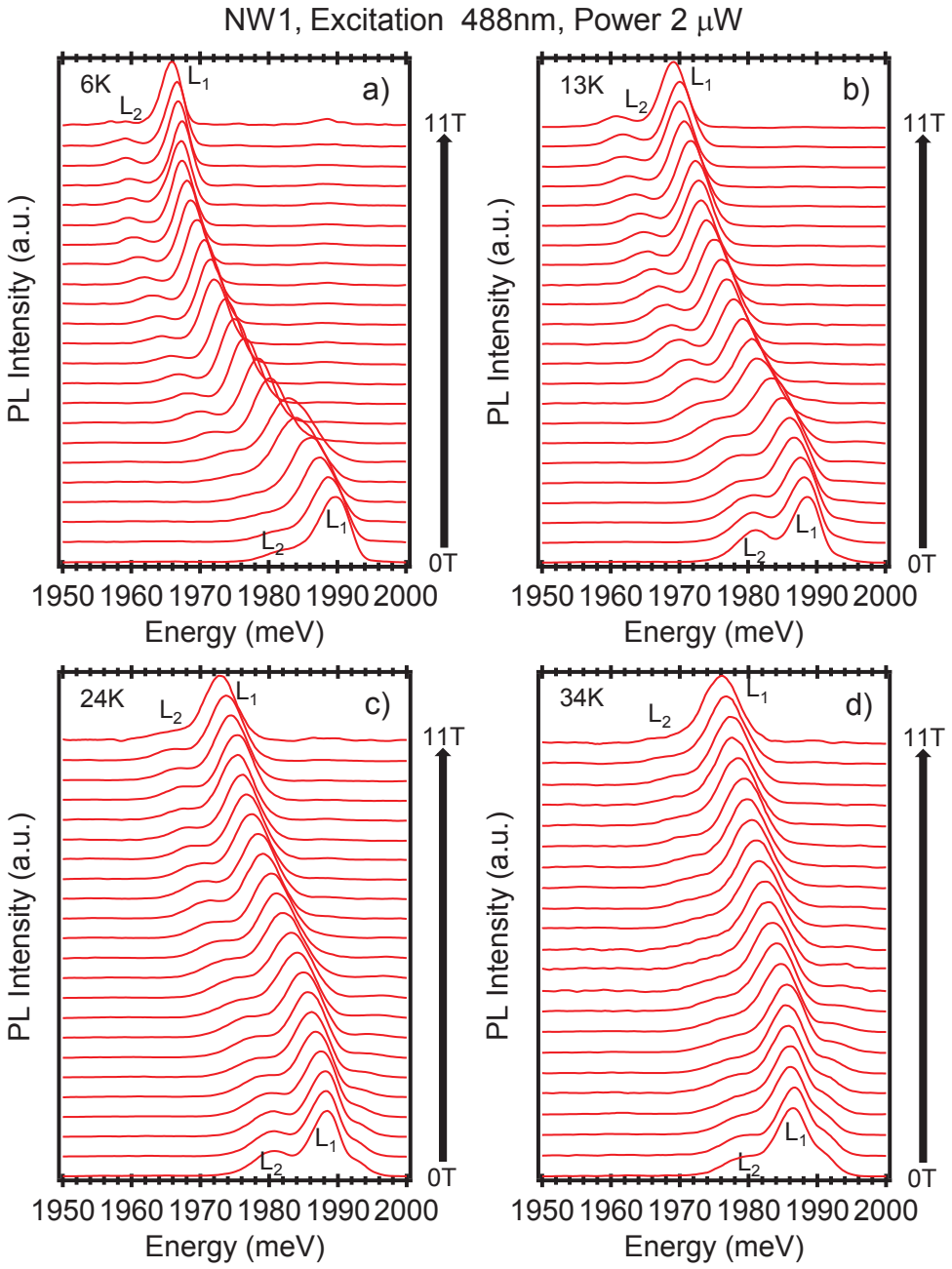

FIGURE 3.3: (Cd,Mn)Te QD emission studied under magnetic field, with a minimum step of 0.5T, at a) 6K b) 13K c) 24K d) 34K

These results are more clearly shown in Figure 3.4b,c: to trace the emission energies and the Full Width at Half Maximum (FWHM), we used a fit (see Figure 3.4a) with two Gaussians functions related to L_1 and L_2 respectively. At higher temperature: 24K and 34K (see Figure 3.4a) a third line, identified by another Gaussian function, appears: this line is attributed to an excited state called L_3. The nature of this transition will be clarified in Section 3.3.

The Zeeman shift extracted from the micro-PL studies for L_1 and L_2 versus magnetic

field at different temperatures, were also plotted versus $\frac{5\mu_B B}{k_B T_{Mn}}$ which proves to be the relevant parameter as shown in Figure 3.4d,e. The Mn temperature, used to plot the data, is shown in brackets, and this temperature is different from the cryostat one because it takes into account also the phenomenological temperature T_{AF}, a temperature gradient in the sample chamber and possible heating of Mn spins by the laser excitation (see Chapter 1).

It is clear from the dependence of the data on $\frac{B}{T_{Mn}}$, that all shifts are superimposed, and this can be attributed to a magnetic effect related to the presence of Mn atoms inside the (Cd,Mn)Te quantum dot and its coupling with photocreated carriers.

Data in Figure 3.4d,e have been fitted with a Brillouin function (see Chapter 1) with a saturation value of 32meV. The agreement is pretty good at high magnetic field while at low magnetic field there is a clear discrepancy: in this region the red shift is much smaller than expected. This behavior will be carefully analyzed in Section 3.3.

Finally in Figure 3.4f the L_1 and L_3 shifts as a function of $\frac{5\mu_B B}{k_B T_{Mn}}$ are traced. The excited state L_3 shows a good superimposition for the analyzed two temperatures, and a Zeeman shift related to $\frac{B}{T_{Mn}}$, but unlike L_1 and L_2, the line reveals a blueshift by increasing the magnetic field.

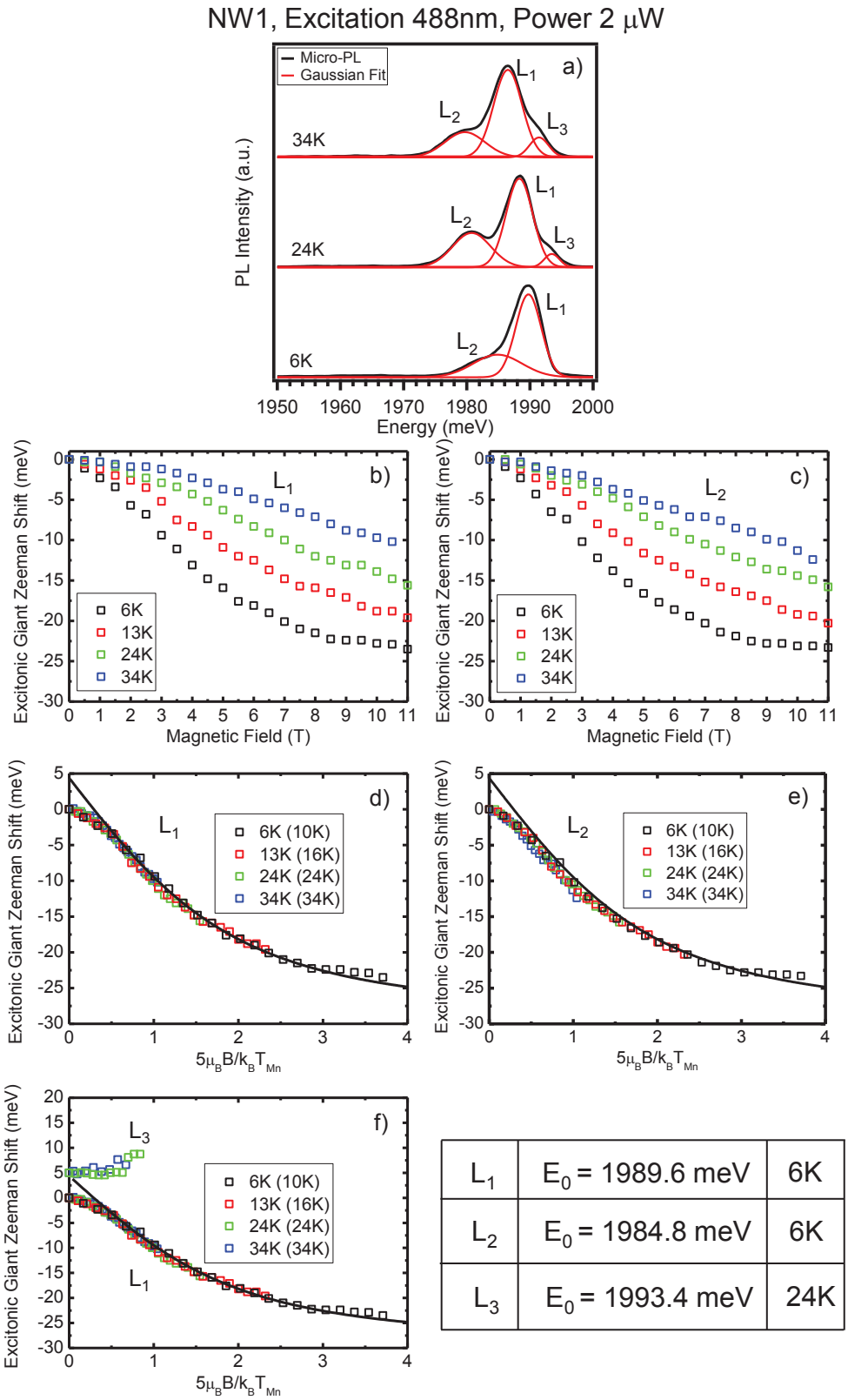

L_1	E_0 = 1989.6 meV	6K
L_2	E_0 = 1984.8 meV	6K
L_3	E_0 = 1993.4 meV	24K

FIGURE 3.4: a) Gaussian fit of the spectra at 6K, 24K and 34K with no magnetic field b) L_1 emission energy positions vs magnetic field for different temperatures c) L_2 emission energy positions vs magnetic field for different temperatures d) L_1 emission energy positions vs $\frac{5\mu_B B}{k_B T_{Mn}}$ for different temperatures e) L_2 emission energy positions vs $\frac{5\mu_B B}{k_B T_{Mn}}$ for different temperatures f) L_1 and L_3 emission energy positions vs $\frac{5\mu_B B}{k_B T_{Mn}}$ for different temperatures

Another powerful tool to check the incorporation of Mn atoms inside the quantum dot is the linewidth. If we look at the Full Width at Half Maximum (FWHM, see Figure 3.5), we can observe a typical linewidth of 6meV: this value is larger than the value of non magnetic quantum dot that is around 3meV (see Chapter 2). This extra broadening is due to Mn spin fluctuations [72] and is usually suppressed by applying a magnetic field.

In the present case, a line broadening for low magnetic field up to 2T is visible, while at higher field the linewidth decreases with magnetic field [12, 17] following a monotonous law: magnetic fluctuations are in fact suppressed by the alignment of Mn spins along the field direction. The non-monotonous trend at low magnetic field, see Figure 3.5b, is something uncommon in DMS systems: this behavior will be explained in Section 3.3.

As shown in Figure 3.5c, the data have been also plotted versus $\frac{5\mu_B B}{k_B T_{Mn}}$ and again they are showing a very good superimposition revealing a clear dependence on $\frac{B}{T_{Mn}}$.

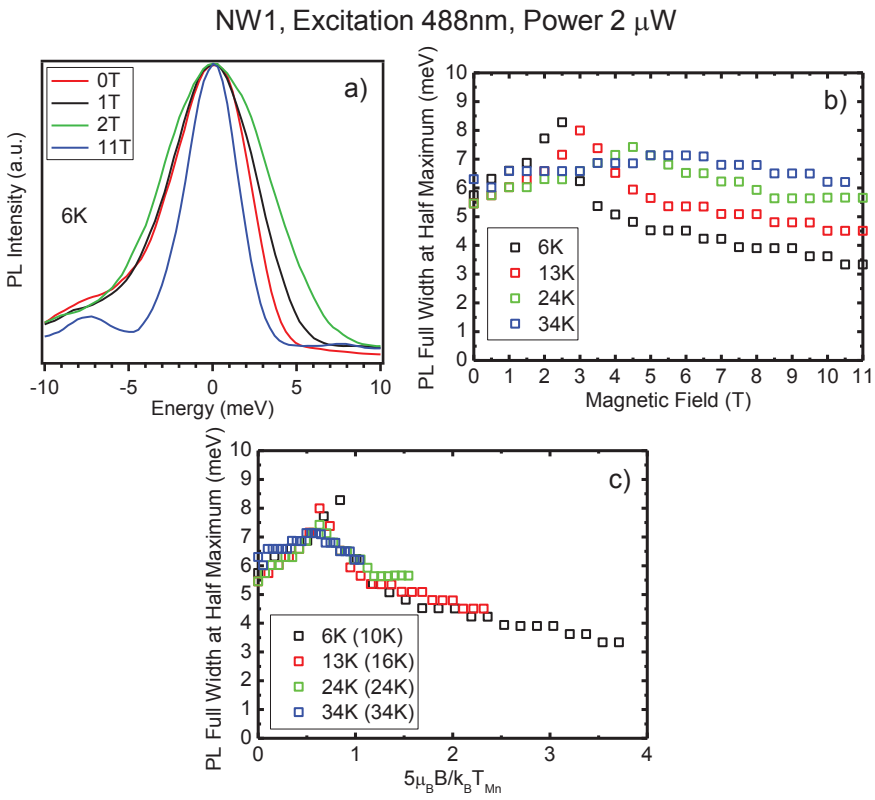

FIGURE 3.5: a) (Cd,Mn)Te Full Width at Half Maximum studied under magnetic field at 6K b) L_1 FWHM for the different magnetic field and temperatures c) L_1 FWHM plotted as function of $\frac{5\mu_B B}{k_B T_{Mn}}$

3.2.1.2 NW2

NW2 was mechanically deposited on a patterned silicon substrate to easily retrieve the position of the nanowire (see Chapter 2). For this nanowire different measurements, under magnetic field, were taken at 2K (see Figure 3.6a) in order to be able to saturate the Giant Zeeman effect. Usually the lowest temperature used for the magneto-optical studies is 6K but for some nanowires (NW2 and NW3) we succeed to perform measurements at 2K. Helium is directly inserted in the cryostat, in order to put the sample in contact with the liquid helium, and then pumped to reach the superfluid state, as required for the optical spectroscopy (no bubbles). This technique is really powerful: it allows to be sure about the sample's temperature (about 2K) thanks to the full immersion of the sample in superfluid helium.
From Figure 3.6a, it is clear that the spectra are dominated by a doublet (at 0T magnetic field): it is possible to identify a main emission component L_1 and an excited one called L_2 at higher energy. The complete identification of the emission lines, done by power dependence studies, was presented in Chapter 2: the main emission component L_1 is attributed to the excitonic state (it is the more intense line at low excitation power). The L_2 state is a state that has not been observed in NW1 and considering the power dependence studies and the magneto-optical one, it could be attributed to another excitonic state coupled with the Mn atoms.
Also for this nanowire, the emission energy of L_1 is decreasing with the increasing of the magnetic field as a result of the alignment of the Mn spins along the magnetic field. The value of the Zeeman shift at 11T, taken at 2K, is around 20meV and it has the same order of magnitude as the one of NW1 (24meV at 6K). When the temperature is increased (see Figure 3.6b,c,d) the amplitude of the Giant Zeeman Shift decreases for both states L_1 and L_2. Moreover, at high magnetic field, a line at lower emission energy L_4 appears starting from the tail of the main line L_1: a state, close to the excitonic one, that becomes more and more populated with the increase of the magnetic field.
It is clear that the fine structure of NW2 is more complicated compared to NW1, with the presence of more emitting states, but a common feature is that both nanowires present a Giant Zeeman effect of the excitonic lines which have similar saturation values.

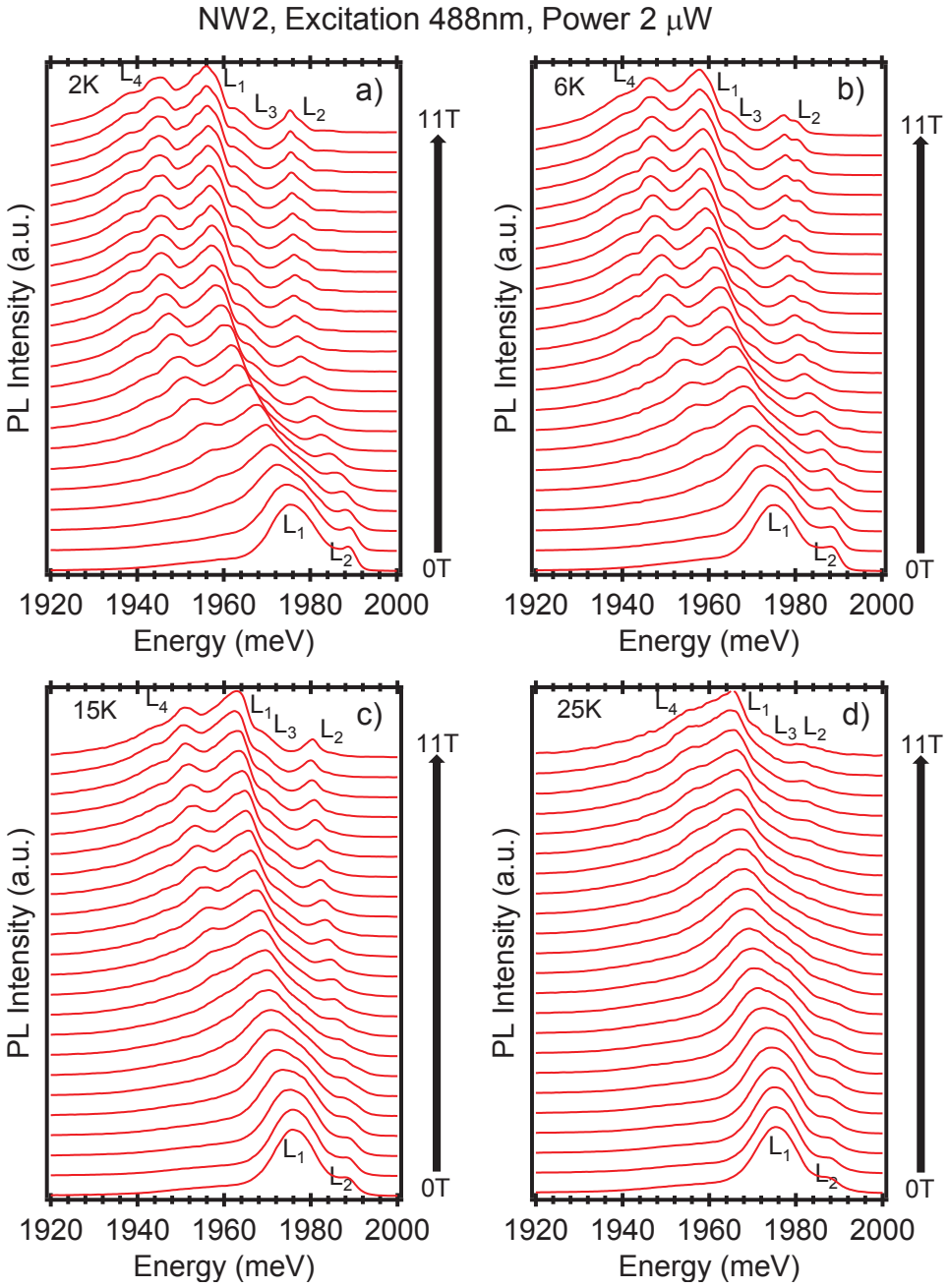

FIGURE 3.6: (Cd,Mn)Te QD emission studied under magnetic field, with a minimum step of 0.5T, at a) 2K b) 6K c) 15K d) 25K

All the results are summarized in Figure 3.7b,c. The energy position of the line L_1 and L_2 were extracted using the fit shown in Figure 3.7a: as for NW1 the emitting components of the spectrum have been fitted using Gaussian functions.
To check that the observed red shift is related to the incorporation of Mn atoms inside the (Cd,Mn)Te quantum dot, data have been traced as function of $\frac{5\mu_B B}{k_B T_{Mn}}$ like for NW1 (see Figure 3.7d,e). Data are perfectly superimposed also for this nanowire, with a clear dependence on $\frac{B}{T_{Mn}}$ (the actual Mn atoms temperatures are given in brackets). The fit used in Figure 3.7d,e is a Brillouin function, with a saturation value of 24.3meV, and the same behavior observed for NW1 is again highlighted with a smaller saturation value (for NW1 it was around 32meV). As for NW1 the fit of the magneto-optical measurements with a Brillouin function is good for high magnetic field values, while at low magnetic field there is a deviation: also in this case the Zeeman shift is smaller than expected. This feature, like for NW1, will be explained in Section 3.3.
Due to the more complicated nature of the emission, composed by more emitting states compared to NW1, it has been chosen to not consider the analysis of the Full Width at Half Maximum under magnetic field for this nanowire. The presence of many lines, nearby the exciton state, introduces big errors in the evaluation of the L_1 FWHM.

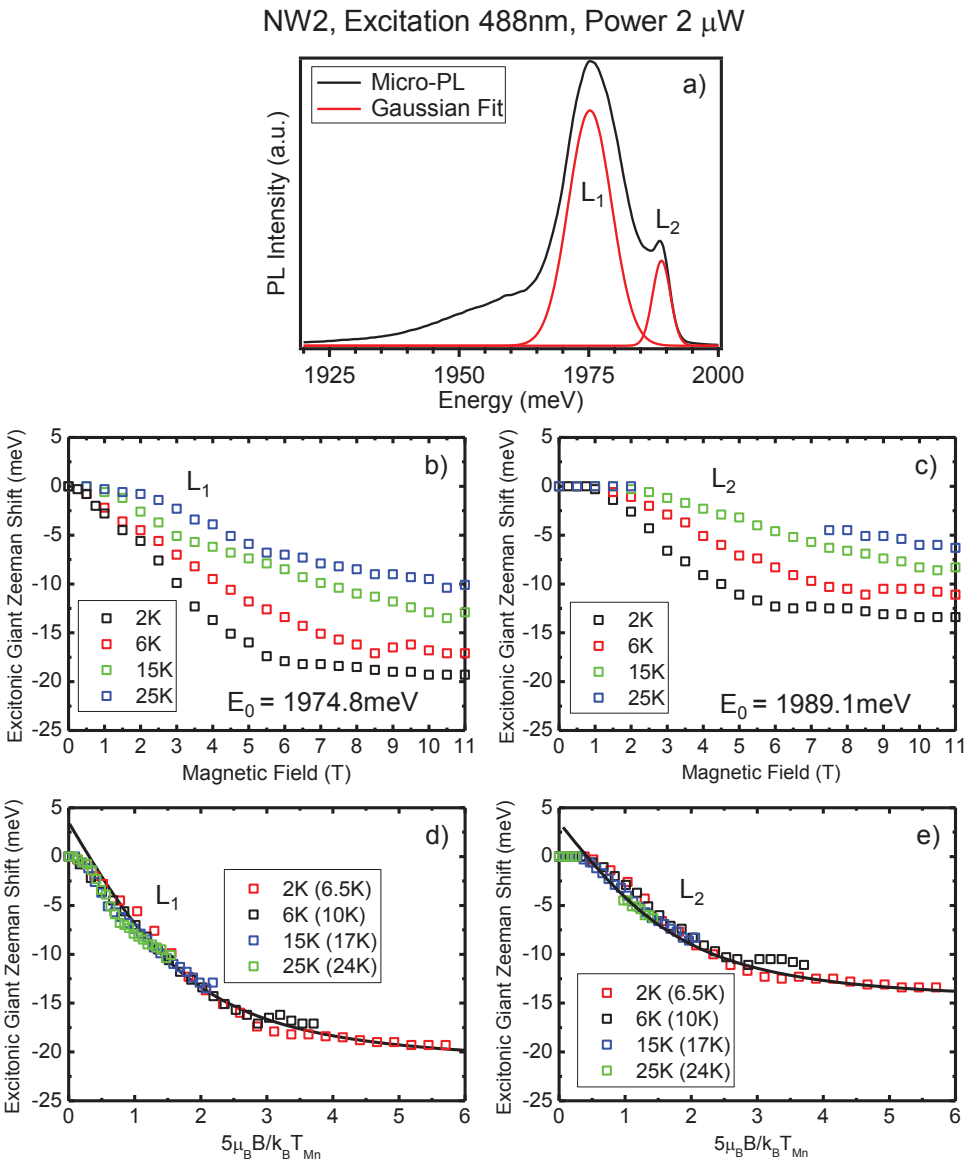

FIGURE 3.7: a) Gaussian fit of the spectrum at 2K with no magnetic field b) L_1 emission energy positions vs magnetic field for different temperatures c) L_2 emission energy positions vs magnetic field for different temperatures d) L_1 emission energy positions vs $\frac{5\mu_B B}{k_B T_{Mn}}$ for different temperatures e) L_2 emission energy positions vs $\frac{5\mu_B B}{k_B T_{Mn}}$ for different temperatures

3.2.2 Magnetic field applied parallel to the nanowire growth axis

NW3 was measured in a different configuration: in this case the magnetic field is applied along the nanowire growth axis, this nanowire was directly measured on the as-grown sample after an identification done by a HRSEM microscope (NW3 is described and shown in Chapter 2).
From Figure 3.8 it is clear that the spectra are dominated by a main line L_1 and an excited state L_2. In Chapter 2 the main line L_1 was attributed to the excitonic state, while the excited state L_2 will be discussed later on.
The magneto-optical studies at 2K are presented in Figure 3.8 where we observe clearly an excitonic Giant Zeeman effect. The emission energy L_1 is red shifting with the increase of the magnetic field at a given temperature and the amplitude of the Zeeman shift becomes smaller with the increase of the temperature. The maximum Zeeman shift is recorded at 2K and is equal to 25meV: again this value is comparable to what has been found for NW1 and NW2. With the increase of the temperature, the Zeeman shift becomes smaller with a minimum value at 26K equal to 14meV. At high magnetic field, like for NW2, a low energy state, that becomes more and more populated, is present and called L_3.
Unlike NW1 and NW2, the excited state L_2 (see Figure 3.9a) is gaining intensity with the increase of the magnetic field. It dominates completely the spectrum at 11T for all temperatures. This is an unusual behaviour for an excited state while the fundamental state L_1 doesn't change so much under magnetic field.
The assignment of this component at low magnetic field values is difficult: it is not clear if it is the state identified by the shoulder observed at higher energy or if it is a component hidden in the main peak L_1 that is characterized by a different evolution under magnetic field. It has been chosen then to characterize more carefully the nature of these emission lines by performing a set of detailed polarization resolved measurements, that will be shown in the next Section.

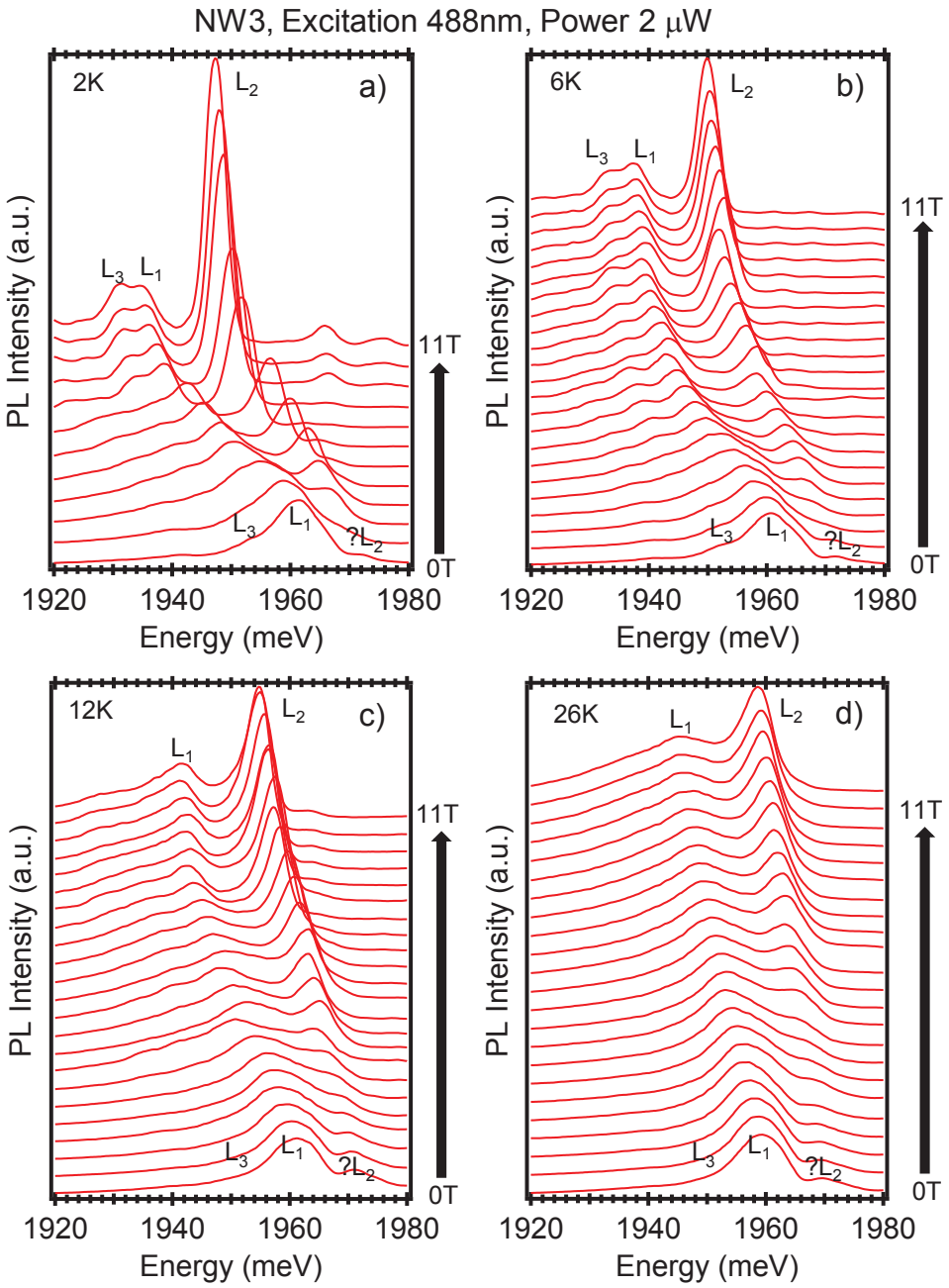

FIGURE 3.8: a) (Cd,Mn)Te QD emission studied under magnetic field, with a minimum step of 1T, at 2K b) (Cd,Mn)Te QD emission studied under magnetic field, with a minimum step of 0.5T, at 6K c) 12K d) 26K

The positions of the lines as function of the magnetic field for the different temperatures are summarized in Figure 3.9b,c. Also for NW3, a Gaussian fit has been chosen to extract the energy positions of the lines: it is shown in Figure 3.9a. As done for NW1 and NW2, data have been traced as function of $\frac{5\mu_B B}{k_B T_{Mn}}$ (see Figure 3.9d,e) with the Mn spins temperatures shown in brackets: it is clear that the good superimposition of the data reveals a dependency on $\frac{B}{T_{Mn}}$ as expected for the Giant Zeeman effect. Moreover for NW3, the data versus $\frac{5\mu_B B}{k_B T_{Mn}}$ could be fitted reasonably by a Brillouin function not only at high field (with a saturation value of 27.5meV of the same order as for NW1 and NW2) but also at low field (contrary to NW1 and NW2). The behaviour of L_2 is more complex. It will be clear, in Section 3.3, why we have different behaviours for nanowires belonging to the same sample: it is in fact related to the orientation of the applied magnetic field which is, in the case of NW3, along the nanowire growth axis while for the others nanowires it is perpendicular to the nanowire axis.
Before that, we present the complementary studies done on the polarization of the emission of NW3.

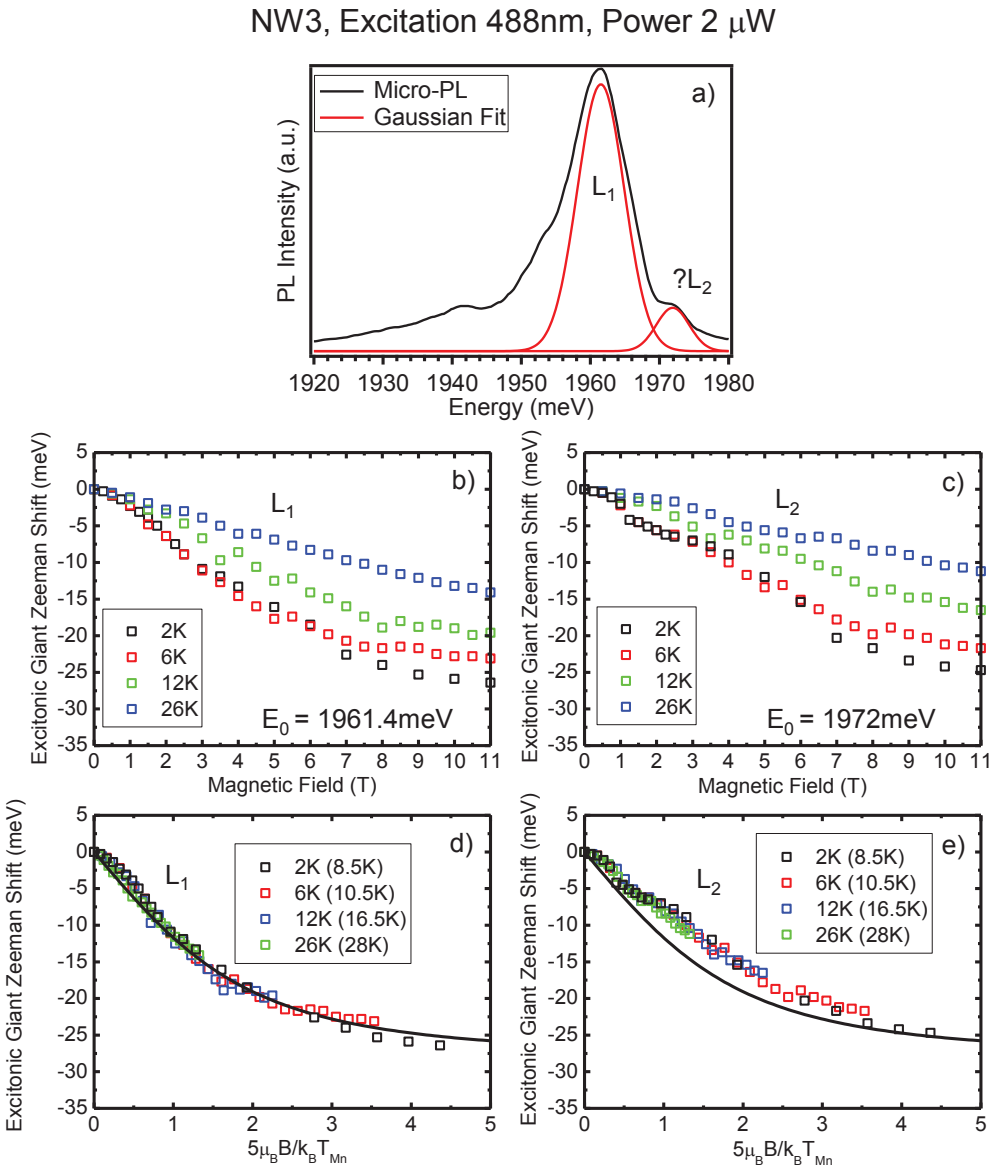

FIGURE 3.9: a) Gaussian fit of the spectrum at 2K with no magnetic field b) L_1 emission energy positions vs magnetic field for different temperatures c) L_2 emission energy positions vs magnetic field for different temperatures d) L_1 emission energy positions vs $\frac{5\mu_B B}{k_B T_{Mn}}$ for different temperatures e) L_2 emission energy positions vs $\frac{5\mu_B B}{k_B T_{Mn}}$ for different temperatures

3.2.2.1 Polarization under Magnetic field

To properly understand the increase of the intensity of the high energy line L_2 (see Figure 3.8), magneto-optical studies were done by recording the two different polarizations: σ^+ and σ^- under magnetic field. The spectra at 6K, from 0T to 11T, are shown in Figure 3.10. At 0T, the emission is not polarized (the residual polarization is due to experimental errors): by increasing the magnetic field (from 6T), L_2 line gains a large polarization rate and dominates the spectrum at 11T. It is possible to trace the Stokes parameter S_3 (the Stokes parameters are a set of values that describe the polarization state of electromagnetic radiation [79]) and check the polarization rate for line L_1 and line L_2 (see Figure 3.10b). A really unusual behavior comes out from the evolution in the polarization rate: the main line L_1 is almost not polarized suggesting it is related to a transition involving a π dipole transition, while the excited state L_2 is strongly σ^+ polarized reaching a polarization rate of 100% at high magnetic field. This is a crucial information to understand properly the fine structure of the quantum dot (see Section 3.3).

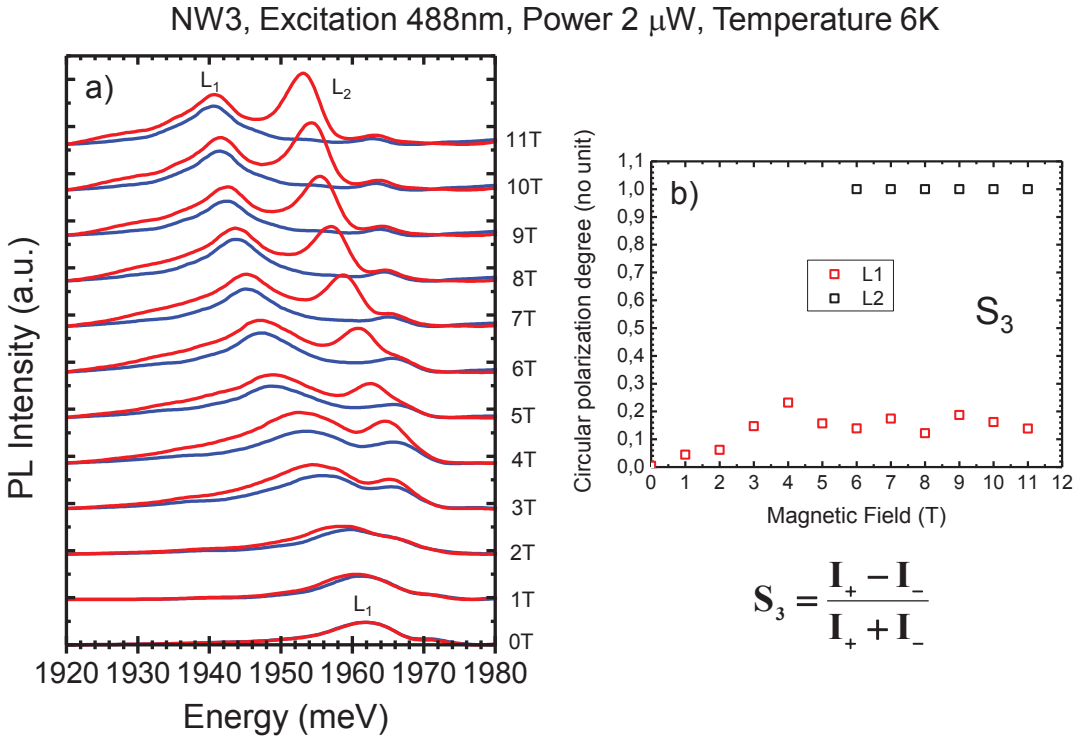

FIGURE 3.10: a) (Cd,Mn)Te QD emission, at 6K, in σ^+ (red) and σ^- (blue) polarization b) Polarization rate of line L_1 and L_2 (Stokes parameter S_3)

More polarization resolved magneto-optical studies were done to complete the Fourier characterization presented in Chapter 2 (see Figure 3.11). The linear polarization,

of the (Cd,Mn)Te quantum dot, was studied for two polarization directions (0°/90° planes and 45°/135°). It was then possible to calculate the two other Stokes parameters S_1 and S_2 and to compare them to the values obtained in Chapter 2 from the Fourier analysis (see Figure 3.11c,d). It is clear that the linear polarization rate for L_1 and L_2 is almost zero: this is expected from a quantum dot owning a circular shape symmetry in the plane perpendicular to the nanowire axis. These measurements are complementary studies to what has been shown in Chapter 2 concerning the Fourier imaging. We found, in fact, the same values, for the Stokes parameter S_1 and S_2, in zero field, like in the Fourier analysis.

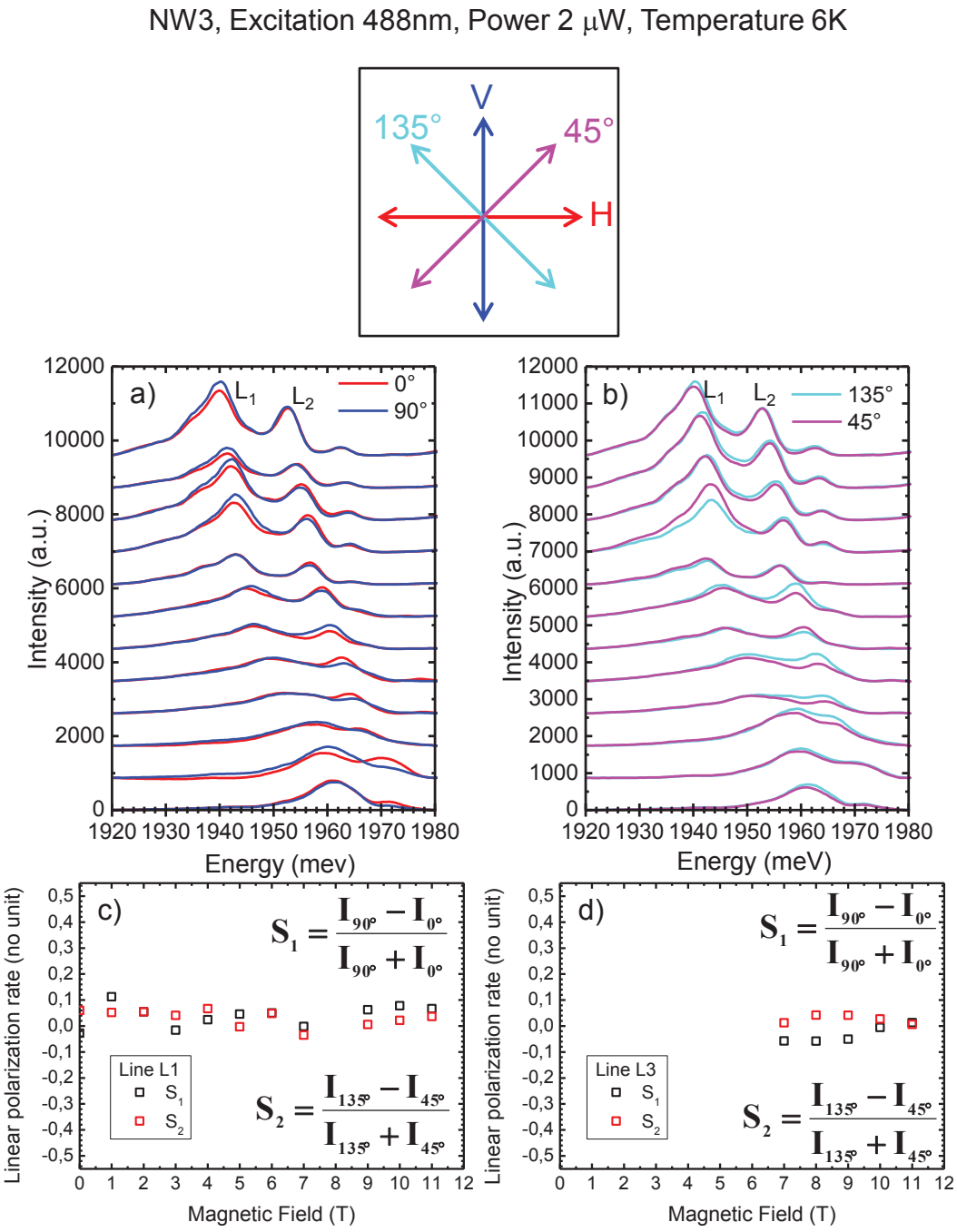

FIGURE 3.11: a) (Cd,Mn)Te QD polarized resolved emission, recorded at 6K, as a function of the magnetic field, for vertical polarization in blue and horizontal polarization in red b) (Cd,Mn)Te QD polarized resolved emission, recorded at 6K, as a function of the magnetic field, for 45° polarization in magenta and 135° polarization in cyan c) Stokes parameter S_1 and S_2 for the L_1 component d) Stokes parameter S_1 and S_2 for the L_1 component

3.3 Theoretical model

3.3.1 Calculation of the Hamiltonian under magnetic field

3.3.1.1 Confined carrier in a magnetic field

It has been shown that when the magnetic field is applied perpendicular to the nanowire growth axis, the Brillouin function, introduced in Chapter 2 doesn't explain properly the physics of the system (see Figure 3.4d,e and Figure 3.7d,e). Then it is necessary to reexamine the sp-d exchange interaction when the applied magnetic field is perpendicular to the nanowire growth axis by considering the hole anisotropy.
Figure 3.12 shows the band scheme of the quantum dot: we consider a single electron level in the conduction band and two hole levels in the valence band: a light hole $|\pm\frac{1}{2}\rangle$ and a heavy hole $|\pm\frac{3}{2}\rangle$ state. The splitting between the light hole and the heavy hole state is called ΔE (it is the hole anisotropy and it was introduced in Chapter 1 and in Chapter 2) and it will be very important in the explanation of the experimental data.

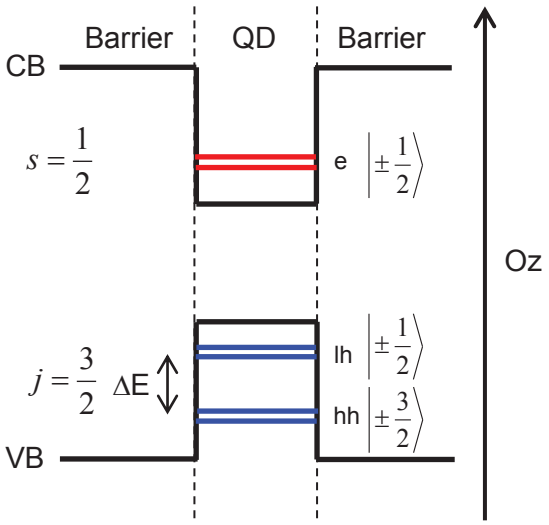

FIGURE 3.12: Scheme of the quantum dot confinement with quantization axis along z

We start with the definition of the total Hamiltonian of the (Cd,Mn)Te quantum dot inserted in the ZnTe nanowire system:

$$H_{tot} = H_{sp-d} + H_{an} + H_e + H_h + H_{e-h} \tag{3.1}$$

Here H_e describes the electron quantum confinement, H_h describes the hole quantum confinement, H_{e-h} describes the electron-hole Coulomb interaction: these terms are assumed to be constant under magnetic field.
H_{sp-d} describes the exchange interaction between Mn spins and the carriers inside the QD and H_{an} is the anisotropy term that takes into account the light hole-heavy hole splitting: these two terms will be affected by the magnetic field and will be considered in the following.
When the QD is illuminated by a laser, there is the creation of an exciton, composed by a hole and an electron. The exchange interaction Hamiltonian for a carrier, characterized by a wavefunction $\psi_j(\vec{r})$ (with $j = e$ for the electron and $j = h$ for hole) and a spin operator $\vec{\sigma}_e$ for the electron and kinetic momentum operator $\vec{J}_h$ for the hole, can be written using a Kondo like form (see Chapter 1):

$$H_{sp-d} = H_{e-Mn} + H_{h-Mn} = -\alpha \sum_{\vec{R}_i} \vec{S}_i \cdot \vec{\sigma}_e |\psi_e(\vec{R}_i)|^2 - \frac{\beta}{3} \sum_{\vec{R}_i} \vec{S}_i \cdot \vec{J}_h |\psi_h(\vec{R}_i)|^2 \tag{3.2}$$

Where α and $\frac{\beta}{3}$ are the exchange integrals for electron and hole respectively. $\vec{R}_i$ is the position of the magnetic ions characterized by spin operators $\vec{S}_i$. $|\psi_e(\vec{R}_i)|^2$ and $|\psi_h(\vec{R}_i)|^2$ are the envelop functions for electron and hole [81] and they take into account the overlap between the carrier wavefunction and Mn spins (for simplicity we considered the same envelop function for light and heavy hole). If one defines the Mn atoms volume density $\rho(\vec{r})$ as $\rho(\vec{r}) = \sum_i \delta(\vec{r}_i - \vec{R}_i)$ it is possible to transform $\sum_{\vec{R}_i}$ with $\int d^3r$. The H_{sp-d} can be rewritten then as:

$$\begin{aligned} H_{sp-d} = &-\alpha \int \rho(\vec{r}) \vec{S} \cdot \vec{\sigma}_e |\psi_e(\vec{r})|^2 d^3r + \\ &-\beta \int \rho(\vec{r}) \vec{S} \cdot \vec{J}_h |\psi_h(\vec{r})|^2 d^3r \end{aligned} \tag{3.3}$$

In our case we will consider that:

$$\rho(\vec{r}) = \begin{cases} N_0 x_{eff} & \text{inside QD,} \\ 0 & \text{outside QD.} \end{cases} \tag{3.4}$$

Where N_0 is the volume density of cation sites and x_{eff} is the effective Mn concentration. For the complete overview of the behaviour under magnetic field it remains

to write the anisotropy Hamiltonian H_{an} (see Equation 3.1) that takes into account the light hole heavy hole splitting induced by the strain and the quantum confinement. If we consider the z axis as the quantization axis, H_{an} can be written with a uniaxial anisotropy spin Hamiltonian [20] such as:

$$H_{an} = \frac{\Delta E}{2}(J_{h_z}^2 - \frac{J(J+1)}{3}) \tag{3.5}$$

3.3.1.2 Calculation of the electron and hole levels

Using a mean field approximation approach it is possible to replace the operator $\vec{J}$ in equation 3.3, by its averaged value at thermal equilibrium $\langle\vec{J}\rangle$ (see Chapter 1). In this approximation, it is then possible to calculate the averaged values of matrix elements of H_{sp-d} for the different electron and hole states. It leads to:

$$\langle H_{sp-d}\rangle_{Mn} = \langle H^e_{sp-d}\rangle_{Mn} + \langle H^h_{sp-d}\rangle_{Mn} \tag{3.6}$$

Where the $\langle H^e_{sp-d}\rangle$ is the contribution from the electron states and $\langle H^h_{sp-d}\rangle$ is the contribution from the hole states. The effect of the applied magnetic field on the carriers can be written then as:

$$\begin{aligned}\langle H_{sp-d} + H_{an}\rangle_{Mn} &= \langle H_{sp-d}\rangle_{Mn} + \langle H_{an}\rangle_{Mn} = \\ &= E_{se}\langle m_z\rangle.\langle\sigma_{e_z}\rangle + E_{sh}\langle m_z\rangle.\langle J_{h_z}\rangle + \frac{9}{2}\Delta E\langle\frac{\sigma_{h_z}^2 - 5}{36}1\!\!1\rangle\end{aligned} \tag{3.7}$$

Here $\langle\vec{m}\rangle$ is the averaged normalized magnetic moment of a Mn spin, parallel to the applied magnetic field, in the quantum dot. Its magnitude is given by:

$$\langle m_z\rangle = \frac{\langle M_z\rangle}{M_{sat}} = \mathrm{B}_{5/2}\left(\frac{5\mu_B B}{k_B(T+T_{AF})}\right) = \mathrm{B}_{5/2}\left(\frac{5\mu_B B}{k_B T_{Mn}}\right) \tag{3.8}$$

E_{se} and E_{sh} are the energies at saturation for the electron and hole respectively (defined in Chapter 1) and they are given by:

$$2E_{se} = N_0\alpha x_{eff}|\widetilde{\psi_e}|^2 S \tag{3.9}$$

$$2E_{sh} = N_0|\beta|x_{eff}|\widetilde{\psi_h}|^2 S \tag{3.10}$$

Equation 3.7 is composed by three terms where $\langle H^e_{sp-d}\rangle_{Mn}$ is defined by a $2x2$ matrix and $\langle H^h_{sp-d}\rangle_{Mn}$ is given by a $4x4$ matrix. The matrix element for the σ^e_γ and J^h_γ spin operators are given by:

$$\sigma^e_x = \begin{pmatrix} 0 & \frac{1}{2} \\ \frac{1}{2} & 0 \end{pmatrix} \quad \sigma^e_y = \begin{pmatrix} 0 & -\frac{i}{2} \\ \frac{i}{2} & 0 \end{pmatrix} \quad \sigma^e_z = \begin{pmatrix} \frac{1}{2} & 0 \\ 0 & -\frac{1}{2} \end{pmatrix} \tag{3.11}$$

$$J^h_x = \begin{pmatrix} 0 & \frac{\sqrt{3}}{2} & 0 & 0 \\ \frac{\sqrt{3}}{2} & 0 & 1 & 0 \\ 0 & 1 & 0 & \frac{\sqrt{3}}{2} \\ 0 & 0 & \frac{\sqrt{3}}{2} & 0 \end{pmatrix} \quad J^h_y = \begin{pmatrix} 0 & -\frac{i\sqrt{3}}{2} & 0 & 0 \\ \frac{i\sqrt{3}}{2} & 0 & -i & 0 \\ 0 & i & 0 & -\frac{i\sqrt{3}}{2} \\ 0 & 0 & \frac{i\sqrt{3}}{2} & 0 \end{pmatrix}$$

$$J^h_z = \begin{pmatrix} \frac{3}{2} & 0 & 0 & 0 \\ 0 & \frac{1}{2} & 0 & 0 \\ 0 & 0 & -\frac{1}{2} & 0 \\ 0 & 0 & 0 & -\frac{3}{2} \end{pmatrix}$$

The values of $N_0\alpha$ and $N_0\beta$ were given in Chapter 1 and for (Cd,Mn)Te are equal to 220meV and 880meV respectively [28, 33]. x_{eff} was introduced in Chapter 1, ψ_e and ψ_h are the envelope functions for electron and hole. The integrals of the envelope functions ψ_e and ψ_h, limited to the quantum dot volume, are called $|\widetilde{\psi_e}|^2$ and $|\widetilde{\psi_h}|^2$ and are defined by:

$$0 < |\widetilde{\psi_e}|^2 = \int_{QD} |\psi_e(\vec{r})|^2 d^3r < 1 \tag{3.12}$$

$$0 < |\widetilde{\psi_h}|^2 = \int_{QD} |\psi_h(\vec{r})|^2 d^3r < 1 \tag{3.13}$$

Since all the magnetic field dependent terms have been defined, it is possible to calculate the energy of the photoluminescence state for a (Cd,Mn)Te quantum dot, using equation 3.7 for any magnetic field applied perpendicular or parallel to the

nanowire growth axis. There are eight possible transitions. Only six are optically allowed (see Figure 3.13a): two transitions are σ^- polarized, two transitions are σ^+ polarized and two transitions are π polarized.

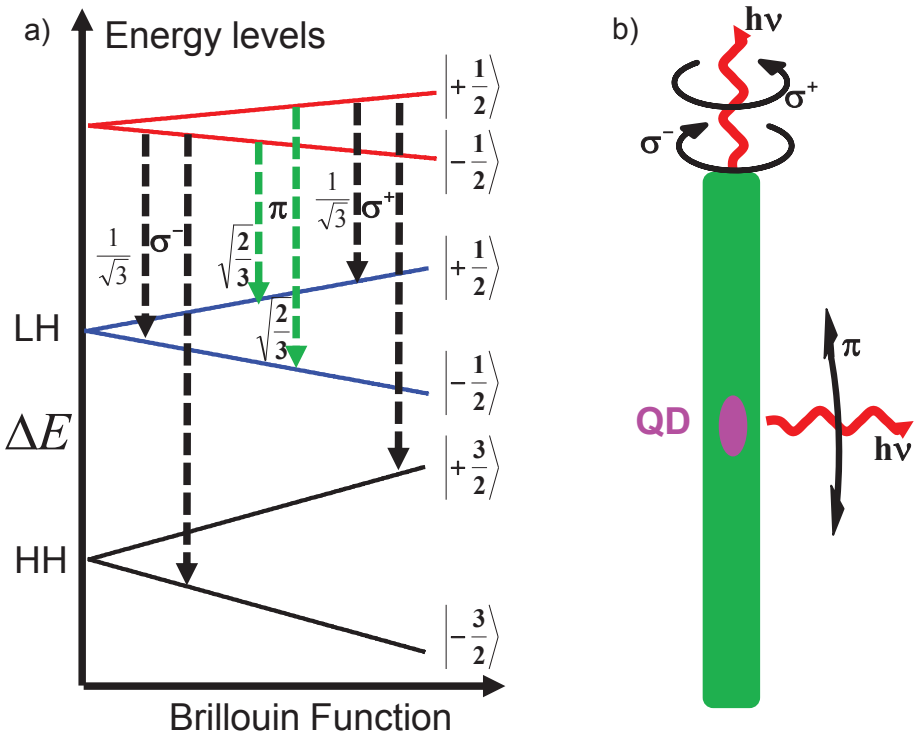

FIGURE 3.13: a) Fine structure scheme showing the optically allowed transitions b) Emission scheme of the allowed optical transitions

The transition probabilities (see Figure 3.13) can be calculated using the Fermi Golden rule [76] as the square of the following dipole matrix elements given by:

$$P_x = \begin{array}{c} \\ |\frac{1}{2}\rangle \\ |-\frac{1}{2}\rangle \end{array} \begin{array}{c} \begin{array}{cccc} |\frac{3}{2}\rangle & |\frac{1}{2}\rangle & |-\frac{1}{2}\rangle & |-\frac{3}{2}\rangle \end{array} \\ \begin{pmatrix} 0 & \frac{i}{\sqrt{6}} & 0 & -\frac{i}{\sqrt{2}} \\ \frac{i}{\sqrt{2}} & 0 & -\frac{i}{\sqrt{6}} & 0 \end{pmatrix} \end{array} \quad P_y = \begin{array}{c} \\ |\frac{1}{2}\rangle \\ |-\frac{1}{2}\rangle \end{array} \begin{array}{c} \begin{array}{cccc} |\frac{3}{2}\rangle & |\frac{1}{2}\rangle & |-\frac{1}{2}\rangle & |-\frac{3}{2}\rangle \end{array} \\ \begin{pmatrix} 0 & \frac{1}{\sqrt{6}} & 0 & \frac{1}{\sqrt{2}} \\ \frac{1}{\sqrt{2}} & 0 & \frac{1}{\sqrt{6}} & 0 \end{pmatrix} \end{array}$$

$$P_z = \begin{array}{c} \\ |\frac{1}{2}\rangle \\ |-\frac{1}{2}\rangle \end{array} \begin{array}{c} \begin{array}{cccc} |\frac{3}{2}\rangle & |\frac{1}{2}\rangle & |-\frac{1}{2}\rangle & |-\frac{3}{2}\rangle \end{array} \\ \begin{pmatrix} 0 & 0 & i\sqrt{\frac{2}{3}} & 0 \\ 0 & i\sqrt{\frac{2}{3}} & 0 & 0 \end{pmatrix} \end{array}$$

The transition probabilities for σ^+ and σ^- polarization are given by the square of the matrix elements of:

$$P_{\sigma^+} = P_x + iP_y \tag{3.14}$$

$$P_{\sigma^-} = P_x - iP_y \tag{3.15}$$

The matrix elements for the transition probabilities of σ^+ and σ^- will be then given by:

$$P_{\sigma^+} = \begin{array}{c} \\ |\frac{1}{2}\rangle \\ |-\frac{1}{2}\rangle \end{array} \begin{array}{c} \begin{array}{cccc} |\frac{3}{2}\rangle & |\frac{1}{2}\rangle & |-\frac{1}{2}\rangle & |-\frac{3}{2}\rangle \end{array} \\ \begin{pmatrix} 0 & i\sqrt{\frac{2}{3}} & 0 & 0 \\ i\sqrt{2} & 0 & 0 & 0 \end{pmatrix} \end{array} \quad P_{\sigma^-} = \begin{array}{c} \\ |\frac{1}{2}\rangle \\ |-\frac{1}{2}\rangle \end{array} \begin{array}{c} \begin{array}{cccc} |\frac{3}{2}\rangle & |\frac{1}{2}\rangle & |-\frac{1}{2}\rangle & |-\frac{3}{2}\rangle \end{array} \\ \begin{pmatrix} 0 & 0 & 0 & -i\sqrt{2} \\ 0 & 0 & -i\sqrt{\frac{2}{3}} & 0 \end{pmatrix} \end{array} \tag{3.16}$$

It is possible now to write the equation for the energy of the photoluminescence state: whereas all the measurements were taken at very low temperature it will be necessary to take into account just the lowest possible transition. Considering equation 3.3 we can write the photoluminescence energy:

$$E_X = E_h(1) + E_e(1) + E_0 \tag{3.17}$$

Where $E_h(1)$ and $E_e(1)$ are respectively the first hole and the first electron state energy. These two terms are magnetic field dependent and they are calculated from equation 3.7. The term E_0 is a constant and it takes into account all the terms that are not magnetic field dependent. E_0 is in fact related to the quantum dot confinement, to the electron-hole Coulomb interaction and to the bandgap that we suppose it does not depend on the applied magnetic field. E_0 comes from the calculation of the mean value of $\langle H_e + H_h + H_{e-h} \rangle$.

3.3.1.3 Giant Zeeman effect for different field configurations

In the previous Section we saw how to calculate the photoluminescence energy from equation 3.17. At a given temperature, the equation essentially depends on three parameters: ΔE, E_{se} and E_{sh}. By choosing these three parameters, it is then possible to calculate the emission energy of a (Cd,Mn)Te quantum dot for any magnetic field

applied parallel or perpendicular to the nanowire growth axis.

If E_{se} and E_{sh} are fixed, there will be four different emission lines of the quantum dot. Depending on the sign of ΔE, the first hole level will have a light hole or a heavy hole character and the Zeeman shift of these two states have to be calculated for the two different magnetic field orientation leading to four possible configurations (see Figure 3.14).

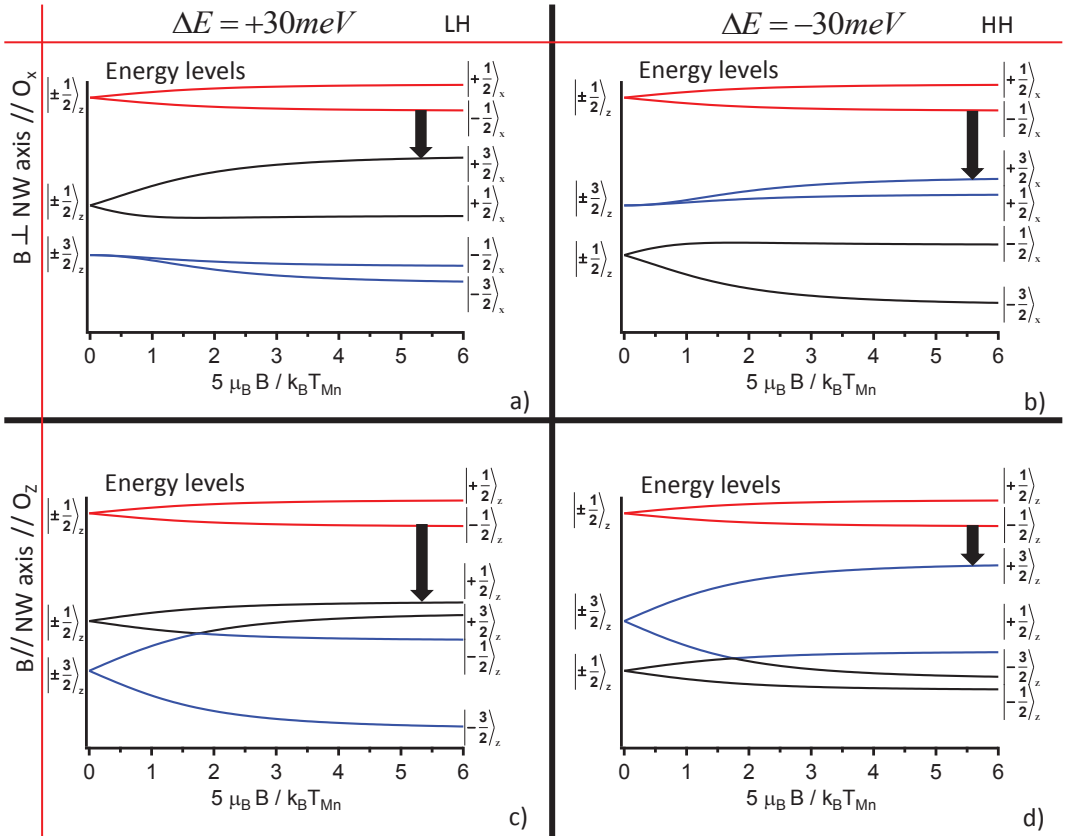

FIGURE 3.14: Zeeman energy diagram of a light hole exciton with a) an applied perpendicular magnetic field c) an applied parallel magnetic field. Zeeman energy diagram of a heavy hole exciton with b) an applied perpendicular magnetic field d) an applied parallel magnetic field

To be able to compare the theoretical model with experimental data, all the electron and hole energy levels have been traced as a function of $\frac{5\mu_B B}{k_B T_{Mn}}$. The transition which corresponds to the experimental line, at low temperature, is indicated by a black arrow (see Figure 3.14). From Figure 3.14 is clear that the quantum dot Zeeman energy diagram really depends on the direction of the applied magnetic field: when the magnetic field is applied perpendicular to the quantization axis we can see that the Zeeman shift of a heavy hole exciton, presents a flatness at low applied magnetic field. This feature is not present in all the other cases.

With the whole Zeeman energy diagram, it is possible to plot the expected theoretical

Giant Zeeman shift of the photoluminescence line for the four different configurations (Figure 3.15).

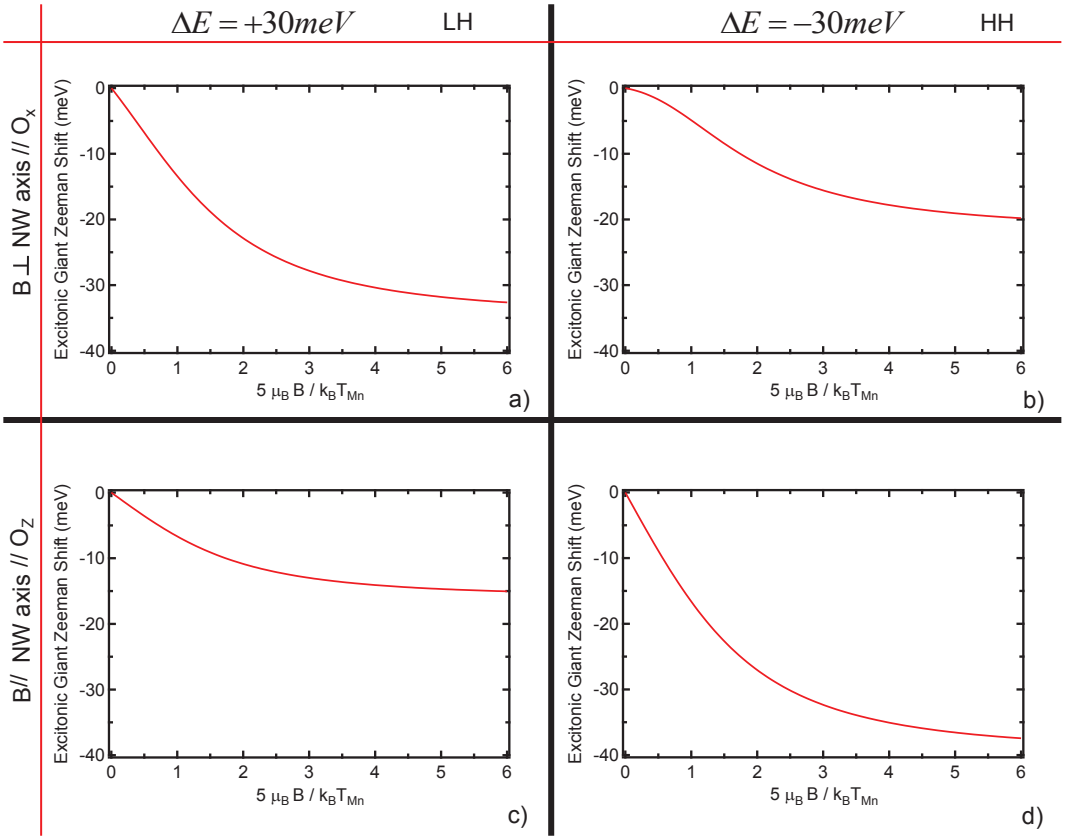

FIGURE 3.15: Giant Zeeman Shift for a light hole type exciton with a) a perpendicular applied magnetic field c) a parallel applied magnetic field. Giant Zeeman Shift for a heavy hole exciton with b) a perpendicular applied magnetic field d) a parallel applied magnetic field

From Figure 3.15, it is notable that the Giant Zeeman effect is strongly dependent on the orientation of the magnetic field: the saturation value is bigger for field applied along (perpendicular) the quantization axis for a heavy hole exciton (light hole exciton). Moreover for a heavy hole exciton, when the field is applied perpendicular to the quantization axis, we have a flat region at small magnetic field: the variation of the Giant Zeeman shift is in fact slower in this range. In this case, the deviation from a Brillouin function is the largest. With the Zeeman energy diagrams calculated for the two possible magnetic field configurations and the two different types of holes, it is possible to analyze quantitatively the experimental data.

3.3.2 Analysis of the experimental data

3.3.2.1 NW1

We start with NW1 which feature a simple and well resolved emission spectrum. We consider first the shift of the main line L_1. The experimental spectra have been shown in Section 3.2 (see Figure 3.4d). We will now compare the theoretical predictions (for a magnetic field applied perpendicular to the nanowire growth axis) derived in the previous Section with the experimental data. The best fit is shown in Figure 3.16.

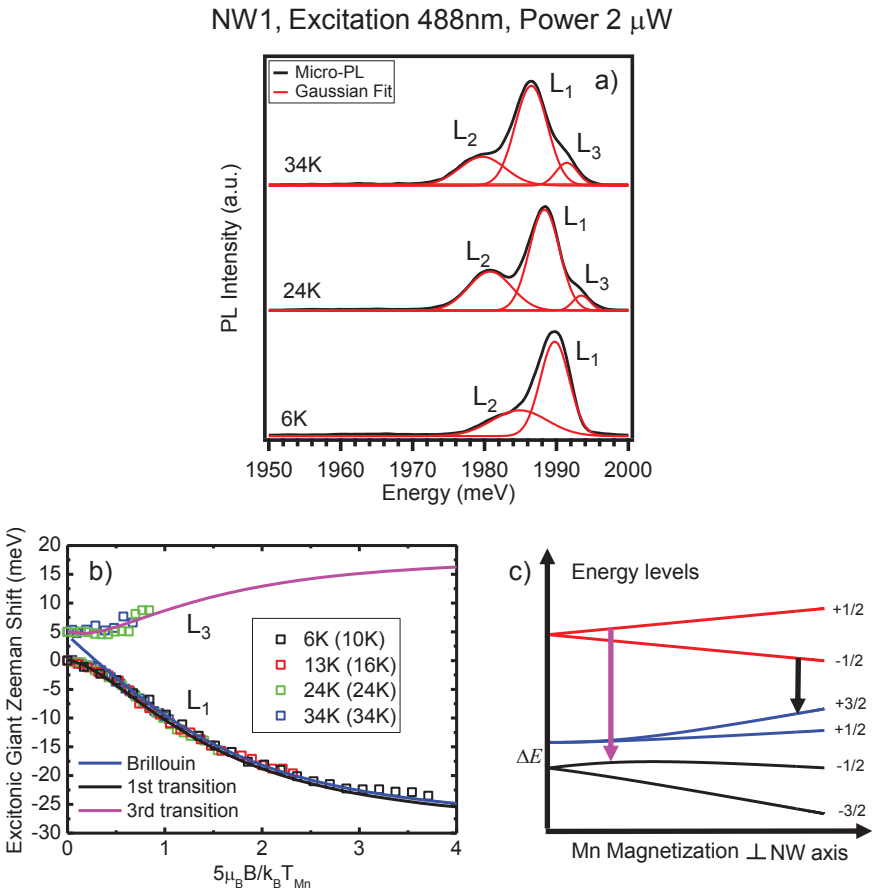

FIGURE 3.16: a) Gaussian fit of the spectra at 6K, 24K and 34K with no magnetic field b) Theoretical model applied to the states L_1 and L_3 of NW1 c) Zeeman energy diagram, with fundamental state a heavy hole exciton, showing in black the first transition and in magenta the third one.

Figure 3.16b shows the experimental data (shown already in Figure 3.4f) concerning the main line L_1 and the excited state L_3. The Gaussian fit used to retrieve the line positions is shown in Figure 3.16a. At high magnetic field, the L_1 excitonic line corresponds to the optical transition between the first projected heavy hole state $|+\frac{3}{2}\rangle_x$ and the first electron level $|-\frac{1}{2}\rangle_x$. The optical transition associated to L_3 corresponds to a transition between the projected light hole state $|-\frac{1}{2}\rangle_x$ with the electron level $+|\frac{1}{2}\rangle_x$ (see Figure 3.16c).

From Figure 3.16b it is clear that there is a deviation from a Brillouin function at small magnetic fields. This deviation is related to the hole anisotropy ΔE, which is equal to 5meV for the present nanowire: this value has been chosen experimentally by the observation of the excited state L_3 (see Figure 3.16a). This line corresponds indeed to an optical transition involving the light hole excited state (see Figure 3.16c). For the nanowire NW1, the two other fitting parameters E_{se} and E_{sh} have been extracted from the fit of the Giant Zeeman shift of the excitonic line. For the best fit conditions, we found E_{se}=8.5meV and E_{sh}=24meV. As shown in Chapter 2, EDX images were done on this particular nanowire. It allowed us to extract the concentration of the Mn atoms inside the quantum dot and to fix the value of x_{eff} that appears in the definitions of the two quantities E_{se} and E_{sh}. Knowing the value of x_{eff}, that is around 4%, we can discuss the values of E_{se} and E_{sh}. E_{se} has been taken equal to 8.5meV: this quantity is close to the saturation value 11meV. E_{sh} has been taken equal to 24meV: this value is really different from the saturation one, expected for a quantum dot with $x_{eff} = 4\%$ that is around 44meV (see Chapter 1). If we look again at the formula that defines E_{sh} we see that it depends on x_{eff} but also on the integral of the presence probability $|\widetilde{\psi_h}|^2$. Due to the large conduction band offset, for the electron we can suppose a strong confinement in the quantum dot, with an integrated presence probability $|\widetilde{\psi_e}|^2 \cong 1$, while for the hole, as a consequence of the smaller valence band offset, we have to consider a weaker confinement leading to an integrated presence probability equal to $|\widetilde{\psi_h}|^2 = 0.55$. Unfortunately there are no experimental measurements that can determine the correct values for the presence probabilities but there are some techniques that can highlight if the quantum dot confinement is strong or weak: these are the time resolved photoluminescence measurements presented for NW2 in Chapter 2. From the time resolved measurements it has been observed that the typical decay time of the excitonic state is around 800ps. The value of this decay time is quite long if we compare it to the typical decay time observed for (Cd,Mn)Te self assembled quantum dot that is around 200ps [17]. This difference highlights the fact that the quantum dot confinement of this sample could be rather

weak leading to a partially delocalized hole wavefunction around the quantum dot region. This delocalization allows a smaller coupling between the hole wavefunction and the Mn atoms wavefunction: this smaller overlap is responsible for the observed smaller excitonic Giant Zeeman saturation value and then could explain the reduced value of E_{sh}=24meV.

3.3.2.1.1 Full Width at Half Maximum

We saw that the magneto-optical results can be explained by considering the fundamental transition (L_1) between the electron state $|-\frac{1}{2}\rangle$ and the hole one $|+\frac{3}{2}\rangle$ and the excited state L_3 is an optical transition between the electron state $|+\frac{1}{2}\rangle$ and the hole one $|-\frac{1}{2}\rangle$. We can note from the Zeeman diagram, that the excited state described by the transition between the electron state $|-\frac{1}{2}\rangle$ and the hole one $|+\frac{1}{2}\rangle$ is missing. In this Section we try then to improve the fit of the magneto-optical results by considering also this excited state: by its inclusion in the fitting model, it will be possible also to explain the uncommon behaviour observed for the FWHM under magnetic field. The non monotonous trend is in fact related to the presence of this excited state, that is really close to the fundamental one, and which has a transition probability which becomes small at high magnetic field. The new fit, using two components to reproduce the main line L_1 instead of one is shown in Figure 3.17.

As shown in Figure 3.17 a good agreement between the fit and the experimental data can be found. We can try now, to look at the theoretical Zeeman energy diagram.

Figure 3.18a shows the experimental points (symbols) taken from the fit using a three level transition scheme shown in Figure 3.18b. The Zeeman energy diagram is the same as the one shown in Figure 3.16b with the presence of the second hole state transition.
Now we have to check if this fit, with two lines, could explain the broadening of the photoluminescence line at low magnetic field. We can now trace the FWHM of the first and the second transitions as a function of $\frac{5\mu_B B}{k_B T_{Mn}}$ (see Figure 3.19).

Figure 3.19a shows the FWHM of the excitonic state L_1, under magnetic field, taken from the Section 3.2 while Figure 3.19b shows the experimental linewidths of the two transitions used for the fit (for simplicity we considered them equal). The observed experimental non monotonous behaviour at low magnetic field (see Figure 3.19a) can be explained then by the unresolved two transitions, that both present Giant Zeeman effect. It leads to a photoluminescence peak given by the sum of the two

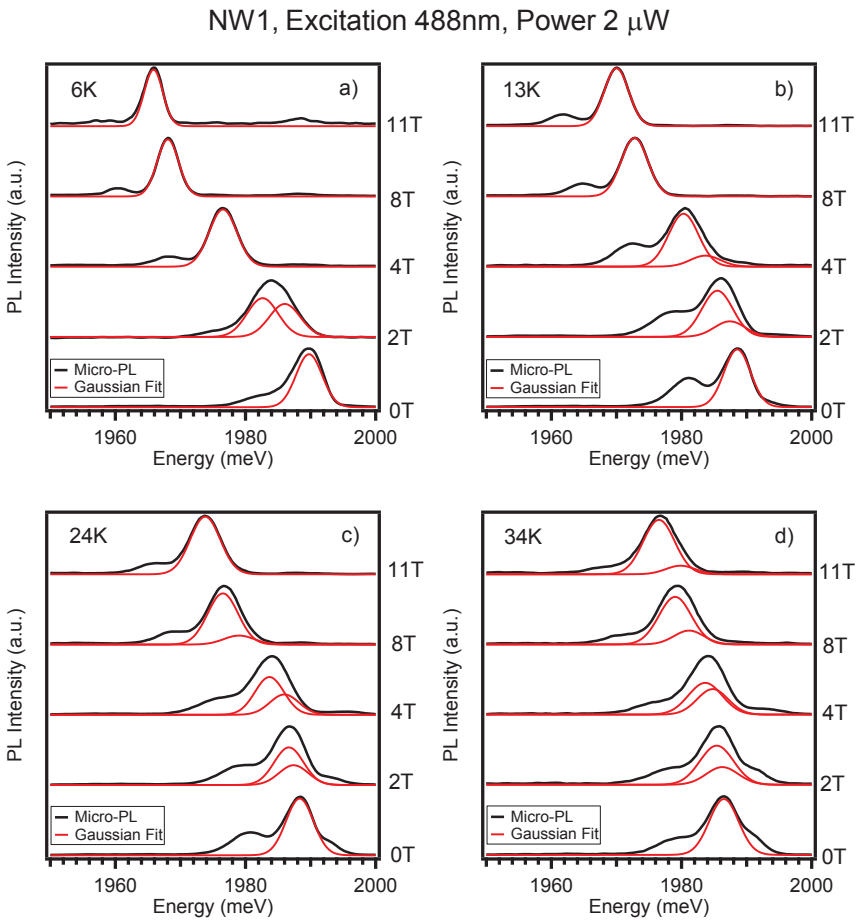

FIGURE 3.17: (Cd,Mn)Te QD emission fitted using two components, for some values of the applied magnetic field, at a) 6K b) 13K c) 24K d) 34K

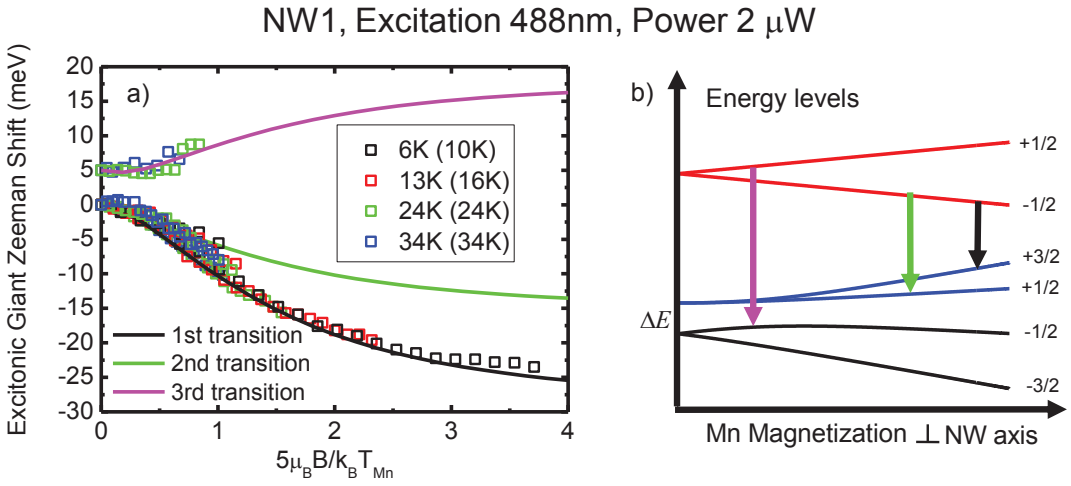

FIGURE 3.18: a) Theoretical model applied to the three exciton states of NW1 b) Zeeman energy diagram, with fundamental state a heavy hole exciton, showing in black the first transition, in green the second and in magenta the third one

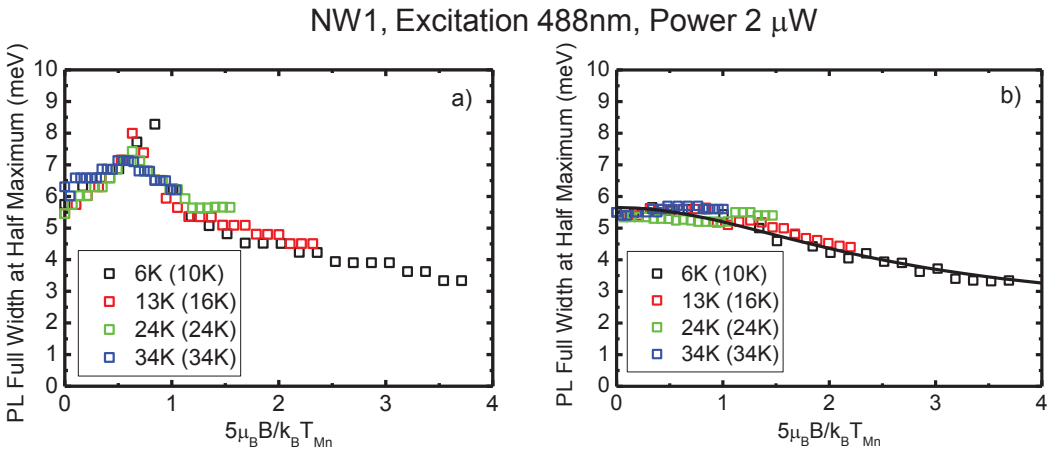

FIGURE 3.19: a) L_1 FWHM plotted as function of $\frac{5\mu_B B}{k_B T_{Mn}}$ b) Calculated FWHM of the first and second transition plotted as function of $\frac{5\mu_B B}{k_B T_{Mn}}$ and fitted by equation 3.19

Gaussian functions that describe the two different hole transitions. If we now look at the calculated FWHM of the two transitions (Figure 3.19b) we get the common behaviour expected for the FWHM of (Cd,Mn)Te quantum dots under magnetic field. It is in fact possible to fit the data with the formula that expresses the variation of the linewidth ΔE_{FWHM}, due to the Mn spin fluctuations, as a function of the magnetic field [17]:

$$\Delta E_{FWHM} = \sqrt{8\ln(2) k_B T_{Mn} E_P} \tag{3.18}$$

Where E_P is the Magnetic Polaron energy. E_P is proportional to the magnetic susceptibility $\chi_V \propto \frac{d\langle M\rangle}{dB}$ and hence, for the FWHM, we obtain:

$$\Delta E_{FWHM} \propto \Delta E_0 \sqrt{\frac{d}{dB}\left[B_{\frac{5}{2}}\left(\frac{g_{Mn}\mu_B BS}{k_B T_{Mn}}\right)\right]} \tag{3.19}$$

where ΔE_0 is the typical linewidth of a (Cd,Mn)Te quantum dot at zero magnetic field. This expression is related to the fact that the square of the linewidth can be expressed as a second moment of the line, hence of the magnetization through the Giant Zeeman Effect.

3.3.2.2 NW2

Figure 3.20a shows the Gaussian fit used to retrieve the energy positions of the main components that dominate the spectra of NW2. In Figure 3.20c the modeling, used to describe the excitonic Giant Zeeman shift of the main line of NW2, is presented. A heavy hole exciton has been also taken, as a fundamental state, for this nanowire (see Figure 3.20b): in fact, like for NW1, it is good to remember that the applied magnetic field is perpendicular to the nanowire axis (it is the only case where we can have a deviation from a Brillouin like behaviour as explained in Section 3.3). All the measurements were done at low temperature and then it is possible to consider just one optical transition. The main line L_1 (see Figure 3.20c) corresponds to an optical transition between the first projected heavy hole state $|+\frac{3}{2}\rangle_x$ and the first electron level $|-\frac{1}{2}\rangle_x$.

Unlike NW1, it is not possible to retrieve experimentally the value of ΔE: the spectra is much broader, involving different optical transitions and the second line L_2 is exhibiting a Giant Zeeman effect (and so a redshift) comparable to the behaviour of the main line L_1. This trend is not compatible with a possible optical transition involving the light hole excited state. If we look at the Zeeman energy diagram, shown in Figure 3.20b, we would have expected a blue shift as in the case of NW1. The state described by L_2 has to be then another optical transition involving a heavy hole state with $|+\frac{3}{2}\rangle_x$ and an electron level with $|-\frac{1}{2}\rangle_x$.

From Figure 3.20c,d it is clear that both lines L_1 and L_2 show an excitonic Giant Zeeman effect but the values at saturation are really different: for L_1 the saturation value is in fact around 20meV while for L_2 is 14meV. In Chapter 2, when we described the time resolved photoluminescence measurements, it has been shown that the two components had different decay times: 810ps for L_1 and 900ps for L_2. The larger decay time values may suggest a weaker hole confinement for the L_2 line (the electron wavefunction remains probably fully confined because of the more pronounced conduction band offset). It would be possible to have a delocalized hole state around the quantum dot that is weakly coupled with the Mn atoms inside the (Cd,Mn)Te region. The fact that the two components L_1 and L_2 have slightly different decay times could be explained by the fact that are associated to different excitonic states with different delocalized hole wavefunctions. We will try then to fit the experimental Giant Zeeman shifts with two different transitions with different hole wavefunction and hence two different values for E_{sh}.

Also if we don't have experimental measurements on the value of ΔE we can use all

the informations extracted by the combined studies on NW1, like the Mn concentration and the hole anisotropy parameter ΔE, to try to describe NW2. We take a value of ΔE=-5meV as for NW1. For the estimations of E_{se} and E_{sh} we assume that NW1 and NW2 have the same Mn concentration (they are coming from the same sample). For E_{se} we take 8.5meV: this quantity is very close to the saturation value 11meV suggesting again an electron well confined inside the quantum dot. For E_{sh} we take 16.5meV: this value is really different from the saturation one, expected for a quantum dot with x_{eff} = 4% which is around 44meV. It shows that the hole wavefuction is even more delocalized than in the case of NW1.

For the L_2 component, we take the same value for ΔE and E_{se} but a smaller value of E_{sh} ($E_{sh} = 10meV$). In Figure 3.20 we plot the Giant Zeeman shifts of the two components L_1 and L_2 and the fit calculated with the parameters discussed above.

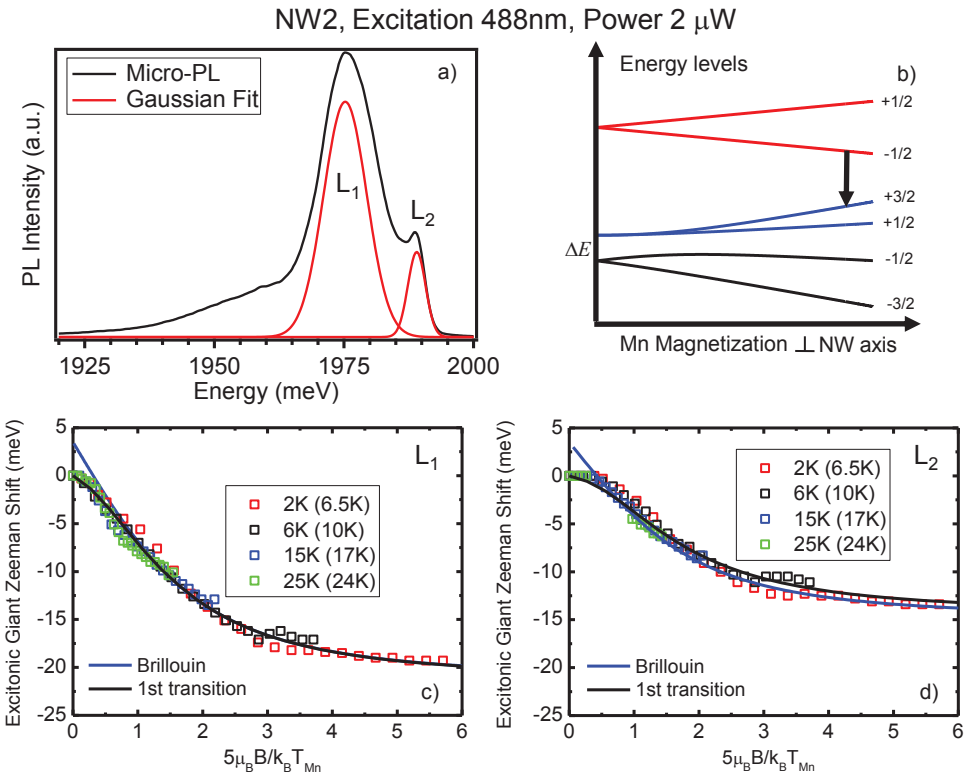

FIGURE 3.20: a) Gaussian fit of the spectra at 2K with no applied magnetic field b) Zeeman energy diagram, with fundamental state a heavy hole exciton, showing in black the first transition c) Theoretical model applied to the states L_1 of NW2 d) Theoretical model applied to the states L_2 of NW2

3.3.2.3 NW3

When the applied magnetic field is parallel to the nanowire growth axis, as for NW3, the Giant Zeeman effect can be more easily explained (from both light hole-heavy hole exciton we have a Brillouin like behaviour, see Section 3.3). At the same time less informations can be extracted in comparison to the case where the magnetic field is applied perpendicular to the nanowire axis (NW1 and NW2): in the presence of just the fundamental state, it is not possible to determine the hole anisotropy ΔE without applying magnetic fields parallel and perpendicular to the quantization axis. The field dependent studies done on NW3 are summarized in Figure 3.21. The energy line positions were extracted using a Gaussian fit (as already mentioned) this fit was introduced in the Section 3.2.

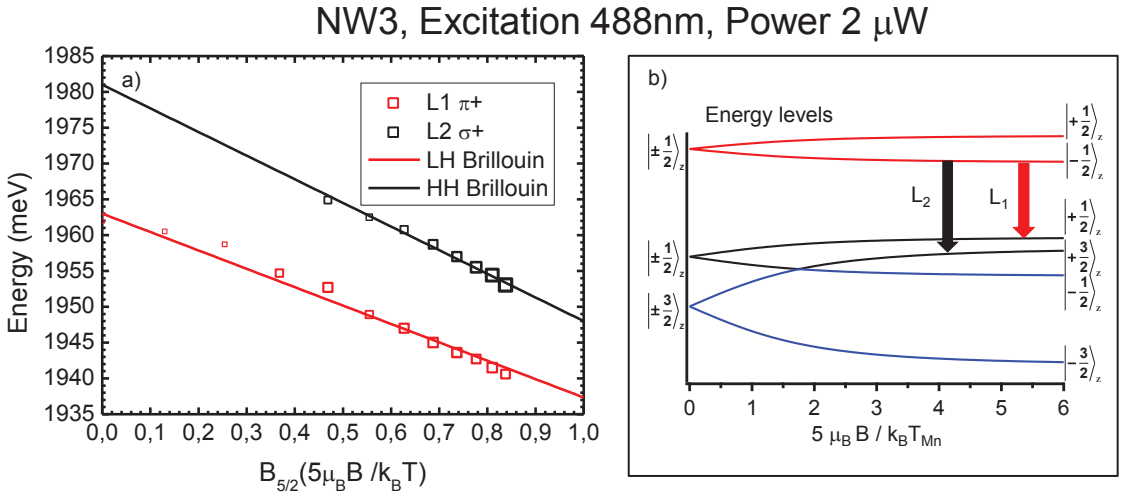

FIGURE 3.21: a) L_1 and L_2 Giant Zeeman Shifts as a function of $B_{\frac{5}{2}}(\frac{5\mu_B B}{k_B T_{Mn}})$ (the dimension of the points is proportional to the experimental intensity) b) Zeeman energy diagram, with fundamental state a light hole exciton, showing in red the first transition L_1 and in black the second transition L_2

The Giant Zeeman effect can be described by a Brillouin function. Unfortunately in this situation it is not possible to extract the value of ΔE from the fit of the exciton component L_1. For NW3, without the detailed polarization analysis that we have done, it would be impossible to determine if the exciton fundamental state has a light hole or a heavy hole nature: as shown in Section 3.3, for a configuration where the applied magnetic field is applied along the nanowire axis, the only difference between the two types of exciton is the value at saturation of the Giant Zeeman shift, that is smaller for a light hole ground state than for a heavy hole one. Unfortunately, in the presence of a weak hole confinement we could have a much smaller Zeeman

shift also for a heavy hole exciton due to the weaker coupling with the Mn atoms.
The detailed polarization resolved studies were essentials to understand the emission properties of NW3 (see Section 3.2.2.1). We found that L_1 is almost not polarized while L_2 becomes circularly polarized under magnetic field reaching a polarization rate of 100% at high magnetic field. The L_1 component is then associated to a π polarized transition whereas the L_2 to a σ one (these considerations are supported also by the Fourier analysis shown in Chapter 2). The only exciton that has an optical allowed π transition is the light hole one: the L_1 state is then associated to a transition between hole state $|+\frac{1}{2}\rangle$ and the electron one $|-\frac{1}{2}\rangle$ (see Figure 3.21b). We fit then the L_1 Giant Zeeman shift (see Figure 3.21a) by a light hole Brillouin function: the saturation energy is given by $E_{se} + \frac{E_{sh}}{3}$ with E_{se}=11meV and E_{sh}=44meV (see Chapter 1).
The identification of L_2 is a bit more complicated: it is unusual that an excited state, under magnetic field, gains so much intensity dominating the spectrum at $11T$. The L_2 component cannot be attributed to the pure light hole transition between the hole state $|+\frac{1}{2}\rangle$ and the electron one $|+\frac{1}{2}\rangle$: the shift at saturation for this transition would have been smaller compared to the experimental one. We can then suppose that the light hole state $|+\frac{1}{2}\rangle$ crosses with the heavy hole one $|+\frac{3}{2}\rangle$ at high magnetic field ($6T$). We fit the Giant Zeeman shift with a heavy hole Brillouin function weakly confined (the saturation energy is given by $E_{se} + \frac{E_{sh}}{2}$ instead of $E_{se} + E_{sh}$). It is then a heavy hole state that is weakly coupled to the Mn atoms (the hole saturation energy is in fact half of the expected one, for L_1 we took in fact $E_{sh} = 44meV$). We will discuss more in details the L_2 behaviour in the Conclusion Section.
By assuming that the two components L_1 and L_2 are associated to a light hole and a heavy hole transition respectively, it is possible to estimate a hole anisotropy that is equal to ΔE = 18meV.

3.4 Conclusions

To summarize, the three studied nanowires NW1,NW2 and NW3 present common features but also some differences. The common properties are:

1. A clear excitonic Giant Zeeman effect: the amplitude of the shift at saturation decreases by increasing the temperature proving the good incorporation of the Mn atoms inside (Cd,Mn)Te quantum dots.
2. Both heavy hole and light hole emissions lines can be observed. These two states are really close in energy and can be measured in NW1 and NW3. In NW1 a light hole excited state appears by increasing the temperature while in NW3 a heavy hole excited state that manifests itself by applying a large magnetic field.
3. The Zeeman shift at saturation for the electron E_{se} corresponds to the expected value of a highly concentrated (Cd,Mn)Te quantum dot ($x_{eff} = 4\%$) with a maximum variation of about 20%. This shows a well confined electron in the quantum dot as expected from the high conduction band offset.
4. The exciton lifetime is quite long ranging from 800ps up to 2ns denoting a hole not perfectly confined.

The main differences are:

1. The exciton ground state and hence the hole ground state can have a light hole or a heavy hole character.
2. In the case of a light hole ground state, the Zeeman shift at saturation of the hole (E_{sh}) corresponds to the expected value of a highly concentrated (Cd,Mn)Te quantum dot ($x_{eff} = 4\%$). In the case of a heavy hole ground state, E_{sh} is systematically smaller than the expected value (by about 50%, see Table 3.1).

We believe that these peculiar similarities and differences between the different studied nanowires result from the interplay between the value of the heavy hole-light hole splitting (controlled by the dot aspect ratio) and of the valence band offset.

TABLE 3.1: Main results on Sample 1

	ΔE	E_{se}	E_{sh} (heavy hole)	E_{sh} (light hole)
NW1	-5meV	8.5meV	24meV	–
NW2	-5meV	8.5meV	16.5meV	–
NW3	18meV	11meV	22meV	44meV

Heavy hole-light hole splitting

The nature of exciton ground state (light hole or heavy hole) is controlled by the sign of the hole anisotropy ΔE. Due to the small value of the hole anisotropy, the nature of the exciton ground state changes from nanowire to nanowire (belonging to the same sample: Sample 1). In Chapter 2 we calculated the strain effect on a CdTe quantum dot inserted in an infinite ZnTe matrix as a function of the aspect ratio $\frac{L}{D}$ (see Figure 3.22). In this calculation, we consider quantum dots with an ellipsoid shape embedded in a thick ZnTe shell and we take identical isotropic elastic coefficients everywhere.

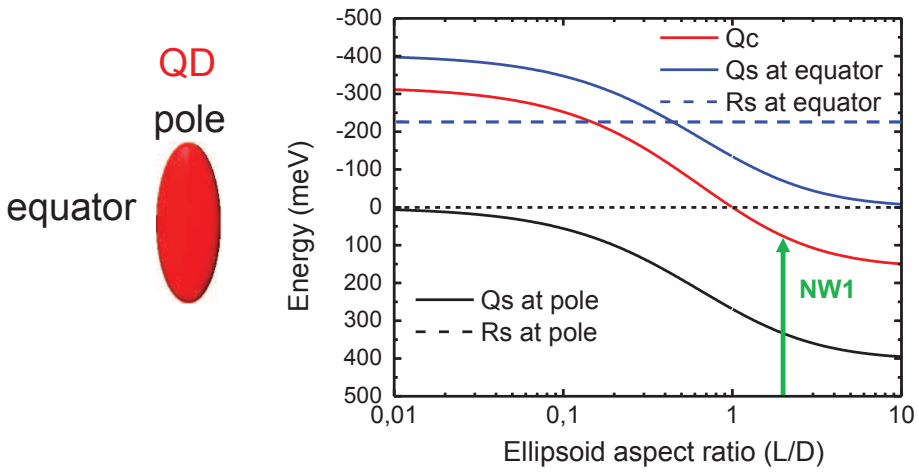

FIGURE 3.22: Strain Hamiltonian parameters for a CdTe ellipsoidal quantum dot in a ZnTe nanowire, the index c denotes the core while the index s denotes the shell

A single parameter called Q_c controls the valence band splitting induced by strain in the dot. Two parameters called Q_s and R_s control the valence band splitting induced by strain in the shell around the dot. Q_c is uniform for an ellipsoid dot and given by analytical formula. Q_s and R_s are not uniform and decrease down to zero far away from the dot. Using the continuity relation of the strain and stress tensors, we calculate their value from Q_c at the interface of the dot for the equator and the pole (see Figure 3.22).

Q_c and Q_s are proportional to ε_{axial} and split the valence band (light hole-heavy hole splitting). R_s mixes the heavy hole and light hole states. A positive value of Q_c or Q_s favors a heavy-hole ground state.
If we consider the EDX measurements done on NW1 (see Chapter 2) we have a quantum dot aspect ratio $\frac{L}{D} \simeq 2$ (green arrow in Figure 3.22). From Figure 3.22, we have a value of Q_c=70meV, meaning that we expect a light hole ground state well separated from the heavy one by a large splitting ΔE (ΔE being equal to $2Q_c$=140meV, or even more if one takes into account the additional contributions from confinement). In the ZnTe barrier, the axial contribution Q_s at the equator is opposite for $\frac{L}{D} \simeq 2$ and additionally there is a strong mixing contribution R_s. Both terms are expected to decrease away from the interface (as $\frac{1}{r}$ for an aspect ratio close to 1 and as $\frac{1}{r^2}$ for an elongated dot).

Valence band offset

The valence band offset V_0 between CdTe and ZnTe is small. The order of the band alignment between both material is unknown (Type I or Type II) for vanishing strain. V_0 has not been determined precisely up to now, but it is estimated to be between -50meV<V_0<50meV. For (Cd,Mn)Te, the presence of Mn in the dot increases the band gap and pushes even more the configuration towards a Type II band alignment. With 10% Mn, the blue shift of the bandgap is 170meV, of which one generally considers that around 1/3 is in the valence band. Hence it is not unreasonable to consider that -100meV<V_0<0meV between (Cd,Mn)Te and ZnTe.

In an heterostructure, the valence band offset is also modified by the isotropic component of elastic strain. This contribution is difficult to estimate because the hydrostatic deformation parameter of the valence band is not well known.

To discuss qualitatively the influence of the band offset on the light hole heavy hole splitting, we plot in Figure 3.23 schematic valence band profiles of ellipsoid (Cd,Mn)Te/ZnTe dots for different values of V_0. Note that we use electron like energy diagram for the holes (hole energy). The profiles are plot in a plane perpendicular to the dot axis. We take $\frac{L}{D} \simeq 2$ (value of NW1) and we use Q_c=70 meV, Q_s=-70 meV, R_s=-225 meV (see Figure 3.22). If one does not take into account the valence band offset, we expect with previous parameters a light hole ground state well separated from a heavy hole one (ΔE=140meV).

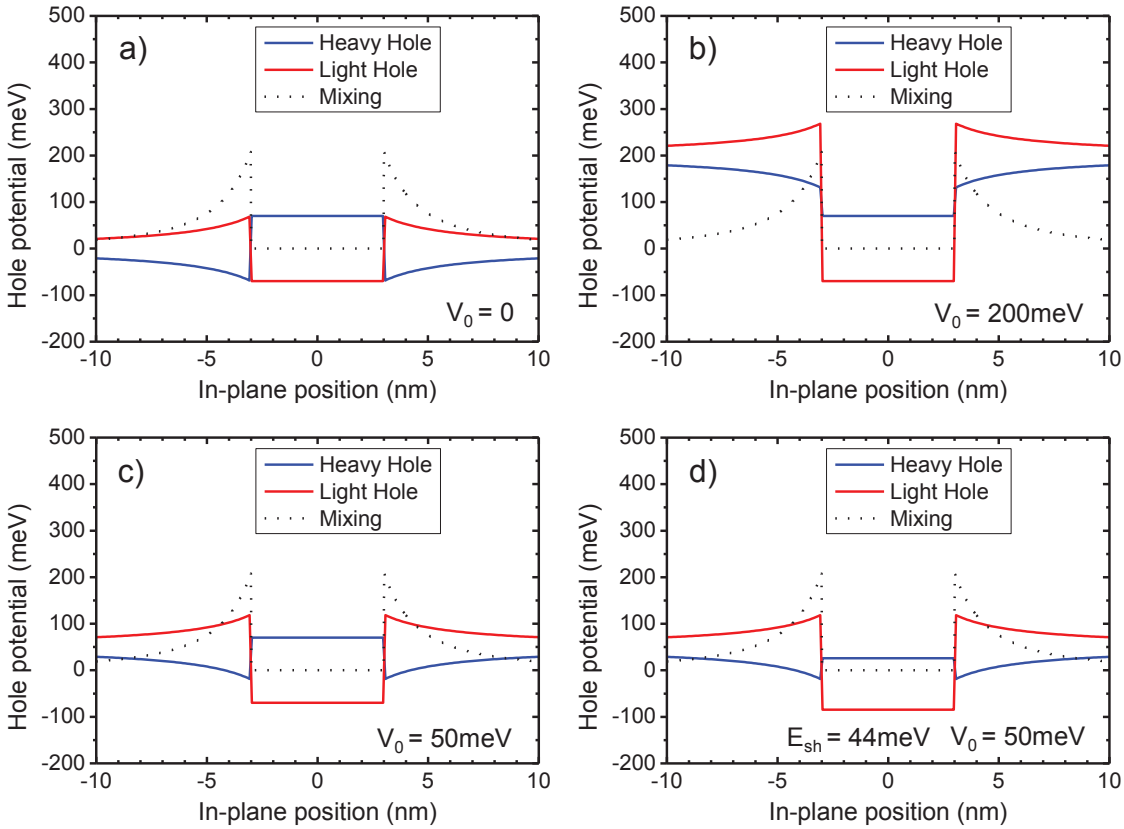

FIGURE 3.23: Heavy hole and light hole potentials for a) zero valence band offset b) Type I quantum dot (V_0=200meV) c) Type II quantum dot (V_0=50meV) with x_{eff} = 4% d) Type II quantum dot (V_0=50meV) with x_{eff} = 4% under magnetic field, supposing to be at saturation (E_{sh}=44meV) (R_s has been omitted for simplicity). For these calculation we used Q_c=70 meV, Q_s=-70 meV and R_s=-225 meV

If the valence offset is small (say V_0=0meV, Figure 3.23a) elastic strain induces an attractive confinement potential for light holes and a repulsive one for heavy holes. Then, we expect a light hole state confined in the dot and a heavy one delocalized in the barrier at the interface of the dot.

If the valence band offset is definitely Type I (say V_0=200meV, Figure 3.23b), the holes are deeply confined in the dot and the ground state is expected to be light hole. Note however that the heavy hole is already less confined in the dot (the barrier height is in fact smaller).

For non zero valence band offset (say V_0=50meV), we plot two band profiles: one in zero magnetic field (Figure 3.23c) and one for large magnetic fields (with a saturated heavy hole giant Zeeman splitting E_{sh}=44meV, see Figure 3.23d). According to the band profiles, one can draw the following conclusions:

- The light-hole / heavy-hole splitting is expected to be smaller than 140 meV and can even be inverted promoting a heavy hole ground state delocalized in the barrier at the interface with the quantum dot. Note that in that case we keep a heavy hole ground state for a quantum dot having an aspect ratio $\frac{L}{D}$ larger than 1.
- The hole is not well confined in the dot and the mixing term R_s must be taken into account. A reduced Zeeman shift at saturation is also expected due to the weak hole confinement.
- Under magnetic field, the giant Zeeman Effect lowers the heavy hole and light hole band edges in the dot increasing V_0. Then, we expect a large influence of the magnetic field, better confining the hole in the quantum dot.

Discussion

After having recalled the influence of the band offset on the hole anisotropy in the dot, we can discuss the experimental values of light hole-heavy hole splitting and of the Zeeman shift at saturation obtained in the different nanowires.

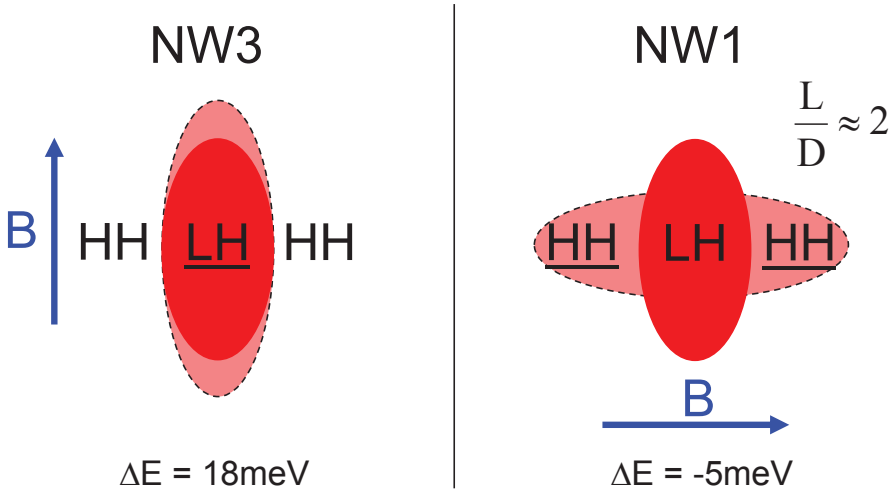

FIGURE 3.24: Main results found on Sample 1: in the case of a light hole exciton fundamental state, the hole is partially delocalized in the pole region while for a heavy hole exciton the hole is delocalized at the equator

In NW1 and NW2, we found a small hole anisotropy ΔE=-5meV with a heavy hole ground state. The hole Zeeman shift at saturation is about 20meV (instead of 44meV as expected for this sample). These values are consistent with a rather small valence band offset shown in Figure 3.23c and Figure 3.23d: the small valence band offset

induces a splitting between heavy hole and light hole states much lower than the band edge splitting (equal to 140meV for $\frac{L}{D} \simeq 2$). Moreover it reverses the order of the hole states expected for a dot with $\frac{L}{D} > 1$. A scheme showing the extension of the hole wavefunction in the equator of the dot is shown in Figure 3.24b (as shown in Figure 3.22, Q_s<0 at the equator and Q_s>0 at the pole leading to heavy holes attracted in the equator plane). The relatively large value of the Zeeman shift at saturation may be due to the increase of the valence band offset under magnetic field (Figure 3.23d).

For NW3, we found a small hole anisotropy ΔE=18meV with a light hole ground state. The hole Zeeman shift at saturation is equal to almost 15meV. These values are also consistent with a small valence band offset: as in the previous case, the small valence band offset induces a reduced heavy hole light hole splitting, but the hole ground state remains a light hole one. The hole Zeeman shift at saturation is close to the value expected for a hole well confined in the dot ($\frac{1}{3}E_{sh} = \frac{44}{3}$meV for light hole and an applied magnetic field along the nanowire axis). We believe that the hole is well confined under magnetic field (Figure 3.23d) but remains weakly confined in zero field (no Magnetic Polaron observed, long exciton lifetime) with a delocalization of the hole along the poles of the dots (attraction of the light hole by Q_s>0 at the poles). As explained in the previous paragraph, the giant Zeeman effect increases the valence band offset which increases the hole confinement in the dot. This property is confirmed by the appearance of the heavy hole exciton line at high magnetic field. Figure 3.24a shows qualitatively the extension of the hole wavefunction along the poles.

Prospects

I would like to conclude by discussing few outlooks of these studies. By depositing the nanowires onto Si_3N_4 membranes and by performing the magneto-optical polarized resolved measurements with a vectorial magnetic field, it would be possible to determine more systematically the nature of the exciton by applying the magnetic field parallel and perpendicular to the nanowire growth axis. With this type of experiment we would determine the value of the hole anisotropy also in a case of large ΔE (even if we don't have the possibility to observe the light hole-heavy hole splitting in the same photoluminescence spectrum for a given magnetic field configuration). By coupling the magneto-optical results with a detailed strain calculation and a precise EDX chemical analysis, it would be possible to reconstruct precisely the properties of

the system. The determination of the strain effects and hence of the hole anisotropy is a really interesting tool for the possible realization of magnetic memories (as you will see in the General Conclusions).

The change in the hole confinement under magnetic field, can be proved by performing time resolved photoluminescence experiments at different fields and measuring the changing in the exciton lifetime.

We showed that the hole may be partially delocalized in the ZnTe barrier leading to a Type II structure. One solution to push back the hole inside the quantum dot is to increase the valence band offset by for example introduce Mg all around the quantum dot. This is what will be presented in the next Chapter.

Chapter 4

Light Hole Magnetic Polaron Formation

4.1 Introduction

In this Chapter we present the Magnetic Polaron formation in a (Cd,Mn)Te quantum dot, inserted in a (Zn,Mg)Te nanowire. We showed in the previous Chapter that the nanowires of Sample 1 present a delocalized hole wavefunction proof of a weak hole confinement inside the quantum dot. The hole Zeeman splitting E_{sh} values were smaller than expected according to the high Mn concentration (10% in the dot), revealed by EDX measurements (see Chapter 2). These results are in agreement also with the time resolved photoluminescence experiments, presented in Chapter 2, that suggest a Type II quantum dot character.
To improve the quantum confinement, we chose to insert Mg all around the quantum dot so that, thanks to the more pronounced valence band offset, the hole confinement in the dot would be stronger (see Figure 4.1).

This sample is called Sample 2 (see Chapter 2), and in this Chapter we describe the photoluminescence studies done on a nanowire of this sample, called MP1 that was studied directly on the as grown sample and identified by the use of a HRSEM. The applied magnetic field, used to characterize the Giant Zeeman effect of this sample, is always parallel to the nanowire growth axis.
We did, on MP1, a power dependence study (like for the nanowires of Sample 1 presented in Chapter 2) to understand the nature of the emitting lines. Moreover, as for

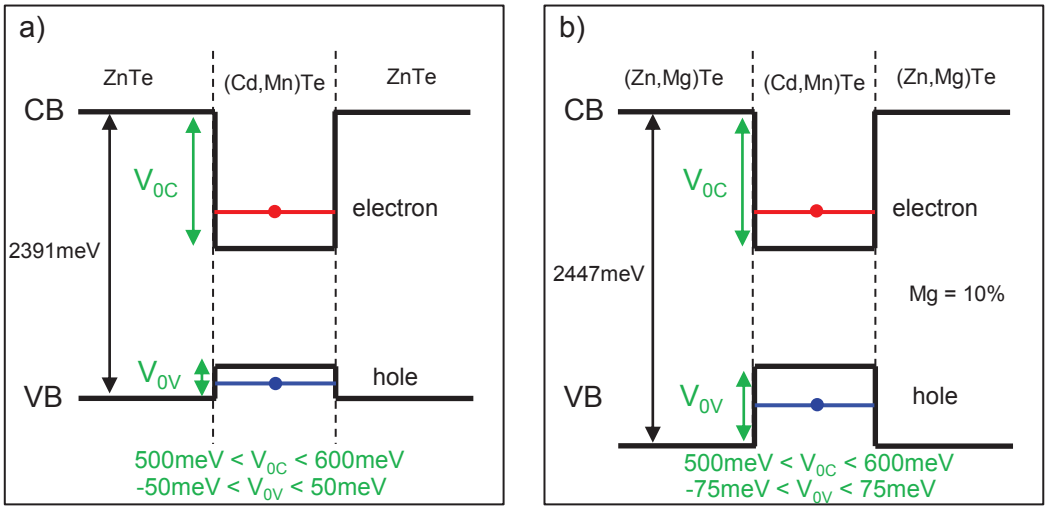

FIGURE 4.1: a) Bands offsets of a (Cd,Mn)Te QD inserted in a ZnTe nanowire b) Bands offsets of a (Cd,Mn)Te QD inserted in a (Zn,Mg)Te nanowire

the nanowires of Sample 1, we use the power dependence study to chose the proper excitation power to avoid the heating of the Mn atoms.

The Chapter is organized as follows: Section 4.2 presents the experimental measurements done on the nanowire MP1. In the first part we show the power dependence measurements used to identify the exciton emission and the photoluminescence studies done as function of the sample's temperature to retrieve its characteristic temperature fingerprint (see Chapter 1). After, we discuss time resolved photoluminescence experiments, with a temporal resolution of 80ps recorded with a micro-PL set up equipped with a streak camera. With these measurements, we extract the characteristic time τ_f of the Magnetic Polaron formation and its energy E_P. At the end of Section 4.2, we show the magneto-optical studies, done on the nanowire, at different temperatures, in order to retrieve the hole anisotropy ΔE and to check the good incorporation of the Mn atoms as done for the nanowires presented in Chapter 3.

The second part of the Chapter consists in Section 4.3: we present a theoretical model used to describe the temperature dependence data, the time resolved photoluminescence measurements and the magneto-optical studies. We used the same set of parameters to fit all the experimental data in order to be the most consistent as we could. This model is based on the calculation of the total free energy of a (Cd,Mn)Te quantum dot: we will show how to use it to determine the magnetic moment magnitude and orientation with respect to the quantization axis, for any given values of the temperature and the applied magnetic field.

4.2 Experimental results

4.2.1 MP1 emission spectrum

In this Section we present the power dependence studies done on MP1 in order to characterize the emission properties of the (Cd,Mn)Te quantum dot. The photoluminescence results, recorded at 5K, are shown in Figure 4.2.

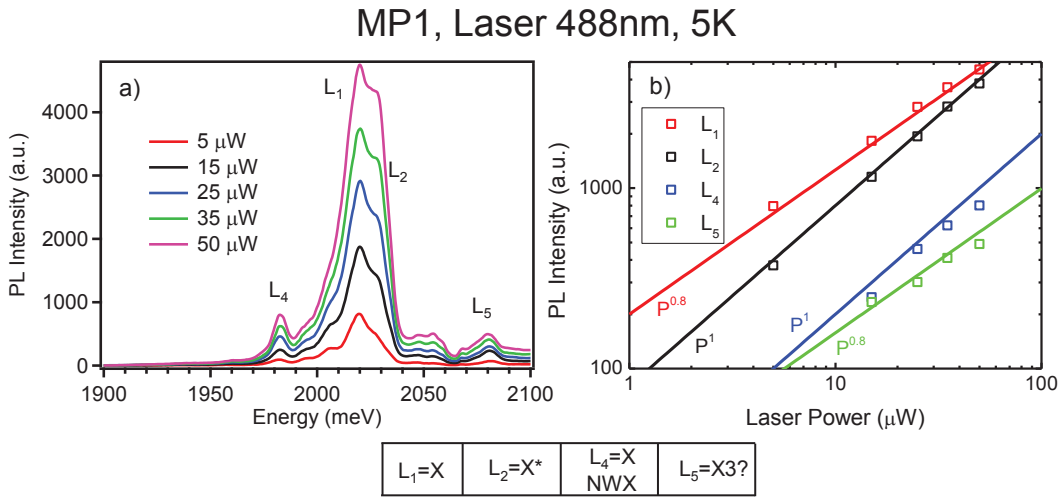

FIGURE 4.2: a) MP1 quantum dot emission spectra at different excitation powers b) PL intensities of the main lines versus the excitation power (the component L_3 will appear in the streak camera measurements, shown later in this Chapter)

Like for the nanowires of Sample 1, described in Chapter 2 and in Chapter 3, the spectrum at low power is broad and composed of different emitting lines from which we can easily identified two main components L_1 and L_2 by a Gaussian fit. If we increase the excitation power, it is possible to observe other photoluminescence lines called L_4 and L_5. The intensities of these lines as a function of the laser power are traced in Figure 4.2b.

First it is notable that the dependencies, on the laser power, of the two components L_1 and L_2 are not very different. The L_2 component is growing a bit faster in power compared to L_1 and we can see that at higher power we would have also a crossing of the intensities: the spectrum would be then dominated by the L_2 state. The L_1 component may be attributed to the neutral exciton state X, whereas L_2 could be attributed to an excited state noted X^* (a charged excitonic state for instance).

The L_4 emission component is probably associated with a different exciton state: as you will see in the following, it could be attributed to the excitonic state of another

nanowire, called NWX. These measurements were in fact taken in a high density region and then it is possible to have contributions coming from other nanowires (we tried our best to spatially localized the emission of just MP1 using diaphragms but it is impossible to cut completely the emission of a very nearby object without affecting the collection of MP1 signal).
To conclude this part I would like to discuss the state described by the L_5 photoluminescence line. It is difficult to determine the nature of this state: the dependency on the laser power is not superlinear but the separation in energy from the state L_1, $60meV$, is comparable to what has been observed for the triexciton for all the other nanowires of Sample 1. We could suppose that the maximum laser power, that we have used, was not sufficient to start to populate this excited level but however, from just these considerations, we cannot attribute the triexciton state to the L_5 photoluminescence line.
Nevertheless, like for all the studied nanowires of this thesis, we will focus our attention on the fundamental ground state L_1.

4.2.2 Fingerprint of the Magnetic Polaron formation

As mentioned in Chapter 1 and in Chapter 3, there are two different ways, using cw measurements, to characterize the exchange interaction between Mn atoms and the photocreated electron-hole pair inside the quantum dot. The first one is to perform photoluminescence studies under magnetic field: by applying a magnetic field we polarize the Mn spins and this polarization induces a Zeeman shift due to the exchange interaction between the Mn spins and the exciton ones (this is the so called Excitonic Giant Zeeman effect). The second way to study the exchange interaction between the Mn atoms and the electron-hole pair, is to exploit the zero field Mn spins polarization induced by the exchange field of the exciton: this is the well known Exciton Magnetic Polaron (EMP) (for a review of some experiments done to study the properties of the Magnetic Polaron state see Chapter 1, Section 1.4). To characterize the EMP formation, using cw measurements, we need to perform photoluminescence experiments at different temperatures (see Figure 4.3).

Figure 4.3a shows the photoluminescence spectra of MP1 at different temperatures, with the doublet composed by the components L_1 and L_2 discussed in the previous paragraph.
Figure 4.3b shows the photoluminescence spectra of a CdTe quantum dot, inserted

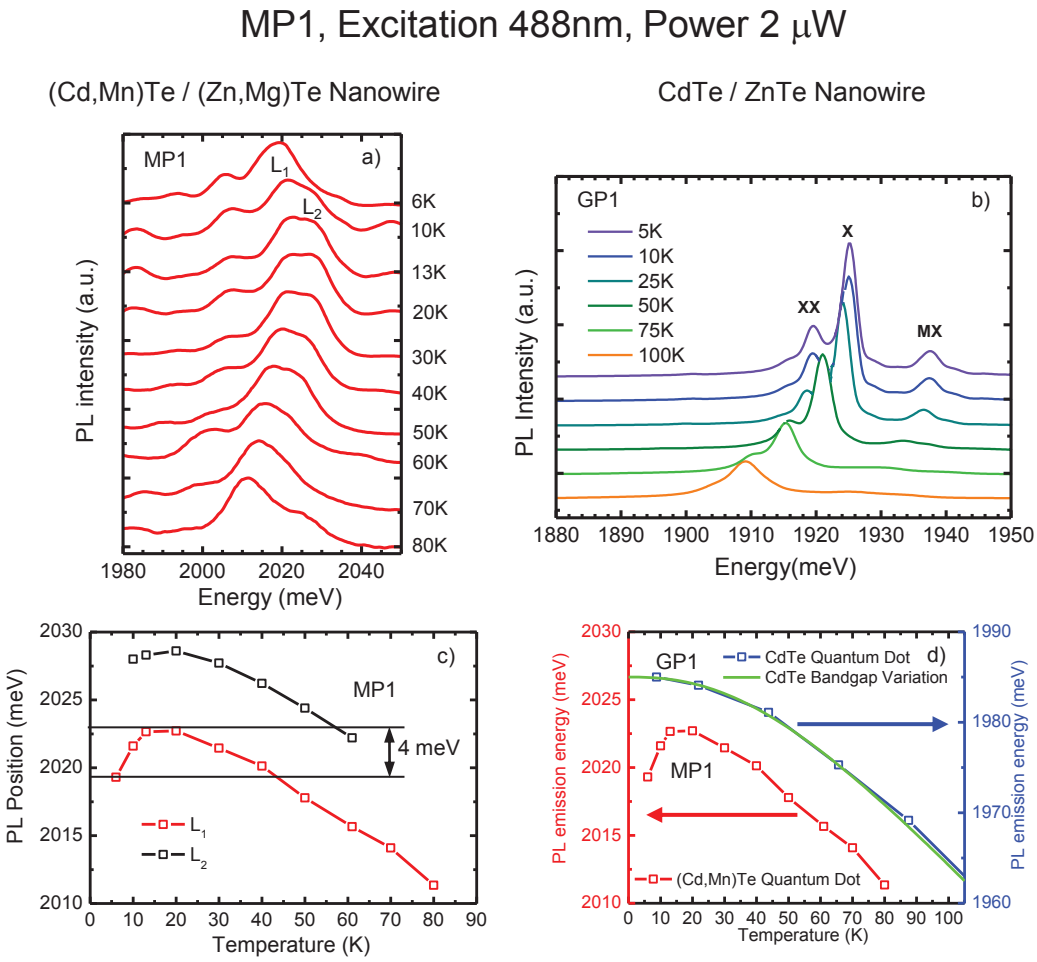

FIGURE 4.3: Photoluminescence spectra at different temperatures of a) the (Cd,Mn)Te QD of MP1, from 6K to 80K b) a CdTe QD in a ZnTe nanowire, from 5K to 100K taken from [17] c) Energy of L_1 and L_2 in a), as a function of temperature d) Energy of L_1 in a) and X in b), as a function of temperature

in a ZnTe nanowire, (for the complete overview see [17]) as function of the temperature, from 5K to 100K. The spectrum at 5K is dominated by the excitonic line X: at low temperature, it is possible also to observe the biexcitonic state XX and a multiexcitonic line MX.

The evolution in temperature of the two quantum dots is different. If we compare first the spectra at the lowest temperature (Figure 4.3a,b), we can see that there is a big difference in the linewidth: MP1 presents a broader excitonic line (around 10meV, in agreement with the expected linewidth for a 10% Mn concentrated quantum dot as discussed in Chapter 2) compared to the excitonic line of the sample without Mn (around 3meV). This broadening is induced by the spin fluctuations of the Mn atoms incorporated inside the quantum dot [72]. Second, the temperature evolution of the two excitonic lines (Figure 4.3c,d) is different. The exciton X of the sample with a

pure CdTe quantum dot is following the Varshni-like monotonous temperature dependence (following the bandgap variation of the quantum dot, see Section 4.7). The excitonic line L_1 of MP1 presents a non-monotonous variation, with a red shift when the sample's temperature decreases below 20K. This red shift is the fingerprint of a Magnetic Polaron formation (see Chapter 1).
The red shift of the excitonic line shows that the system is gaining energy: we are in fact in a regime where the Mn atoms become polarized by the sp-d exchange interaction with the exciton. It is possible to have a first estimate of the Magnetic Polaron energy by looking at the value of the red shift, that is around 4meV for MP1 (Figure 4.3b). In the ideal case, this value should give the energy of the Magnetic Polaron but we should not forget that we are using excitons. The formation time of the Magnetic Polaron state may be limited by the lifetime of the exciton (the recombination time of the electron-hole pair). To be not limited by the exciton lifetime we performed time resolved measurements on MP1 (see in the following Section).
To conclude this Section we compare the temperature dependence of the photoluminescence spectra of MP1 and NW2 (see Figure 4.4). NW2 is the nanowire of Sample 1 presented in Chapters 2 and Chapter 3.

In both nanowires the excitonic line L_1 presents a non-monotonous temperature behaviour: as already explained, for MP1, the excitonic line start to red shift at 20K with a maximum shift of about 4meV (Figure 4.4c) while for NW2 the line L_1 presents a smaller red shift, of about 0.6meV, that starts at lower temperature 10K (Figure 4.4d). The smaller red shift in temperature of NW2 reveals a much weaker Magnetic Polaron, and for this reason, in the theoretical treatment of the data of Sample 1 (see Chapter 3), it has not been taken into account.
We showed in Chapter 3, for the nanowires of Sample 1, that the hole confinement is not so strong and, as a consequence, the quantum dots present a smaller sp-d exchange interactions between photocarriers and Mn atoms in contrast to the value that is expected for a Mn concentration of 10%. This can explain why the Magnetic Polaron state is not so much pronounced in this sample (see Figure 4.4d). In Sample 2, we added Mg all around the quantum dot to better confine the hole wavefunction in the magnetic quantum dot. The stronger kink in energy, observed from the temperature dependent measurements (Figure 4.4c), could be a first hint of the better hole confinement in the dot: the exchange sp-d interaction in this case is bigger thanks to the better overlap between the hole wavefunction and Mn spins. To be sure about the polaron parameters in Sample 2, we performed time resolved photoluminescence experiments (as already explained in Chapter 2) which will be presented in

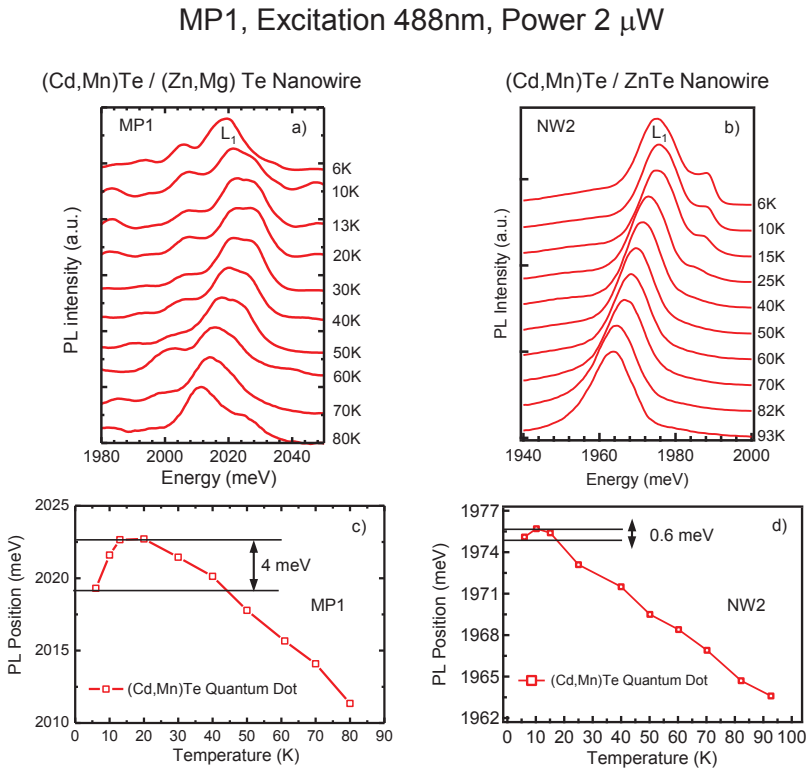

FIGURE 4.4: Photoluminescence spectra at different temperatures of a) the (Cd,Mn)Te QD of MP1, from 6K to 80K b) the (Cd,Mn)Te QD of NW2, from 6K to 93K c) Energy of L_1 in a), as function of the temperature d) Energy of L_1 in b), as function of the temperature

the next Section.

4.2.3 EMP formation revealed by streak camera measurements

4.2.3.1 Identification of the MP1 emission

Nanowire MP1 is located in a high density region of the as-grown sample (see Figure 4.5a,b).

To perform the temperature dependent photoluminescence studies, presented in the previous Section, we use the conventional micro-PL set-up described in Chapter 1. As explained in Chapter 1, the first step of the nanowire analysis, is to identify the nanowires using a HRSEM after the mechanical deposition on the patterned substrate. After the identification of the nanowires, we characterized them by means of different techniques thanks to the use of patterned supports. All the set-ups that we used are equipped with a white light lamp that allows to record optical images of the

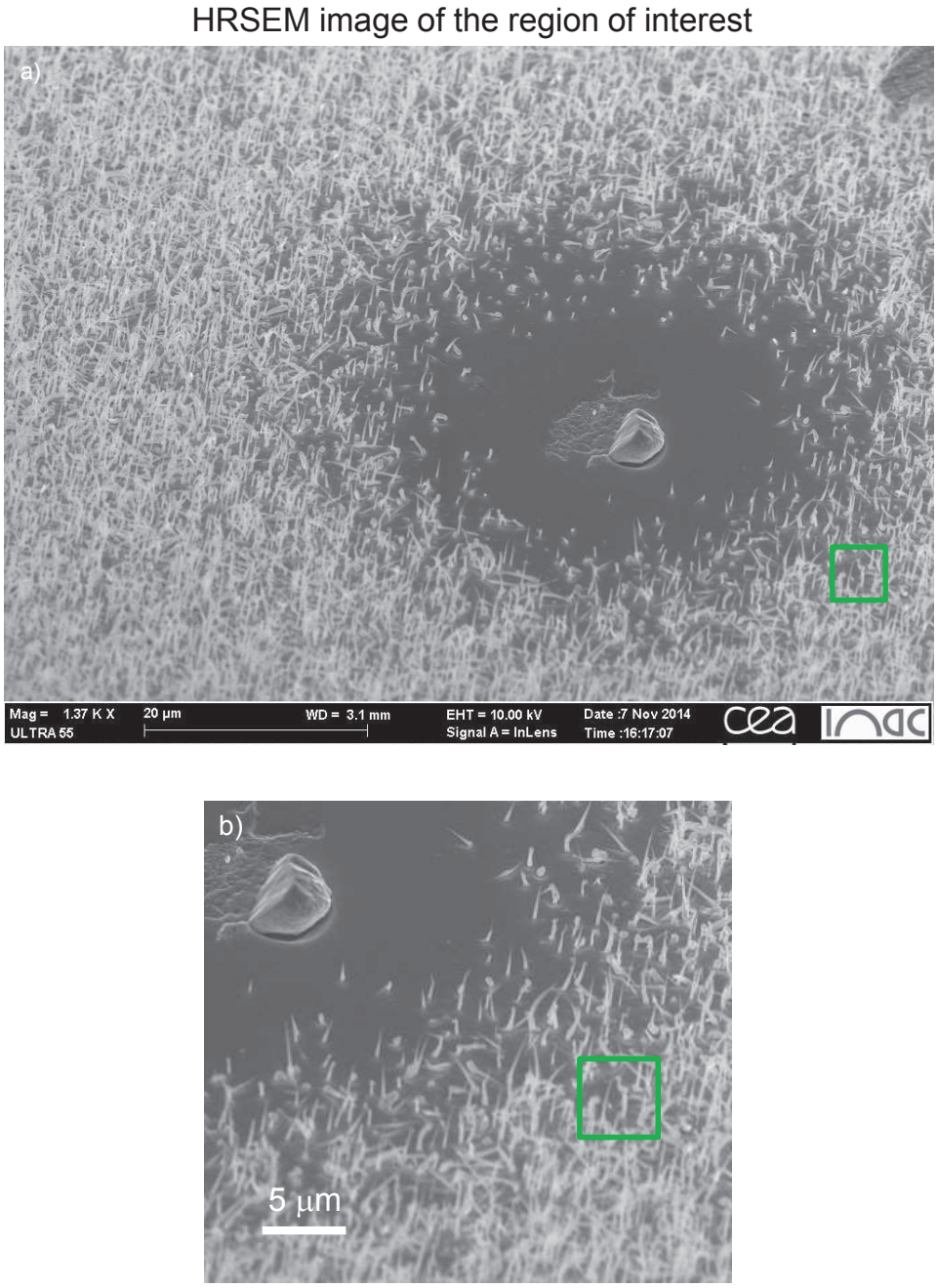

FIGURE 4.5: a) HRSEM image of the region of interest b) Zoom to show the ensemble of nanowires where MP1 has been identified

samples and then to identify the selected nanowires. For MP1 the situation is a little bit more complicated: we chose to study MP1 thanks to its extremely good photoluminescence properties and then, in the present case, as a first step we did photoluminescence measurements. We retrieve the nanowire position by taking some optical images with a white light lamp and afterwards we look at the region of interest using the HRSEM microscope (see Figure 4.5a). As you can see, the density in this region is

not low and due to the fact that the laser spot was $4\mu m^2$ it is not possible to precisely identify which nanowire is MP1 in the green area of Figure 4.5b.
In this Section we present the time resolved photoluminescence experiments that have been done using a micro-PL set-up equipped with a streak camera (see Chapter 1). We used a white light lamp to position the laser spot in the region of interest, where we previously identified MP1 (green square in Figure 4.5b). Then, the collected signal was analyzed by a spectrometer equipped with a CCD camera. We took different CCD images and we compared the recorded spectra to the ones presented in the previous Section. The CCD images, taken in this set-up, associated to MP1 are shown in Figure 4.6.

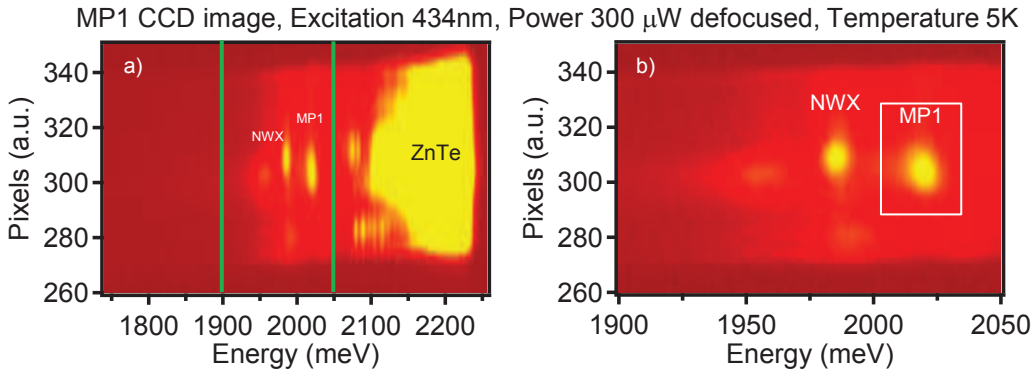

FIGURE 4.6: a) Image of the CCD signal recorded in the Magnetic Polaron region b) Zoom on the (Cd,Mn)Te emission signal

As you can see from Figure 4.6, due to the use of a few μm^2 wide laser spot, differents photoluminescence signals are recorded. Figure 4.6 shows the signal associated to MP1 and the excitonic emission of another nanowire called NWX. Moreover it is also possible to see the broad ZnTe emission that is composed by the contribution of all the nanowires excited in this region.

Figure 4.7 presents the comparison between two PL spectra taken in the two different set-ups (cw micro-PL and time resolved photoluminescence set-up): the superimposition of the two CCD spectrum is traced. The blue signal is the spectrum acquired during the time resolved measurements while the green one is relative to the temperature dependent studies presented in the previous Section. We can see that the superimposition between the spectra is almost perfect for the L_1 component (excitonic state).
If we look now more carefully at the spectrum obtained from the CCD (Figure 4.6) we see that it is composed by more emitting states (see Figure 4.7b). The spectrum is composed by three different states called L_1, L_3 and L_4, identified by fitting the

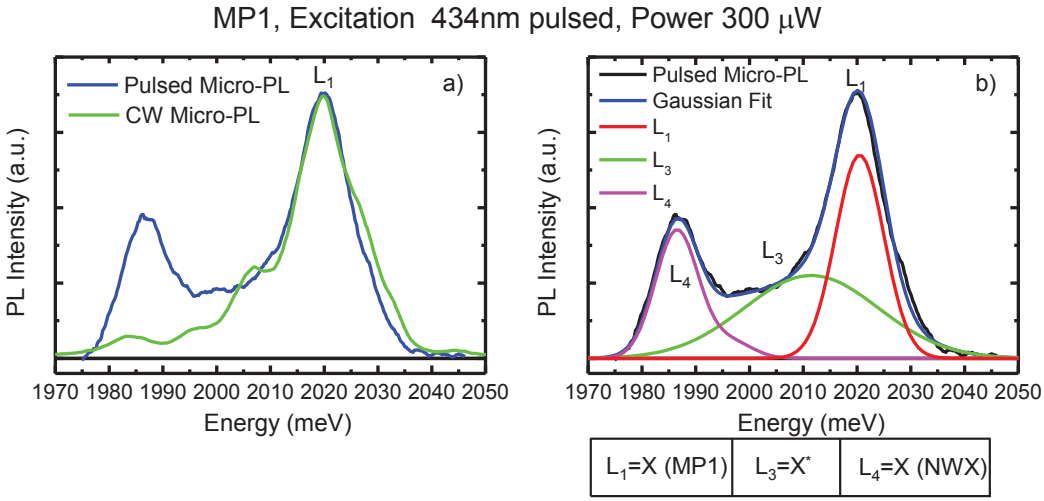

FIGURE 4.7: a) Comparison of the MP1 signals taken in the two different set-ups b) Gaussian fit of the MP1 spectrum showing that is composed by the three components L_1, L_3 and L_4

spectrum with three Gaussian functions. If we look back to the Figure 4.7a, it is clear that the states L_3 and L_4 can not be identified on the spectrum recorded during the temperature dependent studies. This is because when we performed this set of measurements, we used a more focused laser ($2\mu m^2$ instead of $4\mu m^2$) and we were able to select and study just the excitonic state L_1. When we did the time resolved photoluminescence experiments, we used a more defocused laser (to be able to retrieve easily the previously identified MP1) and consequently there are emitting states associated to different nanowires. The L_4 component is in fact the excitonic signal coming from the nanowire NWX (see Figure 4.6).

4.2.3.2 Time Resolved Photoluminescence experiments at 5K

To extract the correct value of the exciton Magnetic Polaron energy, it is necessary to perform time resolved photoluminescence measurements to be not limited by the exciton lifetime. We took for MP1 transient spectra by the use of micro-PL set-up, described in Chapter 1, equipped with a streak camera. The combined use of a spectrometer and a streak camera allows us to resolve the spectra both in energy and in time with a 80ps temporal resolution and with a total temporal window of about 2ns. To be able to record the transient shift of the excitonic photoluminescence, it is necessary to use a pulsed laser. In fact, by the synchronization of the laser with the streak camera, it is possible to follow the photoluminescence displacement that is linked to the magnetization of the Mn atoms, after the creation of an electron-hole pair inside

the quantum dot done by one laser pulse at the initial time t=0ps. The time resolved measurements done on MP1, recorded at 5K, are shown in Figure 4.8.

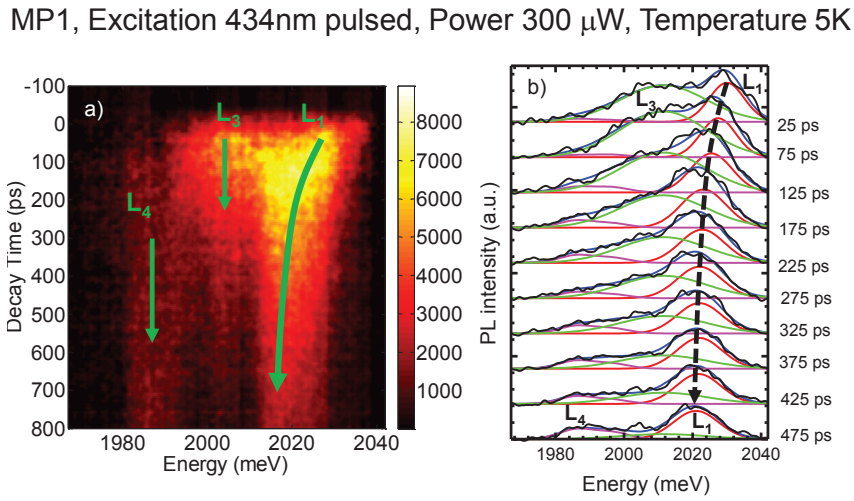

FIGURE 4.8: a) Streak camera image showing the transient map of the photoluminescence spectrum from 0ps to 800ps b) Some selected slices of a), showing the time evolution of the photoluminescence spectrum and the three components L_1, L_3 and L_4, taken each 50ps

Figure 4.8a presents the temporal evolution of the MP1 photoluminescence spectrum and the time evolution of the three components L_1, L_3 and L_4. From the Figure is clear that the excitonic line L_1 is red shifting in time while the other emission states don't move in energy. To be able to quantitatively analyze the energy shift of L_1, the transient image of Figure 4.8a was cutted off and divided in slices. In Figure 4.8b some selected slices of Figure 4.8a are plotted at different times: the spectra have been fitted using Gaussian functions with the same fitting parameters used to fit the first slice at t=0 (the spectrum in Figure 4.7b is the result of the integration of all the slices at different times). Thanks to this fit, we follow more easily the different time evolutions of the three components: we can see in fact that the excitonic line L_1 is red shifting in time, reaching a maximum shift of about 13meV while L_3 and L_4 don't move in energy. The most interesting features of the three components L_1, L_3 and L_4, as function of the time, are summarized in Figure 4.9. We can see that the lifetime of the three states are really different: L_3 has a very fast decay time while the excitonic state L_1 is more stable in time (see Figure 4.9b). The L_4 component has a very long decay time but it is good to remember that it is coming from a different emitting nanowire NWX and so we will not analyze it in details. We will analyze the decay time and transient energy shift of L_1 for three different temperatures in the next Section.

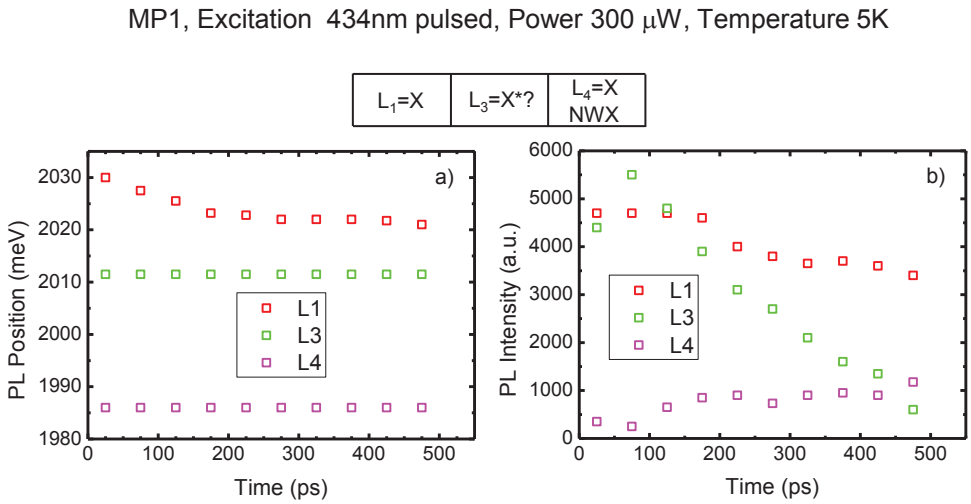

FIGURE 4.9: a) Photoluminescence emission energy as a function of the time for the three components L_1, L_3 and L_4 b) Photoluminescence emission intensity as a function of the time for the three components L_1, L_3 and L_4

4.2.3.3 Extraction of the Magnetic Polaron parameters

In this Section we show how to extract the Magnetic Polaron parameters for the nanowire MP1. We acquired streak camera images at two other temperatures (28K and 46K) in order to study how the temperature affects the polarization of the Mn spins. The images are shown in Figure 4.10a,c. Also for these two set of data, we select slices at different times (see Figure 4.10b,d): it is notable that the excitonic line L_1 is still red shifting in time, but its amplitude is reduced when the temperature increases. At 5K the maximum shift of L_1 was around 13meV while at 46K it is almost 4meV: the polarization of the Mn spins is more and more reduced due to the increase of the temperature and this behaviour is reflected in the smaller red shift of the excitonic line L_1. From Figure 4.10 we can observe also that the L_4 component, associated to the nanowire NWX, is still there and doesn't move in time. The L_3 state is weak for the data taken at 28K and invisible for the ones at 46K (in comparison to the measurements taken at 5K).

It has been shown here and in the previous Section that due to the presence of the L_3 state, that is not moving in time, it is difficult to easily identify the position of the excitonic state L_1 without fitting it systematically. Now we present the data where the component L_3 has been removed, after having being fitted for all the studied temperatures. The result of this data treatment is shown in Figure 4.11 for all the studied temperatures.

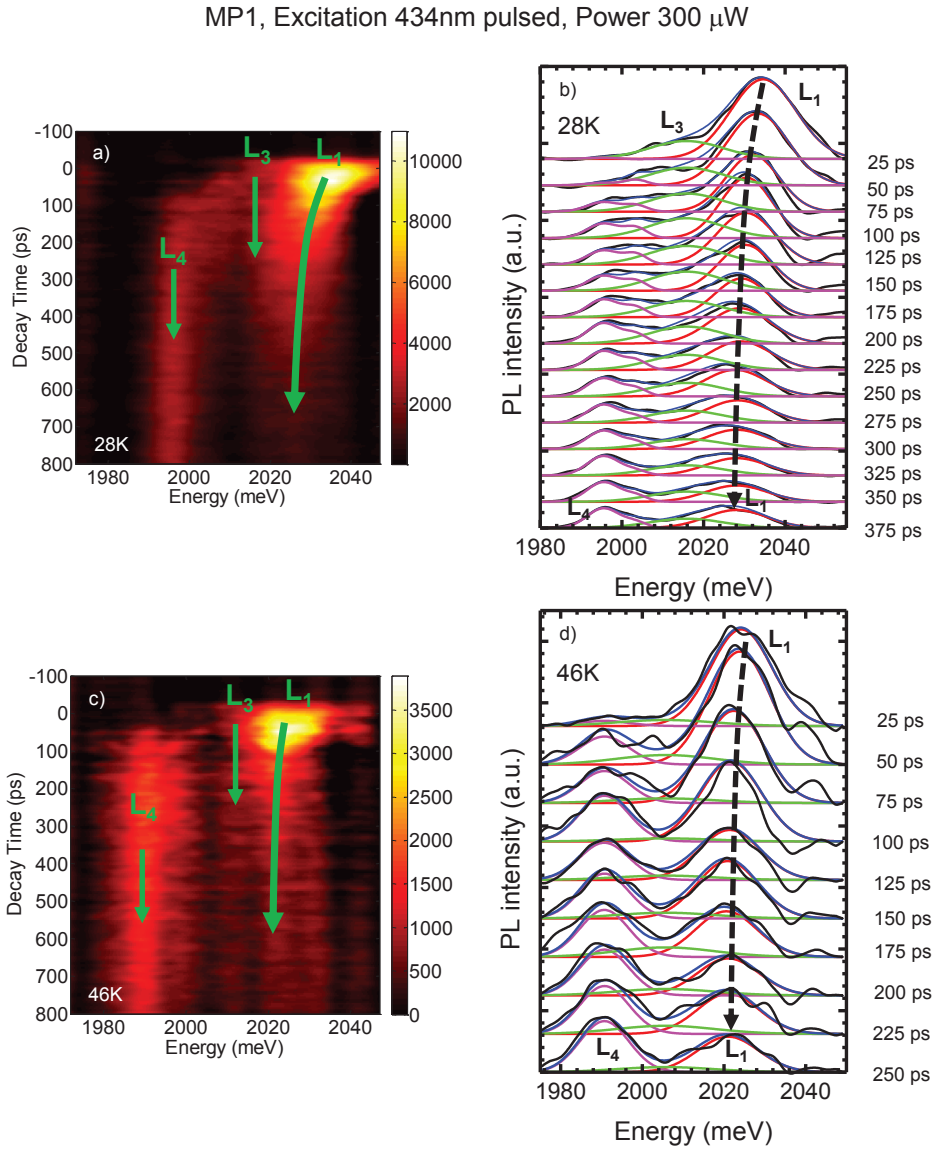

FIGURE 4.10: Streak camera images showing the transient map of the photoluminescence spectrum from 0ps to 800ps for a) 28K c) 46K. Some selected slices, as a function of time, showing the evolution of the three components L_1, L_3 and L_4, taken each 25ps for b) 28K d) 46K.

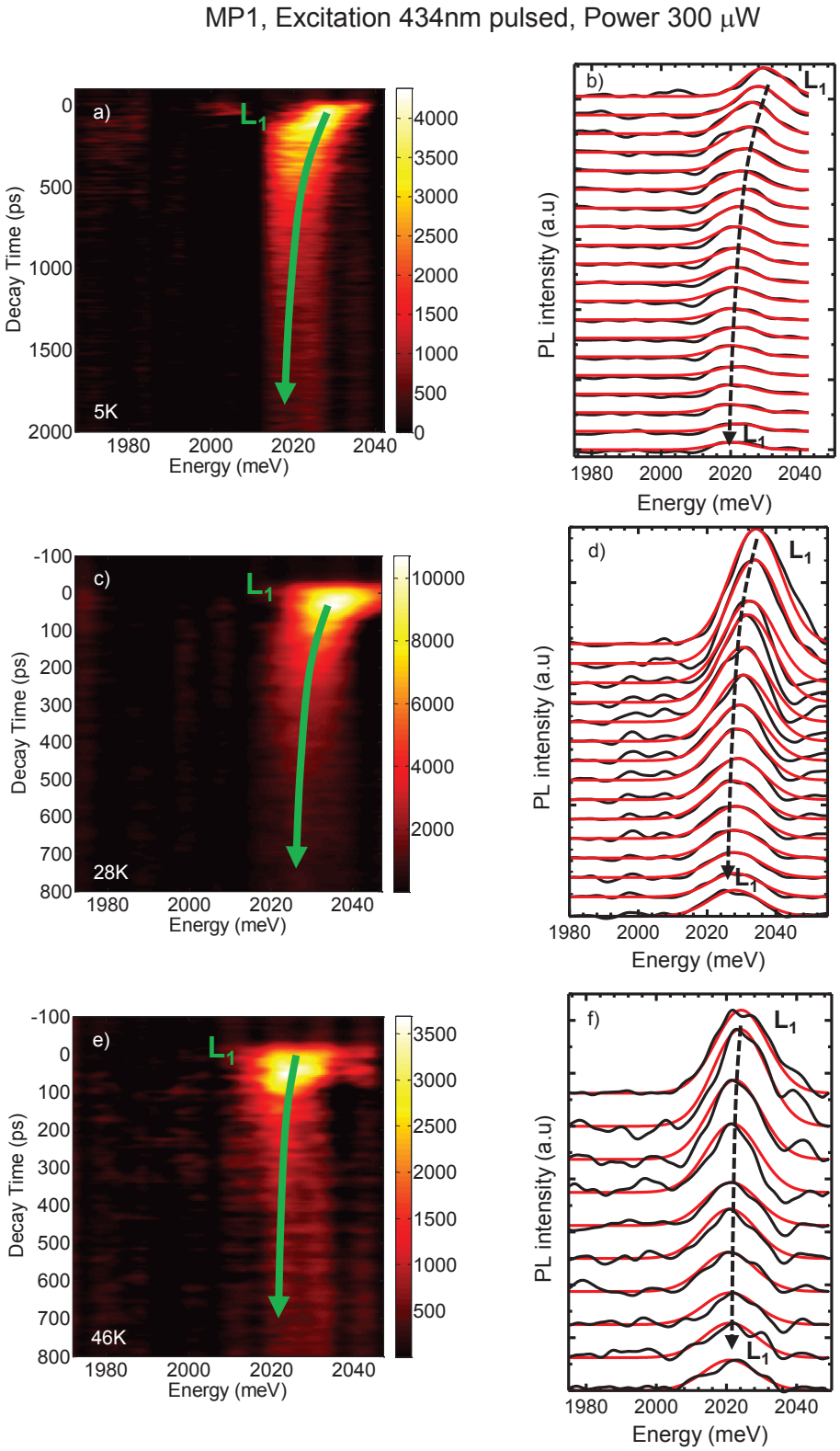

FIGURE 4.11: Streak camera images showing the transient map of just the L_1 line of MP1 at a) 5K (from 0 up to 2ns) c) 28K (from 0 up to 800ps) e) 46K (from 0 up to 800ps). Some selected slices, as a function of time, showing the evolution of L_1, taken each 25ps, for b) 5K d) 28K f) 46K.

Since all the data at different temperatures have been presented, it is possible to extract the Magnetic Polaron parameters. The summary containing the key features of the excitonic line L_1 is shown in Figure 4.12.

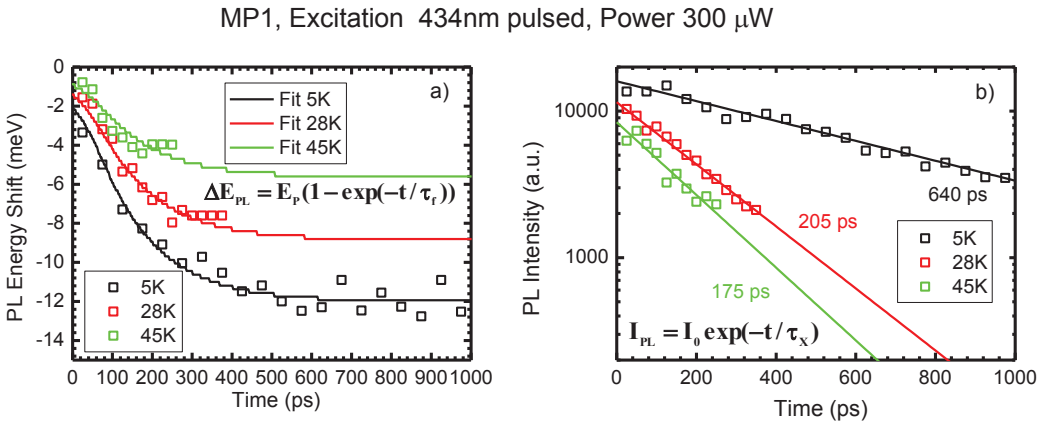

FIGURE 4.12: a) L_1 emission energy positions vs time for the three different temperatures b) Decay Time of the L_1 state for the three different temperatures

From the fit of the photoluminescence emission energy as function of the time, using an exponential law $\Delta E_{PL} = E_P(1-\exp(-t/\tau_f))$ (see Chapter 1), it is possible to retrieve the Magnetic Polaron Energy E_P and the characteristic formation time τ_f. From Figure 4.12a it is clear that the Magnetic Polaron energy (MPE) strongly depends on the Mn temperature. For higher temperature the MPE is strongly reduced and around 46K the Magnetic Polaron state is almost suppressed.

TABLE 4.1: Magnetic Polaron parameters

5K	E_P=13meV	τ_f=90ps
28K	E_P=8.5meV	τ_f=90ps
46K	E_P=5.5meV	τ_f=90ps

In Figure 4.12b the intensity decay for the L_1 component versus time is plotted for the three different temperatures. By fitting the photoluminescence intensity with a mono-exponential decay $I = I_0\exp(-t/\tau_X)$ it is possible to determine the exciton lifetime at the different temperatures. As expected [82, 83] the decay time is strongly reduced by increasing the temperature: in fact with the increase of the temperature more and more non radiative de-excitation channels are favorable, leading to a decrease of the total radiative lifetime. The decay time τ_X is given in the following table (for the three different temperatures):

TABLE 4.2: Exciton lifetimes at different temperatures

5K	τ_X=640ps
28K	τ_X=205ps
46K	τ_X=175ps

The decay time (τ_X) at 5K is around 640ps: this value is much bigger than the characteristic Magnetic Polaron formation time that is around 90ps. This means that we are in presence of a fully formed and stable Magnetic Polaron state.
The decay time at 5K remains relatively large if we compare it to a Type I magnetic quantum dot one, that is around 200ps [17] but it is smaller compared to the values found for the nanowires of Sample 1 (800ps and 1.7ns), shown in Chapter 2. This means that we can draw two conclusions: first the incorporation of Mg all around the quantum dot helped to better confine the hole in the dot, achieving a stronger and more stable Magnetic Polaron state. As a second point, we see that the exciton lifetime is still quite big compare to a Type I quantum dot: this means that the hole may be still partially delocalized and then it is possible to increase even more the coupling with the Mn atoms by adding for example more Mg around the quantum dot.

4.2.4 Excitonic Giant Zeeman Effect

In this Section we present the magneto-optical studies done on MP1. The (Cd,Mn)Te quantum dot emission was studied by the use of the magneto-optical set-up described in Chapter 1. To check the good incorporation of the Mn atoms inside the quantum dot, we analyzed the Zeeman shift of the exciton line L_1 that manifests itself through Giant Zeeman effect (see Chapter 3). We performed photoluminescence measurements under magnetic field in a Faraday configuration: the excitation and the detection are parallel to the magnetic field that is applied parallel to the nanowire growth axis.
Figure 4.13 shows the spectra evolution, of MP1, at 8K and 15K, with the applied magnetic field. At zero magnetic field, we retrieve a spectrum composed mainly by two components L_1 and L_2. The maximum value of the applied magnetic field is 11T for the measurements taken at 8K while for the one at 15K we stopped at 8.5T (due to the difficulty to retrieve the photoluminescence signal of the nanowire as you will see below).
From Figure 4.13 a,b it is clear that both components are red shifting under magnetic

field exhibiting a Giant Zeeman effect but with very different saturation values: for L_1 it is about 22meV at 11T while for L_2 we have a smaller value, close to 16meV (see Figure 4.13). Like in Chapter 3, to check that the red shift is related to the coupling between the photocarriers and the Mn atoms, we took another set of magneto-optical measurements at a different temperature: 15K (see Figure 4.13b). As expected, the amplitude of the excitonic Giant Zeeman shift is slightly reduced for both components L_1 and L_2.

Doing magneto-optical measurements on a dense region (like for MP1) is a very difficult experiment. By applying a magnetic field we change the coupling between the laser and the nanowire: the piezoelectric scanner in fact slightly moves changing the position of the nanowire. It is necessary then to optimize the exciton PL signal at each applied magnetic field without "jumping" and then measuring another nanowire (to avoid the Mn heating effect, it is not possible to increase the laser excitation power). When the temperature is increased, more states are excited making even more difficult to catch just the MP1 signal (for this reason we stopped at 8.5T for the measurements at 15K).

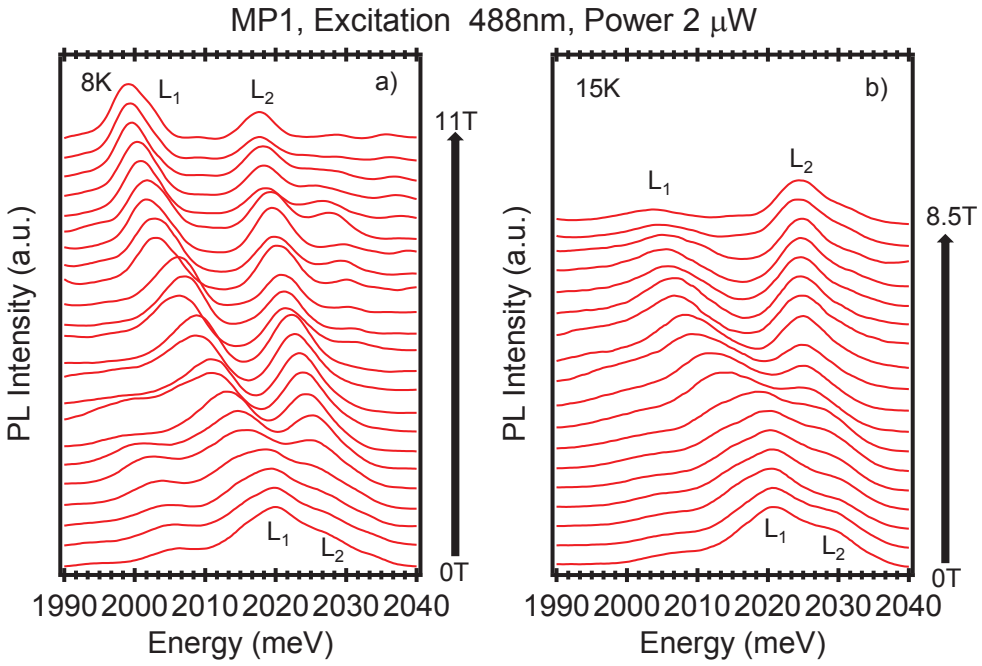

FIGURE 4.13: (Cd,Mn)Te QD emission studied under magnetic field, with a minimum step of 0.5T at a) 8K b) 15K

We summarize the magneto-optical results in Figure 4.14. To correctly trace the energy positions of the two components L_1 and L_2, we used a Gaussian fit shown in Figure 4.14a. We retrace all the data extracted from the micro-PL studies, under magnetic field, as function of $\frac{5\mu_B B}{k_B T_{Mn}}$ (see Figure 4.14b,c). The Mn temperature is shown in

bracket.
Like for NW1,NW2 and NW3, also MP1 shows a clear dependence on $\frac{B}{T_{Mn}}$: the measurements taken at 8K and 15K are in fact superimposed highlighting the presence of Mn atoms inside the (Cd,Mn)Te quantum dot.
We tried also to fit this set of data using a Brillouin function: as explained in Chapter 3 when the applied magnetic field is parallel to the nanowire growth axis, it doesn't matter if the fundamental state of the quantum dot is a light or a heavy hole exciton. In both cases in fact, the first allowed transition (the measurements were done at very low temperature and we can consider just the first transition) should be modeled by a Brillouin function. For this particular nanowire, where a Magnetic Polaron has been found, the Brillouin function should be translated along the x axis by the internal magnetic field generated by the zero field magnetic moment of the Magnetic Polaron (see Chapter 1). Figure 4.14d,e, shows that, for low magnetic field, there is a strong deviation from a Brillouin function, highlighting an uncommon behaviour. The magnetic dependence of this nanowire is then more complicated compared to the ones described in Chapter 3 and it will be explained in the last part of this Chapter where all the magneto-optical and temperature dependent studies will be analyzed using a theoretical model describing the Magnetic Polaron formation under magnetic field.

Finally the L_2 component has a much smaller saturation energy (10 meV), compared to L_1 (see Figure 4.14c,e) and it is possible to fit the exciton Giant Zeeman effect with a Brillouin function. The behaviour then, under an applied magnetic field, is more common but unfortunately without any supplementary measurements it is difficult to understand the nature of the state associated to the L_2 component.

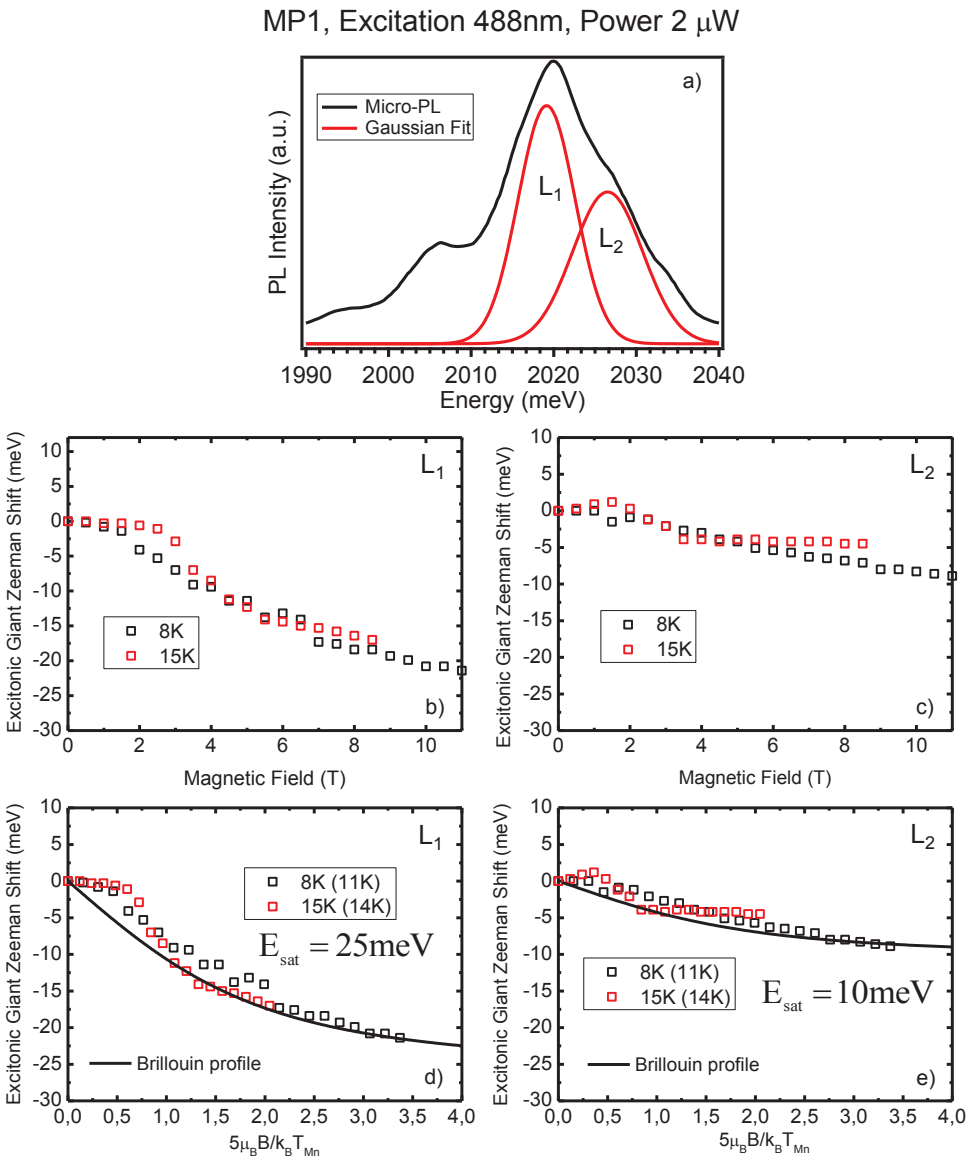

FIGURE 4.14: a) Gaussian fit of the spectra at 8K with no magnetic field b) L_1 emission energy positions vs magnetic field for different temperatures c) L_2 emission energy positions vs magnetic field for different temperatures d) L_1 emission energy positions vs $\frac{5\mu_B B}{k_B T_{Mn}}$ for different temperatures e) L_2 emission energy positions vs $\frac{5\mu_B B}{k_B T_{Mn}}$ for different temperatures

4.3 Magnetic Polaron model based on total free energy

In this Section of Chapter 4 we show how to analyze and understand the data taken on MP1.

The approach that we will present is based on the calculation of the quantum dot free energy introduced in [9], this paper was presented in Chapter 1 in Section 1.4. In [9], the free energy approach is used to calculate the probability distribution of the spin splitting for a donor (an electron localized on a shallow donor) Magnetic Polaron in a bulk diluted magnetic semiconductors (Cd,Mn)Se crystals (see Figure 4.15).

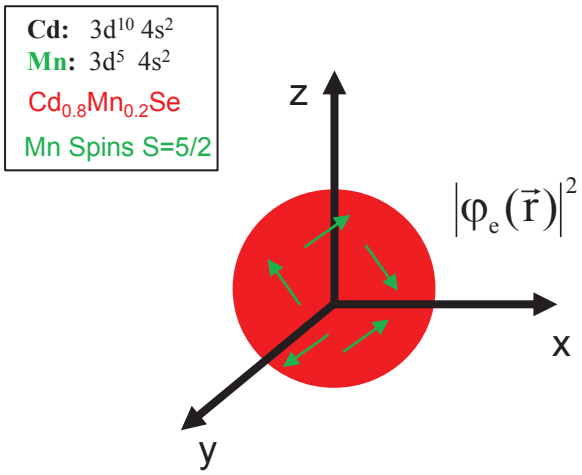

FIGURE 4.15: (Cd,Mn)Se quantum dot of [9]

For a donor, we have an isotropic configuration with a spherical symmetry. In the paper, the thermodynamic fluctuations of the magnetization are taken into account: this is a really important point, as you will see, because it allows to determine all the possible configurations of the total magnetic moment.

In this Section we are going to extend the model introduced in [9] in order to describe the Magnetic Polaron of an exciton in a (Cd,Mn)Te magnetic quantum dot. We will also add the contribution of the hole anisotropy (see Figure 4.16). As you will see, this approach is really powerful compared to the commonly used Mean Field Approximation (MFA, see Chapter 1) where the magnetic fluctuations are not taken into account: MFA supposes in fact that the system remains at very low temperature. On the contrary, the free energy approach is valid at low and high temperatures: it is then very useful to model and analyze the micro-PL measurements taken at different temperatures. With this model, we will be able to determine the direction and the magnitude of the quantum dot magnetic moment, respect to the nanowire axis,

for a chosen value of the applied magnetic field or a given temperature.
Considering that we studied the properties of the Magnetic Polaron formation by means of photoluminescence experiments, we will also explain how to calculate the exciton photoluminescence spectrum at different magnetic field and temperatures by using the total free energy.
In the first part we introduce a free energy approach used to model the system and understand the evolution in time of the Magnetic Polaron.
In the second part we use the same free energy approach to understand the evolution of the Magnetic Polaron magnetization when we apply a magnetic field along the NW growth axis.

4.3.1 Total free energy

4.3.1.1 Introduction

Figure 4.16 shows the (Cd,Mn)Te quantum dot system. In the quantum dot, we have N_{eff} Mn atoms that have spin $S = \frac{5}{2}$.

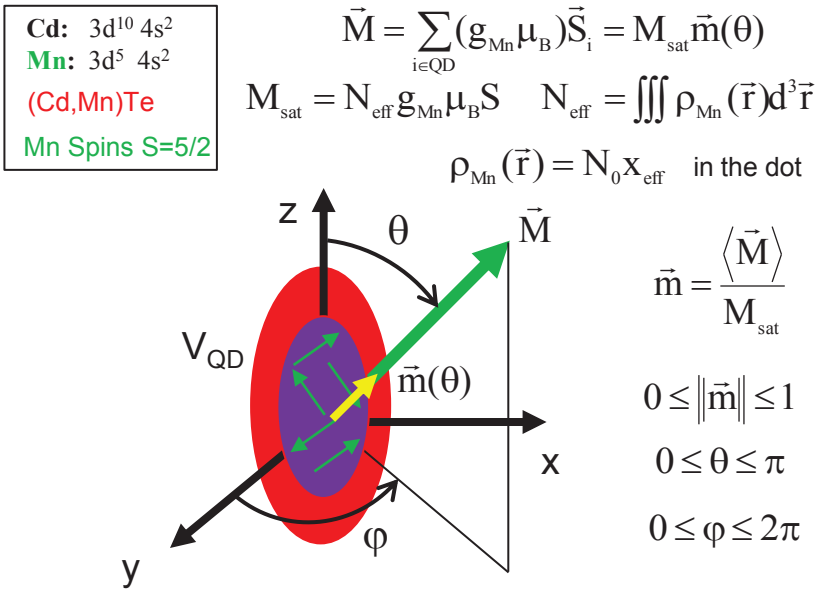

FIGURE 4.16: (Cd,Mn)Te quantum dot in spherical coordinates

There are exchange interactions between the Mn spins and the photocreated excitons. These exchange interactions are described by a Kondo-like Hamiltonian, introduced in Chapter 1, given by:

$$H_{sp-d} = -\alpha \sum_{\vec{R}_i} \vec{S}_i \cdot \vec{\sigma}_e |\psi_e(\vec{R}_i)|^2 - \frac{\beta}{3} \sum_{\vec{R}_i} \vec{S}_i \cdot \vec{J}_h |\psi_h(\vec{R}_i)|^2 \tag{4.1}$$

Where α and β are the exchange constants for electron and hole respectively. $\vec{R}_i$ is the position of the magnetic ions characterized by spin operators $\vec{S}_i$. $\vec{\sigma}_{e_i}$ is the spin operator for the electron and $\vec{J}_{h_i}$ is the kinetic momentum of the hole. $|\psi_e(\vec{R}_i)|^2$ and $|\psi_h(\vec{R}_i)|^2$ are the envelop functions for electron and hole [81] and they take into account the overlap between the carriers wavefunctions and the one of the magnetic impurities (for simplicity we considered the same envelope function for light and heavy hole).
We can define a magnetic moment for the system such as:

$$\vec{M} = \sum_{i \in QD} g_{Mn} \mu_B \vec{S}_i \tag{4.2}$$

The common assumption which is used to simplify the calculation is the so-called "Exchange Box Model" introduced in Chapter 1, Section 1.4.2.1. Usually this model is used with the so called Mean Field Approximation (MFA) that doesn't consider thermal fluctuations (it is supposed to be valid at low temperature).
We extend the model that can be found in [9] for a donor to an anisotropic quantum dot containing a neutral exciton. We will show also that by using this model where the thermal fluctuations are taken into account, it is possible to calculate the photoluminescence spectrum at a given value of magnetic field or temperature.
The main idea is to define the free energy of the system (at a constant volume), described in Figure 4.16, $F(T, \vec{M})$ where T is the temperature and $\vec{M}$ is the magnetic moment of the system. In spherical coordinates, we can write the magnetic moment such as:

$$\vec{M} = M_{sat} \vec{m}(\theta, \varphi) \tag{4.3}$$

Where $M_{sat} = N_{eff} g_{Mn} \mu_B S$ and $0 \leq ||\vec{m}|| \leq 1$. In the following we consider another approximation: we suppose that the system has a circular symmetry, losing then the dependence on the azimuthal angle φ. This assumption is reasonable if we think about the EDX results (see Section 2.1.1.1) where the quantum dot is modeled by an ellipsoid.

For an empty quantum dot, the probability to have a magnetic moment $\vec{M}$ is given by:

$$P\left(\vec{M}\right) = Ae^{-\frac{F(T,\vec{M})}{k_B T}} = P(m,\theta)\begin{cases} 0 \leq m \leq 1 \\ 0 \leq \theta \leq \pi \end{cases} \tag{4.4}$$

With the calculation of $P(m,\theta)$ for different values of (m,θ), it is then possible to reconstruct all the possible configurations for the total magnetic moment $\vec{M}$ in the cylindrical space for an arbitrary value of the applied magnetic field and for any given temperature.

4.3.1.2 Calculation of the Mn spin free energy

In Appendix B we show how to calculate the partition function Z and then all the fundamental quantities like the Helmholtz free energy for a system with a total angular momentum J in an external magnetic field B. We can then use the formula B.5 introduced in Appendix B to calculate the Helmholtz free energy for a (Cd,Mn)Te quantum dot. This system is composed by N paramagnetic spins ($S = -5/2, ..., +5/2$) forming discrete non degenerate quantum states with energies $e_S = g_S \mu_B SB$. Using equation B.4, the expression for $y = g_S \mu_B B\beta$ (where we recall that $\beta = \frac{1}{k_B T_{\text{Mn}}}$) and the Lande g-factor $g_S = 2$ (for Mn) we have for the partition function:

$$Z = \frac{\sinh\left(\frac{6\mu_B B}{k_B T_{\text{Mn}}}\right)}{\sinh\left(\frac{\mu_B B}{k_B T_{\text{Mn}}}\right)} \tag{4.5}$$

It is now possible to write down the Helmholtz free energy $F(T,B)$ and deduce the quantum dot magnetic moment $M(T,B)$ which follows a Brillouin function, using respectively equations B.5 and B.6:

$$F(T,B) = -N_{eff} k_B T_{\text{Mn}} \ln\left[\frac{\sinh\left(\frac{6\mu_B B}{k_B T_{\text{Mn}}}\right)}{\sinh\left(\frac{\mu_B B}{k_B T_{\text{Mn}}}\right)}\right] \tag{4.6}$$

$$M(T,B) = -\left(\frac{\partial F(B,T)}{\partial B}\right)_T = N_{eff} g_{Mn} \mu_B S \mathrm{B}_{5/2}\left[\frac{g_{Mn}\mu_B B}{k_B T_{\mathrm{Mn}}}\right] = M_{sat}\mathrm{B}_{5/2}\left[\frac{g_{Mn}\mu_B B}{k_B T_{\mathrm{Mn}}}\right] \quad (4.7)$$

At this point, it is better to rewrite the free energy $F(T,B)$ as function of the temperature and the magnetic moment $F^*(T,M)$ using a Legendre transform [84, 85]. A Legendre transform enables, in fact, to replace an independent variable of a thermodynamic potential (B in our case) by its conjugate (M): the function produced corresponds to the relevant thermodynamic potential at constant conditions of the new independent variables. It is the same process to retrieve the definition of the free energy F(T,V,N) from the definition of the internal energy E(S,V,N) (in Thermodynamic statistics the transform is used to extract all the principal thermodynamic potential such as the Helmholtz free energy, the Gibbs energy and the Enthalpy):

$$\begin{cases} \mathscr{L}[E(S,V,N)] = F(T,V,N) = E(S^*,V,N) - TS^* \\ \frac{\partial E(S,V,N)}{\partial S}\big|_{S=S^*} = T \end{cases} \quad (4.8)$$

When we describe a magnetic system, we start with the free energy: $F(T,B)_V$ and the definition of the magnetic moment $M = -\left(\frac{\partial F(B,T)}{\partial B}\right)_T$. We can now apply the Legendre transform to the free energy $F(T,B)_V$ to retrieve $F^*(T,M)_V$ by switching the two conjugate variables M and B:

$$\begin{cases} \mathscr{L}[F(T,B)] = F^*(T,M) = F(T,B^*) + MB^* \\ -\frac{\partial F(T,B)}{\partial B}\big|_{B=B^*} = M \end{cases} \quad (4.9)$$

We have then to calculate B^* and substitute it in equation 4.9 to obtain $F^*(T,M)$. B^* is given by (equation 4.7):

$$-\frac{\partial F(T,B)}{\partial B}\big|_{B=B^*} = M \Longrightarrow B^* = \left(\frac{Nk_BT}{M_{sat}}\right)\mathrm{B}_{5/2}^{-1}\left(\frac{M}{M_{sat}}\right) \quad (4.10)$$

Where M_{sat} is defined as $M_{sat} = N_{eff} g_{Mn} \mu_B S$ and $\mathrm{B}_{5/2}^{-1}$ is the reciprocal function of the Brillouin function. The expression for $F^*(T,M)$, that for simplicity will be called

just $F_{Mn}(T,M)$, will be given by substituting the expression of B^* in equation 4.9 leading to:

$$F_{Mn}(T,M) = -N_{eff}k_B T_{\mathrm{Mn}} ln\left[\frac{\sinh\left(\frac{6}{5}\mathrm{B}_{5/2}^{-1}\left(\frac{M}{M_{sat}}\right)\right)}{\sinh\left(\frac{1}{5}\mathrm{B}_{5/2}^{-1}\left(\frac{M}{M_{sat}}\right)\right)}\right] + N_{eff}k_B T_{\mathrm{Mn}}\frac{M}{M_{sat}}\mathrm{B}_{5/2}^{-1}\left(\frac{M}{M_{sat}}\right) \tag{4.11}$$

The expression 4.11, obtained above, is a function of the total magnetic moment magnitude M (it has been derived also in [86]): for a real quantum dot, the free energy depends on the magnetization profile in the dot $\vec{M}(\vec{r})$ with a functional $F(V,T,\vec{M}(\vec{r}))$ which is very difficult to calculate. In the following we will not take into account non uniform magnetization profiles inside the quantum dot.
If an external magnetic field is applied, we have to add also the Mn Zeeman contribution given by:

$$F_S(\vec{M}) = F_{Mn}(\vec{M}) - \vec{M}\cdot\vec{B} = F_{Mn}(\vec{M}) - M_{sat}\vec{m}\cdot\vec{B} \tag{4.12}$$

4.3.1.3 Calculation of the carrier free energy

To describe the Hamiltonian and then the free energy that takes into account the carriers, we use the results presented in Chapter 1 and in Chapter 3. The Hamiltonian of the system is composed by electron, hole exchange terms and an anisotropy term. If we consider the nanowire axis (z axis) as the quantization axis, they are given by:

$$H_{carriers} = \frac{E_{sh}\vec{m}\cdot\vec{J}_h}{3} + E_{se}\vec{m}\cdot\vec{\sigma}_e + \frac{\Delta E}{2}(J_{h_z}^2 - \frac{J(J+1)}{3}) + E_X \tag{4.13}$$

Where $\vec{J}_h$ and $\vec{\sigma}_e$ are the spin operators for hole and electron respectively. E_X is the Hamiltonian that describes the exciton composed by one electron and one hole confined in the quantum dot and coupled by Coulomb interaction. We assume that E_X is constant under magnetic field.

To take into account the carrier free energy noted F_X, we can follow the same procedure shown in Chapter 3. We first calculate the eigenstates and eigenvalues associated to the electron and to the hole E_e, E_h by diagonalizing F_X. We can then write down the expressions for the electron and hole partition functions, using:

$$\begin{aligned} Z_h &= \sum_{j=1}^{4} e^{-E_h(j)/k_B T} \\ Z_e &= \sum_{i=1}^{2} e^{-E_e(i)/k_B T} \end{aligned} \tag{4.14}$$

Where the four hole level and the two electron ones are traced in Figure 4.17.

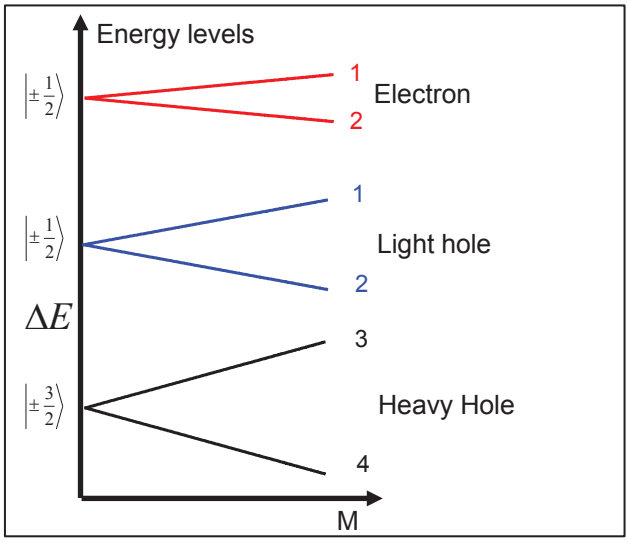

FIGURE 4.17: Electron and Hole level, equation 4.14

With the two partition functions Z_e and Z_h, it is now trivial to extract the Helmholtz Free Energy for the electron and the hole using the equation $F_{e,h} = -Nk_B T \ln Z_{e,h}$:

$$\begin{aligned} F_h &= -k_B T \ln Z_h \\ F_e &= -k_B T \ln Z_e \end{aligned} \tag{4.15}$$

The free energy for the carriers will be then given by the sum of the two free energy of the electron and of the hole and it will be noted F_X:

$$F_X = -k_B T[\ln(Z_h) + \ln(Z_e)] + E_X \tag{4.16}$$

Where E_X is the energy of the exciton (see equation 4.13).

4.3.1.3.1 To summarize

The total free energy ($F_{tot}(\vec{M}) = -k_B T \ln(P[\vec{M}])$) of the occupied quantum dot, describing the Mn magnetic moment fluctuations in the presence of carriers is finally the sum of four terms depending on $\vec{m}$ (unitary vector which gives the orientation of the quantum dot magnetic moment) and E_X that describes just the electron-hole pair:

$$F_{tot}(\vec{M}) = F_{Mn}(\vec{m}) - M_{sat}(\vec{m}\cdot\vec{B}) + E_X + F_e(E_{se}\vec{m}) + F_h(E_{sh}\vec{m}) \tag{4.17}$$

The last two terms of equation 4.17 which take into account the exchange coupling between the electron-hole pair and the Mn atoms and the hole anisotropy are given by:

$$\begin{aligned} F_e(\vec{m}) &= -k_B T \ln Tr_i \left[e^{-\frac{E_{se}\vec{m}\cdot\vec{\sigma}_e}{k_B T}} \right] \\ F_h(\vec{m}) &= -k_B T \ln Tr_j \left[e^{-\frac{E_{sh}\vec{m}\cdot\vec{J}}{3k_B T} + \frac{\Delta E}{2k_B T}\left(J_{hz}^2 - \frac{J(J+1)}{3}\right)} \right] \end{aligned} \tag{4.18}$$

When the quantum dot is empty, the expression for the total free energy will be given by:

$$F_{tot}(\vec{M}) = F_{Mn}(\vec{M}) - M_{sat}(\vec{m}\cdot\vec{B}) \tag{4.19}$$

For an occupied quantum dot, the probability to have a magnetic moment $\vec{M}$ has to be calculated by taking the partial trace of the total free energy $F_{tot}(\vec{M})$ over the

electron operator σ (defined by the index i) and the hole kinetic momentum one J (defined by the index j):

$$P[\vec{M}] = Tr_{i,j}\left[e^{-\frac{F_{\sigma,J}[\vec{M}]}{k_B T}}\right] \tag{4.20}$$

4.3.2 Fitting procedure used with the total free energy

4.3.2.1 Presentation of the model

In the previous Section we recall the expression of the total free energy of a (Cd,Mn)Te quantum dot system (equation 4.17). The power of using the total free energy treatment is that it is possible to calculate the probability that the magnetic moment of the quantum dot is $\vec{M}$, it will be noted $P_{occ}[\vec{M}]$, this was introduced in Section 4.3.1.1. The photoluminescence spectrum associated to $\vec{M}$ can be calculated by the equation:

$$I_{\vec{M}}(\varepsilon) = \sum_{i,j} f_{i,j}\delta(\varepsilon - E_{i,j})P^{eh}_{i,j} \tag{4.21}$$

Where $\delta(\varepsilon - E_{i,j})$ has been replaced by a Gaussian line with a linewidth of few meV in order to take into account the broadening induced by the spectral diffusion [70] and the other quantities are defined in the following.

4.3.2.1.1 Oscillator Strengths

The equation 4.21 is the sum of eight emission lines at energies $E_{i,j} = E_X + E_{ei} + E_{hj}$ (the energies and the eigenstates are obtained by diagonalizing equation 4.13 for a given $\vec{M}$) where the index are $1 \leq i \leq 2, 1 \leq j \leq 4$ and the oscillator strengths are given by $f_{ij} = |\langle\varphi_{ei}|\, p_\alpha \,|\varphi_{hj}\rangle|^2$ [76] with the index α that represents the three directions x, y, z and p_α is the component of the momentum operator $\vec{p}$. The optically allowed transitions, in the presence of an applied magnetic field for a heavy hole-light hole exciton ground state are shown in Figure 4.18.

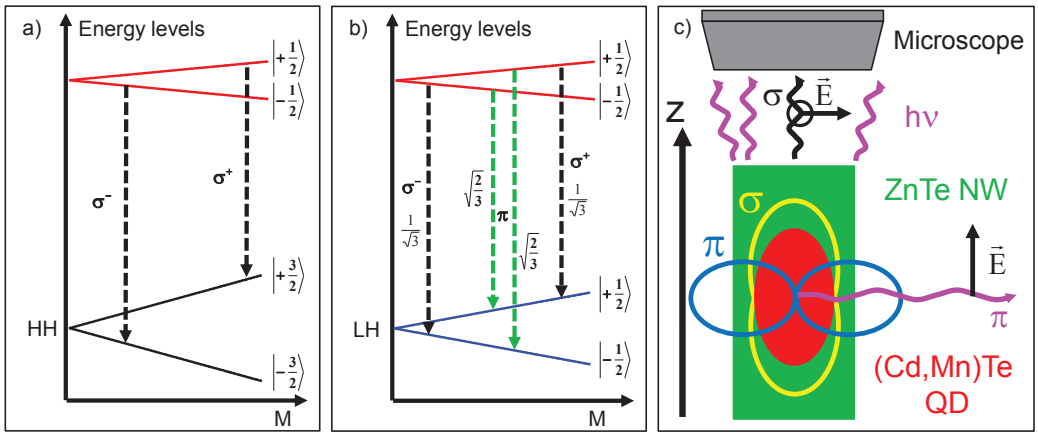

FIGURE 4.18: Optical allowed transitions in the presence of an external magnetic field for a) a heavy hole exciton b) a light hole exciton c) Radiation properties of a σ and a π polarized light

Figure 4.18a,b show that at zero magnetic field, there are six optical allowed transitions with six different oscillator strengths f_{ij}. Four of the six transitions involve the light hole exciton ground state (two of them are σ polarized while the other two are π polarized) and two transitions (σ polarized) are associated with the heavy hole exciton state.

4.3.2.1.2 Thermalization of the carriers

To reconstruct the photoluminescence spectra, we assume that electron and hole are at thermal equilibrium:

$$P_{i,j}^{eh} = \frac{e^{-\frac{E_h(j)}{k_B T}} e^{-\frac{E_e(i)}{k_B T}}}{Z_h Z_e} \tag{4.22}$$

where $E_h(j)$ and $E_e(i)$ are the hole and electron confined levels. In the case of Figure 4.18b, the fundamental transition will be between the electron state $|-\frac{1}{2}\rangle$ and the first light hole state $|+\frac{1}{2}\rangle$ and it will be π polarized. Thanks to the thermal activation law (equation 4.22) we take into account also all the other possible transitions but with an intensity that will decrease according to equation 4.22.

4.3.2.1.3 Calculation of the photoluminescence spectrum

The real photoluminescence spectrum will be given by a numerical calculation which sums up all the contributions of the different values of the magnetic moment $\vec{M}$, with the following expression:

$$I(\varepsilon) = \int d^3\vec{M} P_{occ}[\vec{M}] I_{\vec{M}}(\varepsilon) \tag{4.23}$$

The maximum of $I(\varepsilon)$ can be extracted and used to fit the experimental values for the different magnetic fields and temperatures that have been studied in the experimental Section. This spectrum corresponds to the fully formed Magnetic Polaron at thermal equilibrium. It assumes that the polaron formation time is much smaller than the exciton lifetime: this is in agreement with the experimental results show in in the experimental Section 4.2.3.3.

4.3.2.1.4 Fitting Parameters

Before showing how the model succeeds to fit all the experimental values, we highlight all the fitting parameters, necessary to calculate the total free energy. The fitting parameters are in total five and they are: ΔE,N_{eff},E_{se}, E_{sh} and E_X.

- ΔE is the light hole-heavy hole splitting and it takes into account the hole anisotropy along the z axis (see Figure 4.18);
- E_{se}, E_{sh} are the Zeeman splittings at saturation for electron and hole respectively: we need them to calculate the free energy for the electron and hole respectively (see equations 4.18);
- N_{eff} is the effective number of Mn spins and it is the value that defines the total magnetic moment of the quantum dot (see equation 4.3). Assuming an effective Mn concentration x_{eff}, it is related to the quantum dot volume by $N_{eff} = N_0 x_{eff} V_{QD}$;
- E_X is the energy of the exciton without the incorporation of Mn atoms: it takes into account the confinement energies and the Coulomb interaction between the electron and the hole. We supposed that it does not change under magnetic field and with the temperature.

4.3.2.2 Example of calculated spectra of heavy hole and light hole Magnetic Polarons

We showed how to calculate the photoluminescence spectra using equation 4.23. Now we present some calculated spectra, under a magnetic field applied parallel to the nanowire growth axis, with different values of the light hole heavy hole splitting ΔE, keeping the other fitting parameters (N_{eff},E_{se}, E_{sh}) constant and assuming an internal exchange field of 2.9T (this internal magnetic field correspond to a light hole Magnetic Polaron energy $E_P^{lh} = 13$meV, see equation 4.27).

TABLE 4.3: Parameters for the calculated Giant Zeeman effect

$N_{eff} = 59$	$E_{se} = 11$meV	$E_{sh} = 38.5$meV	$\Delta E = 0$meV, -20meV, $+20$meV

Figure 4.19 shows the calculated spectra from 0T to 11T for characteristic values of ΔE.

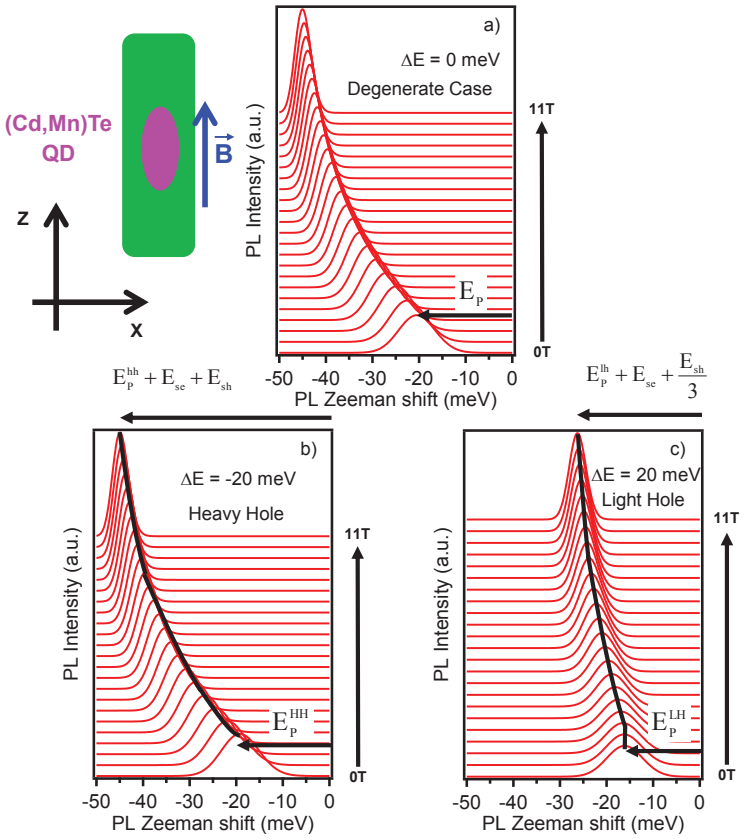

FIGURE 4.19: Calculated spectra of a Magnetic Polaron state, under a magnetic field from 0T to 11T with a step of 0.5T, using equation 4.23 for a) $\Delta E = 0$meV degenerate case b) $\Delta E = -20$meV heavy hole Magnetic Polaron c) $\Delta E = +20$meV light hole Magnetic Polaron

Figure 4.19a corresponds to the degenerate case ($\Delta E = 0$), Figure 4.19b to a heavy hole exciton ($\Delta E < 0$) while Figure 4.19c to a light hole exciton ($\Delta E > 0$). The main difference between the two situations is the amplitude of the Giant Zeeman effect at 11T: for a heavy hole exciton we have a shift of about 26meV while for the light hole exciton is only about 10meV.
The spectra, at 0T, are not centered at the origin of the energy axis because the model takes into account the Magnetic Polaron formation with two different values for the heavy hole exciton E_P^{hh} and light hole exciton E_P^{lh} Magnetic Polaron energies. We showed, in Chapter 1, that using the "Exchange Box Model" it is possible to define the electron and hole exchange magnetic fields given by the following expression:

$$B_{ex_z}^{ele} = \frac{\alpha}{2g_{Mn}\mu_B V_{QD}} = \frac{E_{se}}{M_{sat}} > 0 \tag{4.24}$$

$$B_{ex_z}^{hole} = \frac{-\beta}{2g_{Mn}\mu_B V_{QD}} = \frac{E_{sh}}{M_{sat}} > 0 \tag{4.25}$$

We can retrieve then the Magnetic Polaron energies for a heavy hole and a light hole exciton given by:

$$E_P^{hh} = \langle M_z \rangle [B_{ex_z}^{e^-} + B_{ex_z}^{hole}] \tag{4.26}$$

$$E_P^{lh} = \langle M_z \rangle [B_{ex_z}^{e^-} + \frac{B_{ex_z}^{hole}}{3}] \tag{4.27}$$

4.3.2.2.1 Giant Zeeman Shift

As we we have calculated the photoluminescence spectra, under magnetic field, we can extract the maximum of each spectrum and plot it as function of the magnetic field (see Figure 4.20). Figure 4.20a shows the Giant Zeeman shift for a light hole exciton while Figure 4.20b shows the one for a heavy hole exciton. The parameters used for the calculation are shown in Table 4.4.

TABLE 4.4: Parameters for the calculated Giant Zeeman effect

$N_{eff} = 59$	$E_{se} = 11$meV	$E_{sh} = 38.5$meV	$\Delta E = -50$meV, $+50$meV

We add a modified Brillouin function, shifted by the Magnetic Polaron exchange field $B_{ex}^{e^-} + B_{ex}^{hole}$ (see Chapter 1) to fit the degenerate case ($\Delta E = 0$).

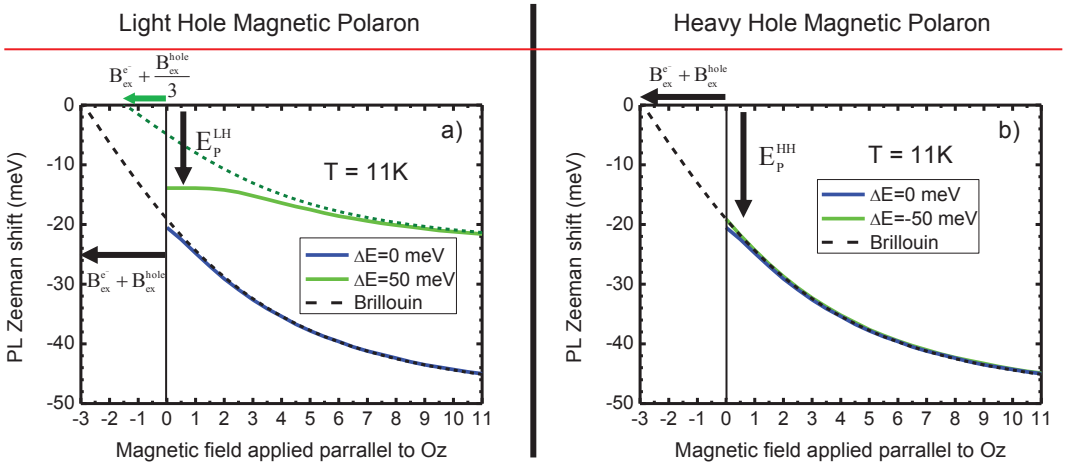

FIGURE 4.20: Giant Zeeman shift extracted from the spectra calculated using equation 4.23 with an applied magnetic field parallel to the nanowire growth axis for a) light hole Magnetic Polaron b) heavy hole Magnetic Polaron

The differences between the two cases are remarkable: not only the amplitude of the Giant Zeeman shift is really different (with a bigger value at saturation for the heavy hole exciton), but also there is a large difference in the Zeeman shift at low magnetic field and the Magnetic Polaron energies are really different.

For a heavy hole exciton (see Figure 4.20b) the Giant Zeeman shift follows a translated Brillouin function for all values of ΔE.

For a light hole exciton (with $\Delta E = 50$meV, see Figure 4.20a) the data follow a translated Brillouin function (by the light hole Magnetic Polaron exchange field given by: $B^{e^-}_{ex_z} + \frac{B^{hole}_{ex_z}}{3}$) only for high magnetic field. At low magnetic field there is a pronounced deviation that becomes bigger for large ΔE (not shown on the Figure 4.20). This behaviour is due to the combined effect of the Magnetic Polaron formation and of the hole anisotropy. We saw in fact (see Chapter 3) that without the presence of a Magnetic Polaron, for the nanowire studied in a Faraday geometry (NW3), the Giant Zeeman shifts can be fitted by a Brillouin function.

In the next Section we will analyze in details the behaviour under small magnetic field of the magnetic moments in the case of a light hole Magnetic Polaron.

4.3.2.2.2 Free energy maps

Using the total free energy, equation 4.17, it is possible to determine the average angle θ between the magnetic moments $\langle \vec{M} \rangle$ and the nanowire growth axis for an occupied and an empty quantum dot at a given value of B and at a given temperature T.

By performing the numerical calculation of the total free energy ($F(T,M)$), as function of $\vec{m}$ and the angle θ (see Section 4.3.1.1) where $0 \leq m \leq 1$ and $0 \leq \theta \leq \pi$, it is possible to determine the value of the magnetic moment at thermal equilibrium $\langle\vec{M}\rangle$ by looking at the minimum of $F(T,M)$. In these simulations, we used the set of parameters shown in the following table:

TABLE 4.5: Parameters for the calculated Giant Zeeman effect

$N_{eff} = 59$	$E_{se} = 11$meV	$E_{sh} = 38.5$meV	$\Delta E = 12$meV

In Figure 4.21 we show an example of such calculated maps, for 0T, 2T and 5T.

We see that in all the cases the formation of a Magnetic Polaron allows the system to gain energy (if the minimum of $F(T,M)$, dark blue, is not visible, please look at the digital version of Figure 4.21). Moreover, while for 0T (see Figure 4.21a) the total magnetic moment is perpendicular to the nanowire growth axis, at 5T (Figure 4.21c) the total magnetic moment is along the nanowire axis. For the intermediate case (magnetic field equal to 2T, see Figure 4.21b), the total magnetic moment tends to align itself in the direction of the magnetic field but due to the Magnetic Polaron formation it is not parallel to either the x axis or the z one.

4.3.2.2.3 Magnetic Polaron formation process

To be able to better analyze the evolution of the total magnetic moment $\langle\vec{M}\rangle$ we show some slices extracted from the free energy maps for different magnetic field, 0T, 2T and 5T in Figure 4.22.

To produce Figure 4.22 we calculate the total free energy $F(T,M)$ for particular values of θ ($\theta = 0°$, $\theta = 90°$ and $\theta = 29.5°$) and for an occupied and an empty quantum dot state.
We are going to discuss now the photoluminescence process for different values of the applied magnetic field. At the beginning (B=0T), the quantum dot is empty, having then a total magnetic moment $\langle\vec{M}\rangle = 0$. Under the laser excitation, there is a creation of an (e,h) pair followed by the formation of the Magnetic Polaron state that leads to $\langle\vec{M}\rangle \neq 0$ by lowering the system total energy. After, there will be the (e,h) recombination with the emission of a photon followed by the relaxation of the system. Figure 4.22a shows the orientation of the magnetic moment $\vec{m}$ at 0T. When we inject an electron-hole pair inside the quantum dot, there is the formation of the Magnetic Polaron state that polarizes the magnetic moment perpendicular to the nanowire

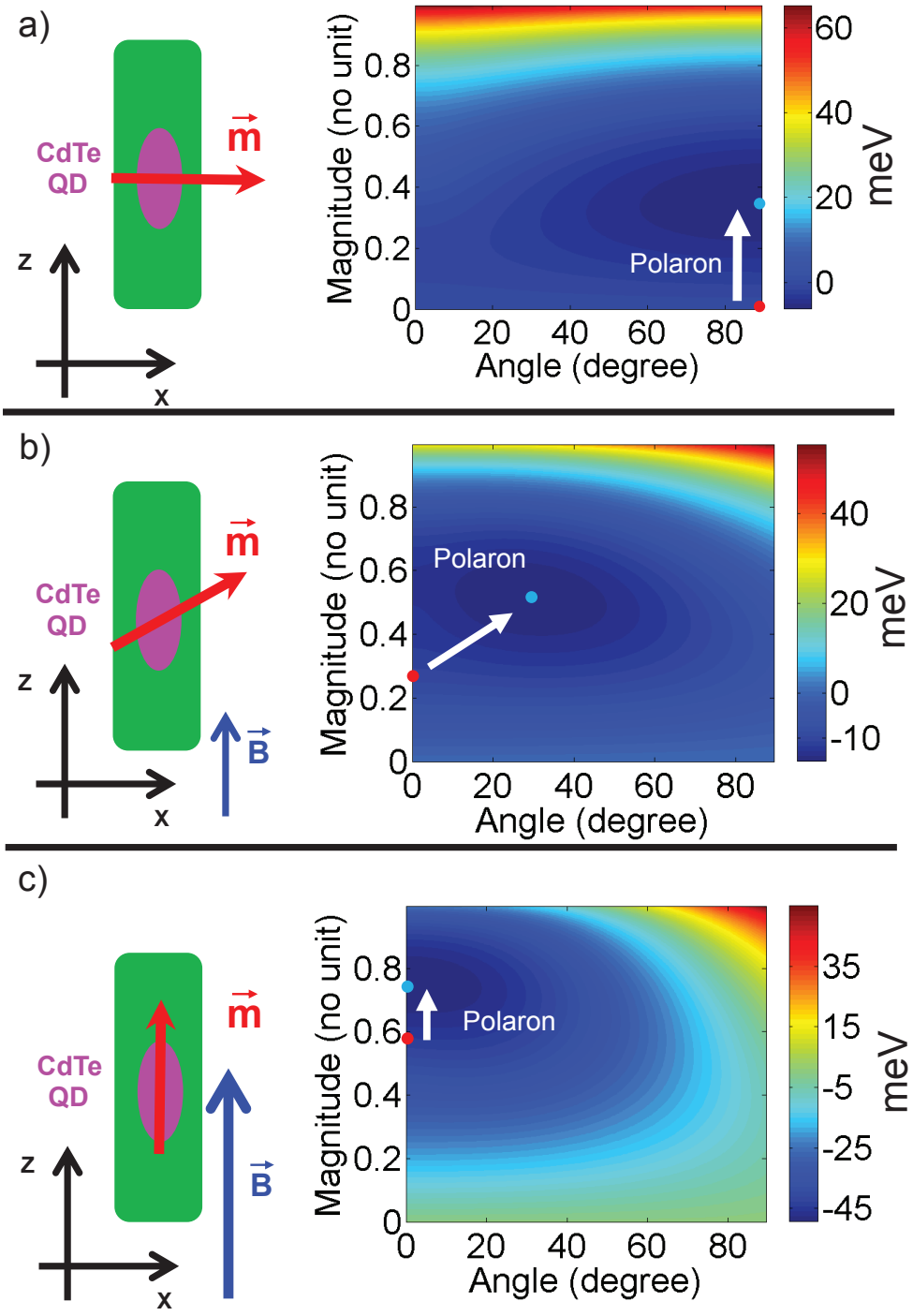

FIGURE 4.21: Total free energy maps of an occupied dot with a light hole exciton $\Delta E > 0$, under different magnetic fields a) 0T b) 2T c) 5T

growth axis.

When we start to apply a magnetic field along the nanowire growth axis, we are trying to flip the magnetic moment along the direction of the magnetic field. Then, there is a competition between the polarization caused by the magnetic field and the one induced by the effective exchange field of photocarriers. For B=2T, the magnetic

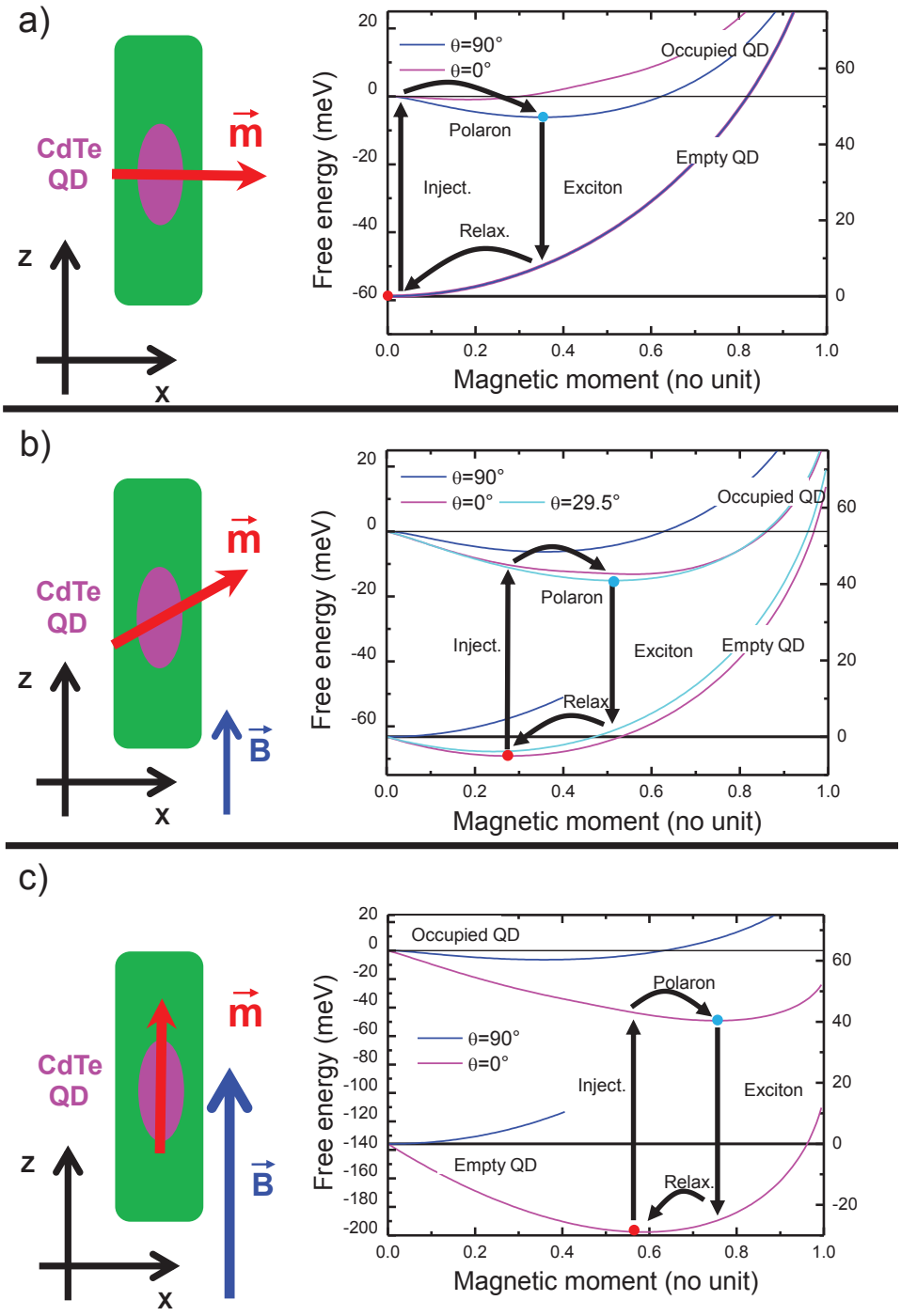

FIGURE 4.22: Total free energy calculation with a light hole Magnetic Polaron $\Delta E >$ 0, under different magnetic fields a) 0T b) 2T c) 5T

moment (see Figure 4.22b) will then lie in a plane comprised between the nanowire growth axis and the perpendicular direction.

When we apply a very strong magnetic field (B=5T, see Figure 4.22c) we force the magnetic moment to align along the nanowire growth axis.

The competition between the polarization induced by the exciton exchange field and

the one induced by the applied magnetic field, can explain the deviation from a Brillouin function observed in the Giant Zeeman shift at small magnetic field (Figure 4.20a). This fingerprint is a characteristic feature of a light hole Magnetic Polaron when the magnetic field is applied along the z direction, i.e. along the hole anisotropy axis (hard axis).

4.4 Identification of light hole Magnetic Polaron: application of the model to analyze the experimental data

4.4.1 Fitting of the Giant Zeeman Effect

In this Section we show how to analyze the magneto-optical measurements shown in Section 4.2.4. The experimental and the theoretical data are shown in Figure 4.23.

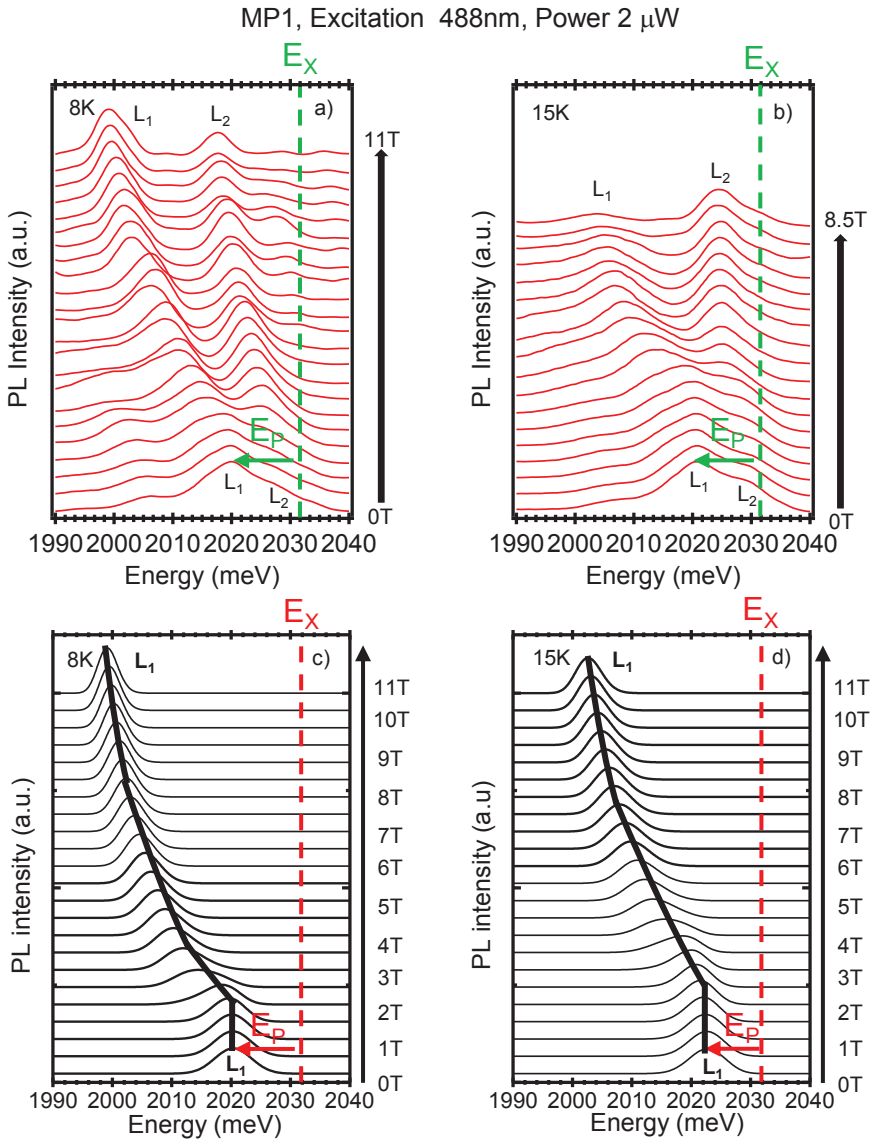

FIGURE 4.23: Experimental Giant Zeeman effect at a) 8K b) 15K. Calculated Giant Zeeman effect, using equation 4.23, at c) 8K d) 15K

Figure 4.23a,b shows the magneto-optical data taken at 8K and 15K respectively while in Figure 4.23c,d are traced the calculated spectra using equation 4.23 for the excitonic component L_1. We calculated the theoretical spectra using equation 4.23 with the fitting parameters shown in the following table.

TABLE 4.6: Fitting parameters for the theoretical Giant Zeeman effect

$E_X = 2032$meV	$N_{eff} = 59$	$E_{se} = 11$meV	$E_{sh} = 38.5$meV	$\Delta E = 12$meV

To reproduce the evolution of photoluminescence spectra as function of the magnetic field (Figure 4.23c,d), we had to consider a light hole exciton ground state (ΔE = 12meV). As explained in Chapter 1, this is the only case where the photoluminescence Zeeman shift does not follow a monotonous law.
From the table of the fitting parameters, we see that we have to play with five fitting parameters to reproduce the experimental data. In the next Section we will show that it is possible to find relations between some of them, reducing then the number of free parameters. Others are given by the different experiments done on MP1.

4.4.1.1 How to determine the five fitting parameters

In the previous Section we showed that we have to play with five fitting parameters to fit the magneto-optical measurements. These parameters are E_X (the exciton photoluminescence energy without considering the coupling with the Mn atoms), N_{eff} (the number of effective Mn spins that are involved in the exchange interaction), E_{se} (the Giant Zeeman shift at saturation of the electron), E_{sh} (the Giant Zeeman Shift at saturation of the hole) and ΔE (the hole anisotropy parameter).
The position in energy of the light hole transition E_X could be extracted by considering the energy of the Magnetic Polaron state E_P^{LH} = 13meV (at 5K) retrieved from the time resolved photoluminescence measurements, shown in Section 4.2.3.3. The energy E_X is in fact given by $E_X(T = 5K) = E_{PL}^{exp}$(T=5K) + $E_P^{lh}(T = 5K)$ = 2019meV + 13meV = 2032meV.
We can also fix the energy at saturation of the electron E_{se}. The confinement potential acting on the conduction electron is very strong and we can then suppose an electron fully confined in the quantum dot. By considering then the EDX results, done on NW1 of the Sample 1 (see Chapter 2), where we found an effective Mn concentration x_{eff} = 4%, we could suppose the same value for Sample 2 (Sample 1 and Sample 2, were in fact, grown with the same growth conditions and the same day, see [14] and Chapter 1). The energy at saturation of the electron will be then taken as the

maximum one $E_{se} = 11\text{meV}$.

We have then only three parameters over five that can be changed to fit the experimental data: N_{eff}, E_{sh}, ΔE. These parameters are however linked from some definitions presented in Chapter 1. The energies of a light hole Magnetic Polaron (along the x direction) and a heavy hole one (along the z direction) are given by:

$$E_P^{lh} = \frac{(S+1)\left(E_{se} + \frac{2}{3}E_{sh}\right)^2}{3k_B T N_{eff} S} \tag{4.28}$$

$$E_P^{hh} = \frac{(S+1)(E_{se} + E_{sh})^2}{3k_B T N_{eff} S} \tag{4.29}$$

The hole anisotropy parameter ΔE is defined by the photoluminescence emission energies of the light hole and heavy hole exciton and is given by:

$$\Delta E = \frac{E_X^{lh} - E_X^{hh}}{2} = \frac{(E_{PL}^{lh} + E_P^{lh}) - (E_{PL}^{hh} + E_P^{hh})}{2} \tag{4.30}$$

By using a graphical method, we will show that it is possible to determine E_{sh} and to deduce E_{PL}^{hh}. By knowing E_{sh} it is possible to calculate E_P^{hh} (equation 4.29). With E_P^{hh}, E_{PL}^{lh}, E_{PL}^{hh} and $E_P^{lh} = 13\text{meV}$ ($E_P^{lh} = 13\text{meV}$ is given by the time resolved photoluminescence experiments while E_{PL}^{lh} is the photoluminescence emission energy) we can use equation 4.30 and then calculate also ΔE.

Before showing how we deduced E_{sh}, we make another consideration. It is not possible to fit the Giant Zeeman shift by considering only a light hole Magnetic Polaron state. The Zeeman shift of the photoluminescence emission at saturation is too high for a light hole state even for the highest effective Mn concentration ($E_{sh} = 44\text{meV}$, see Chapter 1). The saturation energy for a light hole Magnetic Polaron oriented along the z direction is given by:

$$E_{sat}^{lh} = E_X^{lh} - \left(E_{se} + \frac{E_{sh}}{3}\right) = 2032\text{meV} - 25.7\text{meV} = 2006.3\text{meV} \tag{4.31}$$

From the experimental data, the E_{PL} at 11T is 2000meV, a much smaller value compared to the Giant Zeeman saturation one (2006.3meV) for a light hole Magnetic Polaron. We can then suppose that for high magnetic field values, there is a transition

of the system from a light hole Magnetic Polaron state to a heavy hole one. The situation is then more complicated to what has been calculated in Chapter 1.
To retrieve the value of E_{sh}, we have fitted the experimental data supposing a heavy hole Magnetic Polaron state for high magnetic field values. We plotted the Giant Zeeman shift (for the measurement at 8K) in Figure 4.24a.

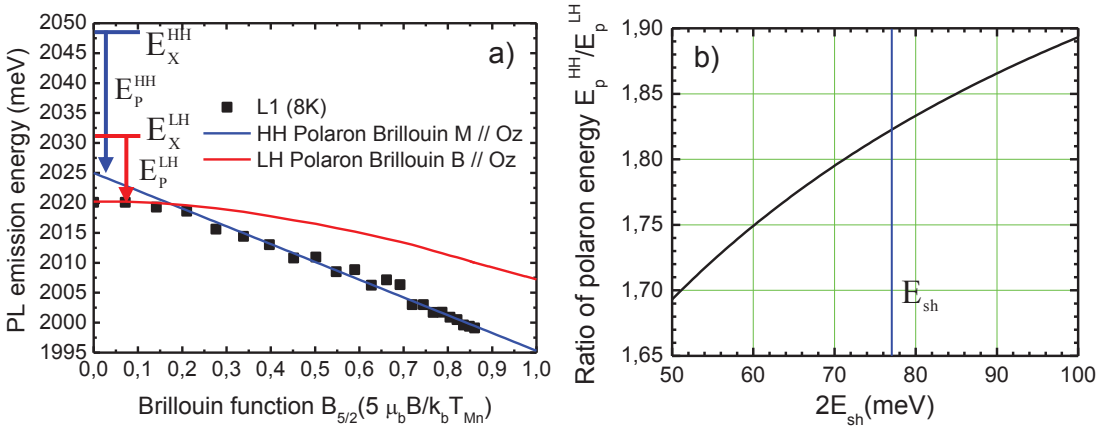

FIGURE 4.24: a) Giant Zeeman shifts as a function of $\mathrm{B}_{\frac{5}{2}}\left(\frac{5\mu_B B}{k_B T_{\mathrm{Mn}}}\right)$ b) Ratio of the heavy hole - light hole Magnetic Polaron energy as a function of E_{sh}

The Giant Zeeman shift, which follows a shifted Brillouin function $B_{\frac{5}{2}}\left(\frac{5\mu_B(B_z+B^{e^-}_{exz}+B^{hole}_{exz})}{k_B T_{\mathrm{Mn}}}\right)$, has been traced as function of $\mathrm{B}_{\frac{5}{2}}\left(\frac{5\mu_B B}{k_B T_{Mn}}\right)$: the curve is almost a straight line leading to a more simple determination of E_{sh}.
By fitting the experimental points, at high magnetic field values (see Figure 4.24a), we retrieved a value of E_{sh} = 38.5meV and the heavy hole Magnetic Polaron emission E^{hh}_{PL}. We can now calculate the heavy hole Magnetic Polaron energy graphically (see Figure 4.24b) for a given value of E_{sh} having $E^{hh}_P = 23.6meV$.
By having E^{hh}_P, E^{lh}_P, E^{hh}_X, E^{lh}_X we can also calculate ΔE using equation 4.30 and then have all the system parameters. We retrieved for the hole anisotropy ΔE=12meV.

4.4.1.2 Final Results

In this Section we present the results obtained with the total free energy approach (with the fitting parameters presented in the previous Section). The good agreement between the theoretical and experimental photoluminescence energy positions is shown in Figure 4.25a.

In zero field, we have a light hole Magnetic Polaron state; this is the first time that it has been observed in a II-VI DMS nanostructures.

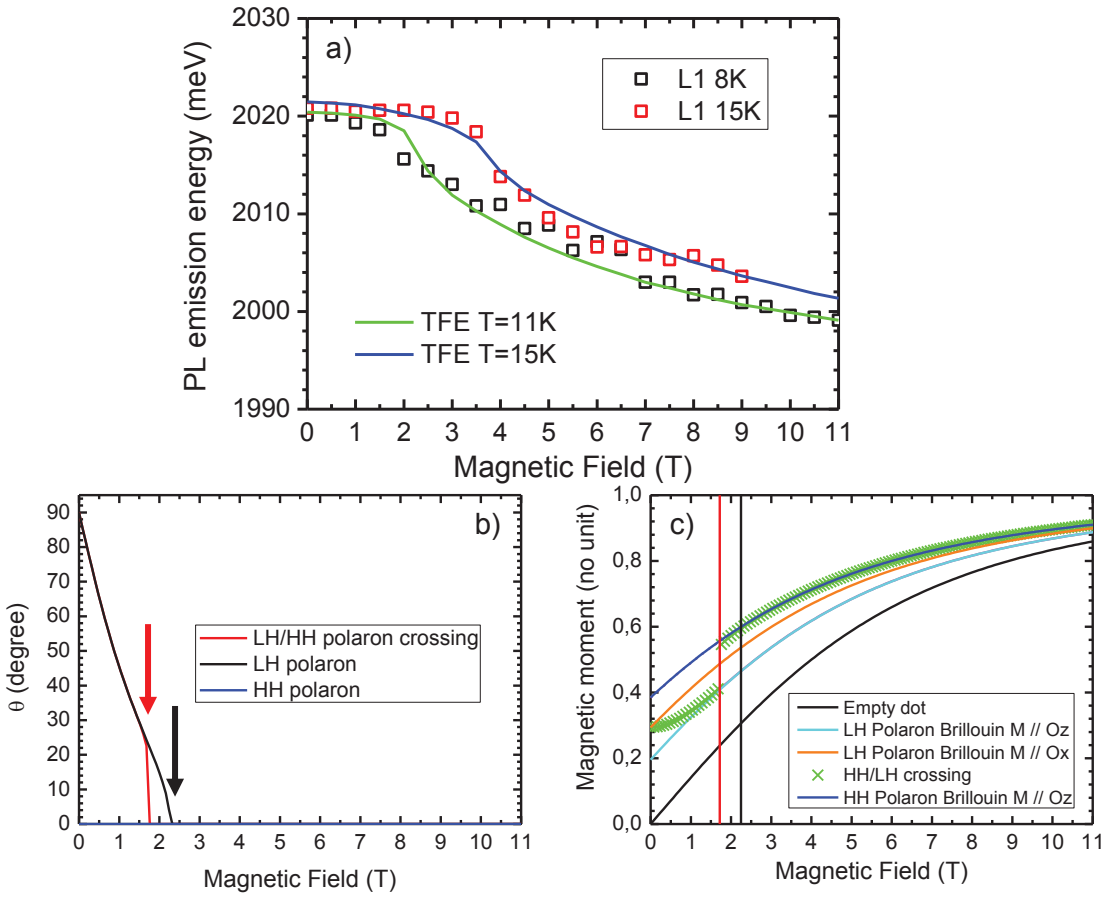

FIGURE 4.25: a) Giant Zeeman shifts with the theoretical calculated energy points using the total free energy approach b) Angle θ of the total magnetic moment as function of the magnetic field for the L_1 component c) Magnetic moment intensity as function of the magnetic field

We can extract some interesting informations concerning the flipping of the total magnetic moment, by calculating the angle θ of the total magnetic moment and its amplitude using the total free energy. From the calculation shown in Figure 4.22, we know that we can turn the magnetic moment for high values of the magnetic field. We can see the flipping of the magnetic moment quantization axis in Figure 4.24b where the angle θ is traced as function of the applied magnetic field. For the data at 8K the flipping is around 1.8T (Figure 4.24b): the quantization axis of the magnetic moment turns from the x axis to the z axis "jumping" on the heavy hole state. The jump on the light hole state (black arrow), with the spin projection along the z axis, is expected to be around 2.4T ($B_z = B_{ex_z}^{hole}$).

This behaviour is confirmed also by the intensity of the magnetic moment as a function of applied magnetic field (see Figure 4.24c). After having reached the critical magnetic field value needed to rotate the magnetic moment along the z direction, we have a transition onto the heavy hole state. As expected, for high magnetic field,

the magnetic moment intensity, follows a heavy hole Brillouin function with $\langle \vec{M} \rangle$ oriented along the z direction.

4.4.2 Consistency with streak camera measurements

In the previous Section, we showed how to analyze the magneto-optical measurements of Section 4.2.4, by taking into account the Magnetic Polaron formation. To fit the data, we use the value of the Magnetic Polaron energy E_P at 5K, determined by the time resolved photoluminescence data of Section 4.2.3.3. In this Section we check the consistency with the streak camera measurements performed at the two other temperatures (28K and 46K). By using the same fitting parameters (see table 4.6) we calculate the photoluminescence spectra of MP1 as function of the temperature and hence we determine the Magnetic Polaron energies of the system respect to the known energy position E_X, see Figure 4.26a.

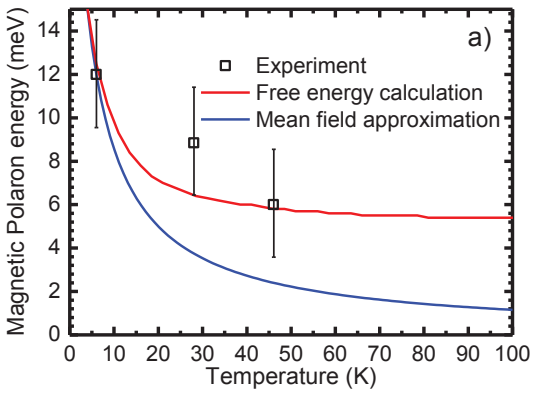

FIGURE 4.26: Magnetic Polaron energy fitted by the total free energy calculation

Figure 4.26 shows that the expected Magnetic Polaron energies, for the temperatures studied by the time resolved measurements, are in agreement with the corresponding expected value (except the data taken at 28K that it enters hardly on the fit). We think however that this treatment describes very well the data because we didn't consider the experimental error on the measured temperatures.

Moreover we can see that the total free energy approach, which is valid from low temperature (5K) up to high temperature (100K in our case), describes better the experimental data than the Mean Field Approximation (see Figure 4.26). The MFA approach succeeds in modeling the data at 5K, as expected, but it is not accurate at high temperature (starting from T=20K).

4.4.3 Consistency with the temperature measurements

In the previous Section we show the good agreement between the theoretical model, based on the total free energy approach, and the time resolved photoluminescence measurements.

In this Section we check the consistency between the theoretical model and the temperature dependent photoluminescence data. We calculate the expected photoluminescence spectra, at different temperatures, using equation 4.23 and keeping the same fitting parameters (see Table 4.6). In Figure 4.27 we trace the results of the calculation.

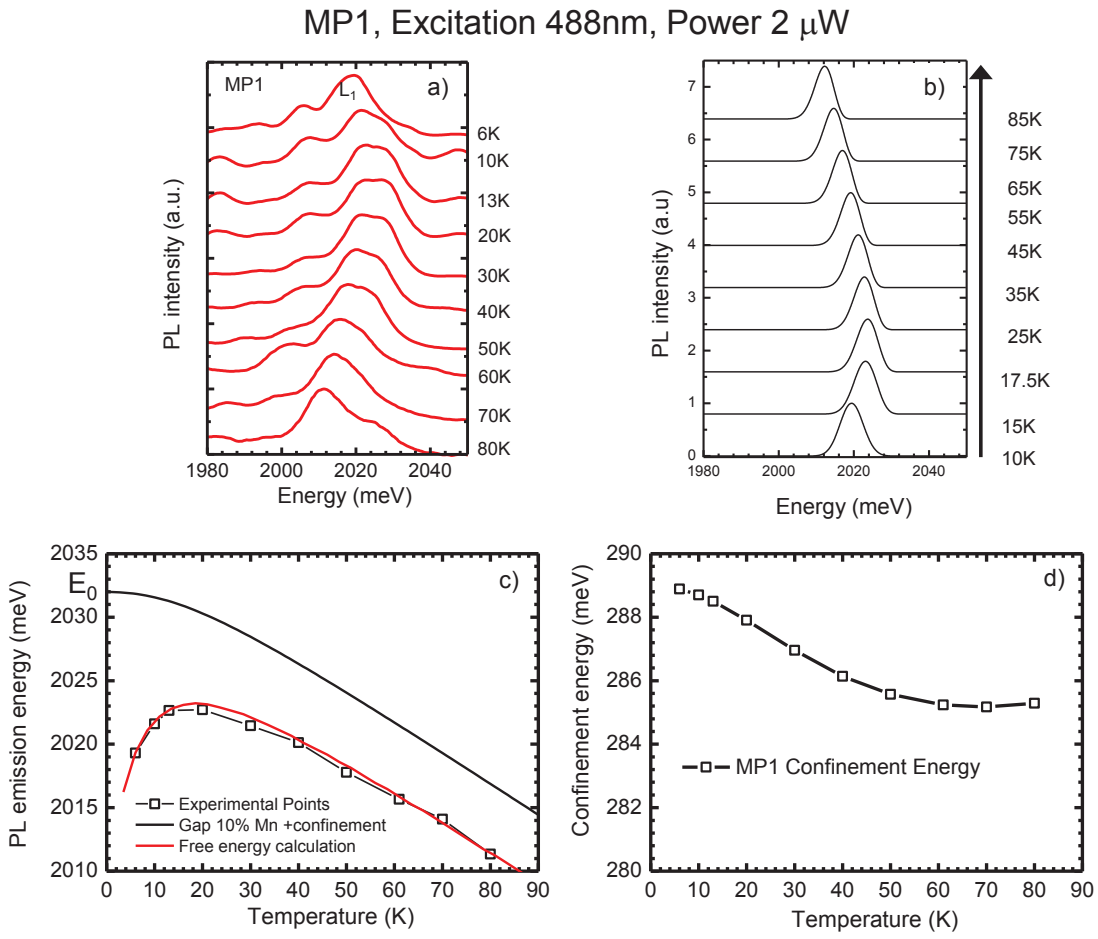

FIGURE 4.27: a) Experimental temperature evolution of the exciton line L_1 of MP1 b) Calculated temperature evolution of the excitonic line L_1 of MP1 c) Superimposition of the experimental micro-PL position and the total free energy fit taking into account the variation of the hole confinement d) Variation of the hole confinement as function of the temperature

Figure 4.27a shows the experimental spectra taken at different temperatures while in Figure 4.27b there are the calculated spectra for exciton line L_1. Figure 4.27c presents

the plot of the photoluminescence experimental energy points with the theoretical fit as function of the temperature. To be able to fit the experimental data, we have to consider a slightly variation of the hole confinement which is plotted, as a function of the temperature in Figure 4.27d.

By using the total free energy approach, it is possible to explain the behaviour of the photoluminescence line as function of the temperature. In Figure 4.27c we fit the theoretical energy position extracted from Figure 4.27b. The photoluminescence energy position is given by:

$$E_{PL}(T) = E_{PL}^{gap}(T) + E_P(T) + E_{conf}(T) \tag{4.32}$$

Where $E_P(T)$ is the energy of the Magnetic Polaron as function of the temperature that has been presented in Section 4.4.2. $E_{PL}^{gap}(T)$ is the (Cd,Mn)Te bandgap variation without the presence of a Magnetic Polaron order and $E_{conf}(T)$ is the confinement energy of the (Cd,Mn)Te quantum dot. We considered for the expression of $E_{PL}^{gap}(T)$ the following equation taken from [87, 88]:

$$E_{PL}^{gap}(T) = E_0 - \frac{\alpha\Theta_P}{2}\left[\sqrt{1+\left(\frac{2T}{\Theta_P}\right)^P} - 1\right] \tag{4.33}$$

Where the parameter $\alpha = S(\infty)$ represents the magnitude of the slope for $T \longrightarrow \infty$: $S(T) = -\frac{dE_{PL}^{gap}(T)}{dT}$ and Θ_P is connected to the average phonon energy: $\Theta_P \approx \frac{\bar{\varepsilon}}{k_B}$. The exponent p is related to the ratio of the first $\bar{\varepsilon}$ and second $\Delta\varepsilon$ moment of the phonon dispersion by the following approximated relation:

$$\frac{\Delta\varepsilon}{\bar{\varepsilon}} = \frac{1}{\sqrt{p^2-1}} \tag{4.34}$$

It has been shown in [17, 89], that expression 4.33 models in a more accurate way the experimental data in the low-temperature region compare to the common used Varshni empirical formula [90]. To be able to reproduce the experimental points of Figure 4.27c, we had to use the following parameters (shown in Table 4.7) to model the (Cd,Mn)Te bandgap variation using equation 4.33:

To have reasonable fitting parameters for the bandgap variation of MP1, comparable with what has been observed for CdTe/ZnTe nanowire in [17] (see the table) we had

TABLE 4.7: Comparison between the fitting parameters of MP1 and the ones of CdTe quantum dots inserted in ZnTe nanowires

MP1	$E_0 = 1596$meV	$\alpha = 0.25$	$\Theta_p = 45$	$p = 2.415$
CdTe/ZnTe	$E_0 = 1925$meV	$\alpha = 0.35$	$\Theta_p = 134$	$p = 2.415$

to take a not constant energy confinement (equation 4.32) shown in Figure 4.27d. A very small variation of the exciton confinement energy (few percents) is required to model the behaviour in temperature. The hole wavefunction may be still partially delocalized (the decay time is still big 640ps compared to the one of a Type 1 quantum dot 100ps-300ps) and could slightly change as function of the temperature.

4.4.4 Complementary considerations on the fitting parameters

We show in Section 4.4 that it is possible to use the same set of parameters, table 4.6, to model all the photoluminescence studies done on MP1. In this Section we show that the "Exchange Box Model" is a model oversimplified: it fails in fact to describe correctly the experimental values.
In Chapter 2, Section 2.1.1.1, we show that by using the EDX images we can determine the quantum dot dimensions. It is possible then, to calculate the quantum dot volume that, for an ellipsoidal quantum dot, is given by:

$$V_{QD}^{EDX} = \frac{4}{3}\pi(a \times b \times c) = \frac{4}{3}\pi(4^2 \times 7.5) \cong 500nm^3 \tag{4.35}$$

Where a=b=4nm and $c = \frac{15\text{nm}}{2}$=7.5nm. By using the "Exchange Box Model", we can compare this volume to the effective one that is given by:

$$N_{eff} = x_{eff} V_{QD}^{box} N_0 \tag{4.36}$$

For MP1, if we use the values for $N_{eff} = 59$ and $x_{eff} = 4\%$ (from the EDX measurements, Section 2.1.1.1) we find $V_{QD}^{box} \cong 100\text{nm}^3$. This value is of the same order of magnitude as V_{QD}^{EDX} but still it is smaller than expected. The "Exchange Box Model" doesn't describe correctly the experimental values: we have to consider the electron and hole envelope functions. In Appendix D we will present some approximated

calculations that, by taking into account simplified envelope functions, succeed to explain the measured effective volume.

4.5 Conclusions

In this Chapter we study nanowires containing concentrated (Cd,Mn)Te quantum dots surrounded by a (Zn,Mg)Te alloy. With these nanowires, we succeed to observe, for the first time, the formation of exciton Magnetic Polaron in magnetic quantum dot inserted in a nanowire. The properties of these polarons are very original: at low magnetic field the ground state is a light hole Magnetic Polaron with a magnetic moment perpendicular to the nanowire axis (easy plane configuration). This is also the first time that such a light Magnetic Polaron is reported in diluted magnetic semiconductors. Above a critical field of few Tesla, a switch from a light hole Magnetic Polaron ground state towards a heavy hole one is observed. The magnetic moment rotates from the radial plane towards the nanowire axis.

The formation of Magnetic Polaron is first revealed qualitatively by a large temperature red shift of the exciton emission energy (almost 5 times larger than the one observed in Sample 1 in which there is no Mg around the quantum dot). To extract quantitative values of the Magnetic Polaron energies, we perform streak camera measurements with a single nanowire (MP1) at different temperatures. To determine the nature of the hole ground state and to estimate the light hole-heavy hole splitting, we perform magneto-optical studies with magnetic field applied along the nanowire axis.

We develop a theoretical model based on the calculation of the total free energy. This model goes beyond the Mean Field Approximation and it is valid in the whole experimental temperature range. It extends the one done for isotropic donors: it is based on exciton, it takes into account the hole anisotropy and it uses an expression of the free energy valid up to large magnetic field. To our knowledge, this is the first time that such extension was done and used to fit various experimental data recorded on the same nanowire. With this model we succeed to fit all the experimental data with the same set of parameters

We recall the MP1 Magnetic Polaron parameters in the following table.

TABLE 4.8: Magnetic Polaron parameters at $5K$

$E_P^{lh} = 13$meV	$E_P^{hh} = 23.6$meV	τ_f=90ps	τ_X=640ps

The insertion of Mg all around the quantum dot helps to better confine the hole in the dot: the measured decay time τ_X=640ps is in fact smaller than the decay time

measured in the nanowires of Sample 1 (see Chapter 2 and 3). The stronger hole confinement led to a stronger Magnetic Polaron state compared to Sample 1 (see Section 4.2.2). The small Magnetic Polaron formation time τ_f=90ps compared to the exciton lifetime ensures that the Magnetic Polaron formation has the time to take place.

At 5K, the energy of the light hole Magnetic Polaron formed in a dot with a Mn concentration about 10% is 13meV. To compare the stability of this Magnetic Polaron with the one reported in self quantum dots [12, 35], we calculate the expected energy for a heavy hole Magnetic Polaron (E_P^{hh}=23.6meV at 5K). The following table summarizes the comparison.

TABLE 4.9: Comparison with self assembled quantum dots

MP1	E_P^{hh}=23.6meV (T=5K)	τ_f=90ps	τ_X=640ps	$Mn = 10\%$
[12]	E_P^{hh}=13meV (T=8K)	τ_f=110ps	τ_X=220ps	$Mn = 20\%$
[35] (Sample 1)	E_P^{hh}=25.4meV (T=7K)	τ_f=0.35ns	τ_X=17.2ns	$Mn = 5.2\%$
[35] (Sample 3)	E_P^{hh}=34.4meV (T=7K)	τ_f=0.48ns	τ_X=7ns	$Mn = 5.2\%$

The Magnetic Polaron energy E_P^{hh} is larger than the value reported in [12] with less concentrated quantum dots. Moreover the sample studied in this PhD is not probably fully optimized. The hole might be still partially delocalized in the barrier as suggested by the long exciton decay time. By increasing the hole confinement, we may obtain larger Magnetic Polaron energies and maybe comparable with the ones measured in [35] (Note that in our case electron and hole would contribute to the Magnetic Polaron energy).

A light hole exciton ground state was also observed in the nanowire NW3 of Sample 1. NW3 and MP1 have almost the same Zeeman shifts at saturation (for electrons and holes) and the same hole anisotropy. By contrast to MP1 (belonging to Sample 2), we do not observe surprisingly any evidence of Magnetic Polaron formation in NW3. As shown in Figure 4.28, the Mg around the dot may strongly reduce the delocalization of the light hole in zero field along the poles of the dot. The moderate value of ΔE in MP1 may result either from a quantum aspect ratio $1<\frac{L}{D}<2$ or a partial delocalization in the barrier. Under large magnetic fields, the light hole is well confined in the dot for both nanowires due the increase of the valence band offset induced by the giant Zeeman effect (see Conclusion of Chapter 3).

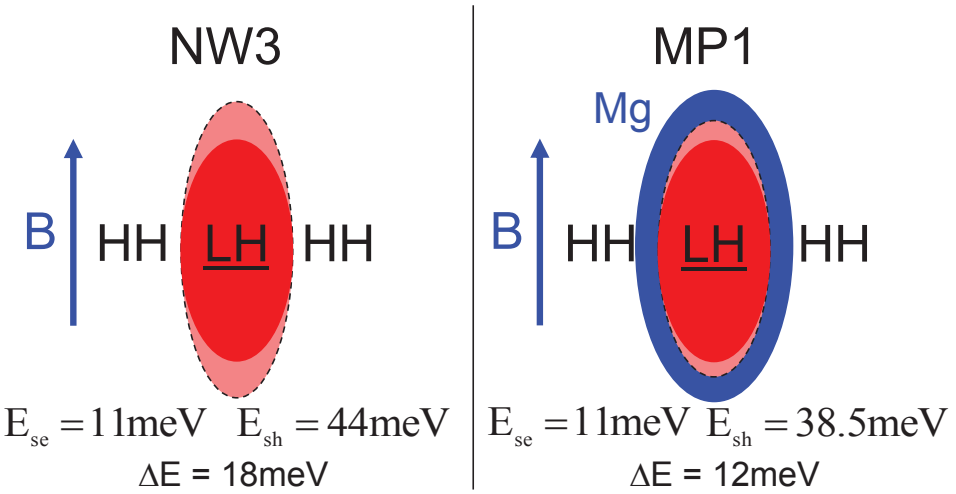

FIGURE 4.28: Comparison between Sample 1 (where there is no Magnetic Polaron) and Sample 2 (where it has been found a strong and stable Magnetic Polaron) after having add Mg all around the dot

Prospects

Optical measurements have been performed on vertical nanowires located on the as-grown sample (Sample 2). Further measurements have to be done with isolated nanowires in order to combine optical and structural studies on the same nanowire (as we did for NW1 of Sample 1). More magneto-optical experiments have to be done at different temperatures and with different magnetic field orientation.

The effective exchange volume deduced for the Magnetic Polaron parameters seems to be smaller than the real volume of the dot indicating a failure of the "Exchange Box Model" approximation. To account properly for the rather small (Cd,Mn)Te/ZnTe valence band offset, realistic light hole and heavy hole envelope functions have to be calculated and incorporated in the free energy model.

From the temperature dependent measurements we saw also that there is a small variation of the exciton confinement energy with temperature. This effect is not well understood and has to be confirmed by further studies (decay time measurements at different temperatures).

Sample 2 has a light hole heavy hole splitting ΔE of about 12meV. Further studies have to be done with samples with larger ΔE (quantum dot with larger aspect ratio or/and larger Mg concentration around the dot). Investigation of quantum dot with different aspect ratio has to be done in order to obtain a pure light hole or a pure heavy hole Magnetic Polaron on demand.

The experiments have been carried out with quantum dot with a large Mn concentration (close to 10%). A more systematic study of the influence of the Mn concentration has to be performed. We think however that larger Mn concentration will not increase much the Magnetic Polaron energy (effective Mn concentration close to the maximum of 4%).

General Conclusions

The aim of this work was to study the formation of Magnetic Polarons in (Cd,Mn)Te quantum dots inserted in ZnTe nanowires by magneto-optical spectroscopy. This has required to address different steps:

1. Characterization of ZnTe and of ZnTe/(Zn,Mg)Te core shell nanowires, evaluation and modeling of the strain profile, estimation of the light hole heavy hole splitting in the nanowire core and in the dot; preparation of patterned substrates and self suspended membranes in order to combine different experimental techniques (cathodoluminescence, TEM, EDX, magneto-optics) on single nanowires containing a magnetic quantum dot.

2. Characterization of single nanowire containing a CdTe or (Cd,Mn)Te quantum dot by SEM and cathodoluminescence; single dot spectroscopy and identification of exciton lines. Measurement of the polarized emission diagram in zero field.

3. Magneto-optical spectroscopy of (Cd,Mn)Te quantum dots; quantitative analysis of the exciton Giant Zeeman shift in (Cd,Mn)Te quantum dot containing 10% Mn. Determination of the nature of the hole ground state and estimate of the hole anisotropy.

We checked first the good crystalline quality of our nanowire structures (Chapter 2). We started with the study of pure ZnTe nanowires: we observed the near band edge emission by microphotoluminescence and cathodoluminescence experiments [16]. Due to the low emission intensity, we decided to add a (Zn,Mg)Te shell to enhance the emission properties. We obtained a photoluminescence signal 10^4 higher compared to the pure ZnTe nanowires.

The difference in the lattice parameter between the ZnTe core and the (Zn,Mg)Te outer shell induces elastic strain in the core part leading to a red shift of the emission energy with a heavy hole exciton fundamental state. To explain quantitatively the shift induced by strain, we calculate the elastic strain profile in core/shell nanowires by solving the Lamé-Clapeyron-Navier equation and by taking into account the anisotropy of elastic constants. We try also to evaluate the elastic strain profile in nanowires containing a quantum dot. As this problem cannot be solved analytically we consider the simplified case of an ellipsoidal dot inserted in an infinite matrix (the so called Eshelby inclusion). With the well known solution to this problem, we obtain an estimate of the expected hole anisotropy ΔE (heavy hole light hole splitting) in a quantum dot as a function of its aspect ratio $\frac{L}{D}$.

These theoretical values were compared to the experimental ones obtained with (Cd,Mn)Te quantum dots whose aspect ratio was determined by EDX analysis. We obtain a theoretical hole anisotropy of about ΔE=140 meV with a light hole ground state. To determine the nature of the hole ground state, we analyze the emission diagram of the exciton line by performing Fourier microscopy (in collaboration with M. Jeannin and G. Nogues). To our knowledge, it is the first time that this technique is used with quantum dots inserted in nanowires. In the studied sample, the emission and polarization diagrams reveal unambiguously an emission from a light hole exciton (as expected from the strain model). We develop a quantitative model taking into account properly the heavy hole light hole mixing terms and the dielectric environment around the dot (modeled as a radiating dipole inserted in a finite length tapered nanowire deposited in an infinitely thick ZnTe buffer). By fitting the magneto-optical results, we obtain a hole anisotropy parameter of ΔE=18meV for the studied sample.

To study more directly the hole anisotropy, we performed single dot magneto-optical spectroscopy with magnetic fields applied perpendicular or parallel to the nanowire growth axis. Due to the difference of spin properties of heavy holes and light holes, the nature of the hole ground state and an estimate of the hole anisotropy can be obtained by fitting the Giant Zeeman shift of the quantum dot exciton line. A mean field approximation exchange box model with anisotropic quantum dots was used to fit the experimental data (note that this is an effective model with a hole confined in the quantum dot). With nanowires containing quantum dots with well resolved lines (as the one studied both in optics and by EDX), a direct estimate of ΔE can be done thanks to the observation of both heavy hole and light hole excitons at high

TABLE 4.10: Main results on Sample 1

	ΔE	E_{se}	E_{sh} (heavy hole)	E_{sh} (light hole)
NW1	-5meV	8.5meV	24meV	–
NW2	-5meV	8.5meV	16.5meV	–
NW3	18meV	11meV	22meV	44meV

temperature. The main results concerning the three nanowires are summarized in Table 4.10.

One has to mention that we always use an effective model with a hole ground state J=$\frac{3}{2}$ quadruplet split into a light hole and a heavy hole doublet. If holes becomes partially delocalized in the barrier, the value of the light hole-heavy hole splitting may differ significantly from the ones calculated assuming a full confinement in the dot. In both methods (emission diagram and Zeeman shift), the experimental values of hole anisotropy are smaller than the theoretical ones estimated from the quantum dot aspect ratio. Moreover, both light hole and heavy hole ground states can be observed depending on the studied nanowire.

The fit of the exciton Zeeman shifts allows us to estimate also the Zeeman shift at saturation of the electron (noted E_{se}) and of the hole (noted E_{sh}) confined in the dot. According to the "Exchange Box Model", E_{se} and E_{sh} are given by $\frac{1}{2}N_0\alpha x_{eff}$ and $\frac{1}{2}N_0\beta x_{eff}$. With quantum dots with 10% Mn, one expects 11meV for electron and 44meV for holes. As shown in the table, the experimental value for the shift at saturation of electron (E_{se}) are closed to the expected values. For the holes, there is a dispersion in the experimental values. We can conclude that for a light hole state, the value at saturation is in agreement with the theoretical one, this is the proof of a better coupling with the Mn atoms. For heavy hole states, the hole Zeeman shifts are significantly smaller than the expected ones. Such reduced values result probably from a partial delocalization of the heavy hole states in the barrier.

To better confine the hole inside the quantum dot, we study a second type of samples containing (Cd,Mn)Te quantum dots surrounded by (Zn,Mg)Te alloys. The incorporation of Mg increase the valence band offset between the dot (Cd,Mn)Te and the barrier (Zn,Mg)Te and hence the hole confinement.

With these samples, the formation of Magnetic Polaron is revealed qualitatively by the non monotonous temperature variation of the quantum dot emission energy. To retrieve the Magnetic Polaron parameters (formation time and energy) we performed time resolved spectroscopy with a streak camera on a single nanowire. This

TABLE 4.11: Main results on Sample 2

	ΔE	E_{se}	E_{sh}	E_P^{lh}	E_P^{hh}
MP1	12meV	11meV	38.5meV	13meV (T=5K)	23.6meV (T=5K)

was a particularly challenging experiment with a single (Cd,Mn)Te dot (small count rate with low power excitation, quantum dot line broadening induced by Mn spin fluctuations). This is the first time with a magnetic quantum inserted in a nanowire. We summarize the main characteristic of Magnetic Polarons in Table 4.11.

We are in the presence of a stable Magnetic Polaron with a polaron energy at 6K of 13meV. Its formation time τ_f=90ps is much smaller than the exciton lifetime τ_x=640ps.

We complete these experiments with continuous magneto-optical spectroscopy in order to determine the nature of the hole ground state. We apply a magnetic field parallel to the nanowire axis, revealing a complex Giant Zeeman shift of the exciton line. Using the "Exchange Box Model" allows us to fit the exciton Giant Zeeman shift which reveals the light hole character of the hole confined in the dot. In order to have a polaron model valid up to high temperatures (typically 50K for the highest temperature used with the streak camera measurements), we develop a model which takes into account the magnetic fluctuations using the free energy. To our knowledge, this is the first time that such models, initially developed with isotropic donors, have been adapted to anisotropic systems.

To compare our results with the results reported with self assembled quantum dots or in more recent Type II quantum dots with heavy holes, we extract the heavy hole Magnetic Polaron energy expected at 5K E_P^{hh}=23.6meV. This value is higher than the one reported in Type I self assembled quantum dots [12] and comparable to the more recent values reported with Type II dots [35]. However, for our system, there is still room for improvement: the exciton lifetime is still large compared to the one of a Type I quantum dot, suggesting again a partial hole confinement. We may then increase even more the Magnetic Polaron energy by confining better the hole in the quantum dot.

Prospects

The hole confinement is the keypoint which determines the nature and the strength of the Magnetic Polaron. It is then necessary to perform a calculation that goes beyond the exchange box approximation and that takes into account electron and hole envelope functions. Ab initio calculations of the electronic structure of CdTe quantum dots inserted in ZnTe nanowires are under progress in collaboration with Y.M Niquet from CEA Grenoble.

The low heavy hole-light hole splitting estimated in the sample studied so far seems to suggest that holes are weakly confined in the dot due to a low valence band offset. A solution to this problem would be to grow additional samples with a higher Mg content in the (Zn,Mg)Te shell surrounding the quantum dot or with a ZnSe shell.

A Mn concentration around 10% leads to an effective concentration of 4% that is already very close to the maximum value achievable. We cannot then play too much with the Mn concentration to have stronger Magnetic Polarons. If holes remain partially delocalized in the barrier, Mn could be added in the (Zn,Mg)Te barrier around the dot in order to increase the overlap between holes and Mn spins and hence increase the Magnetic Polaron energy. It has been done in a recent experiment based on ZnTe/(Zn,Mn)Se and (Zn,Mn)Te/ZnSe Type II self assembled quantum dots [35] where high Magnetic Polaron energies have been found but the hole confinement remains to be further investigated. By extending the same idea to nanowires containing quantum dots with different aspect ratio, very stable 0D Magnetic Polarons with a well controlled anisotropy could be obtained. It may be possible to implement a magnetic memory device based on a nanowire containing two (Cd,Mn)Te quantum dots (see Figure 4.29): one with a heavy hole character and the other with a light hole one. By applying a bias voltage we would control the ferromagnetic phase of the device while the read out process will be based on the different polarization of the emitted light.

As shown in this thesis, one way to determine the nature (heavy hole or light hole) of the hole ground state in a (Cd,Mn)Te quantum dot, is to perform magneto-optical measurements with magnetic field applied parallel and perpendicular to the quantum dot quantization axis which is parallel to the nanowire growth axis. Micro-PL experiment with a vectorial magnet would be particularly convenient to record exciton Giant Zeeman effect with both magnetic field orientations for each studied nanowire.

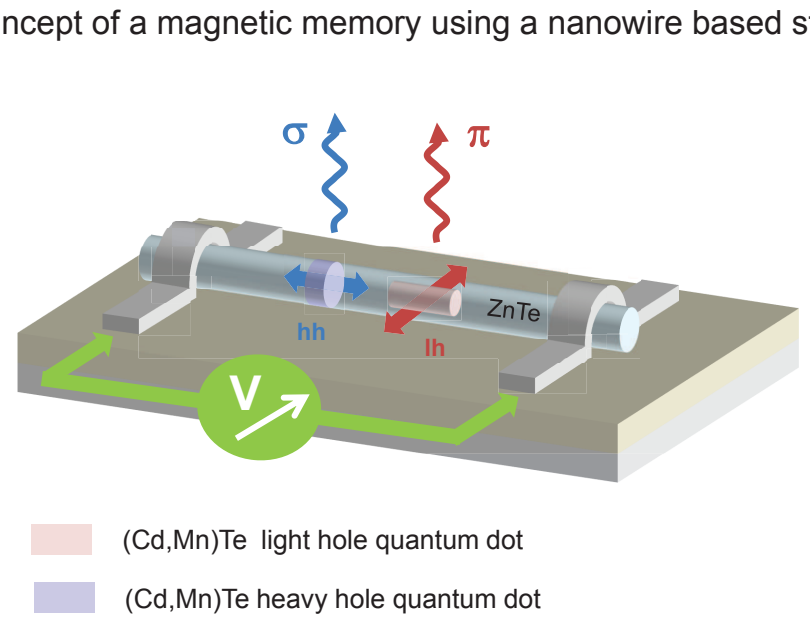

FIGURE 4.29: Concept of a magnetic memory based on a double (Cd,Mn)Te quantum dot nanowire

A comparison with the analysis of the emission diagram performed under applied magnetic field would be also particularly interesting.

In this work, we show that II-VI magnetic nanostructures inserted in ZnTe nanowires are feasible. ZnTe epilayers grown by molecular epitaxy can be heavily p doped using nitrogen. Research are presently under progress in the group in order to evaluate the possibility to dope p type ZnTe nanowires (PhD Marta Orrú). This may opens-up new possibilities of modulation doped heterostructures ((Cd,Mn)Te quantum dots with p-type modulation doping resulting in the presence of a permanent hole for example).

Appendix A

Helmholtz free energy

To retrieve the magnitude and orientation of the magnetic moment in the presence of a Magnetic Polaron, we used a free energy approach based on the minimization of the total free energy of the system. In this Appendix, we show how we can retrieve the expression of the free energy using the partition function Z.
The probability p_i of occupying a state i with energy E_i at temperature T is:

$$p_i = \frac{e^{-E_i/k_B T}}{Z} \tag{A.1}$$

Where Z is the single-particle partition function which is used to normalize the probability such that:

$$\sum_i p_i = 1 \tag{A.2}$$

This implies that Z is given by:

$$Z = \sum_i e^{-E_i/k_B T} \tag{A.3}$$

Now it is possible to define the two quantities that will be used to calculate the expected value of the energy $\langle E \rangle$. These are given by:

$$\beta = \frac{1}{k_B T}$$

$$\frac{\partial Z}{\partial \beta} = -\sum_i E_i e^{-\beta E_i}$$

The expected value of the energy $\langle E \rangle$ is then:

$$\langle E \rangle = -\sum_i E_i p_i = \frac{\sum_i E_i e^{-\beta E_i}}{Z} = -\frac{1}{Z}\frac{\partial Z}{\partial \beta} = -\frac{\partial ln Z}{\partial \beta} \tag{A.4}$$

It is possible also to define the entropy of the system as:

$$S = -k_B \sum_i p_i ln p_i \tag{A.5}$$

Using equation A.1 and A.5 it is possible to rewrite the entropy such as:

$$S = -k_B \sum_i \frac{e^{-\beta E_i}}{Z}[-\beta E_i - ln Z] = k_B ln Z + \frac{\langle E \rangle}{T} \tag{A.6}$$

For N independent distinguishable particles, the appropriate partition function becomes Z^N and so the total energy is given by $E = N\langle E \rangle$.
The first law of thermodynamics can be expressed as:

$$dE = TdS - pdV - MdB \tag{A.7}$$

The Helmholtz free energy F is defined by:

$$F = E - TS \tag{A.8}$$

and is related to the partition function Z by:

$$F = -Nk_B T lnZ \tag{A.9}$$

Combining equation A.7 and A.8 we can have:

$$dF = -SdT - pdV - MdB \tag{A.10}$$

The Helmholtz free energy is a function of $F = F(S, p, M)$, and for example we can see how to calculate easily the magnetization of the system using the Helmholtz free energy:

$$M = -\left(\frac{\partial F}{\partial B}\right)_{T,V} = Nk_B T \left(\frac{\partial lnZ}{\partial B}\right)_{T,V} \tag{A.11}$$

Appendix B

Free energy for a system with total angular momentum J

In this Appendix we show how to calculate the total free Energy for a general system defined by a total angular momentum J and how the Brillouin Function is defined. First we have to write down the partition function Z and after it will be possible to derive the Helmholtz free Energy F using equation A.9.
The system with total angular momentum J in an external magnetic field B is described in Figure B.1.

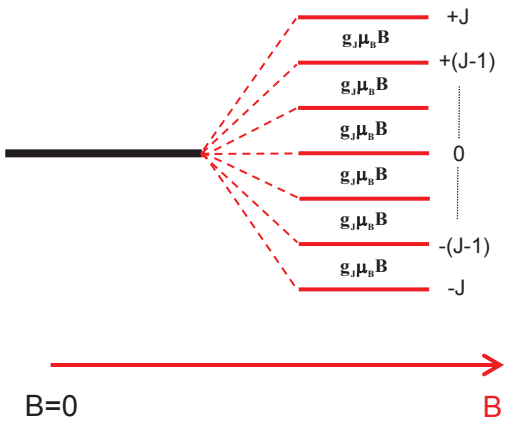

FIGURE B.1: A system with total angular momentum J in an external magnetic field B

There are $(2J+1)$ states with energy given by:

$$e_J = g_J \mu_B B m_J \tag{B.1}$$

Where g_J is the Lande g-factor and $m_J = -J, -(J-1), ..., 0, ..., +(J-1), +J$. Let's take a new variable y to easily develop the calculation of the partition function:

$$y = g_J \mu_B B \beta$$

With $\beta = 1/k_B T$. We can then calculate the partition function:

$$Z = \sum_{m_J=-J}^{J} = e^{g_J \mu_B B \beta} = \sum_{m_J=-J}^{J} e^{y m_J} \tag{B.2}$$

From equation B.2 it is possible to rewrite the sum on m_J as:

$$Z = \sum_{m_J=-J}^{J} e^{y m_J} = e^{-yJ} \sum_{m_J=0}^{2J} e^{y m_J} \tag{B.3}$$

It is possible to expand the exponential and to write:

$$\begin{aligned} Z = e^{-yJ} \sum_{m_J=0}^{2J} e^{-y m_J} = e^{-yJ} \frac{e^{(2J+1)y-1}}{e^{y-1}} = \frac{e^{(J+1)y} - e^{-Jy}}{e^{y} - 1} = \\ = \frac{e^{(J+\frac{1}{2})y} - e^{-(J+\frac{1}{2})y}}{e^{\frac{1}{2}y} - e^{-\frac{1}{2}y}} = \frac{sinh(J+\frac{1}{2})y}{sinh\frac{y}{2}} \end{aligned} \tag{B.4}$$

Now that the partition function has been calculated for a general case of a system with total angular momentum J, we can retrieve the equation for the Helmholtz free energy using equation A.9:

$$F = -Nk_BTlnZ = -Nk_BT\left[ln\left(sinh\left(J+\frac{1}{2}\right)y\right) - ln\left(sinh\frac{y}{2}\right)\right] \tag{B.5}$$

Without entering too much into the details of the calculation, now that the Helmholtz free energy has been defined, we can retrieve the equation for the magnetization of a general system with total spin J using equation A.11. The magnetization of such a system is in fact given by:

$$M = g_J\mu_B\frac{\partial F}{\partial y} = g_J\mu_B\left[\left(J+\frac{1}{2}\right)coth\left(J+\frac{1}{2}\right)y - \frac{1}{2}coth\frac{y}{2}\right] = g_J\mu_B JB_J(y) \tag{B.6}$$

Where the function $B_J(y)$ is the Brillouin function that is given by:

$$B_J(y) = \frac{1}{J}\left[\left(J+\frac{1}{2}\right)coth\left(J+\frac{1}{2}\right)y - \frac{1}{2}coth\frac{y}{2}\right] \tag{B.7}$$

Appendix C

Model to fit the CL profiles

In this Appendix we show how to extract the equation that models the cathodoluminescence profiles, presented in Chapter 2.
The $1D$ diffusion equation is given by:

$$\frac{d^2 n(x)}{dx^2} = \frac{n(x)}{L_D^2} \tag{C.1}$$

where the diffusion length is $L_D = \sqrt{D\tau}$ and $n(x)$ is the exciton density at the point x. The parameters are two: D is the diffusion constant and τ is the lifetime of the exciton in the nanowire.
When the electron beam excite the point 0, it spreads into two different carrier fluxes ϕ_0^+ and ϕ_0^- towards $x > 0$ and towards $x < 0$ respectively. The total flux is given by:

$$\phi_0 = \phi_0^+ + \phi_0^- \tag{C.2}$$

We can write down the two general solutions of equation C.1 for $x > 0$ and $x < 0$:

$$\begin{aligned} n^+(x) &= \widetilde{A} e^{-\frac{x}{L_D}} + \widetilde{B} e^{+\frac{x}{L_D}} \\ n^-(x) &= \widetilde{C} e^{-\frac{x}{L_D}} + \widetilde{D} e^{+\frac{x}{L_D}} \end{aligned} \tag{C.3}$$

We have now to apply the boundary conditions to equation C.3. We start with $n^-(x)$ and the flux $\phi^-(x)$ far away from the quantum dot region.

$$\phi^-(x) = -D\left(\frac{dn^-(x)}{dx}\right) \quad \phi^-(x \longrightarrow -\infty) = 0 \Longrightarrow \widetilde{C} = 0 \tag{C.4}$$

The solution $n^-(x)$ will be then given by:

$$n^-(x) = \widetilde{D}e^{\frac{x}{L_D}} \tag{C.5}$$

$\phi_0^- = -\phi^-(x=0) = \frac{D}{L_D}\widetilde{D}$ and then the solution for $n^-(x)$ that is given by:

$$n^-(x) = \frac{L_D\phi_0^-}{D}e^{\frac{x}{L_D}} \tag{C.6}$$

For the solution towards the quantum dot region, $n^+(x)$, we have:

$$n^+(x): \begin{cases} -D(\frac{dn(x)}{dx})_{x>0} = \phi_0^+(x) & \\ n^+(x_0) = 0 & \text{(QD is a perfect trap)} \end{cases} \tag{C.7}$$

We write first $n^+(x_0) = 0$ using equation C.3:

$$n^+(x_0) = \widetilde{A}e^{-\frac{x_0}{L_D}} + \widetilde{B}e^{+\frac{x_0}{L_D}} = 0 \tag{C.8}$$

From equation C.8 we can extract the value of $\widetilde{B}$:

$$\widetilde{B} = -\widetilde{A}e^{-\frac{2x_0}{L_D}} \tag{C.9}$$

The equation C.9 leads to the following expression for $n^+(x)$:

$$n^+(x) = \widetilde{A}\left[e^{-\frac{x}{L_D}} - e^{-\frac{2x_0}{L_D}} e^{\frac{x}{L_D}}\right] \tag{C.10}$$

By the substitution of equation C.10 in equation C.7 we retrieve the expression of ϕ_0^+:

$$\phi_0^+ = \phi^+(x=0) = -\frac{D}{L_D}\widetilde{A}\left[-1 - e^{-\frac{2x_0}{L_D}}\right] \tag{C.11}$$

By substituting it in the expression of $n^+(x)$ we get the real solution of the problem for $x > 0$:

$$n^+(x) = \frac{L_D\phi_0^+}{D}\frac{\sinh\left(\frac{x_0-x}{L_D}\right)}{\cosh\left(\frac{x_0}{L_D}\right)} \tag{C.12}$$

To have the final expression of the diffusion inside the quantum dot, we have to connect the two different solutions $n^-(0)$ and $n^+(0)$ in the excitation point 0. We will have then:

$$\begin{cases} n^+(0) = n^-(0) \Longrightarrow \frac{L_D\phi_0^+}{D}\frac{sinh\left(\frac{x_0}{L_D}\right)}{cosh\left(\frac{x_0}{L_D}\right)} = \frac{L_D\phi_0^-}{D} \\ \phi_0^+ + \phi_0^- = \phi_0 \end{cases} . \tag{C.13}$$

We can then retrieve the equation for ϕ_x^+ from the previous equation that is given by:

$$\phi_0^+ = \phi_0 e^{-\frac{x_0}{L_D}}\cosh\left(\frac{x_0}{L_D}\right) \tag{C.14}$$

We can then substitute equation C.14 in equation C.12 leading to the final expression:

$$n^+(x) = \frac{L_D\phi_0}{D}e^{-\frac{x_0}{L_D}}\sinh\left(\frac{x_0-x}{L_D}\right) \tag{C.15}$$

As we have calculated $n^+(x)$ we can retrieve the flux at the level of the quantum dot $x = x_0$ that will be proportional (equal in the case of purely radiative recombination processes) to the number of the emitted photons. The flux is given by:

$$\phi_{QD} = -D\left(\frac{d(n^+(x))}{dx}\right)_{x=x_0} = \phi_0 e^{-\frac{|x_0|}{L_D}} \tag{C.16}$$

To fit the cathodoluminescence profile we have added a trapping region to the diffusion solution, equation C.16, that simulates the size of the quantum dot or more precisely the recombination region that is linked to the chemical potential of the quantum dot ($2x_t$ in Figure 2.23a). The diffusion solution will be then given by:

$$\begin{cases} I_{QD}(x) = \phi_0 e^{\frac{-|x_0-x_t|}{L_{base}}} & x < -x_t \\ I_{QD}(x) = \phi_0 e^{\frac{-|x_0-x_t|}{L_{top}}} & x > x_t \\ I_{QD}(x) = \phi_0 & -x_t < \mid x \mid < x_t \end{cases} \tag{C.17}$$

In the presented treatment we have supposed a point-like electron beam excitation. In the conditions used to acquire the cathodoluminescence, the electron beam has not an infinitely small size. We have calculated then, using a Monte-Carlo simulation software [91] the dimension of the electron beam at the measurement conditions looking at the electron dispersion given by the backscattering processes. The CdTe quantum dot has been considered as a 10nm×10nm cube inserted in a 100nm thick matrix of ZnTe. We found a dimension of the electron beam (FWHM) between 80nm and 100nm. We then model the beam spot with a Gaussian function defined by:

$$\phi_{beam}(x_0) = \frac{\phi_0}{\sqrt{2\pi\sigma}} e^{-\frac{x_0^2}{2\sigma^2}} \tag{C.18}$$

To fit the CL signal, we used then the following convolution equation:

$$\widetilde{I}_{QD}(x_0) = \int I_{QD}(x)\phi_{beam}(x_0 - x)\,dx \tag{C.19}$$

Appendix D

Complementary considerations on the "Exchange Box Model"

In this Appendix, we discuss the validity of the "Exchange Box Model". We show that, without taking into account the electron and hole envelope functions, this model fails to explain the experimental values. The calculations that we are going to present are very preliminary and far to be the final one.
In Chapter 2, Section 2.1.1.1, we show that by using the EDX images we can determine the quantum dot dimensions. It is possible then, to calculate the quantum dot volume that, for an ellipsoidal quantum dot, is given by:

$$V_{QD}^{EDX} = \frac{4}{3}\pi(a \times b \times c) = \frac{4}{3}\pi(4^2 \times 7.5) \cong 500nm^3 \tag{D.1}$$

Where a=b=4nm and $c = \frac{15\text{nm}}{2}$=7.5nm. This is the quantum dot real volume: in the next Section we recall how it could be linked to the effective number of Mn spins by using the "Exchange Box Model".

D.1 Number of spins

We showed that the common approximation used, to model the sp-d exchange interactions between excitons and Mn atoms is the "Exchange Box Model", as explained in Chapter 1. The quantum dot is assumed to be a box with Mn moments distributed

homogeneously inside it. By using this model, we can define an effective number of spins that are participating to the sp-d exchange interaction by:

$$N_{eff} = x_{eff} V_{QD}^{box} N_0 \tag{D.2}$$

We can observe that by the definition D.2, we can also define an exchange box volume given by: $V_{QD}^{box} = \frac{N_{eff}}{x_{eff} N_0}$. Here x_{eff} is the effective Mn concentration and N_0 is the cation density ($N_0 \cong 15 \frac{\text{atoms}}{\text{nm}^3}$ (see Chapter 1). For MP1, if we use the values for $N_{eff} = 59$ and $x_{eff} = 4\%$ (from the EDX measurements, Section 2.1.1.1) we find $V_{QD}^{box} \cong 100\text{nm}^3$.
This value is of the same order of magnitude as V_{QD}^{EDX} but still it is smaller than expected.
The "Exchange Box Model" supposes a constant hole wavefunction inside the quantum dot and then a uniform overlap between the hole wavefunction and Mn atoms. We showed, from the EDX images (Section 2.1.1.1), that the Mn atoms are reasonably homogeneously distributed inside the (Cd,Mn)Te region: the only way to explain the significant discrepancy between the physical quantum dot volume and the theoretical one is to suppose a delocalized hole wavefunction. This has been suggested by the long decay time of MP1 (shorter compare to sample 1) that is equal to 640ps.

D.2 Influence of the envelope functions

We can try to use a more sophisticated model, that takes into account the electron-hole envelope functions.
We showed (in the "Exchange Box Model" approximation, see Chapter 1) that it is possible to define, the Magnetic Polaron energy for a heavy hole exciton by:

$$E_P^{hh} = \frac{(S+1)(E_{se} + E_{sh})^2}{12 k_B T N_{eff} S} \tag{D.3}$$

If now we take into account the envelope functions for electron and hole, by considering a MFA, we can show that we get (see [17]):

$$E_P^{hh} = \frac{(S+1)(E_{se}+E_{sh})^2}{3Sk_BT} \frac{\left[\alpha^2\widetilde{\varphi_e^4} + \beta^2\widetilde{\varphi_h^4} + 2\alpha|\beta|\widetilde{\varphi_e^2\varphi_h^2}\right]}{\left[\alpha\widetilde{\varphi_e^2} + |\beta|\widetilde{\varphi_h^2}\right]^2} \tag{D.4}$$

Where $\widetilde{\varphi_e^n} = \int d^3\vec{r}\rho(\vec{r}) \mid \varphi_e(\vec{r}) \mid^n$ and $\widetilde{\varphi_h^n} = \int d^3\vec{r}\,\rho(\vec{r}) \mid \varphi_h(\vec{r}) \mid^n$ and $\widetilde{\varphi_e^2\varphi_h^2} = \int d^3\vec{r}\,\rho(\vec{r}) \mid \varphi_e(\vec{r}) \mid^2 \mid \varphi_h(\vec{r}) \mid^2$.
We can define the effective number of Mn spins coupled to the exciton by imposing the consistency with the expression of the Magnetic Polaron energy found from the "Exchange Box Model" (equation D.4 and equation D.3) as:

$$N_{eff} = \frac{\left[\alpha\widetilde{\varphi_e^2} + |\beta|\widetilde{\varphi_h^2}\right]^2}{\left[\alpha^2\widetilde{\varphi_e^4} + \beta^2\widetilde{\varphi_h^4} + 2\alpha|\beta|\widetilde{\varphi_e^2\varphi_h^2}\right]} \tag{D.5}$$

If we assume a constant Mn spin concentration in the quantum dot $\varrho(\vec{r}) = N_0 x_{eff}$ we can define an exchange volume V_{QD}^{exc} by using $N_{eff} = N_0 V_{QD}^{exc} x_{eff}$ where V_{QD}^{exc} is given by:

$$V_{QD}^{exc} = \frac{\left[\alpha\widehat{\varphi_e^2} + |\beta|\widehat{\varphi_h^2}\right]^2}{\left[\alpha^2\widehat{\varphi_e^4} + \beta^2\widehat{\varphi_h^4} + 2\alpha|\beta|\widehat{\varphi_e^2\varphi_h^2}\right]} \tag{D.6}$$

with $\widehat{\varphi_e^n} = \int d^3\vec{r} \mid \varphi_e(\vec{r}) \mid^n$ and $\widehat{\varphi_h^n} = \int d^3\vec{r} \mid \varphi_h(\vec{r}) \mid^n$ and
$\widehat{\varphi_e^2\varphi_h^2} = \int d^3\vec{r} \mid \varphi_e(\vec{r}) \mid^2 \mid \varphi_h(\vec{r}) \mid^2$.
Unfortunately the evaluation of D.6 is not easy: we don't know in fact the envelop functions of electron and hole. In the next Section we will show how to fix some limits on the electron-hole presence probabilities using the Giant Zeeman shift and the physical quantum dot volume.

D.3 Presence probabilities inside the quantum dot

We can define two limits to determine a range for the values of $|\varphi_e(\vec{r})|^2$ and $|\varphi_h(\vec{r})|^2$. The first constraint is deduced from the Giant Zeeman shifts. The energy shift, at saturation, E^X_{sat} of the Giant Zeeman effect is in fact given by (see Chapter 1):

$$E_{se} + E_{sh} = E^X_{sat} = N_0 x_{eff} \left[\alpha \widehat{\varphi_e^2} + |\beta| \widehat{\varphi_h^2} \right] = 55\text{meV} \tag{D.7}$$

We can compare the value of equation D.7 with the one expected from the "Exchange Box Model":

$$P_1 = \frac{E^{exc}_{sat}}{E^{box}_{sat}} = \frac{\left[\alpha \widehat{\varphi_e^2} + |\beta| \widehat{\varphi_h^2} \right]}{[\alpha + |\beta|]} \cong 0.9 \tag{D.8}$$

The second constraint is on the effective volume:

$$P_2 = \frac{V^{exc}_{QD}}{V^{EDX}_{QD}} \cong 1 = \frac{1}{V^{EDX}_{QD}} \frac{\left[\alpha \widehat{\varphi_e^2} + |\beta| \widehat{\varphi_h^2} \right]^2}{\left[\alpha^2 \widehat{\varphi_e^4} + \beta^2 \widehat{\varphi_h^4} + 2\alpha|\beta| \widehat{\varphi_e^2 \varphi_h^2} \right]} \tag{D.9}$$

The exchange sp-d volume has to be equal to the physical one if we consider a homogeneous Mn distribution in the quantum dot region, as confirmed by the EDX measurements described in Chapter 2.

D.4 Examples of some possible presence probabilities configurations

We tried then to determine some possible "configurations" concerning the electron-hole envelope functions. We assumed that the electron-hole wavefunctions have cylindrical symmetry (we considered an infinite long quantum dot) and they could be written as the product of two different wavefunctions:

$$\varphi_e = \varphi_e(\widehat{\rho})\varphi_e(\widehat{z}) \tag{D.10}$$

$$\varphi_h = \varphi_h(\widehat{\rho})\varphi_h(\widehat{z}) \tag{D.11}$$

Where $\widehat{\rho}$ is the radial part and $\widehat{z}$ is along the nanowire axis.
For the electron wavefunction, we used Bessel function for the radial part and the solution for an infinite potential for the z direction:

$$\varphi_e = A_e J_0\left(\frac{x_{1,0}\rho}{R}\right)\cos\left(\frac{\pi z}{L}\right) \tag{D.12}$$

We supposed in all the cases an electron perfectly confined inside the quantum dot. For φ_h instead we considered the product of two different Gaussian test functions, for the radial part and along the nanowire axis:

$$\varphi_h = A_h e^{\frac{-(\rho-\rho_0)^2}{2\sigma_\rho^2}} e^{\frac{-z^2}{2\sigma_z^2}} \tag{D.13}$$

The fitting parameters are then $\rho_0, \sigma_\rho, \sigma_z$ where ρ_0 defines the hole delocalization in the barrier.
We will present now two possible cases where the two constraints are satisfied.

D.4.1 Case 1

For the first case we assumed that the two wavefunctions are centered in the same place $\rho_0 = 0$ (center of the dot) and the result is shown in Figure D.1.

$P_1 \cong 0.9$	$P_2 \cong 0.85$	$\sigma_\rho = 1.8$nm	$\sigma_z = 1.5$nm

We can see, from the table, that the two limits P_1 and P_2 are satisfied.
For this case the hole presence probability in the quantum dot is very high and equal to $\mathscr{P}_h = 98\%$. This is the ideal case: we have a hole wavefunction completely confined leading to a Type 1 quantum dot.

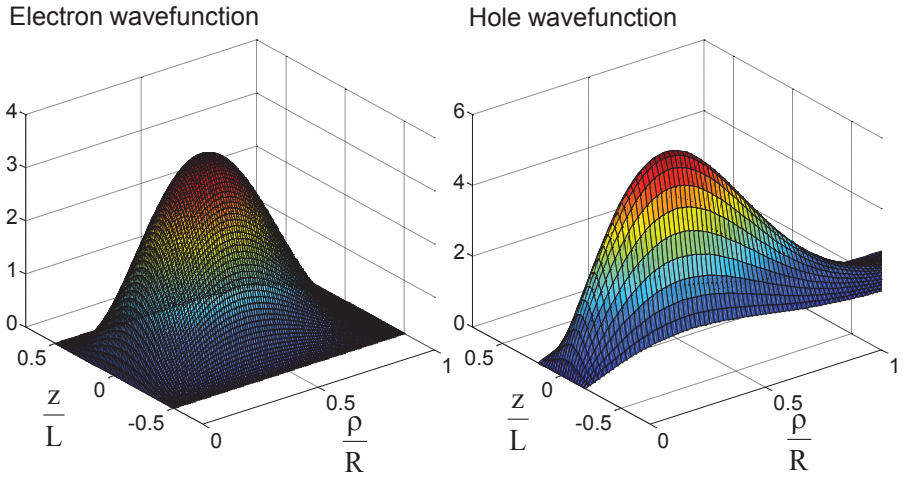

FIGURE D.1: Electron-hole wavefunctions

We know, from the time resolved photoluminescence experiments, that due to the long exciton lifetime (640ps for MP1), we are in the presence of a more Type II quantum dot. In the next Section, we will consider another case with a more delocalized hole wavefunction.

D.4.2 Case 2

For the second case, we have considered a hole wavefunction delocalized with ρ_0=3.48nm. Also for this case we have found that the two constraints are satisfied, the results are traced in Figure D.2.

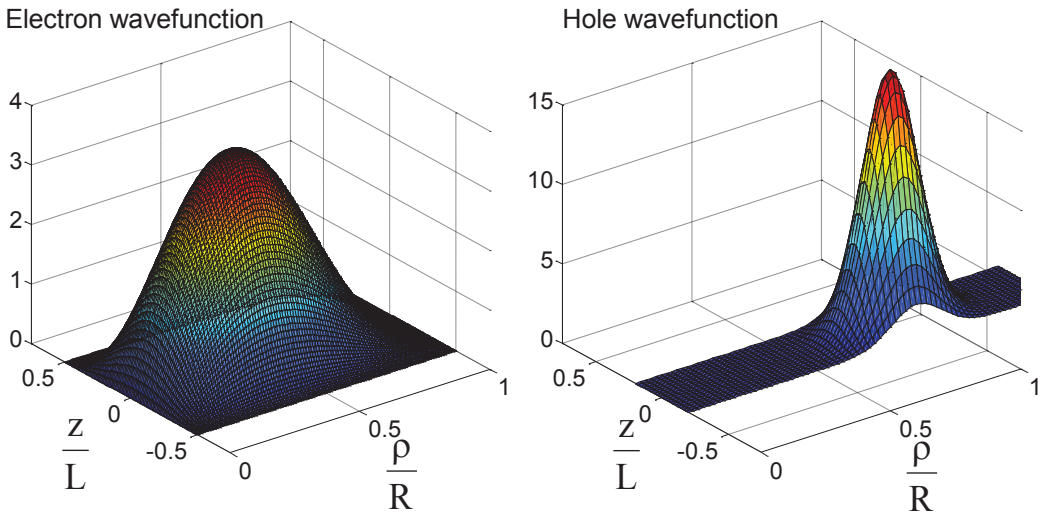

FIGURE D.2: Electron-hole wavefunctions

$P_1 \cong 0.9$	$P_2 \cong 0.85$	$\sigma_\rho = 0.4$nm	$\sigma_z = 1.5$nm

In this case, for a hole partially delocalized in the barrier, we had to consider a more peaked hole wavefunction to satisfy the two limits defined by P_1 and P_2.
For this second case the hole wavefunction presence probability is $\mathscr{P}_h = 88\%$. We have then a partially delocalized hole wavefunction that could lead to a more Type II structure and explain the high exciton lifetime that has been found.
If we consider what we presented in Chapter 2, Section 2.2, we see that due to the strain, we have a very strong trapping potential at the (Cd,Mn)Te/ZnTe barrier leading to non diagonal terms in the hole Bir-Pikus Hamiltonian. This potential could trap the hole leading to a situation similar to this calculated "Case 2".

Bibliography

[1] M. N. Baibich, J. M. Broto, A. Fert, F. Nguyen Van Dau, F. Petroff, P. Etienne, G. Creuzet, A. Friederich, and J. Chazelas. Giant magnetoresistance of (001)fe/(001)cr magnetic superlattices. *Phys. Rev. Lett.*, 61(21):2472–2475, 1988.

[2] Supriyo Datta and Biswajit Das. Electronic analog of the electroâĂŘoptic modulator. *Applied Physics Letters*, 56(7):665–667, 1990.

[3] H. Ohno, H. Munekata, T. Penney, S. von Molnár, and L. L. Chang. Magnetotransport properties of *p* -type (in,mn)as diluted magnetic iii-v semiconductors. *Phys. Rev. Lett.*, 68(17):2664–2667, 1992.

[4] A. Haury, A. Wasiela, A. Arnoult, J. Cibert, S. Tatarenko, T. Dietl, and Y. Merle d'Aubigné. Observation of a ferromagnetic transition induced by two-dimensional hole gas in modulation-doped cdmnte quantum wells. *Phys. Rev. Lett.*, 79(3):511–514, 1997.

[5] H. Boukari, P. Kossacki, M. Bertolini, D. Ferrand, J. Cibert, S. Tatarenko, A. Wasiela, J. A. Gaj, and T. Dietl. Light and electric field control of ferromagnetism in magnetic quantum structures. *Phys. Rev. Lett.*, 88(20):207204, 2002.

[6] P. Wojnar, J. Suffczyński, K. Kowalik, A. Golnik, G. Karczewski, and J. Kossut. Microluminescence from $cd_{1-x}mn_xTe$ magnetic quantum dots containing only a few mn ions. *Phys. Rev. B*, 75(15):155301, 2007.

[7] L. Besombes, Y. Léger, L. Maingault, D. Ferrand, H. Mariette, and J. Cibert. Probing the spin state of a single magnetic ion in an individual quantum dot. *Phys. Rev. Lett.*, 93(20), 2004.

[8] J Kobak, T Smoleński, M Goryca, M Papaj, K Gietka, A Bogucki, M Koperski, J-G Rousset, J Suffczyński, E Janik, et al. Designing quantum dots for solotronics. *Nature communications*, 5, 2014.

[9] T. Dietl and J. Spałek. Effect of fluctuations of magnetization on the bound magnetic polaron: Comparison with experiment. *Phys. Rev. Lett.*, 48(5):355–358, 1982.

[10] M. Nawrocki, R. Planel, G. Fishman, and R. Galazka. Exchange-induced spin-flip raman scattering in a semimagnetic semiconductor. *Phys. Rev. Lett.*, 46(11): 735–738, 1981.

[11] M. Bugajski, P. Becla, P. A. Wolff, D. Heiman, and L. R. Ram-Mohan. Acceptor-bound magnetic polarons in $cd_{1-x}mn_xte$. *Phys. Rev. B*, 38(15):10512–10516, 1988.

[12] Ł. Kłopotowski, Ł. Cywiński, P Wojnar, V Voliotis, K Fronc, T Kazimierczuk, A Golnik, M Ravaro, R Grousson, G Karczewski, T Wojtowicz, et al. Magnetic polaron formation and exciton spin relaxation in single cd 1- x mn x te quantum dots. *Phys. Rev. B*, 83(8):081306, 2011.

[13] Piotr Wojnar, Elżbieta Janik, Lech T. Baczewski, Sławomir Kret, Elżbieta Dynowska, Tomasz Wojciechowski, Jan Suffczyński, Joanna Papierska, Piotr Kossacki, Grzegorz Karczewski, Jacek Kossut, and Tomasz Wojtowicz. Giant spin splitting in optically active znmnte/znmgte core/shell nanowires. *Nano Letters*, 12(7):3404–3409, 2012.

[14] P. Carolina Rueda-Fonseca. *Magnetic quantum dots in II-VI semiconductor nanowires*. Phd thesis, These de Doctorat de l'Universite Joseph Fourier - Grenoble I, 2015.

[15] T. Dietl and J. Spałek. Effect of thermodynamic fluctuations of magnetization on the bound magnetic polaron in dilute magnetic semiconductors. *Phys. Rev. B*, 28(3):1548–1563, 1983.

[16] A. Artioli, P. Rueda-Fonseca, P. Stepanov, E. Bellet-Amalric, M. Den Hertog, C. Bougerol, Y. Genuist, F. Donatini, R. André, G. Nogues, K. Kheng, S. Tatarenko, D. Ferrand, and J. Cibert. Optical properties of single znte nanowires grown at low temperature. *Applied Physics Letters*, 103(22):222106, 2013.

[17] P. Stepanov. *Magneto-optical spectroscopy of semiconductor magnetic quantum dots*. Phd thesis, These de Doctorat de l'Universite Joseph Fourier - Grenoble I, 2013.

[18] Christophe Couteau. *Vers une Source de Photons Uniques Indiscernables Produits par des BoËĘıtes Quantiques Semiconductrices II-VI*. Phd thesis, These de Doctorat de l'Universite Joseph Fourier - Grenoble I, 2005.

[19] Rafał Oszwałdowski, Igor Žutić, and A. G. Petukhov. Magnetism in closed-shell quantum dots: Emergence of magnetic bipolarons. *Phys. Rev. Lett.*, 106(17): 177201, 2011.

[20] P.Y. Yu and M. Cardona. *Fundamentals of Semiconductors*. Springer, 2010.

[21] Leonid A. Kosyachenko. *Solar Cells - New Approaches and Reviews*. INTECH, 2015.

[22] Guy Fishman. *Energie et fonction d'onde des semi-conducteurs*. Les éditions de physique, 1988.

[23] JM Luttinger. Quantum theory of cyclotron resonance in semiconductors: General theory. *Physical Review*, 102(4):1030, 1956.

[24] Le Si Dang, G Neu, and R Romestain. Optical detection of cyclotron resonance of electron and holes in cdte. *Solid State Communications*, 44(8):1187–1190, 1982.

[25] L. Vegard. Die konstitution der mischkristalle und die raumfüllung der atome. *Zeitschrift für Physik*, 5(1):17–26, 1921.

[26] Stöhr Joachim and Siegmann Hans Christoph. *Magnetism: From Fundamentals to Nanoscale Dynamics*. Springer, 2006.

[27] Jacek Kossut and Jan A. Gaj. *Introduction to the Physics of Diluted Magnetic Semiconductors*. Springer Series in Materials Science, 2010.

[28] J.A. Gaj, R. Planel, and G. Fishman. Relation of magneto-optical properties of free excitons to spin alignment of mn2+ ions in cd1âĹŠxmnxte. *Solid State Communications*, 29(5):435 – 438, 1979.

[29] JA Gaj, W Grieshaber, C Bodin-Deshayes, J Cibert, G Feuillet, Y Merle d'Aubigné, and A Wasiela. Magneto-optical study of interface mixing in the cdte-(cd,mn)te system. *Physical Review B*, 50(8):5512, 1994.

[30] Jan A Gaj and Jacek Kossut. *Introduction to the Physics of Diluted Magnetic Semiconductors*. Springer Science & Business Media, 2011.

[31] Stephen Blundell. *Magnetism in Condensed Matter*. Oxford University Press, 2001.

[32] Roland Winkler. *Spin-orbit coupling effects in two-dimensional electron and hole systems*. Springer, 2003.

[33] J. K. Furdyna. Diluted magnetic semiconductors. *Journal of Applied Physics*, 64 (4):R29–R64, 1988.

[34] Rémi Beaulac, Lars Schneider, Paul I. Archer, Gerd Bacher, and Daniel R. Gamelin. Light-induced spontaneous magnetization in doped colloidal quantum dots. *Science*, 325(5943):973–976, 2009.

[35] B. Barman, R. Oszwałdowski, L. Schweidenback, A. H. Russ, J. M. Pientka, Y. Tsai, W-C. Chou, W. C. Fan, J. R. Murphy, A. N. Cartwright, I. R. Sellers, A. G. Petukhov, I. Žutić, B. D. McCombe, and A. Petrou. Time-resolved magnetophotoluminescence studies of magnetic polaron dynamics in type-ii quantum dots. *Phys. Rev. B*, 92(3):035430, 2015.

[36] Xiangfeng Duan, Yu Huang, Yi Cui, Jianfang Wang, and Charles M Lieber. Indium phosphide nanowires as building blocks for nanoscale electronic and optoelectronic devices. *Nature*, 409(6816):66–69, 2001.

[37] Rehan Kapadia, Zhiyong Fan, Kuniharu Takei, and Ali Javey. Nanopillar photovoltaics: Materials, processes, and devices. *Nano Energy*, 1(1):132 – 144, 2012.

[38] Q. F. Meng, C. B. Jiang, and S. X. Mao. Ohmic contacts and photoconductivity of individual znte nanowires. *Applied Physics Letters*, 94(4), 2009.

[39] Adrien Tribu, Gregory Sallen, Thomas Aichele, Régis André, Jean-Philippe Poizat, Catherine Bougerol, Serge Tatarenko, and Kuntheak Kheng. A high-temperature single-photon source from nanowire quantum dots. *Nano Letters*, 8(12):4326–4329, 2008.

[40] S. Bounouar, M. Elouneg-Jamroz, M. den Hertog, C. Morchutt, E. Bellet-Amalric, R. André, C. Bougerol, Y. Genuist, J.-Ph. Poizat, S. Tatarenko, and K. Kheng. Ultrafast room temperature single-photon source from nanowire-quantum dots. *Nano Letters*, 12(6):2977–2981, 2012.

[41] Emanuel Knill, Raymond Laflamme, and Gerald J Milburn. A scheme for efficient quantum computation with linear optics. *Nature*, 409(6816):46–52, 2001.

[42] Alexios Beveratos, Rosa Brouri, Thierry Gacoin, André Villing, Jean-Philippe Poizat, and Philippe Grangier. Single photon quantum cryptography. *Phys. Rev. Lett.*, 89(18):187901, 2002.

[43] Zhe Liu, Gui Chen, Bo Liang, Gang Yu, Hongtao Huang, Di Chen, and Guozhen Shen. Fabrication of high-quality znte nanowires toward high-performance rigid/flexible visible-light photodetectors. *Opt. Express*, 21(6):7799–7810, 2013.

[44] Pavle V Radovanovic, Carl J Barrelet, Silvija Gradecak, Fang Qian, and Charles M Lieber. General synthesis of manganese-doped ii-vi and iii-v semiconductor nanowires. *Nano Letters*, 5(7):1407–1411, 2005.

[45] Alexei Bouravleuv, George Cirlin, Victor Sapega, Peter Werner, Alexander Savin, and Harri Lipsanen. Ferromagnetic (ga,mn)as nanowires grown by mn-assisted molecular beam epitaxy. *Journal of Applied Physics*, 113(14), 2013.

[46] Piotr Wojnar, Elżbieta Janik, Lech T. Baczewski, Sł awomir Kret, G. Karczewski, Tomasz Wojtowicz, Mateusz Goryca, Tomasz Kazimierczuk, and Piotr Kossacki. Growth and optical properties of cdte quantum dots in znte nanowires. *Applied Physics Letters*, 99(11), 2011.

[47] Małgorzata Szymura, Piotr Wojnar, Ł ukasz Kł opotowski, Jan Suffczyński, Mateusz Goryca, Tomasz Smoleński, Piotr Kossacki, Wojciech Zaleszczyk, Tomasz Wojciechowski, Grzegorz Karczewski, Tomasz Wojtowicz, and Jacek Kossut. Spin splitting anisotropy in single diluted magnetic nanowire heterostructures. *Nano Letters*, 15(3), 2015.

[48] P. Rueda-Fonseca, E. Bellet-Amalric, R. Vigliaturo, M. den Hertog, Y. Genuist, R. André, E. Robin, A. Artioli, P. Stepanov, D. Ferrand, K. Kheng, S. Tatarenko, and J. Cibert. Structure and morphology in diffusion-driven growth of nanowires: The case of znte. *Nano Letters*, 14(4):1877–1883, 2014.

[49] A Golnik, JA Gaj, M Nawrocki, R Planel, and C Benoit a la Guillaume. *J. Phys. Soc. Japan*, A49:p. 819, 1980.

[50] T. KASUYA and A. YANASE. Anomalous transport phenomena in eu-chalcogenide alloys. *Rev. Mod. Phys.*, 40(4):684–696, 1968.

[51] G. Mackh, W. Ossau, D. R. Yakovlev, A. Waag, G. Landwehr, R. Hellmann, and E. O. Göbel. Localized exciton magnetic polarons in $cd_{1-x}mn_xte$. *Phys. Rev. B*, 49(15):10248–10258, 1994.

[52] A Golnik, J Ginter, and J A Gaj. Magnetic polarons in exciton luminescence of cd 1-x mn x te. *Journal of Physics C: Solid State Physics*, 16(31):6073, 1983.

[53] SM Ryabchenko. Spin-correlation effects for a large-radius electron center in a magnetically mixed semiconductor. *Zh. Eksp. Teor. Fiz*, 84:1419–1421, 1983.

[54] A. A. Maksimov, G. Bacher, A. McDonald, V. D. Kulakovskii, A. Forchel, C. R. Becker, G. Landwehr, and L. W. Molenkamp. Magnetic polarons in a single diluted magnetic semiconductor quantum dot. *Phys. Rev. B*, 62(12):R7767–R7770, 2000.

[55] K. V. Kavokin, I. A. Merkulov, D. R. Yakovlev, W. Ossau, and G. Landwehr. Exciton localization in semimagnetic semiconductors probed by magnetic polarons. *Phys. Rev. B*, 60(24):16499–16505, 1999.

[56] D. R. Yakovlev, G. Mackh, B. Kuhn-Heinrich, W. Ossau, A. Waag, G. Landwehr, R. Hellmann, and E. O. Göbel. Exciton magnetic polarons in short-period cdte/$cd_{1-x}mn_x$te superlattices. *Phys. Rev. B*, 52(16):12033–12038, 1995.

[57] David Ferrand and Joel Cibert. Strain in crystalline core-shell nanowires. *European Physical Journal: Applied Physics*, 67:30403, 2014.

[58] Fabrice Donatini and Le Si Dang. A single-step electron beam lithography of buried nanostructures using cathodoluminescence imaging and low temperature. *Nanotechnology*, 21(37):375303, 2010.

[59] Zeiss nvision 40 dualbeam set-up. URL http://cmtc.grenoble-inp.fr/equipements/meb-fib-zeiss-nvision-40-684574.kjsp?RH=CMTC_ACTIVITES.

[60] M Yu Gutkin, I A Ovid'ko, and A G Sheinerman. Misfit dislocations in wire composite solids. *Journal of Physics: Condensed Matter*, 25(12):5391, 2000.

[61] W. Wardzyński, W. Giriat, H. Szymczak, and R. Kowalczyk. Stress-induced splitting of excitons due to exchange interaction in zinc telluride. *physica status solidi (b)*, 49(1):71–83, 1972.

[62] Le Si Dang, J. Cibert, Y. Gobil, K. Saminadayar, and S. Tatarenko. Optical study of residual strains in cdte and znte layers grown by molecular beam epitaxy on gaas. *Applied Physics Letters*, 55(3):235–237, 1989.

[63] Don Berlincourt, Hans Jaffe, and L. R. Shiozawa. Electroelastic properties of the sulfides, selenides, and tellurides of zinc and cadmium. *Phys. Rev.*, 129(3): 1009–1017, 1963.

[64] J. D. Eshelby. The determination of the elastic field of an ellipsoidal inclusion, and related problems. *Proceedings of the Royal Society of London A: Mathematical, Physical and Engineering Sciences*, 241(1226):376–396, 1957.

[65] J. D. Eshelby. The elastic field outside an ellipsoidal inclusion. *Proceedings of the Royal Society of London A: Mathematical, Physical and Engineering Sciences*, 252(1271):561–569, 1959.

[66] M. Zieliński. Fine structure of light-hole excitons in nanowire quantum dots. *Phys. Rev. B*, 88(11):115424, 2013.

[67] J. Camacho, A. Cantarero, I. HernÃąndez-CalderÃşn, and L. GonzÃąlez. Raman spectroscopy and photoluminescence of znte thin films grown on gaas. *Journal of Applied Physics*, 92(10):6014–6018, 2002.

[68] Maarten H. M. van Weert, Nika Akopian, Freek Kelkensberg, Umberto Perinetti, Maarten P. van Kouwen, Jaime Gómez Rivas, Magnus T. Borgström, Rienk E. Algra, Marcel A. Verheijen, Erik P. A. M. Bakkers, Leo P. Kouwenhoven, and Val Zwiller. Orientation-dependent optical-polarization properties of single quantum dots in nanowires. *Small*, 5(19):2134–2138, 2009.

[69] Jianfang Wang, Mark S Gudiksen, Xiangfeng Duan, Yi Cui, and Charles M Lieber. Highly polarized photoluminescence and photodetection from single indium phosphide nanowires. *Science*, 293(5534):1455–1457, 2001.

[70] Grégory Sallen, Adrien Tribu, Thomas Aichele, Régis André, Lucien Besombes, Catherine Bougerol, Maxime Richard, Serge Tatarenko, Kuntheak Kheng, and J-Ph Poizat. Subnanosecond spectral diffusion measurement using photon correlation. *Nature Photonics*, 4(10):696–699, 2010.

[71] Peter Blood and John Wilfred Orton. *The electrical characterization of semiconductors: majority carriers and electron states*. Academic Pr, 1992.

[72] G. Bacher, A. A. Maksimov, H. Schömig, V. D. Kulakovskii, M. K. Welsch, A. Forchel, P. S. Dorozhkin, A. V. Chernenko, S. Lee, M. Dobrowolska, and J. K. Furdyna. Monitoring statistical magnetic fluctuations on the nanometer scale. *Phys. Rev. Lett.*, 89(12):127201, 2002.

[73] R Hanbury Brown and Richard Q Twiss. Correlation between photons in two coherent beams of light. *Nature*, 177(4497):27–29, 1956.

[74] B. Patton, W. Langbein, and U. Woggon. Trion, biexciton, and exciton dynamics in single self-assembled cdse quantum dots. *Phys. Rev. B*, 68(12):125316, 2003.

[75] G. Bacher, R. Weigand, J. Seufert, V. D. Kulakovskii, N. A. Gippius, A. Forchel, K. Leonardi, and D. Hommel. Biexciton versus exciton lifetime in a single semiconductor quantum dot. *Phys. Rev. Lett.*, 83(21):4417–4420, 1999.

[76] Lucien Besombes. *Spectroscopie optique de boîtes quantiques uniques de semiconducteurs II-VI*. Phd thesis, These de Doctorat de l'Universite Joseph Fourier - Grenoble I, 2001.

[77] Grzegorz Grzela, Ramón Paniagua-Domínguez, Tommy Barten, Yannik Fontana, José A. Sánchez-Gil, and Jaime Gómez Rivas. Nanowire antenna emission. *Nano Letters*, 12(11):5481–5486, 2012.

[78] Max Born and Emil Wolf. *Principles of optics: electromagnetic theory of propagation, interference and diffraction of light*. CUP Archive, 2000.

[79] William H. McMaster. Matrix representation of polarization. *Rev. Mod. Phys.*, 33 (1):8–28, 1961.

[80] Thomas Clement. *Etude par spectroscopie optique de la dynamique de spins dans les nanostructures CdMnTe*. Phd thesis, These de Doctorat de l'Universite Joseph Fourier - Grenoble I, 2009.

[81] Gerald Bastard. *Wave mechanics applied to semiconductor heterostructures*. Les Ulis Cedex: Les Edition de Physique, 1988.

[82] Jochen Feldmann, Steven T Cundiff, Markus Arzberger, Gerhard Böhm, and Gerhard Abstreiter. Carrier capture into inas/gaas quantum dots via multiple optical phonon emission. *Journal of Applied Physics*, 89(2):1180–1183, 2001.

[83] S Marcinkevičius and R Leon. Carrier capture and escape in in x ga 1- x a s/gaas quantum dots: Effects of intermixing. *Physical Review B*, 59(7):4630, 2014.

[84] Stephen J. Blundell and Katherine M. Blundell. *Concepts in Thermal Physics*. Oxford University Press, 2010.

[85] Frederick Reif. *Fundamentals of statistical and thermal physics*. Waveland Press, 2009.

[86] R. Oszwałdowski, P. Stano, A. G. Petukhov, and Igor Žutić. Spin ordering in magnetic quantum dots: From core-halo to wigner molecules. *Phys. Rev. B*, 86(20): 201408, 2012.

[87] R Pässler. Parameter sets due to fittings of the temperature dependencies of fundamental bandgaps in semiconductors. *physica status solidi(b)*, 216(2):975–1007, 1999.

[88] R Pässler. Semi-empirical descriptions of temperature dependences of band gaps in semiconductors. *physica status solidi(b)*, 236(3):710–728, 2003.

[89] L. Besombes, K. Kheng, L. Marsal, and H. Mariette. Acoustic phonon broadening mechanism in single quantum dot emission. *Phys. Rev. B*, 63(15):155307, 2001.

[90] Y.P. Varshni. Temperature dependence of the energy gap in semiconductors. *Physica*, 34(1):149 – 154, 1967.

[91] Casino software: monte carlo simulation of electron trajectory in solids. URL http://www.gel.usherbrooke.ca/casino/What.html.